Development of Improved Numerical Techniques for High Strain Rate Deformation Behaviour of Titanium Alloys



Benjamin Thomas Spencer Cousins

Exeter College

University of Oxford

A thesis submitted for the degree of

Doctor of Philosophy

Michaelmas Term, 2016

Dedications

"Dominus illuminatio mea"

27 Psalm

a psalm of David

[1]The Lord is my light and my salvation-
whom shall I fear?
The Lord is the stronghold of my life-
of whom shall I be afraid?

[2]When the wicked advance against me
to devour me,
it is my enemies and my foes
who will stumble and fall.
[3]Though an army besiege me,
my heart will not fear;
though war break out against me,
even then I will be confident.

[4]One thing I ask from the Lord,
this only do I seek:
that I may dwell in the house of the Lord
all the days of my life,
to gaze on the beauty of the Lord
and to seek him in his temple.
[5]For in the day of trouble
he will keep me safe in his dwelling;
he will hide me in the shelter of his sacred tent
and set me high upon a rock.

[6]Then my head will be exalted
above the enemies who surround me;
at his sacred tent I will sacrifice with shouts of joy;
I will sing and make music to the Lord.

[7]Hear my voice when I call, Lord;
be merciful to me and answer me.
[8]My heart says of you, "Seek his face!"
Your face, Lord, I will seek.
[9]Do not hide your face from me,
do not turn your servant away in anger;
you have been my helper.
Do not reject me or forsake me,
God my Savior
[10]Though my father and mother forsake me,
the Lord will receive me.
[11]Teach me your way, Lord;
lead me in a straight path
because of my oppressors.
[12]Do not turn me over to the desire of my foes,
for false witnesses rise up against me,
spouting malicious accusations.

[13]I remain confident of this:
I will see the goodness of the Lord
in the land of the living.
[14]Wait for the Lord;
be strong and take heart
and wait for the Lord

[1]

Acknowledgements

I owe a debt of gratitude and thanks to so many people who have supported me throughout this battle, this is written to you all...

Thanks to all of those who have provided the strategic plan of attack for this mission. Firstly my academic supervisor, Prof. Nik Petrinic for giving me an opportunity which I never thought possible. The words *"time is our biggest enemy"* have been proven true on many occasions. However, your unwavering enthusiasm and confidence in the eventual success of the project have provided the firm nudge required. The professional working environment which we enjoy is also greatly appreciated, the feeling of being a real person with a real job can not be underestimated during the many hours spent Begbroke. The sacrifices you have made to make these things possible have not gone unnoticed. Secondly to my industrial supervisor Matt Thomas, a huge thank you for your patience throughout this sometime agonisingly slow process. Your reassurance and optimism have been exactly what I needed so many times, as has your enthusiasm for research and collaboration have also guided my career aspirations. Thirdly, I would like to thank Fauzan Adziman who provided much needed feedback and advice towards the final stages of my research. The amount of time that you dedicated to both working with me and sharing your experiences has been truly invaluable and are hugely appreciated. Your attention to detail and thorough working ethic have been essential to the research presented herein.

On the front lines of this battle have been the colleagues around me, all of whom I need to thank for their unabated help whenever called upon. For brevity, I would like to offer special thanks to those who have been unfortunate enough to share a

desk with me over the years. Firstly, thanks go to Antonio Pellegrino, you showed great patience and humility dealing with the hundreds of engineering questions which I fired at you, you also provided a positive and encouraging outlook on the situation which was a great encouragement. Thanks also go to my long suffering extended desk mates, Simone Falco, Kovthaman Murugaratnam and Justus Hoffman. Besides also having patience with my countless questions and constant moaning, I also thank you for the many conversations we shared over the years ranging from studies, relationships, politics, careers and the dealing with the that fact that we're all growing old, regardless of how we try to resist! Finally, my most recent neighbour Antonino Parrinello. It has been a great pleasure to philosophise with you on the deeper meanings of life. Our differing world views and conversations have forced me to think about my faith and how to communicate Christian doctrine more effectively.

A final thank you to all my friends and family who have been with me in the trenches throughout the highs and lows. The battle is won but the war still rages and I know you'll be there with me throughout. Two special thanks go to Esther 'wee-one' Kwan. You have made my time in Oxford a great pleasure, my favourite memories are of coming home and finding you studying then greeting me with a head-butt instead of hello ☺. You work so hard and do so well at everything you turn your attention to, I marvel at your gifts. The journey we have been on together has shaped our spiritual lives and has laid the foundations for our future together as Mr and Mrs. Finally, my Mum. You have never demanded anything from me and shown me immeasurable grace even though I have been far from an attentive son, at times. You seamlessly combine having constant faith in me whilst also reminding me that whatever I achieve or fail to achieve is ultimately irrelevant to your love for me and view of me. This thought never fails to relax me ☺

Development of Improved Numerical Techniques for High Strain-Rate Deformation Behaviour of Titanium Alloys

Benjamin Cousins, Exeter College, University of Oxford
For the degree of D.Phil. in Engineering Science, Michaelmas Term 2016

...

Within the aerospace industry, the reduction of costs associated with operation, manufacture and development of gas turbine engines is a primary objective. Component and assembly design optimisations can satisfy weight reductions which correspond to operational and manufacturing cost reductions. Development cost can be reduced by implementing additional numerical validation stages as an alternative to experimental validation alone. Therefore, the overarching purpose of this research is the development of a computationally efficient constitutive modelling tool, which predicts the macroscopic deformation and failure of fan system components and assemblies during dynamic and highly non-linear thermo-mechanical loading.

At the macroscopic scale a series of physical deformation and failure phenomena have been identified from the literature which are necessary for accurate representation of the dynamic behaviour of Ti-6Al-4V. Across the surveyed literature these capabilities have not been implemented together within a single constitutive framework prior to the commencement of this research. Experimental support provides validation data for the subsequent constitutive modelling activities, whilst also demonstrating the importance of strain-rate sensitivity, tension-compression asymmetry and anisotropic behaviour associated with texture orientation in Ti-6Al-4V. Numerical studies were also conducted to develop a robust procedure for rapid assimilation of uni-axial experimental data within constitutive benchmarking models, for development purposes.

Further parametric studies of sub-component plate impact benchmarks revealed several limitations within the commercially available solutions. These limitations are related to mesh sensitivity and damage evolution. A technique has been proposed

which couples damage evolution and imposes a directional length-scale. This provides enhanced mesh insensitivity and damage evolution rate control. However, a single damage evolution mechanism was demonstrated to be insufficient when representing shear damage mechanisms in uni-axial and multi-axial loading regimes. Therefore, an additional damage mechanism has been developed and coupled with the mesh sensitivity and localisation technique. The resulting cumulative and competitive damage evolution and localisation capabilities reflect the localisation characteristics observed in the literature.

The variability of alloy manufacture and the subsequent macroscopically observed behaviour remain a limitation within an isotropic framework. This has motivated the development of both asymmetric and anisotropic formulations, integrated within the newly proposed multi-mode damage localisation framework. The ability of the newly implemented non-isotropic framework successfully provides both asymmetric yielding and hardening capabilities and anisotropic evolution.

These developments have been demonstrated against experimentally obtained results for validation and calibration purposes. Together these capabilities allow for accurate representation of a wide range of macroscopically observable phenomena based upon micro mechanical mechanisms.

Contents

1 Introduction **1**

1.1 Background and motivation 1

1.2 Aim and objectives 3

1.3 Research strategy 3

1.4 Thesis outline 4

2 Literature Review: Background **6**

2.1 Gas turbines 6

2.1.1 Gas turbine theory 7

2.1.2 Turbofan 8

2.1.3 Fan system 8

2.2 Titanium and titanium alloys 10

2.2.1 Crystallography 11

2.2.2 Alloying Chemistry 13

2.2.3 Microstructure of Ti-6Al-4V 15

2.2.4 Texture of Ti-6Al-4V 16

2.2.5 Manufacture of Ti-6Al-4V 17

2.3 Industrial alloy development 18

2.3.1 Texture control 18

2.3.2 Component lifing techniques 20

2.4 Mechanical performance 21

2.4.1 Elastic deformation 22

2.4.2 Inelastic deformation 23
2.5 Inelastic phenomena in Ti-6Al-4V 25
2.5.1 Strain-rate dependence 25
2.5.2 Temperature dependence 27
2.5.3 Pressure dependence 27
2.5.4 Anisotropic plasticity 28
2.5.5 Failure mechanisms 29
2.6 Summary 30

3 Literature Review: State of the Art **32**
3.1 Continuum mechanics 32
3.1.1 Governing equations 33
3.1.2 Element equations 37
3.1.3 Constitutive modelling approach 38
3.1.4 Continuum damage mechanics 40
3.2 Ductile deformation mechanisms 42
3.2.1 Ductile damage mechanisms 43
3.2.2 Multiple mode damage 47
3.3 Plastic asymmetry and anisotropy 50
3.3.1 Asymmetric deformation 50
3.3.2 Anisotropic deformation 51
3.4 Summary 53

4 Experimental Support **55**
4.1 Uni-axial loading experiments 55
4.1.1 Split-Hopkinson bar 56
4.1.2 Rate sensitivity 67
4.1.3 Directionality trends 71
4.2 Ballistic testing 76

4.2.1 Pressurised gas-gun apparatus 76
4.2.2 Plate impact 79
4.3 Summary 81

5 Constitutive Modelling **82**
5.1 Macroscopic numerical model 82
5.1.1 Constitutive equations 84
5.1.2 Constitutive implementation 93
5.1.3 Constitutive parameters 95
5.2 Uni-axial benchmark 101
5.2.1 Tensile sensitivity 102
5.3 Multi-axial ballistic benchmark 103
5.3.1 Numerical model 104
5.3.2 Ballistic limit simulation 106
5.4 Parametric ballistic study 107
5.4.1 Plate mesh sensitivity 107
5.4.2 Projectile mesh sensitivity 110
5.4.3 Projectile velocity study 111
5.5 Summary 115
5.6 Mesh insensitivity technique 115
5.6.1 Regularisation implementation 116
5.6.2 Regularisation validation 118
5.7 Summary 121

6 Isotropic Damage Developments **123**
6.1 Isotropic damage developments 123
6.1.1 Constitutive equations 124
6.1.2 Constitutive implementation 128
6.2 Isotropic damage validation 130

6.2.1 Tensile damage evolution 131
6.2.2 Tensile damage summary 134
6.2.3 Compressive damage evolution 134
6.2.4 Compressive damage summary 137
6.2.5 Plate impact damage evolution 137
6.2.6 Plate impact damage summary 143
6.3 Summary 143

7 Non-Isotropic Constitutive Developments 145

7.1 Asymmetric developments 145
7.1.1 Constitutive equations 146
7.1.2 Constitutive implmentation 148
7.1.3 Parameter identification 150
7.2 Anisotropic developments 151
7.2.1 Constitutive equations 152
7.2.2 Consitutive implementation 153
7.2.3 Parameter identification 155
7.3 Asymmetric validation 157
7.3.1 Asymmetric yield surface 157
7.4 Anisotropic validation 160
7.4.1 Anisotropic yield surfaces 161
7.4.2 Anisotropic evolution 165
7.5 Summary 172

8 Conclusions 173

8.1 Summary 173
8.2 Contributions 174
8.3 Future work 176

Appendix A Numerical Support **179**

A.1 Software platforms 179

A.1.1 DEST 179

A.1.2 LS-DYNA 180

A.1.3 ABAQUS 181

A.2 Uni-axial simulations 181

A.2.1 Split-Hopkinson Tension Bar 181

A.2.2 Dispersions 183

A.3 Component rationalisation 186

A.3.1 SHTB - 1 187

A.3.2 SHTB - 2 191

A.3.3 SHTB - 3 194

A.3.4 SHTB - 4 198

A.3.5 SHTB - 5 200

A.3.6 Computation time 201

A.4 Summary 201

List of Symbols

Following symbols are used in the present work:

φ	Angle of Internal Friction
F	Anisotropic Objective Parameter
G	Anisotropic Objective Parameter
H	Anisotropic Objective Parameter
L	Anisotropic Objective Parameter
M	Anisotropic Objective Parameter
N	Anisotropic Objective Parameter
A_t	Area of Specimen Cross-Section
A	Area
a	Asymmetric Objective Parameter
b	Asymmetric Objective Parameter
b	Body Force
$\boldsymbol{\sigma}$	Cauchy Stress Tensor
σ	Cauchy Stress
$\bar{\boldsymbol{A}}$	Cell Interior Dislocations
$\bar{\boldsymbol{K}}$	Cell Structure Dislocations
$l_{cr.I}$	Characteristic Length - Dilatational Damage
$l_{cr.II}$	Characteristic Length - Distortional Damage
c	Cohesion
σ_f^c	Compressive Failure Strength
$\overset{\nabla}{\boldsymbol{\sigma}}$	Convected Cauchy Stress Tensor

$\overset{\nabla}{\boldsymbol{\alpha}}$	Convected Kinematic Hardening Tensor
J	Coordinate Space Jacobian
σ_y	Current Yield Stress
$\boldsymbol{F}^v$	Deformation Gradient - Dilatational Plastic
$\boldsymbol{F}^p$	Deformation Gradient - Distortional Plastic
$\boldsymbol{F}^e$	Deformation Gradient - Elastic
ς	Deformation History Stress Function
$\mathbf{B}$	Deformation Matrix
$\bar{\rho}$	Density (Intermediate Configuration)
ρ	Density
J_2	Deviatoric Stress Invariant
J_3	Deviatoric Stress Invariant
$\boldsymbol{\sigma}'$	Deviatoric Stress Tensor
m	Dilatational Damage Growth Exponent
D_v	Dilatational Damage
N	Distortional Damage Growth Denominator
n	Distortional Damage Growth Exponent
D_d	Distortional Damage
Ω	Domain
η	Drucker Prager Objective Parameter
ζ	Drucker Prager Objective Parameter
$\bar{\alpha}$	Effective Back-Stress
σ_{ef}	Effective Stress
d_{ii}	Eigenvalues of the Rate of Deformation Tensor
e_{ii}	Eigenvectors of the Rate of Deformation Tensor
$\boldsymbol{w}^e$	Elastic Spin Tensor
$\bar{\boldsymbol{E}}_e$	Elastic Strain
c_e	Elastic Wave Speed

$\mathbf{v}^e$	Elemental Velocity Vector
v^e	Elemental Velocity
S	Entropy
ε_f	Failure Strain
F	Force
Ψ	Free Energy function
$\mathbf{f}^{\mathrm{ext}}$	Global External Nodal Forces
$\mathbf{f}^{\mathrm{int}}$	Global Internal Nodal Forces
$\mathbf{M}$	Global Mass Matrix
$\bar{\boldsymbol{q}}$	Heat Flux
q_f	Heat Flux
q_s	Heat Source
I_1	Hydrostatic Stress Invariant
σ_h	Hydrostatic Stress
l_s^t	Incident Displacement Wave
u_i	Incident Displacement Wave
ε_i	Incident Wave Strain
ρ_0	Initial Density
β	Initial Rate and Temperature Dependent Yield
v_0	Initial Velocity
R_d	Isotropic Hardening Dynamic Recovery
κ	Isotropic Hardening Scalar
R_s	Isotropic Hardening Static Recovery
H	Isotropic Hardening
r_d	Kinematic Hardening Dynamic Recovery
$\boldsymbol{\xi}$	Kinematic Hardening Function
r_s	Kinematic Hardening Static Recovery
$\bar{\xi}$	Kinematic Hardening Tensor Magnitude

$\boldsymbol{\alpha}$	Kinematic Hardening Tensor
h	Kinematic Hardening
λ	Lamé's Constant
r_{00}	Lankford Parameter - Normal to Rolling Direction
r_{90}	Lankford Parameter - Perpendicular to Rolling Direction
r_{45}	Lankford Parameter - Tangential to Rolling Direction
l	Length
c_l	Longitudinal Wave Propagation Velocity
r_f^α	Major Radius of Failure Specimen
r_0^α	Major Radius of Specimen
X	Material Lagrangian Coordinates
r_f^β	Minor Radius of Failure Specimen
r_0^β	Minor Radius of Specimen
c_n	Non-Longitudinal Wave Propagation Velocity
c_n	Objective Functions
A_0	Original Area
l_0	Original Length
$\mathbf{P}$	P Matrix
δ	Phase Angle
c_p	Plastic Wave Speed
ν	Poisson's Ratio
$\bar{t}_x$	Prescribed Traction
$\bar{v}$	Prescribed Velocity
p	Pressure
$\mathbf{n}$	Radial Return Unit Vector
V	Rate Dependence of Yield
f	Rate Dependent Transition
Y	Rate Independent Yield

D_t	Rate of Deformation at Traction Boundary
D_v	Rate of Deformation at Velocity Boundary
t_{II}	Rate of Deformation Normal Vector - Dilatational Damage
n_I	Rate of Deformation Vector - Dilatational Damage
n_{II}	Rate of Deformation Vector - Distortional Damage
D_x	Rate of Deformation
z	Reference Point
u_r	Reflected Displacement Wave
ε_r	Reflected Wave Strain
σ_{sat}	Saturation Stress
$\mathbf{N}$	Shape Function
μ	Shear Modulus
$\boldsymbol{w}$	Skew Symmetric Velocity Gradient
x	Spatial Eulerian Coordinates
C_v	Specific Heat
l_s	Specimen Length
c_m	Speed of Sound in the Material
ε	Strain
$\dot{\varepsilon}$	Strain-rate
R_{ij}	Stress Ratios
$\boldsymbol{d}$	Symmetric Velocity Gradient
G_t	Tangent Modulus
θ	Temperature
T	Temperature
σ_f^t	Tensile Failure Strength
p_t	Tensile Pressure
t	Time
D_t	Total Damage

$\boldsymbol{F}$	Total Deformation Gradient
Γ_t	Traction Boundary
ε_t	Transmitted Wave Strain
χ_v	Triaxiality - Dilatational Damage
χ_d	Triaxiality - Distortional Damage
Γ_v	Velocity Boundary
$\boldsymbol{L}$	Velocity Gradient
v	Velocity
$\mathscr{P}$	Virtual Power
γ	Visco-Plastic Multiplier
$\bar{\boldsymbol{\Phi}}$	Void Dislocations
$\boldsymbol{d}^{pl}$	von Mises Effective Plastic Strain-Rate Tensor
$\bar{d}^p$	von Mises Effective Plastic Strain-Rate
$\bar{d}$	von Mises Effective Strain-Rate
$\boldsymbol{d}^e$	von Mises Effective Strain-Rate
ω	Wave Frequency
Λ	Wave Length
Φ	Yield Function
E	Young's Modulus

List of Figures

2.1 Turbofan illustration highlighting critical design features and engine stages, R-R © 9

2.2 a) Hexagonal Close Packed (HCP) atomic structure, b) Body Centred Cubic (BCC) crystal structure. 11

2.3 a) Pseudo-binary titanium phase diagram b) Characteristics of titanium phase groups. 12

2.4 Alloying element formations: a) substitutional alloys, and b) interstitial alloys. 14

2.5 Typical Ti-6Al-4V microstructures. a) lamellar, b) bimodal (duplex), c) equiaxed [18] 15

2.6 Ti-6Al-4V micrograph RVE texture map. a) Macro-zone, b) expanded macro-zone texture, c) expanded microstructure texture, courtesy of TIMET. 16

2.7 HCP crystallographic slip system examples. 19

2.8 Elastic response of titanium HCP single crystal as a function of declination angle from the *c*-axis [14] 22

2.9 Elastic-plastic stress strain response of a generic alloy during deformation. 23

2.10 Shear strain dislocation motion representation through a crystal lattice. 24

2.11 Shear strain twinning re-orientation representation. 24

2.12 Failure surface depicting both brittle and ductile failure modes. . . . 30

3.1 Reference initial and deformed current configurations in a one-dimensional beam with a fixed end and loaded end. 34
3.2 Generalized schematic representing modelling approaches and their associated computational cost and physical length scales considered for a similar scale problem. 39
3.3 Damage mechanics and fracture mechanics definition reference schematic and specific terminology. 41
3.4 Emerging discontinuities due to void nucleation, growth and coalescence in tension due to initial defect presence. 44
3.5 Dynamic shear band formation in a torsional specimen, macroscopic and microscopic shear band evolution [87]. 45
3.6 Cross section displaying the transition between pure shear and a combination of shear and bending [93]. 46
3.7 Micro-void formation within a shear band plastic zone, adapted from [78]. 48
3.8 Uni-axial compression specimen shear plane tensile and shear stress regional distribution and equatorial plane. 48
3.9 Generalised average stress triaxiality χ and failure strain ε_f locus with associated dominant damage mechanisms. 49
3.10 Fragment Simulating Projectile (FSP) impact cross-section in Ti-6Al-4V annealed below a) and above b) the β transus. 52
3.11 Constitutive modelling solutions corresponding to identified capability requirements. 54

4.1 Typical experimental techniques for a range of strain-rates. 56
4.2 Specimen, incident and transmitted bar interfaces. 57
4.3 Strain gauge signals demonstrating the individual signals received during a SHPB experiment. 58

4.4 Schematic diagram of split-Hopkinson pressure bar arrangement and Lagrangian diagram illustrating stress wave propagation. 60
4.5 Experimental apparatus: a) Electrically screw driven ZWICK 250, b) Tension and compression Hopkinson bars, c) SIMX16 ultra high-speed camera. 62
4.6 Tensile specimen at various strain rates, including critical dimensions. 63
4.7 Compression specimen at various strain rates, including critical dimensions. 63
4.8 Compression dog-bone specimen at various strain rates, including critical dimensions. 64
4.9 Input and output bar forces achieved in tension, with corresponding stain-rate history. 65
4.10 Strain history tension of Ti-6Al-4V during high strain-rate tensile deformation. 65
4.11 Input and output bar forces achieved in compression, with corresponding stain-rate history. 66
4.12 Strain history tension of Ti-6Al-4V during high strain-rate compressive deformation. 66
4.13 Observed macroscopic tensile flow-stress strain-rate sensitivity of Ti-6Al-4V. 68
4.14 Quasi-statically loaded tensile specimens at the point of fracture. . . 69
4.15 High strain-rate loaded tensile specimens at the point of fracture. . . 69
4.16 Observed macroscopic compressive flow-stress strain-rate sensitivity of Ti-6Al-4V. 70
4.17 Quasi-statically loaded compression specimens at the point of fracture. 70
4.18 High strain-rate loaded compression specimens at the point of fracture. 70
4.19 Quasi-static macroscopically observed tangential and axial flow-stress discrepancy trends. 72

4.20 Yield stress and flow stress behaviours for quasi-static tangential and axial tension. 72
4.21 Medium strain-rate macroscopically observed tangential and axial flow-stress discrepancy trends. 73
4.22 Yield stress and flow stress behaviours for medium-rate tangential and axial tension. 74
4.23 High strain-rate macroscopically observed tangential and axial flow-stress discrepancy trends. 75
4.24 Yield stress and flow stress behaviours for high-rate tangential and axial tension. 75
4.25 In-house ballistic gas-gun apparatus with multiple camera arrangement. 77
4.26 Digital image processing with in-house motion tracking software. . . . 78
4.27 Flat-nosed, normal impact experimental arrangement with critical dimensions. 78
4.28 Plate preparation for the applied fixture technique with drilled hole positioning and dimensioning. 79
4.29 Flat-nosed, normal impact image stream illustrating penetration and plugging failure. 80

5.1 Kinematics of dilatational and distortional plastic material in terms of deformation gradient components. 85
5.2 Empirical yield function parameter schematic. 97
5.3 Rate dependence of yield stress, assuming no influences of recovery term ($R_s = R_d = r_s = r_d = 0$), resulting in bilinear hardening. 99
5.4 Parameter optimisation tool for the BCJ model. 100
5.5 Mesh discretisation in the longitudinal direction. 102
5.6 Numerical versus experimental data demonstrating the effect of uniaxial mesh sensitivity in tension at high strain-rates. 103
5.7 Plate impact numerical benchmark arrangement. 105

5.8 Parametric mesh adaptations in both target plate and projectile. . . . 105
5.9 Cross-section view of 125m/s impact event at $t = 300.0\mu$s. 106
5.10 Cross-section view of 142m/s impact event at $t = 300.0\mu$s. 107
5.11 Cross-section view of lateral and axial target plate mesh density variation matrix trials. 108
5.12 Axial velocity profiles of plate mesh variation. 108
5.13 Peak target plate stress concentrations in the lateral position. 109
5.14 Cross-section view of projectile mesh density and lateral target plate mesh density variation matrix. 110
5.15 Axial velocity profiles of projectile mesh and plate mesh variation. . . 111
5.16 Increased velocity trials of E2 mesh configuration, from Figure 5.14. . 112
5.17 Residual velocities for E2 mesh configuration when varying initial velocity. 113
5.18 Increased velocity trials of I3 mesh configuration, from Figure 5.14. . 113
5.19 Residual velocities for I3 mesh configuration when varying initial velocity. 114
5.20 Plug formation for E2 and I3 mesh configurations when subjected to increased impact velocities. 114
5.21 Dilatational damage mode specific planes of emerging discontinuities with associated element characteristic length depictions. 117
5.22 Results of uni-axial mesh in-sensitivity in tension at high strain-rates. 119
5.23 Quarter geometry ballistic limit impact simulations depicting plastic strain accumulation across multiple mesh densities. No Regularisation: A, B and C. Regularisation: D, E and F. 120

6.1 Central element erosion resulting in non-physical fracture during uni-axial compression at high strain-rates. 124
6.2 Distortional damage mode specific planes of emerging discontinuities with associated element characteristic length depictions. 126

6.3 Stress contours and erosion of the central element via dilatational damage growth and necking due to distortional damage. 131
6.4 Dilatational damage contours of high strain-rate uni-axial tension specimen during plasticity, prior to element erosion. 132
6.5 Dilatational damage of high strain-rate uni-axial tension specimen during plasticity, prior to element erosion. 132
6.6 Distortional damage contours of high strain-rate uni-axial tension specimen during plasticity, prior to element erosion. 133
6.7 Distortional damage of high strain-rate uni-axial tension specimen during plasticity, prior to element erosion. 133
6.8 Stress contours and erosion on the 30° plane via distortional damage. 135
6.9 Dilatational damage contours of high strain-rate uni-axial compression specimen during plasticity, prior to element erosion. 135
6.10 Dilatational damage of high strain-rate uni-axial compression specimen during plasticity, prior to element erosion. 136
6.11 Distortional damage contours of high strain-rate uni-axial compression specimen during plasticity, prior to element erosion. 136
6.12 Distortional damage evolution of high strain-rate uni-axial compression specimen during plasticity, prior to element erosion. 137
6.13 Isometric view of target plate rear face with initial velocity of 125 m/s 138
6.14 Isometric view of target plate rear face with initial velocity of 142 m/s 139
6.15 Quarter cross-section view of target plate impact at 142 m/s, contours of dilatational damage. 140
6.16 Probe dilatational damage evolution at 142 m/s, from Figure 6.15. . . 140
6.17 Quarter cross-section view of target plate impact at 142 m/s, contours of distortional damage. 141
6.18 Probe distortional damage evolution at 142 m/s, from Figure 6.17. . . 141
6.19 Element failure characteristics surrounding the ballistic limit. 142

6.20 Element failure and plastic strain localisation at upper and lower bounds of the ballistic limit range. 142

7.1 Two dimensional representation of Drucker-Prager parameters and conical yield surface. 147

7.2 Original circular and elliptical failure profile of a specimen with Lankford parameters. 157

7.3 Normalised influence of the Drucker-Prager friction angle φ on the initial yield surface in principal stress space. 158

7.4 Normalised influence of the Drucker-Prager cohesive intercept c on the initial yield surface in principal stress space. 158

7.5 Experimentally obtained SD effect of absolute uni-axial tension and compression data for Ti-6Al-4V at high strain-rates. 159

7.6 Strength Differential (SD) capabilities for initial yield strength in two-dimensional principal stress space for Ti-6Al-4V at high strain-rates. . 159

7.7 Normalised yield locus evolution of anisotropic Hill parameter F, in isolation. 161

7.8 Normalised yield locus evolution of anisotropic Hill parameter G, in isolation. 162

7.9 Normalised yield locus evolution of anisotropic Hill parameter H, in isolation. 162

7.10 Hill yield surface due to variation of the orthotropic direct stress σ_2. . 163

7.11 Parameter variation relationship for isolated direct stress evolution. . 164

7.13 Effect of shear stress on the Hill yield surface. 164

7.12 Hill yield surface due to variation of the orthotropic transversal stress σ_3. 165

7.14 Load-Extension plots of selected axially and tangentially loaded experimental tension specimens at high strain-rates. 166

7.15 Selected frames during high strain-rate deformation of tangential tension experiments, evaluated using DIC. 167
7.16 Area reduction measurement in a one-dimension based upon DIC particle tracking. 167
7.17 Evolution of the reduction of area and engineering strain during deformation via. Digital Image Correlation. 168
7.18 Lankford parameters estimation based upon a numerical and experimental approach. 168
7.19 Resultant yield surface of high strain-rate Ti-6Al-4V in the tangential direction. 169
7.20 Numerical approximation of high strain-rate axial and tangential tensile experiments. 170
7.21 Numerical approximation of high strain-rate axial orientation tensile experiments. 171
7.22 Numerical approximation of high strain-rate tangential orientation tensile experiments. 171

8.1 Constitutive modelling features developed and implemented during this research. 176

Chapter 1

Introduction

This chapter introduces the work presented within this thesis. Factors affecting the modern civil aerospace industry, within the scope of Impact Engineering, shall be discussed to establish the necessity of the undertaken research and to define the research requirements. The overall objectives of this research and the milestones for their realisation are presented in the aims and objectives. The sequence of completed research and subsequent documentation are briefly summarised in the research strategy and thesis outline sub-sections.

1.1 Background and motivation

Across most industries, competition dictates that costs incurred by the customers be minimised; for commercial airline companies this manifests itself in the reduction of operating costs and / or manufacturing costs. In response, Original Equipment Manufacturers (OEM) such as Airbus, Boeing, Bombardier and their suppliers, such as Rolls-Royce and General Electric, are required to provide products with increased performance and efficiencies whilst maintaining safety tolerances and minimising costs.

Titanium alloys in the fan system constitute a large proportion of total engine weight; therefore increased design efficiencies correspond to potentially significant reductions in relation to manufacturing and operational costs. Achieving these savings necessitates a concurrent and innovative approach throughout the research and

design phases. To remain at the forefront of their respective industries, Rolls-Royce Plc (R-R) and Titanium Metals Corporation (TIMET) work in close collaboration throughout the design and innovation processes by providing their respective expertise in both design and fundamental materials science. Titanium alloys feature a strong macroscopically observable strain-rate sensitivity which is primarily characterised by increased yield and flow stresses at high strain-rates. Understanding this unique characteristic allows engine designers to exploit the improved strength-to-weight ratios of titanium alloys at high strain-rates. Therefore providing the opportunity to reduce component weight through design optimisation, whilst also improving the understanding of dynamic deformation and fracture for enhanced containment design strategies.

Certification authorities such as the European Aviation Safety Agency (EASA) mandate that any such design modifications or innovations be subject to comprehensive validation procedures. An entirely empirical validation approach would be excessively expensive and exceptionally time consuming. Therefore, numerical modelling techniques are becoming increasingly essential during both research and design. The ability to accurately predict highly non-linear dynamic and ballistic events such as the containment of failed rotating components within the fan system is not only beneficial for industry but presents a highly challenging academic endeavour. Current experimental techniques provide limited actionable data during complex dynamic experiments, such as 'bird-strike' and 'blade-off events'. Numerical evaluation provides an actionable assessment of large-scale component and assembly failure processes. Furthermore, numerical techniques allow for the influence of bespoke metallurgical factors - such as texture - to be assessed, providing opportunities for bespoke alloy developments for specific design challenges.

To develop this capability, a deep understanding of the physical phenomena of deformation and failure is required. Secondly, justification of the analytical approach to represent these phenomena is also required. Finally, to provide a feasible solution for

industrial scale applications both accuracy and computational efficiency are needed.

1.2 Aim and objectives

The aims of this project are to provide a systematically enhanced numerical framework which forms the basis for improved gas turbine fan systems design for industrial applications. This overarching aim can be segregated into a series of logical objectives as follows:

- Review of the physical phenomena during dynamic failure in titanium alloys shall be established as a basis for the development of an appropriate numerical framework.
- Identification of the limitations of current macroscopic constitutive numerical frameworks available to industry.
- Development of novel numerical solutions, which demonstrate enhanced predictive capabilities for highly non-linear thermo-mechanical deformation of titanium alloys during dynamic events.
- Demonstration and validation of newly developed capabilities based upon in-house data, observations within the literature and numerical benchmarking.

1.3 Research strategy

The above aims and objectives were guided by a comprehensive literature review. Commercial and in-house software packages were used for numerical comparisons. For numerical simulations to be developed, high strain-rate uni-axial and sub-component simulations were evaluated in terms of their applicability and reliability. Mesh sensitivity due to the limitations of the finite element discretisation technique were highlighted as a limitation during dynamic simulations, subsequently, a technique was proposed which minimises this effect. Representative damage localisation was also

identified as being insufficient within commercially available software, therefore an additional damage mode coupled with a localisation technique has been developed. Finally, the importance of texture was evident throughout the literature: the proposed framework was further expanded to incorporate the effects of anisotropy and asymmetry as a consequence of industrial manufacturing processes. These developments were validated against experimental data and the respective improvements were compared against commercially available solutions at each development stage.

1.4 Thesis outline

This thesis is structured into nine chapters which address current research challenges surrounding the *'Development of Improved Numerical Techniques for High Strain-Rate Deformation Behaviour of Titanium Alloys'*.

Chapter 2 documents the wider contextual literature from gas turbines technologies to metallurgical aspects. This literature review continues in Chapter 3 which explores the literature related to the most pertinent metallurgical phenomena in Ti-6Al-4V and their associated numerical solutions. Together these two chapters establish the objectives of this research from both a metallurgical perspective and from a numerical basis, by identifying limitations and gaps in currently available techniques.

Chapter 4 provides the experimental support for development of models capable of capturing the physical behaviour of Ti-6Al-4V at high strain-rates, the influence of strain-rates and texture are also self-evident from in-house experiments. The appropriateness of numerical reduction benchmarking at high strain-rates is studied within Appendix A. Together these provide a robust approach for further benchmarking exercises, which accurately capture the experimental kinematics and allows for coupling with experimental techniques.

Analysis of the constitutive framework and the development of mesh insensitive constitutive model are presented within Chapter 5. Constitutive developments surround a mesh insensitivity technique coupled with damage are demonstrated and

validated. The development of an isotropic damage constitutive model is described in Chapter 6; this includes constitutive formulations and validation simulations for multi-mode damage in uni-axial and impact scenarios. Chapter 7 focusses on the expansion of the isotropic framework to include asymmetric and anisotropic effects based upon experimentally observed behaviour. Together these chapters address the pertinent phenomena identified within the literature which are required to describe the high strain-rate behaviour of titanium alloys.

The conclusions in Chapter 8 summarise the overall contributions and learning outcomes of the current research. In addition, the proposed enhanced numerical framework shall facilitate further work in the fields of element failure techniques and multi-scale approaches, thus providing complimentary research fields which further benefit macroscopic modelling challenges.

Chapter 2

Literature Review: Background

This chapter introduces the wider literature to contextualise the aforementioned motivations for the undertaken research. The topics which are necessary to contextualise this research range from application to the end-product, through the associated metallurgical effects and culminate with the related computational tools. These closely related research fields are discussed to provide the theoretical background required for detailed discussions.

2.1 Gas turbines

A brief background of the gas turbine shall first be given, culminating in components of the engine relevant to this research. The design and manufacture of gas turbine engines remains one of the most advanced technological engineering challenges. Applications of this technology are found in aerospace propulsion, marine propulsion and industrial power generation. For the purposes of this research the R-R Trent family of aero engines, hereafter simply referred to as gas turbines, shall form the focus of discussion.

Fundamentally, gas turbines consist of three main stages: compressor stages, combustion chamber and turbine stages. Sir Frank Whittle registered the first patent in 1930 for a turbojet design which first flew in 1941. Simultaneously, Dr Hans von Obain was granted a similar patent in 1936 and recorded the first operational flight

in 1939. Therefore, both men are generally regarded as the co-inventors of jet engine technology.

2.1.1 Gas turbine theory

The gas turbine applies thermodynamic principles known as Boyle's Law, Charles's Law and the Gay-Lussac's Law in a continuous cycle known as the Joule-Brayton cycle. This consists of adiabatic compression whilst atmospheric air is drawn in by the fan system and compressed to higher pressures through the multiple compressor stages. Following this, isobaric heating takes place as compressed air is mixed with fuel and ignited creating high gas pressure, temperature and velocities. Energy from adiabatic expansion is extracted from the high pressure and velocity gas flow during explosive expansion through the turbine section. Finally, isobaric cooling occurs as air is cooled and ejected in the form of a high speed jet, producing thrust. More detailed descriptions of the thermodynamics of gas turbines can be found in numerous sources [2, 3].

All applications of this technology share these fundamental principles yet utilise the energy produced in a variety of methods. Industrial static gas turbines are used to drive electrical generators, whilst marine applications extract energy to operate pumps and other electro-mechanical devices such as propellers; these are both large-scale turbine applications. Similar arrangements exist in aerospace applications, however greater emphasis is placed on weight reduction. The turboprop (or turboshaft) design utilises maximum energy from the exhaust flow which is then transmitted to a shroud-less fan system. These are typically used for helicopters, where high efficiencies can be achieved when operating at relatively low aircraft velocities. Conversely, the turbojet design has far lower efficiencies, as the fuel consumption rate J_c increases faster than the propulsive engine thrust J_t can provide. The proportionality of the jet (v_{jet}) in relation to the fuel consumption and thrust are described in equations

(2.1) and (2.2).

$$J_t \propto v_{jet} \tag{2.1}$$

$$J_c \propto v_{jet}^2 \tag{2.2}$$

Propulsive thrust is generated by the jet air stream; this allows the turbojet to excel when comparing thrust per unit weight and unit volume. Supersonic military aircraft take advantage of these unique features [4].

2.1.2 Turbofan

However, modern developments in gas turbine technologies have produced the turbofan design, which is used extensively across the civil aerospace industry due to the high thrust capabilities and relative fuel efficiencies. The turbofan design uses a low pressure turbine at the rear of the engine to drive the intake fan system at the front of the engine [5, 6]. The additional fuel consumption required to drive the fan system is small; however at high bypass ratios of 10:1 the fan provides approximately 80% of the engine's total thrust, thus operating as a shrouded propeller. The enclosed fan and increased number of blades enables efficient operation at higher aircraft velocities, when compared to open rotor turboprops. In addition, the fan casing and elimination of afterburners - common in turbojet designs - reduces noise emissions. Within the Rolls-Royce product portfolio these engine designs are referred to as low specific thrust, high-bypass turbofans; they operate most efficiently at airspeeds of 310 mph to 620 mph, directly between turboprops and turbofan flight speeds [4].

2.1.3 Fan system

The transition from turbofan design concept to commercial success has included numerous innovations from both industrial and academic collaborators. Within the fan systems the recent wide-chord fan blade - developed by R-R - is one such example. The super plastically formed blades are manufactured by diffusion bonding

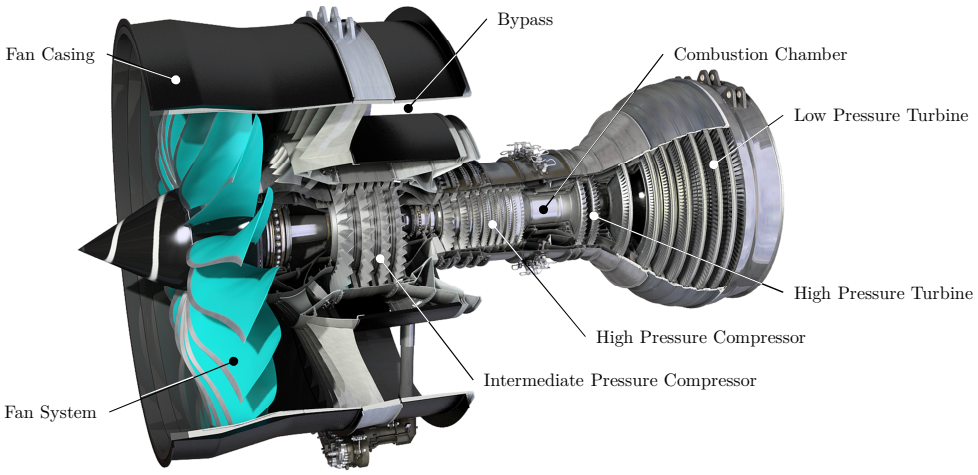


Figure 2.1: Turbofan illustration highlighting critical design features and engine stages, R-R ©

several sections before hot creep forming into the optimal profile [7]. Other technologies include the single-piece ring rolled casing structure. These novel manufacturing techniques were developed concurrently with alloy manufacturers, such as - TIMET - in order to achieve optimal specification. Furthermore, analytical techniques such as Finite Element Analysis (FEA) and Computational Fluid Dynamics (CFD) have also been developed in collaboration with University Technology Centres (UTC's). These contribute towards the holistic approach necessary to enable efficient fan system performance.

Regardless of design optimisation, blade failure events due to high cycle fatigue, bird strike, foreign object damage, overheating, initial material defects and other factors are critical during casing design to maintain aircraft safety. In the unfortunate event of blade release the casing experiences a series of damage stages. Firstly, scratching of the inner surface of the casing occurs due to the blade tip misalignment. Secondly, the casing plastically bulges and eventually forms a crack. Thirdly, crack propagation occurs due to tearing, this is highly sensitive to structural design [8]. During the first stage the blade tip experiences blunting due to bending and compression. The bulge formation acts as the primary energy absorption mechanism for casing components and the crack formation is largely bi-axial tension. This ductile

energy absorption process is where highly non-liner constitutive models are required.

Although full engine blade-off tests are mandated by aviation authorities, they remain extremely expensive and produce limited data due to their inherent complexities. Combined experimental and numerical techniques are therefore used to study these impact events, which are validated against sub-assembly test data. This combined approach results in cost and time reductions, and also increases overall knowledge of structural loading conditions and relative failure modes. Several aspects of these events have been simulated; Carney et al. [9] demonstrated fragmentation, blade-blade interaction and blade-case interactions. The importance of engine-airframe interactions where discussed by Sinah [10] in relation to maintaining dynamic fidelity. Overall mesh size sensitivity and element failure were stated as areas of improvement by Knight Jr et al. [11] and Ambur et al. [12] during simulation. These simulated scenarios highlight the importance of predictive techniques for design and certification in the event of blade containment failure. This research therefore is intended to form part of the numerical design process for fan system optimisation.

2.2 Titanium and titanium alloys

Over the past two decades the gas turbine industry has grown in parallel with the titanium industry. For example, TIMET is the world leading manufacturer of titanium based metal products; their commercial aerospace market accounts over 60% of their +$1 billion annual revenues. Currently titanium products are used for fan blades, discs and casing structures. The density of commercial pure (CP) titanium, $4.5\,\mathrm{g/cm^3}$, does not vary significantly when combined with strengthening alloying element and therefore exhibits a unique strength-to-weight ratio in alloys such as Ti-6Al-4V. Titanium also remains mechanically stable across a range of temperatures and features good environmental degradation resistance, all of which are essential in gas turbine technologies. However, the operational temperatures found in gas turbine engines limit the use of titanium to cooler regions of the engine such as the fan system,

certain compressor components and portions of the fan casing.

The physical metallurgy of titanium is a broad field; the fundamentals relating to macroscopic deformation shall be explored to inform requirements during constitutive developments. Detailed summaries of the physical metallurgy of titanium can be found in numerous sources [13, 14].

2.2.1 Crystallography

Crystalline structures classify the average position of atoms within a unit cell and are measured on the atomistic scale. Two crystalline structures exist in commercially-pure (CP) titanium known as the α-phase (HCP) and β-phase (BCC). These structures are depicted in Figures 2.2 and 2.3 from [15].

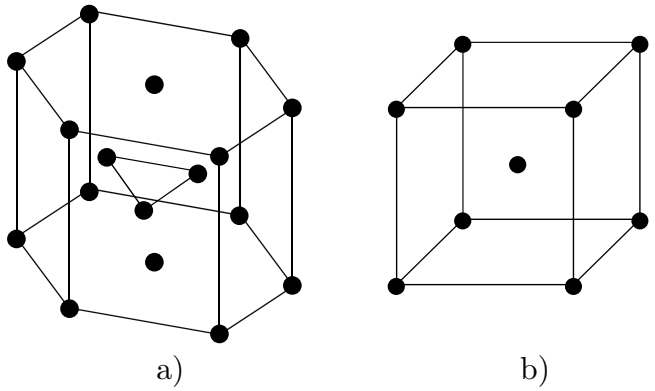


Figure 2.2: a) Hexagonal Close Packed (HCP) atomic structure, b) Body Centred Cubic (BCC) crystal structure.

Titanium alloys generally have large volume fractions of the HCP α-phase, the α-phase remains stable up to 882°C, beyond this transus temperature the β-phase transformation occurs. Additional alloying elements allow the manufacturer to stabilise each phase individually, thus altering the proportions of each phase at room temperature by adjusting the β transus temperature. Furthermore, the morphology of each of these phases varies depending upon process history by creating bimodal structures designed for specific applications [16].

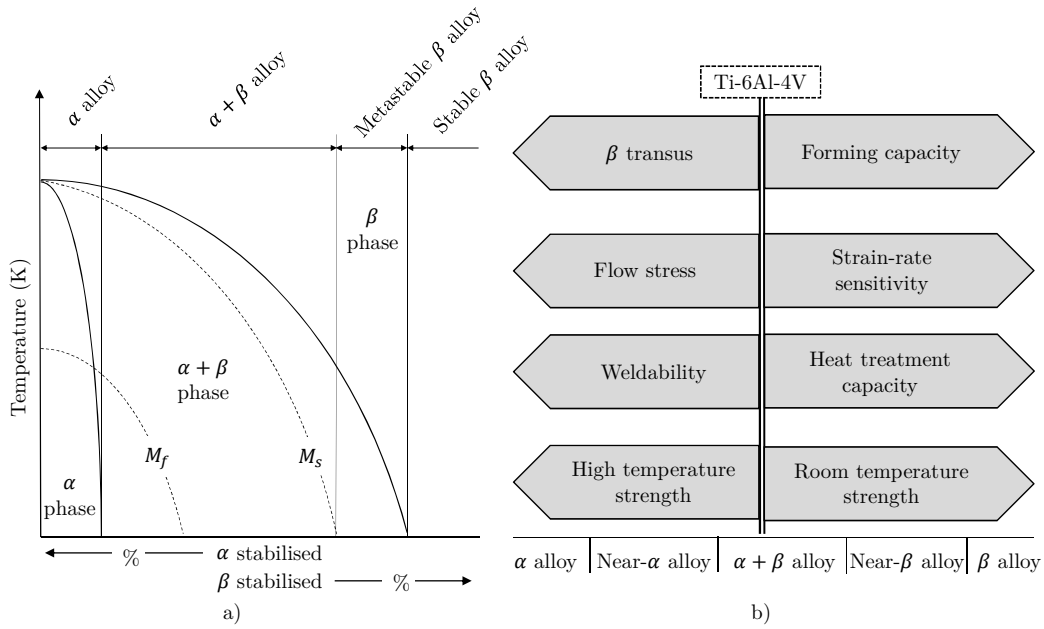


Figure 2.3: a) Pseudo-binary titanium phase diagram b) Characteristics of titanium phase groups.

Titanium alloys pass through a Martensitic transformation phase ($M_f - M_s$) and are broadly classified as being alpha (α), beta (β) or alpha-beta ($\alpha+\beta$) and have the following general characteristics - listed below and in Figure 2.3 - which are exploited for varying applications:

- α-phase alloys: Generally, these alloys demonstrate good weldability whilst beneficial mechanical properties are not easily achieved via heat treatment. They exhibit comparatively lower yield strength with reasonable notch toughness and ductility. Both α and near-α alloys demonstrate high temperature creep strength and oxidation resistance [15].

- β-phase alloys: Similarly, β or near-β alloys offer good weldability. Conversely, they exhibit beneficial mechanical properties during heat treatment and exhibit higher yield strength up to intermediate temperatures. Cold formability also remains sufficient when in a solution treated condition. Common beta stabilising elements include molybdenum and vanadium which are mutually soluble; whilst chromium and manganese form intermetallic compounds by eutectoid

decomposition. This list is not exhaustive, but merely demonstrates the two categories which beta stabilising element can be described [15].

- $\alpha+\beta$ alloys: The $\alpha+\beta$ alloys vary in heat treatability; ductility can also be lost within welded regions of the material. Their creep strength also varies between medium and high [15]. This demonstrates the versatility of $\alpha+\beta$ alloys but also the variability as a consequence of manufacturing.

2.2.2 Alloying Chemistry

Within the categories described above, titanium alloys exist in numerous different grades depending on the chemical composition, ASTM (American Society for Testing and Materials) currently recognises over 30 grades. Commercially pure titanium exists in several different ASTM grades depending on impurities present, such as Oxygen, which ranges from 0.18 - 0.40 wt%. These compositional variations can increase both the Ultimate Tensile Strength (UTS) and proof strength by 210 MPa and 310 MPa, respectively [13]. Oxygen dissolves preferentially in the α-phase and is known as an interstitial element which increases the transformation temperature and also contributes to hardening within the secondary α phase. An interstitial element is characterised by an atomic radius $< 60\%$ that of the host element; these smaller elements interfere with the electrical conductivity and restrict lattice movements, thus creating a higher strength alloy.

The atomic radii of substitutional elements differ by $\pm$ 15% of the host element. This distorts the host lattice and restricts the slip of atomic planes which creates a strengthening mechanism. This is demonstrated in a simple schematic representation of atomic positioning shown in Figure 2.4. The most common titanium alloy in structural aerospace applications is Ti-6Al-4V which is a two phase $\alpha+\beta$ alloy featuring a unique combination of workability, durability and availability whilst maintaining a good strength-to-weight ratio. The constituent chemical alloying elements, and their stabilising characteristics are listed in Table 2.1, courtesy of TIMET and from [13].

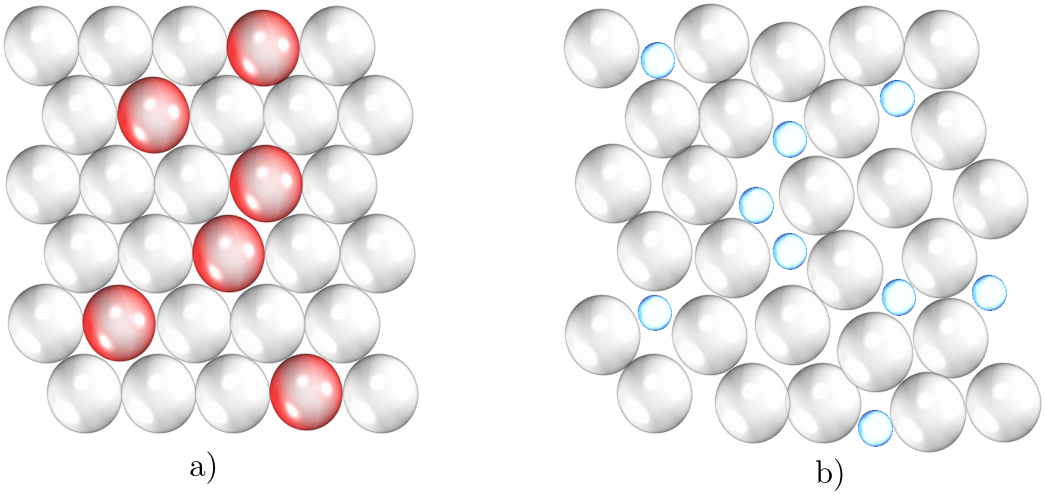


Figure 2.4: Alloying element formations: a) substitutional alloys, and b) interstitial alloys.

This is the alloying chemistry which shall be assumed when discussing Ti-6Al-4V. Substitutional elements, such as aluminium, are preferentially soluble in the α phase and increase the transformation temperature. Interstitials elements such as carbon and nitrogen also increase transformation temperatures. Other interstitials, such as hydrogen, preferentially dissolves in the β phase, thus decreasing the transformation temperature of Ti-6Al-4V. Other β stabilisers are either isomorphorous or eutectoid elements; isomorphorous elements such as molybdenum improve forgability and heat treatability in Ti-6Al-4V. Eutectoid elements such as iron and copper improve hardenability [16]. Silicon acts to segregate dislocations which prevents dislocation climb resulting in creep resistance [17].

For the purpose of this thesis, Ti-6Al-4V shall be the primary focus. Apart from alloying chemistries, the microstructure, texture and processing routes also signi-

Table 2.1: Chemical composition and alloying element stabilising properties of TIMET 6-4 Titanium Alloy (Ti-6Al-4V; ASTM Grade 5).

Element	Al**	C*	H*	Fe	N*	O*	V**	Ti
Range (wt%)	5.5-6.75	<0.080	<0.015	<0.040	<0.050	<0.20	3.5-4.5	Bal.
Stabilizer	α	α	β	β	α	α	β	-

* Interstitial Element
**Substitution Elements

ficantly vary mechanical properties. This is reflected in the reported variability of Ti-6Al-4V across the literature.

2.2.3 Microstructure of Ti-6Al-4V

The microstructure of a material describes the arrangement of phases and defects. As discussed, Ti-6Al-4V is a two phase material which exists in multiple complex arrangements depending on processing parameters and chemical composition. In general, all microstructural variants can be separated into three categories, as depicted in Figure 2.5.

- Lamellar Microstructure: Fine colonies of α lamellae are enclosed within a retained β matrix lamellae. A layer of α is also present at the prior β grain boundaries. Cooling rates determine the α lamellae colony size and thickness.

- Duplex Microstructure: Similarly, colonies of α lamellae are enclosed within the β matrix lamellae. A layer of α is also present at the prior β grain boundaries. In addition, nucleation of primary α grains can be found at β grain triple points due to an additional annealing stage during thermo-mechanical processing.

- Equiaxed Microstructure: This structure consists of connected primary α grains which are created by controlling the cooling rates during recrystallization.

To reiterate, microstructural influences operate on a much finer scale than those considered explicitly during the constitutive portion of this thesis.

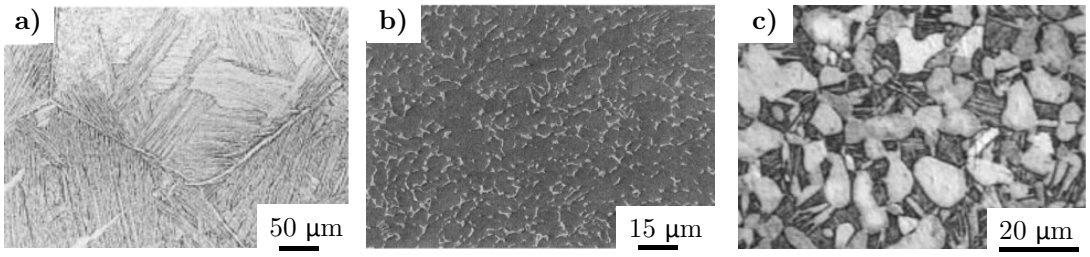


Figure 2.5: Typical Ti-6Al-4V microstructures. a) lamellar, b) bimodal (duplex), c) equiaxed [18]

2.2.4 Texture of Ti-6Al-4V

Microstructurally, Ti-6Al-4V can be formed as a polycrystalline or single crystal material. In a polycrystalline form each crystal has a specific orientation which defines the texture. The texture can influence a range of mechanical properties such as Young's modulus, yield strength, ductility and toughness. Texture can be discussed in terms of micro- and macro-scales as a function of the number of grains in question. For example, micro texture analysis would examine the misorientation between neighbouring grains and the subsequent interaction characteristics. Macro texture describes the dominant orientation which provides information leading to anisotropic properties. The 'macro-zone' in Figure 2.6a) illustrates features important to both textural studies.

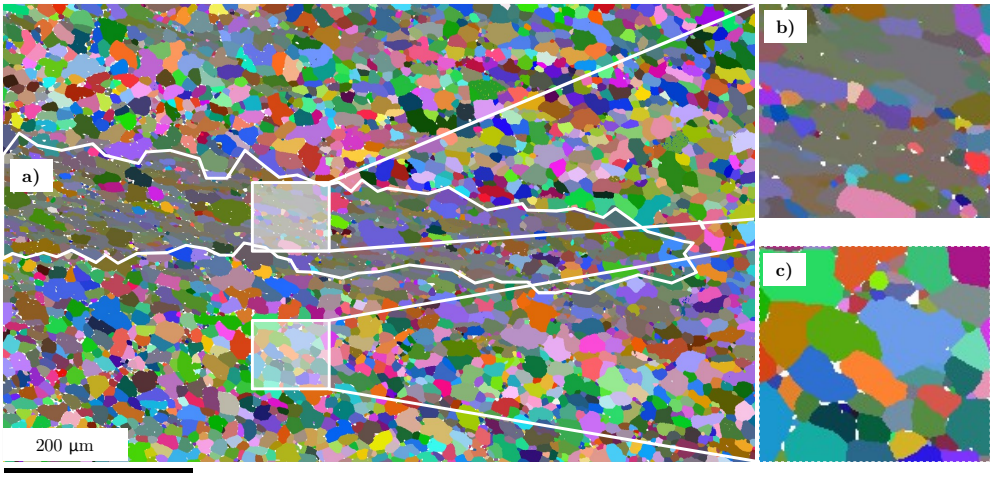


Figure 2.6: Ti-6Al-4V micrograph RVE texture map. a) Macro-zone, b) expanded macro-zone texture, c) expanded microstructure texture, courtesy of TIMET.

This micrograph image shows a texture map of Ti-6Al-4V with an area of several hundred similarly oriented grains. This was established by TIMET as reference for RVE purposes. Grain-scale modelling of these interactions would fall into the realm of crystal plasticity. On a macroscopic scale, deformation via plastic flow softening cannot be explained on the basis of texture alone [19]. Whilst the magnitude of plastic softening has been shown to be related to texture and microstructure, this occurs at

higher temperatures than experienced during fan system operation and hence texture and thermo-mechanical microstructural evolution are not of primary concern during this research [20]. Other research projects performed in parallel with this research are evaluating the grain-level phenomena numerically.

2.2.5 Manufacture of Ti-6Al-4V

Manufacturing can often be a source of variability due to impurities, defects and processing routes. Titanium ore is the fourth most abundant metallic element in the Earth's crust and it can be found in multiple chemical forms and structures - anatase, brookite, rutile (TiO_2), perovskite ($CaTiO_3$), titanite ($CaTiSiO_5$) and ilmentile ($FeTiO_3$), each requiring a customised manufacturing process. The production if titanium products from titanium ore can be sub-divided into separate processes [13, 14, 15]:

- Production of titanium sponge: The most common ore used is rutile; this is reacted with coke and chloride to produce titanium tetrachloride ($TiCl_4$). A further reaction with magnesium produces magnesium chloride and titanium in a sponge-like consistency.

$$TiO_2 + 2Cl_2 + C \rightarrow TiCl_4 + CO_2 \tag{2.3}$$

- Purification of sponge: The magnesium chloride by-product is removed either via a process called acid leaching, but now more commonly via a vacuum distilling process. Inclusions and surface contamination are also minimized.

$$TiCl_4 + 2Mg \rightarrow Ti + 2MgCl_4 \tag{2.4}$$

- Melting and alloying: Vacuum Arc Remelting (VAR) is the most common industrial process for adding alloying elements and creating ingots. Newer techniques such as Electro-Beam Cold Hearth Melting (EBCHM) and plasma-arc melting (PAM) have the added benefit of removing a greater number of defects.

- Fabrication of product: Primary processing describes the thermo-mechanical process to produce billet, bar, strip, sheet, tube and wire. Secondary fabrication describes forging, casting, joining and powder metallurgy processes. These processes influence material properties to varying degrees [13].

2.3 Industrial alloy development

Currently, advanced processing techniques and a robust analytical understanding of material performance have emerged as development requirements. This thesis predominantly concerns dynamic failure. However, since fatigue accounts for approximately 80% of in-service component failures both texture control and lifing techniques are of prime importance to the aerospace industry. Therefore, two areas of research and development interest that heavily influence Ti-6Al-4V development are crystalline texture control and advanced lifing techniques.

2.3.1 Texture control

Texture control also influences both creep life and formability, however within the literature texture control is used extensively to influence fatigue life. In CP titanium and Ti-6Al-4V, high stress triaxiality at stress concentration features such as notches or crack tips have been shown to improve shear strength response in the presence of an appropriate volume fraction of strong basal textured grains [21, 22]. Further research shows a relationship between the responses of notch specimens when thickness is varied. When the loading direction is parallel to the rolling direction, a reduction in energy release rates as thickness increases is observed. Numerically this poses a challenge for isotropic constitutive models. Conversely, loading perpendicular to the rolling direction result in an increased fracture energy release rate, as thickness and the volume of the plastic zone increase [23]. This relationship is less pronounced in Ti-6Al-4V as additional failure mechanisms are activated such as cold-creep at high R-ratios, as identified by Whittaker [22]. Alloys used for validation during this

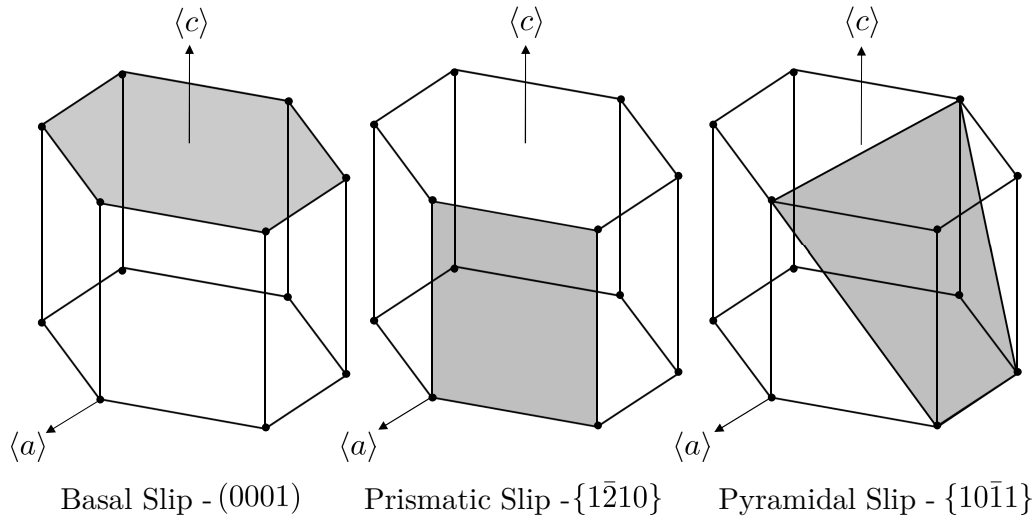


Figure 2.7: HCP crystallographic slip system examples.

research are typically cross-rolled to minimize the effects of anisotropy, as opposed to exploiting the texture control methodologies described. Due to the ring rolling process during manufacture of the fan system, casing cross-rolling is not possible and therefore anisotropy can be expected. The observed anisotropy is caused by the HCP structure packing density along the c-axis or (0001) direction, see Figure 2.7.

This results in a higher Young's modulus, creating an elastic anisotropy across a single crystal. When imposing strain along the c-axis, an increase in deformation twinning and strain hardening rate was observed [24]. On a macroscopic scale this effect is averaged when considering thousands of grains. However, rolling processes which modify the texture and grain boundary orientation also create noticeable anisotropic mechanical property responses, such as elastic yield strength and plastic response, by influencing slip system activation behaviour created by basal and pyramidal textures [25, 26]. Furthermore, Evans [27] found that fatigue crack initiation is influenced by the Basal planes and their orientation with respect to maximum shear stress. However, cyclic stress relaxation during early full reversal fatigue cycles is controlled by the prismatic slip planes, shown in Figure 2.7. Evans also found that higher α grain volume fractions cause greater texture sensitivity, whilst α grain re-

finement increases fatigue life in Ti-6Al-4V. There exists a dearth of texture control influences in the literature with regards to high strain-rate Ti-6Al-4V responses; this highlights the importance of anisotropy.

2.3.2 Component lifing techniques

Combined with failure, fatigue is likely to affect lifing and therefore techniques are required to understand the service-life of components to reduce early retirement of components. Fatigue is not the focus of this thesis, however lifing techniques are required to understand and characterise a components damage accumulation and subsequent probable fracture mechanisms prior to failure whilst in service. Iguchi et al [28] first proposed the concept of impact fatigue on tensile steel specimens with an impulse loading rise time wavelength of $\lambda_t = 1.0 \times 10^{-3}$s. As expected, it was observed that impact fatigue nucleation and propagation lives were reduced when compared to conventional fatigue lives for identical geometries. More recently, variations of impact fatigue have become popularised in the form of high strain-rate full reverse loading [29], which approximates the dynamic cyclic loading experienced during blade-off events. Techniques described below attempt to estimate the point of component failure which enables designers to predict component failure mechanisms and their implications during blade-off scenarios. Full-scale representative testing or pseudo-testing of uni-axial specimens are both expensive and hugely time consuming, leading to the emergence of analytical techniques. However, fatigue life estimations are often overly conservative, meaning components are retired without defect.

Industrial lifing techniques

Common industrial lifing approaches are discussed as follows:

- Life-To-First-Crack: This method can be costly due to inspection processes and associated safety factors which result in a conservative estimation. Repartition is also required with varying geometry, composition, operating temperatures

and surface conditions. This technique also assumes no initial flaws, which is erroneous [30]. Initial flaw size is something which should also be considered during numerical analyses.

- Damage Tolerance Lifing: This technique does assume that initial flaws are present and applies the traditional fracture mechanics approach based on stress concentration factor calculations. Fatigue life during crack initiation and small crack growth are not taken into account, which once again lead to a conservative estimation [31, 32]. R-R have developed a variant of the damage tolerance approach, dubbed Equivalent Initial Flaw Size (EIFS) which extrapolates the initial flaw size based upon known failure events and defects identified during routine maintenance cycles [33].

- Probabilistic Approach: This approach combines aspects of empirical testing with analytical techniques. Statistical analysis can be applied to account for a number of variables, such as residual stress for example [34]. These variables are used within the combined experimental and analytical framework which eliminates geometric variance. For example, defects acting as stress concentrations and crack initiation locations are more severe on a free surface and require a probabilistic approach [35]. Numerical techniques are often applied within the probabilistic approach to account for complex multi-axial stress-states and in order to study the combination of individual variables and their influence on fatigue life, such as temperature and residual stress.

2.4 Mechanical performance

The macroscopic behaviour of titanium shall be discussed in further detail during Chapter 3 and Chapter 4. Firstly, the mechanical response of metallic materials can be generalised and categorised into their stress-strain, strain-rate and subsequent failure mode responses. These concepts are used throughout this research and therefore brief

examples shall be presented for completeness.

2.4.1 Elastic deformation

The elastic portion of deformation can be assumed to be both linear and recoverable. The Young's modulus is the ratio of stress to strain and therefore has the units of pressure, usually MPa or N/mm^2.

$$E \equiv \frac{\sigma}{\varepsilon} = \frac{F/A_0}{\Delta l/l_0} = \frac{F/l_0}{A_0/\Delta l}. \tag{2.5}$$

This allows for the prediction of the magnitude of elastic deformation given the imposed force of a known area, or visa-versa. The HCP α-phase results in single crystal anisotropy. This can be represented as a function of deviation from the c-axis as shown in Figure 2.8. In comparison, the BCC β-phase in Ti-6Al-4V is assumed to have a lower Young's modulus, although this is difficult to confirm as the β-phase is not stable at room temperatures [15]. The primary alloying elements in Ti-6Al-4V influence the elastic response due to their stabilising effects. For example, aluminium acts as an α stabiliser thus increasing the elastic modulus. Conversely, vanadium is a β stabiliser which decreases the elastic modulus.

However, within a polycrystalline two-phase structure, the single crystal aniso-

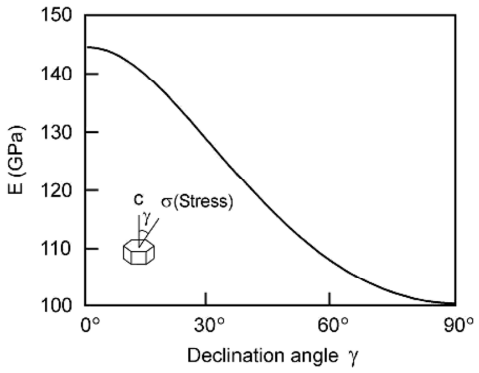


Figure 2.8: Elastic response of titanium HCP single crystal as a function of declination angle from the c-axis [14]

.

tropy becomes far less distinct unless there exists significant texturing [15].

2.4.2 Inelastic deformation

At stress levels beyond the elastic regime, plastic deformation occurs. This type of deformation is the primary focus of this thesis due to the highly non-linear nature of impact and high strain-rate deformations. Schematically, both elastic and plastic one-dimensional stress and strain responses are shown in Figure 2.9. As a basis for constitutive assumptions related to dislocations, the atomistic modes of deformation shall be discussed.

The plastic component of deformation is irreversible and involves the breaking of atomic bonds by the movement of dislocations via either climb or glide; the latter is schematically represented in Figure 2.10. The majority of plastic deformations within Ti-6Al-4V are related to slip planes, which most commonly occur on planes with the highest density of atoms and in directions corresponding to the shortest lattice translation vector. Slip planes (hkl) and slip directions $[uvw]$ constitute a definition of a slip system (hkl) $[uvw]$, families of planes $\{(hkl),(lhk),(hlk)\}$ and

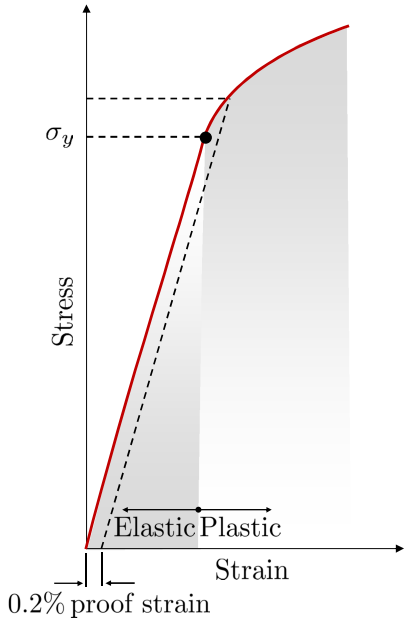


Figure 2.9: Elastic-plastic stress strain response of a generic alloy during deformation.

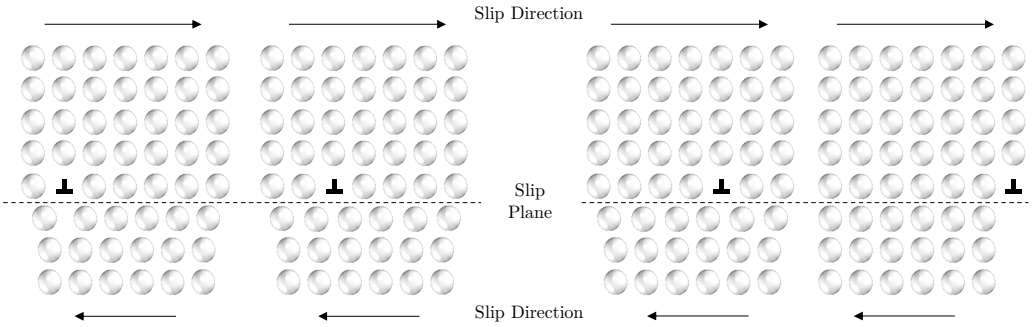


Figure 2.10: Shear strain dislocation motion representation through a crystal lattice.

directions $\langle [uvw], [wuv], [uwv] \rangle$ also exist due to lattice symmetry [36].

The most common slip system, in α-phase of Ti-6Al-4V, is associated with the Burgers vectors $\langle a \rangle$. These are known as the Basal, Prismatic and Pyramidal planes shown in Figure 2.7. Dilatational plastic deformation occurs in HCP α-phase materials, when induced stress exceeds the CRSS (Critically Resolved Shear Stress). The von Mises criterion states that a minimum of five independent slip systems must be activated, from the maximum of twelve, based on all three slip planes and all slip directions [36, 37]. The softer cubic β-phase in Ti-6Al-4V contains only three slip planes and a single slip direction; this is common for BCC metals. Another form of plastic deformation in Ti-6Al-4V is twinning, which occurs when crystal lattices share atoms symmetrically and shear stress causes a mirror re-orientation of the lattice (see Figure 2.11).

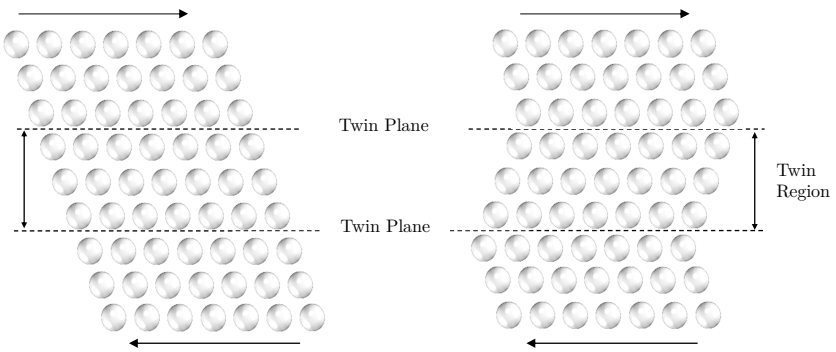


Figure 2.11: Shear strain twinning re-orientation representation.

Twin systems activation in the HCP α-phase of CP titanium differs in tension versus compression when loaded parallel to the c-axis. Aluminium is known to decrease the tendency in Ti-6Al-4V to twin but this cannot be said when variables such as increased strain-rates, high temperatures and texture are considered. Twinning is a unidirectional process which is closely associated with directional strengthening.

2.5 Inelastic phenomena in Ti-6Al-4V

During inelastic behaviour titanium experiences certain phenomena which have been observed to influence the mechanical response. The interdependence of these phenomena in Ti-6Al-4V is a highly complex field. Appreciation of the relevant phenomena and their interdependencies is required for constitutive modelling purposes.

2.5.1 Strain-rate dependence

Strain-rate dependency at the macroscopic level has been observed in a wide variety of alloys including titanium, which shall be discussed toward the later half of this sub-section. More generally, strain-rate effects are caused by dislocation dynamics. Dislocations occur in three distinct stages: thermally activated dislocation motion, drag controlled dislocation motion and relativistic effects.

According to Orowan's relationship [38], an increase in the imposed strain-rate $\dot{\varepsilon}$ is directly related to an increase in dislocation velocity v_d. This relationship is related to the Burger's vector $\langle a \rangle$ and dislocation density ρ_d in equation (2.6)

$$\dot{\varepsilon} = \langle a \rangle \, \rho_d \, v_d. \tag{2.6}$$

Gilmand and Johnson experimentally demonstrated a relationship between dislocation velocity and resolved shear stress. Therefore, since dislocation velocity is stress dependent it follows that an increase in a given strain-rate is accompanied by increased stress [39]. Dislocation dynamics are a function of thermal and mechanical energies, which are required to overcome barriers of travel, i.e. slip. Dislocation barri-

ers are typically conceptualised by a waiting 'time' until activation energy is sufficient for a dislocation to overcome the barrier and slip is allowed to occur. The 'time' dislocations spend overcoming barriers is greater than travelling between barriers. In the event of increased strain rates, the time for dislocations to overcome short-range barriers is reduced and hence the increased energy required is provided by the applied stress [40, 37]. Titanium is known to display strain-rate dependent behaviour on the observed macroscopic scale, in terms of yield strength and flow stress responses.

There exists a wealth of data produced by the Impact Engineering Laboratory to characterise various titanium based alloying chemistries. The most significant change in yield strength and flow stress behaviours can be seen at strain rates from 0.1s^{-1} to 1000s^{-1} and beyond. This is reflected in an increase of the engineering yield stress and reduction in the strain to failure. Zhan [41] examined a higher range of strain-rates which reached $10,000\text{s}^{-1}$ in compression. However, little strain-rate sensitivity beyond 1000s^{-1} was observed, this threshold was therefore deemed as a transition from a thermal activation controlled mechanism to a diffusion fragmentation mechanism at higher rates.

Characteristics such as the underlying microstructures also influence the material response in relation to strain-rates. For example, it has been shown that a Widmanstratten microstructure exhibits a lower failure strain across the same strain-rate range when compared against equiaxed structures [42]. Additional factors such as damage mode accumulation, interstitial concentrations and temperature also influence the apparent strain-rate sensitivity of Ti-6Al-4V. Together these phenomena contribute towards the macroscopically observed deformation strain-rate sensitivity. Some of these factors have been explored further during this research to form a foundation for constitutive modelling developments.

2.5.2 Temperature dependence

Multiple titanium aerospace alloys such as Ti-6Al-4V and Ti-6Cr-5Mo-5V exhibit an increased flow stress temperature sensitivity, compared to strain-rate sensitivity. When discussing temperature dependence two sources exist: internal and external. Internal temperature generation is a product of plastic work done and the magnitudes of these temperature increases differ under the influence of strain-rates imposed. At higher strain-rates adiabatic heating occurs due to the reduced time available for heat to dissipate. Zhan [41] noted that flow softening at 273 K is most likely attributed to adiabatic thermal softening effects. However, formation of adiabatic shear bands, for example, preferentially occurs at higher temperatures as a consequence of alloy morphology. In addition to demonstrating strain-rate dependence of true stress to be within the region of 200 MPa at strain-rates of 10^{-4}s in Ti-6Al-4V, Khan et al [43] also showed that external temperature increases from 233K to 589K can result in a true stress decrease of ~ 400MPa. Khan also showed that the rolling direction can increase true stress sensitivity to 700MPa. For high strain-rates of $\sim 1400\text{s}^{-1}$ Seo et al [44] increased the temperature range further from 475K to 1275K. This results in a peak flow stress reduction of 1300MPa.

This brief review of the literature has demonstrated that internally generated and externally imposed temperature changes modify the flow stress responses of Ti-6Al-4V. There also exists a proportional relationship between temperature sensitivity and strain-rate. Texture is an additional contributing factor, thus making extrapolation of trends difficult and potentially misleading. It is therefore extremely advisable to perform bespoke tests across a range of strain rates, temperatures and representative textures to characterise a material for numerical purposes.

2.5.3 Pressure dependence

The yield strength in uni-axial tension and compression for Ti-6Al-4V is not equal, and the physical origin of this effect will be discussed in detail later. In addition,

during load reversal from tension to compression the yield stress is reduced due to the Bauschinger Effect, which introduces a residual back-stress which similarly results in an asymmetrically observable yield. This is achieved when the centroid of the yield surface moves away from its origin which is known as kinematic hardening [29]. Theoretically, the Bauschinger Effect can therefore be defined as a function of work hardening which leads to internal stresses. On a microscopic scale these stresses are a product of dislocation motion or inclusions leading to the formation of non-homogeneous regions. On a macroscopic scale and from a continuum mechanics perspective, the loading history is represented by both isotropic and kinematic hardening evolutions [45].

Single crystal uni-axial experiments indicate that crystallographic slip is the origin of plasticity [46]. Crystallographic evidence indicates that differential tension-compression strengths for titanium alloys are also required. Furthermore, the proposed constitutive framework is intended to be applied to alternative metallic systems which may experience higher degrees of asymmetric strength responses. Jones and Hutchinson showed that Ti-6Al-4V demonstrates asymmetric strength response or 'pressure dependency' due to $\langle c+a \rangle$ slip on the $\{1\bar{1}01\}$ planes [47]. In compression, the occurrence of additional cross-slip increases the CRSS. If $\Delta\tau$ is the CRSS increase caused by an increase in hydrostatic pressure, or normal stress ($\Delta\sigma$), then $\Delta\tau/\Delta\sigma$ is generally $\sim$1%. However, Lowden and Hutchinson estimated that in Ti-6Al-4V this could be $\sim$20% which becomes far more influential and potentially applicable to macroscopic analyses. The differential in tensile and compressive strength should therefore influence any constitutive developments.

2.5.4 Anisotropic plasticity

One significant phenomena of inelasticity in titanium alloys is that of plastic anisotropy. Anisotropy in metals generally develops due to cold or hot working processes during manufacturing, such as rolling. These continued plastic deformation processes

in poly crystalline materials effects the crystalline structure on the micro mechanical scale. Certain crystallographic planes rotate according to prescribed principal strains to form discernible texture orientations characterised by a fibrous appearance in the direction of rolling, for example [48]. Similar to pressure dependency, anisotropic behaviour is attributed to the HCP α-phase of Ti-6Al-4V and the interaction between crystallographic slip and deformation twinning processes [49]. This results in directional dependence of yield properties, fatigue life and crack propagation sensitivity at quasi-static strain-rates [50]. In polycrystalline aggregates these textures can be complex to quantify, predict and control. This presents both difficulty and opportunity during manufacture and subsequent component design [51].

At higher strain-rates anisotropic morphologies can influence twin formation and hence shear strength. This has been described as vital for aerospace components inheriting anisotropic properties. Millett [38] indicated that at ballistic strain-rates the wider literature is largely contradictory. They highlighted the influence of orientation of the shear strength attained and the occurrence of twin formation during shock loading failure. As twinning is highly sensitive to texture, this provides justification for the rationale and observations.

To conclude, it has been shown that texture and the anisotropic morphologies created during manufacture and deformation of titanium alloys are significant at all loading rates, including ballistics. Development of anisotropic properties is critical to represent textural influences and provide a link to grain-scale modelling exercises in a multi-scale approach.

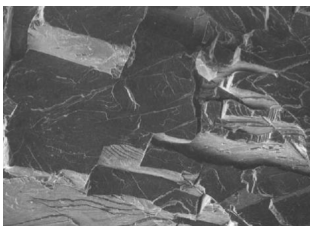
2.5.5 Failure mechanisms

If we define failure as the initiation, growth and coalescence of microstructural features leading to macroscopically observable crack, then Ti-6Al-4V like numerous metallic systems exhibits both ductile and brittle failure modes. In a uni-axial tension test, the specimen will undergo the following failure mechanisms:

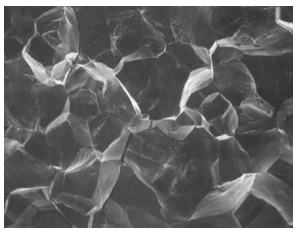
Table 2.2: Brittle to ductile failure mechanisms in tension

Necking Micro-void formation Coalescence of micro-voids (crack formation)	Ductile
Crack initiation Crack propagation, via shear Fracture	Brittle

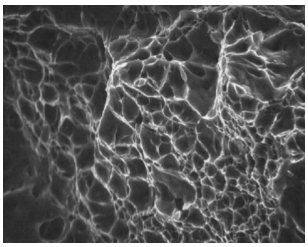
One of the predominant ductile failure mechanism in Ti-6Al-4V is micro-void formation, which is characterised by spherical dimples on the fracture surface. Ductile failure is common during quasi-static deformation, yet also present during dynamic testing. Brittle fracture mechanisms are generally described on the granular scale in terms of intergranular and transgranular cleavage planes, these are another critical failure mode when characterising failure in Ti-6Al-4V. Their respective fractographic surfaces a shown in Figure 2.12.



Brittle fracture surface
(Transgranular)



Brittle fracture surface
(Intergranular)



Ductile fracture surface

Figure 2.12: Failure surface depicting both brittle and ductile failure modes.

2.6 Summary

The background literature provides a wider context to the industrially focussed motivations of this research project. Metallurgical factors which lead to requirements

relevant for numerical development will be discussed in more detail during Chapter 3.

- The application of titanium alloys within gas turbine assemblies has been discussed. This has highlighted their importance within the industry primarily due to their strength-to-weight ratio and formability.
- The metallurgical characteristics of Ti-6Al-4V have been briefly documented to emphasise the complexities of polycrystalline alloys and more importantly their variation. These relationships are driven by the underlying alloy chemistries, microstructures, textures and manufacturing routes.
- The fundamental concept of inelastic deformations are discussed which relate the micro-mechanical behaviour observed at the metallurgical scales to the macroscopically observed thermo-mechanical deformations.
- Observable inelastic behaviour such as strain-rate sensitivity, temperature dependence, asymmetry, anisotropy and variable failure mechanisms have been identified as critical for characterisation of thermo-mechanical deformation behaviour of Ti-6Al-4V. These require further investigation and quantification to inform the development of a representative constitutive approach.

Chapter 3

Literature Review: State of the Art

Building upon the relevant background research, this chapter contains a detailed and specialised analysis of the technologies, techniques, and theories which form the basis of the proposed research activities. Relevant physical phenomena are identified from the literature and the constitutive modelling approaches appropriate to capture such deformation and failure characteristics are discussed. These capabilities are discussed in detail from both physical and numerical perspectives before presenting a summary of current literature.

3.1 Continuum mechanics

Within the growing field of solid mechanics, research is being channelled into micro-mechanical influences of granular and atomistic length scales. In parallel, novel numerical techniques are being developed such as meshless methods and multi-scale approaches in order to simulate these physical phenomena more accurately. The comparatively slow developmental pace in which these technologies and methods can be safely adopted by industry is potentially leading to a disparity in terms of applicable numerical solutions which can offer immediate benefit. This is coupled with the potential increase of computational costs associated with these new techniques.

As a consequence, this chapter shall examine the macro-scale technologies and

methods which provide computationally efficient solutions and facilitate immediate industrial application and modularity. Continuum mechanics allows us to develop numerical solutions in parallel with our expanding metallurgical understanding at a range of length scales.

Transition from the physical space to the numerical space is achieved via the field of mathematical physics known as continuum mechanics. Continuum mechanics provides a platform to simulate the macroscopic behaviour of matter, both fluids and solids. This field assumes that the inherently discontinuous state of matter is continuously distributed over a given domain known as the continuum. The kinematic response of a material subjected to thermo-mechanical loading is then evaluated over the established continuum. Further detailed descriptions can be found in classic texts such as Belytschko [52, 53]. As such, the Finite Element Method is the primary numerical analysis tool used during this research.

The following research is based upon the updated Lagrangian formulation, which has been adopted within multiple commercial codes. This approach is highly robust when dealing with non-linear boundary conditions which emerge along the discretisation interfaces during analyses, and constitutive behaviours which form the core of this thesis. In solid mechanics, history- or path-dependent materials are commonly studied and are well suited to the chosen updated Lagrangian framework.

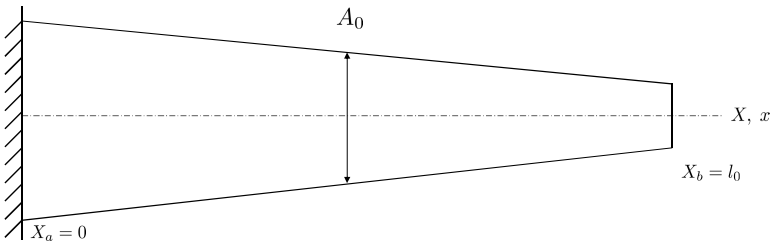
3.1.1 Governing equations

The system of equations used throughout the continuum mechanics approach are called the governing equations. The governing equations consist of the conservation equations, the constitutive equations and the measure of deformation. These are summarised in a one-dimensional form in Table 3.1 from [52]. The chosen dependent variables are Cauchy stress $\sigma(X,t)$ and velocity $v(X,t)$, these dependent variables can be expressed in the Eulerian coordinates as follows

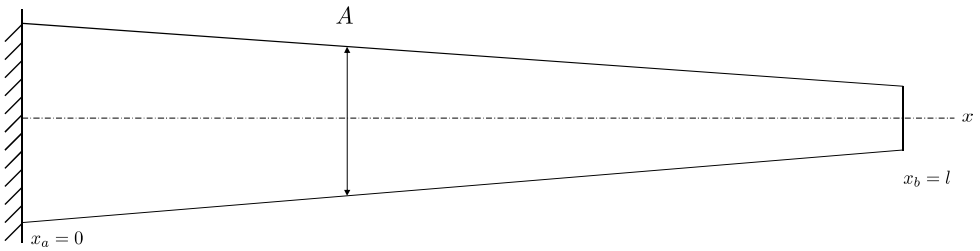
$$X = \phi^{-1}(x,t) \equiv X(x,t), \tag{3.1}$$

where $\phi(X,t)$ maps between the initial and current domains for a given variable. Due to the difficulty of constructing a closed form of an inverse function, variables are typically referred to in element coordinates.

For clarity, the notation describing the following continuum mechanics approach correspond with reference text books [52, 53]. The 'current' or 'deformed' configuration are used within the updated Lagrangian approach, where the spatial Eulerian coordinates are denoted by x and the material Lagrangian coordinates are denoted by X. Therefore, the initial cross sectional area and density of the beam in Figure 3.1 are denoted by $A_0(X)$ and $\rho_0(X)$. Similarly, the current configurations are denoted by $A_0(X,t)$ and $\rho_0(X,t)$, which are functions of space and time.



Initial Configuration (reference configuration)



Current Configuration (deformed configuration)

Figure 3.1: Reference initial and deformed current configurations in a one-dimensional beam with a fixed end and loaded end.

Table 3.1: Governing equations for updated Lagrangian formulation.

Governing Laws	**Updated Lagrangian Formulation**
Conservation of Mass	$\rho J = \rho_0$ or $\rho \dfrac{\partial x}{\partial X} A = \rho_0 A_0$
Conservation of Momentum	$\frac{\partial}{\partial x}(A\sigma) + \rho A b = \rho A \dot{v}$
Conservation of Angular Momentum	$\sigma = \sigma^T$
Measure of Deformation	$D_x = \frac{\partial v}{\partial x}$ or $D_x = v_{,x}$
Constitutive Equations	$\sigma_{,t}(X,t) = \varsigma_t^{\sigma D}(D_x(X,\bar{t}),\ \sigma(X,\bar{t}), \bar{t} \leq t$, etc)
Conservation of Energy	$\rho \dot{\omega}_{int} = \sigma D_x - q_{f,x} + \rho q_s$

The strain measure within the update Lagrangian approach is given by the rate of deformation D_x

$$D_x = \frac{\partial v}{\partial x}, \tag{3.2}$$

In Table 3.1 the updated Lagrangian formulation of the momentum equation is given in terms of spatial Eulerian coordinates x and Cauchy stress σ, current values of the density ρ and area A are also used. The constitutive equations are also given in a rate form $D_x(X,t)$. The Jacobian J and the deformation gradient $\partial x/\partial X$ are used within the conservation of mass formulations. The body force within the conservation of momentum equation is denoted as b and v is velocity. The function S denotes the deformation history of stress, and X is the material Lagrangian coordinate.

Boundary conditions

The boundary conditions imposed on the domain Γ, where $\Gamma = \Gamma_t \cup \Gamma_v$, are as follows

$$v(X,t) = \bar{v}(X,t), \tag{3.3}$$

$$\sigma(X,t) = \bar{t}_x(X,t), \tag{3.4}$$

where $\bar{v}(t)$ from (3.3) is the prescribed velocity acting upon Γ_v, and $\bar{t}_x(t)$ from (3.4) is the traction acting upon Γ_t.

Initial conditions

The dependent variables already described are velocity and stress. The initial conditions are described below, initial displacements can be assumed to be zero.

$$\sigma(X,0) = \sigma_0(X), \tag{3.5}$$

$$v(X,0) = v_0(X). \tag{3.6}$$

Principle of virtual power

The discretisation of the momentum equation in Table 3.1 cannot be achieved using the finite element method directly, therefore the weak-form or principle of virtual power is required. Firstly, the momentum equation, traction boundary condition and interior continuity condition are combined - this is known as the strong-form (3.7). The weak-form (3.8) is then obtained by multiplying the momentum equation by a test function $\partial v(X)$ and integrating over the current domain.

$$\int_{x_a}^{x_b} \partial v \left[(A\sigma)_{,x} + \rho A b - \rho A \frac{D_v}{D_t} \right] dx = 0, \tag{3.7}$$

$$\int_{x_a}^{x_b} \left[\partial v_{,x}\, A\sigma - \partial v \left(\rho A b - \rho A \frac{D_v}{D_t} \right) \right] dx - \left(\partial v A \bar{t}_x \right) \Big|_{\Gamma_t} = 0, \tag{3.8}$$

by multiplying a force ($\rho A b\, dx$) by a velocity $\partial v(X)$ we obtain a power, hence the principle of virtual power $\mathscr{P}$. Therefore the weak-form can also be written as

$$\delta\mathscr{P} = \delta\mathscr{P}^{\text{int}} - \delta\mathscr{P}^{\text{ext}} + \delta\mathscr{P}^{\text{kin}} = 0, \tag{3.9}$$

where $\mathscr{P}^{\text{kin}}$ is the inertial virtual power, $\mathscr{P}^{\text{ext}}$ is the external virtual power and $\mathscr{P}^{\text{int}}$ is the internal virtual power.

$$\delta \mathscr{P}^{\text{int}} = \int_{x_a}^{x_b} \partial v_{,x}\, \sigma A \, dx = \int_{x_a}^{x_b} \partial D_x \sigma A \, dx = \int_{\Omega} \partial D_x \sigma \, d\Omega \tag{3.10}$$

$$\delta \mathscr{P}^{\text{ext}} = \int_{x_a}^{x_b} \partial v \rho b A \, dx + (\delta v A \bar{t}_x)\Big|_{\Gamma_t} = \int_{\Omega} \partial v \rho b A \, d\Omega + (\delta v A \bar{t}_x)\Big|_{\Gamma_t} \tag{3.11}$$

$$\delta \mathscr{P}^{\text{kin}} = \int_{x_a}^{x_b} \partial v \rho \dot{v} A \, dx = \int_{\Omega} \partial v \rho \dot{v} A \, d\Omega \tag{3.12}$$

3.1.2 Element equations

Within the finite element method the domain Ω is subdivided into elements Ω_e. This allows computation of the mass matrix $\mathbf{M}$ and the nodal forces $\mathbf{f}^{\text{int}}, \mathbf{f}^{\text{ext}}$ at the element-level. The element-level quantities are recombined at the global-level to solve the global equation (3.13).

$$\mathbf{M}\ddot{\mathbf{u}} + \mathbf{f}^{\text{int}} = \mathbf{f}^{\text{ext}}, \tag{3.13}$$

For brevity, the associated discrete equations are given below, from Belytschko [52].

$$\mathbf{f}^{\text{int}} = \int_{\Omega} \frac{\delta \mathbf{N}^T}{\delta x} \sigma d\Omega \text{ or } \mathbf{f}^{\text{int}} = \int_{\Omega} \mathbf{B}^T \sigma d\Omega \tag{3.14}$$

$$D_x = \sum_{I=1}^{m} \frac{\delta \mathbf{N}_I}{\delta x} \mathrm{v}_I^e = \mathbf{B}\mathbf{v}^e \tag{3.15}$$

$$\mathbf{f}^{\text{ext}} = \int_{\Omega} \rho \mathbf{N}^T b \, d\Omega + (\mathbf{N}^T A \bar{t}_x)\Big|_{\Gamma_t} \tag{3.16}$$

$$\mathbf{M} = \int_{\Omega} \rho_0 \mathbf{N}^T \mathbf{N} d\Omega_0 \tag{3.17}$$

Strains can be computed from the gathered nodal quantities for each element. The constitutive equations, discussed in detail during this research, are then applied to calculate the element stresses. The nodal internal forces can be calculated by an

operation which assembles both the internal and external nodal forces at the global level.

3.1.3 Constitutive modelling approach

Belytschko defines constitutive modelling as the mathematical description of a material response characterised by constitutive equations, which describe stress as a function of deformation history [53]. Within the continuum approach, the assumption is made that an element is representative of the material and is also subject to near uniform macroscopic stress. The effects of micro-heterogeneities, in terms of stress and strain responses, are averaged and indirectly influenced by internal variables, as described by Chaboche [54]. By maintaining these conditions the constitutive modelling approach within the FE method can be applied to a wide range of physical length scales, such as RVEs. For the purposes of this research the macroscopic component and sub component scales shall be the main focus.

Whilst the term 'constitutive modelling' is applicable to almost all material modelling fields, we shall focus on modelling fields applicable for component and sub-component analyses. The application of the proposed constitutive model is large-scale industry level simulations. A non-exhaustive list and highly generalised relationship between computational cost and physical length scales is depicted in Figure 3.2. This demonstrates an inversely proportional relationship between computational cost and length scales. It is this relationship which motivates physically-based modelling at component and structural length scales. Extensive reviews of fundamental constitutive modelling approaches can be found in numerous textbooks [53, 55, 46, 56]. For the purposes of this thesis, the poignant material modelling approaches will be reviewed.

Phenomenological models use empirical observations to characterise interactions of phenomena such as flow stress, plastic strain, strain rate and temperature. The subsequent numerical framework applies a series of logical mathematical processes

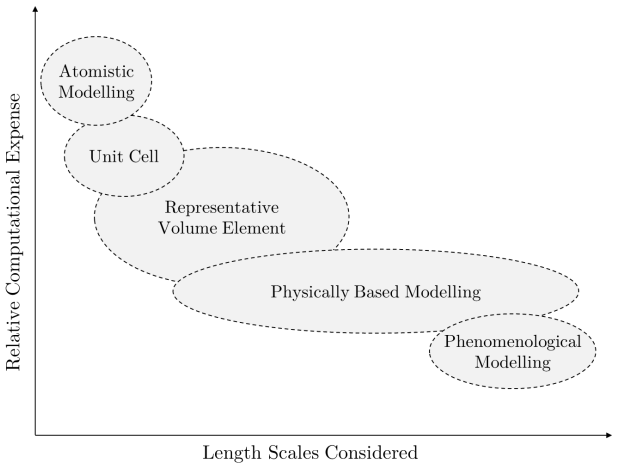


Figure 3.2: Generalized schematic representing modelling approaches and their associated computational cost and physical length scales considered for a similar scale problem.

which are consistent with fundamental theories but do not derive them directly or simulate them explicitly. These are known as empirical and semi-empirical models, such as Johnson-Cook [57] or Zerilli-Armstrong [58]. These phenomenological models are commonly used throughout the aerospace industry due to their ease of implementation and numerical robustness when validating design modifications and new mechanical material test data. Such models lack history effects relating to load path and strain rates [59]. Physically-based models apply thermodynamic principles within the field of Internal State Variable (ISV) theory to relate fundamental phenomena to constitutive formulations. Secondly, ISVs capture the mechanical histories [60]. These ISV's describe material responses relevant to impact and dynamic ductile deformation, such as static and dynamic recovery, isotropic and kinematic hardening, damage accumulation in temperature and time dependent formulations [61, 54, 62, 63, 64]. The foundation of this approach is based upon the physical micro-mechanical response of the alloy under investigation, which will be established during this chapter. The degree of accuracy required is often related to the number of variables representing a material response. This assertion leads to a criticism of certain models due to the difficulty of calibration.

During the development of a kinematic framework for plasticity, Bammann and

Johnson [65] introduced kinematic and isotropic hardening variables. The evolution of these parameters is assumed to be linear with strain rate and unchanged with respect to multiplicative intermediate (stress-free) configurations. The kinematic hardening tensor was further developed by Bammann and Aifantis [66], which drew upon earlier work of Aifantis [67] to introduce the effect of directional back stress (kinematic hardening) based upon dislocation dipoles related to normal internal stress. In general, the process of plasticity introduces dislocations which increase the yield strength of a material. Static and dynamic recovery mechanisms decrease the number of defects via the process of 'annihilation' and 'redistribution'. Stouffer [68] distinguishes between the two as follows: static recovery occurs after deformation as an interaction between the current dislocation forces, known as a sub-grain substructure. This mechanism becomes more important at higher temperatures. In contrast, dynamic recovery occurs simultaneously with deformation and forms an additional substructure known as a dislocation cell, which operates at lower temperatures. Bammann and Aifantis [66] proposed a viscoplastic model incorporating static and dynamic recovery, as part of both the plastic spin tensor and strain rate sensitivity. This thermodynamically motivated framework forms the basis for the study of pressure, strain-rate and temperature dependent deformation processes presented in this thesis for Ti-6Al-4V.

3.1.4 Continuum damage mechanics

Beyond inelastic behaviour we find the field of damage mechanics and fracture mechanics. These fields attempt to describe the structural degradation of a material under the influence of defects, such as voids and cracks which we have discussed earlier. Continuum damage mechanics is the field of numerical modelling which attempts to characterize these micro-mechanical processes by introducing damage variables reflecting the average material degradation on a macro-mechanical scale, i.e. continuum [69]. At the component and sub-component level, the transition from

damage mechanics to fracture mechanics occurs on the element scale, due to the limitations of the simple element deletion technique. The divisible terminology used within this thesis is illustrated in Figure 3.3.

In 1958 Kachanov [70] introduced the idea of a surface with a density of discontinuities. The reduction in the force resisting area is used to directly calculate the so-called 'effective-stress'. Utilising this concept, Kachanov developed a creep damage evolution law. Further significant developments in this field were made by Chaboche and Lamaitre [71] and various contributing authors cited within the work of Lemaitre and Desmorat [72]. A 'unified damage law' was proposed for a range of loading conditions ranging from one-dimensional creep to multi-axial ballistic applications, by utilizing the inherent time dependence of the original formulation proposed by Kachanov. The mechanistic focus on crack initiation and growth forms an appropriate framework for addressing shear crack growth and evolution. Cocks and Ashby [73] suggested an extension to the continuum damage approach which focused on the mechanistic aspects of void growth. This approach suggested several modifications to the traditional approach which were specific to the void growth damage evolution case. Most notably, triaxiality was coupled with diffusional growth and power-law creep growth in a consistent manner, which results in accelerated void growth under high triaxiality conditions. This work was introduced by Bammann et al. [74] within an existing visco-plastic framework coupled with temperature following an Arrhenius

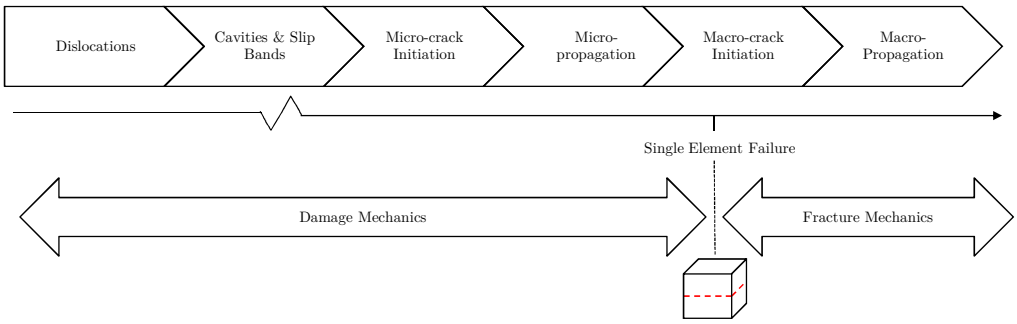


Figure 3.3: Damage mechanics and fracture mechanics definition reference schematic and specific terminology.

form.

An enhanced ISV constitutive model is proposed in this thesis which utilises the visco-plastic and continuum damage framework originally developed at Sandia National Laboratories by several authors [66, 74, 75]. An enhanced pressure dependent multi-mode damage criterion is introduced which allows for cumulative and competitive accumulation of dilatational and distortional damage based upon stress state. Furthermore, a mesh sensitivity control technique is also proposed to reduce limitations of industrial computational capabilities, which violate the principles of continuum mechanics in certain cases.

3.2 Ductile deformation mechanisms

The ductile deformation mechanisms relevant to Ti-6Al-4V shall be examined during this section, with the aim to provide clear objectives for simulating, at a macro-scale, the thermo-mechanical phenomena present during dynamic events. During ductile deformation, strain-rate sensitivity and the influence of temperature are well documented within the literature, Wulf [76] demonstrated that strain rates above 1000s^{-1} result in viscous deformation of titanium alloys. Thermal softening was also indicated as a precursor to catastrophic shear failure. These rate dependent phenomena are still being investigated, albeit on a wider range of length scales. For example, Chichili et al. [77] concluded that the hexagonal close packed (HCP) α-phase in titanium experiences an increase in the sustained flow stress at higher rates of strain ($> 1000\text{s}^{-1}$), and an associated strain hardening and twin density increase. The majority of plastic deformation was concluded to be due to dislocations. Furthermore, studies have shown that with an increase in temperature, a decrease in the sustained flow stress is observed. It has also been demonstrated that temperature is more significant to the flow stress sensitivity than strain rate in titanium alloys [78]. This implies that thermal softening dominates the flow stress response, rather than true strain at strain rates $\sim 1000\text{s}^{-1}$. These two phenomena have a signific-

ant influence on the elastic-plastic transition, however beyond yielding the inelastic flow is also characterised by the damage mechanisms leading towards failure. Consequently, the minimum ability of a constitutive modelling approach should be to couple temperature, strain-rate and hardening.

3.2.1 Ductile damage mechanisms

Generally, metallic materials undergo ductile failure whereby the fracture mechanisms on a macroscopic scale can be classified as dilatational (void evolution) and distortional (shear distortion) deformation mechanisms. The physical nature of these two damage modes and their respective constitutive developments are explored, and the combination of the two mechanisms in a cumulative and competitive approach is proposed.

Void growth

During dilatational plastic deformation, the void fraction increases due to new void formation and void growth. This is known to be a critical mechanism in ductile fracture [79]. Firstly, voids are known to nucleate around inclusions after interface decohesion between particle and matrix. This then leads to plastic straining of the surrounding material which allows the voids to grow asymptotically towards failure [80, 81]. Structural failure finally occurs as voids coalesce together on a plane of emerging discontinuities, illustrated in Figure 3.4. Tvergaard et al. [80, 82, 83] published a series of papers which highlighted the primary role of hydrostatic stress on void growth formation in tension. However, this becomes more complex when considering any observed material pressure dependencies. Wu [79] showed that the rate-dependence of an individual void's growth initially reduces due to hardening rate. Ortiz and Molinari [84] analytically indicated that initial deformation is dominated by the viscous effect, whilst 'long-term' void growth evolution is dominated by inertia. From a constitutive modelling perspective, this highlights a limitation of traditional phenomenological approaches, such as Johnson-Cook [85], which do not account for

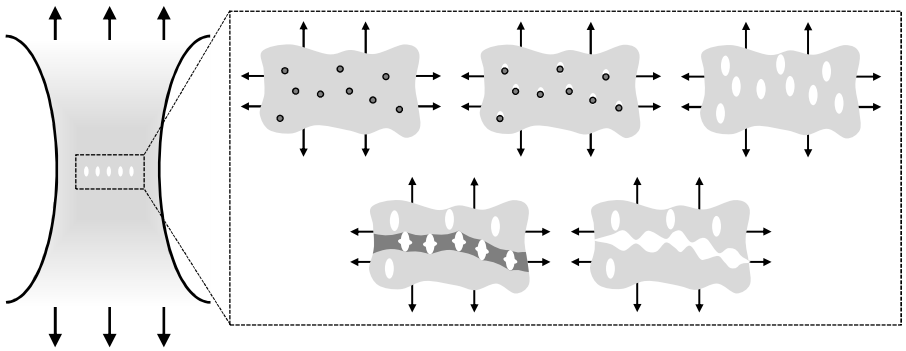


Figure 3.4: Emerging discontinuities due to void nucleation, growth and coalescence in tension due to initial defect presence.

rate dependent effects of damage accumulation. The continuum damage approach is more applicable when attempting to capture the combination of strain-rate and hardening-rate upon damage evolution [60, 61].

Adiabatic shear bands

The field of study surrounding adiabatic shear band (ASB) formation is extensive. This summary attempts to provide a broad overview with a primary focus relevant to dynamic impact. The fundamental relationship which characterises the ASB phenomena is the transition between hardening and thermally induced softening as a consequence of highly localised deformation. This was first observed by Costin, who measured the temperature at the point of localisation during ASB formation. This approach was later refined by fellow colleagues Clifton, Duffy, Hartley and Hawley [86, 87], their technique relied upon a torsional Kolsky bar and infrared photography. Figure 3.5, taken from [87], clearly depicts the phenomena whilst displaying both as highly localised and heavily deformed. For further generalised reading, Dodd and Bai [88] present an extensive review of the experimental aspects of ASB formation.

The maximum reported temperature increase - reported by Hartley et al. - was 450°C. At higher strain-rates, this process is exacerbated because of the relative time difference of the event and heat dissipation. This strain-rate sensitivity of the process

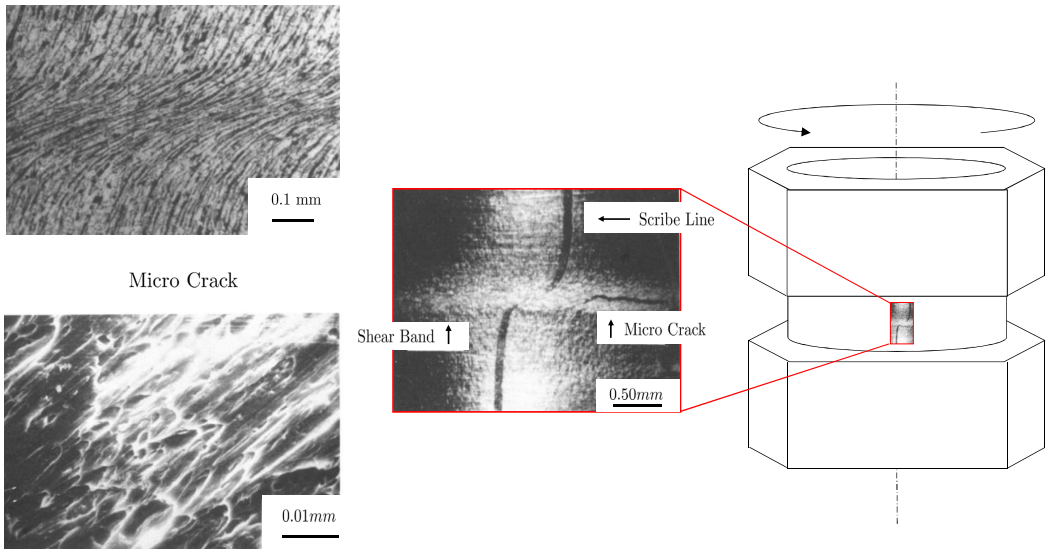


Figure 3.5: Dynamic shear band formation in a torsional specimen, macroscopic and microscopic shear band evolution [87].

is particularly poignant during high and ballistic rates of strain. Combining damage and strain-rate sensitivity within the aforementioned framework is therefore essential.

In terms of failure during impact, Liu et al. [89] demonstrated the relationship between crack propagation and ASB formation in Ti-6Al-4V with differing microstructures. Adiabatic shear bands in the bimodal microstructures are somewhat self-organised and evenly distributed. This corresponds with recent work from Hervé Couque, who presented [90] experimental and numerical solutions for Taylor impact experiments. This reinforced the assumption that shear banding is a critical mechanism during projectile erosion. However, Liu also showed that the ASB in the lamellar microstructures branch and inter-connect causing the crack path to deviate and fragmentation to occur. Spallation and scabbing are less common during impact of ductile materials such as steels and titanium alloys, whilst impact velocity, geometry and incident angle affect the failure mode. Plugging is the dominant mechanism during this research. Li and Jones [91, 92] identified the importance of strain rate as a contributing factor in the transition between ductile tensile rupture and adiabatic shear banding onset, shown in Figure 3.6. This may be use to calibrate damage accumulation and represent the initiation characteristics of shear band formation.

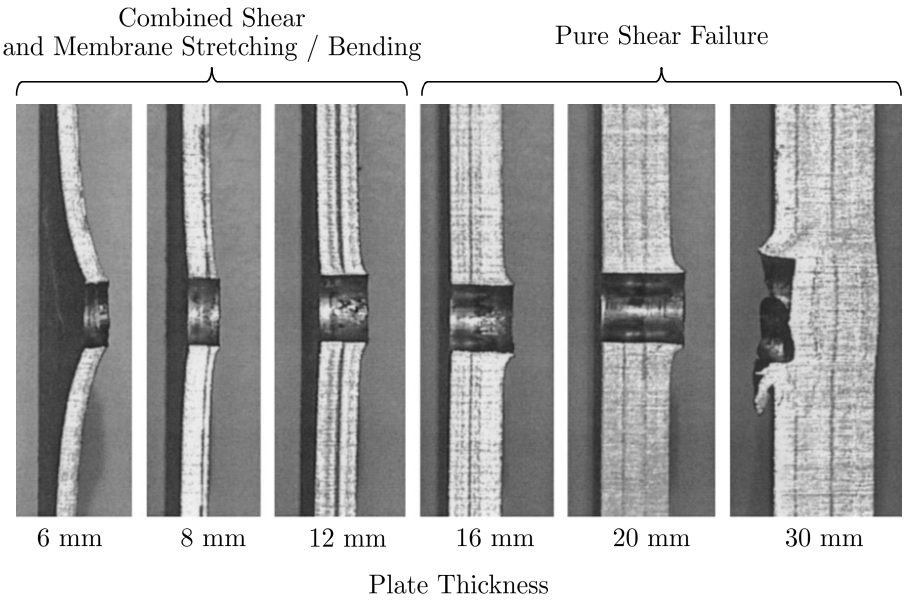


Figure 3.6: Cross section displaying the transition between pure shear and a combination of shear and bending [93].

Tore Børvik and colleagues [94, 93, 95] conducted extensive work in the field of plate impact. The basic process features i) impact-face indentation and compressive deformation, ii) varying localisation during rear-face bulging depending on the strain-rate, iii) global dishing which is dependent of plate thickness, iv) failure is typically characterised by plugging failure or shear rupture, otherwise know as hole enlargement. Other modes such as spalling, scabbing and petaling are not explored in any further detail as part of this research.

During a large experimental campaign of over 100 specimens [93], the deformation process was discovered to become more localised in thicker target plates for a given velocity. This indicates that the kinetic energy is transformed into the narrow areas of shear [95] due to the observed plugging failure mode preference within thicker target geometries. The variation in the failure mode affects the apparent target deformation at velocities close to the ballistic limit. This is evidenced by residual projectile velocities remaining relatively high and permanent deformation of the target increasing with velocity until the ballistic limit is approached, whereby a decrease is observed.

In parallel, over 150 simulations were conducted using various phenomenological models. The author notes that whilst empirical models can resolve approximations of projectile deceleration, for example, they should be applied with caution. Børvik et al. used the Wen-Jones, Bai-Johnson and Ravid-Bodner empirical models [93]. Unfortunately these models were unable to predict the variation in damage mode and failure characteristics when the plate thickness was varied. This was attributed to the assumption of a single physical mechanism dominating the problem when, as we see from the literature, there are multiple damage mechanisms operating in the most basic uni-axial tests. This provides motivation for a variable approach, such as ISV modelling, which does not require calibration to account for damage mechanism transitions and evolution of other variables. The mesh resolution used during these experiments was in the order of 160 elements in the target plate through thickness direction; this resolution is infeasible for industrial scale applications due to the resulting computational cost. Therefore, any proposed numerical solution needs to address mesh limitations, together with the limited ability of a single damage modes' ability to represent complex shear-rupture failure events during plate impact.

3.2.2 Multiple mode damage

The integral nature of dilatational and distortional damage modes has been established. The combination of these effects shall also be considered. Macroscopic dilatational damage due to void growth is largely limited to tensile loading conditions, yet distortional damage is also present in tensile experiments [96], due to shear banding and micro-void formation within the plastic zone (shown in Figure 3.7).

Distortional damage, due to shear stress, is dominant failure mechanism in torsion and compression, but also contributes to more complex loading conditions such as impact [97, 98]. This assertion is a general case as tensile regions exists in laboratory experiments of compression. During dynamic events ($1000s^{-1}$) thermal softening supersedes the effect of strain hardening in areas of localized high strain rates, thus

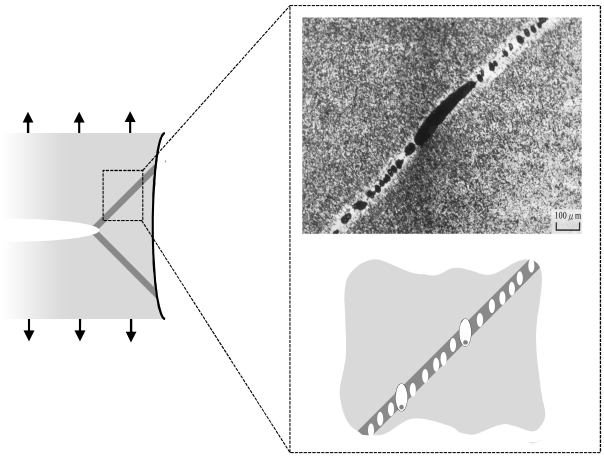


Figure 3.7: Micro-void formation within a shear band plastic zone, adapted from [78].

forming the so-called 'adiabatic' shear band failure planes. Shear band formation has been observed in both cylindrical thin-walls torsion specimens and axisymmetric hat shear specimens [97, 99].

In compression, Ti-6Al-4V along with numerous other alloys demonstrates a deformation instability failure on a 30° plane, corresponding to the loading axis [98, 100]. In addition, microstructural evaluation concludes that at high strain rates the compression fracture surface is also characterized by micro-void formation inside the shear band due to the thermal softening effect [97, 101, 95]. An explanation for the existence of both failure modes was proposed by Lee [78]. The apparent shear failure plane

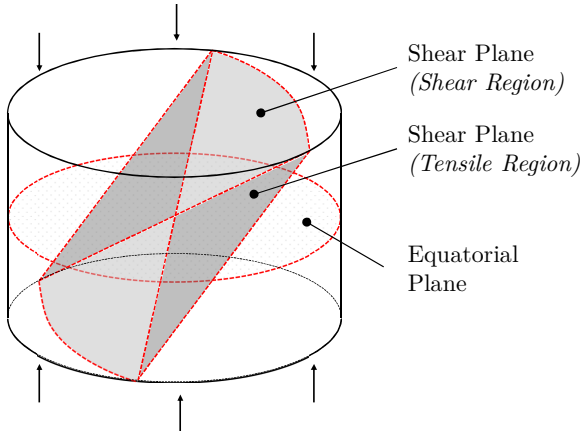


Figure 3.8: Uni-axial compression specimen shear plane tensile and shear stress regional distribution and equatorial plane.

is characterized by areas of shear and tensile stresses as a result of hoop stresses on the equatorial plane, shown schematically in Figure 3.8. Important observations were made in a series of publications by Bao and Wierzbicki [101, 102, 103] who related the stress triaxiality factor to predicted fracture modes. This was later verified by Giglio et al. [104] for Ti-6Al-4V using similar multi-axial experimental capabilities and numerical simulations. Figure 3.9 illustrates this relationship in the form of a fracture locus.

It is clear that a single failure mode is insufficient. Fractographic analyses have highlighted multiple active damage mechanisms leading to failure in the simplest uni-axial cases for tension [83, 85, 102], compression [76, 77, 78, 98, 105], and torsion [97, 106, 30, 107, 108]. Therefore, an appropriate constitutive approach should facilitate multiple damage mechanisms, informed by meso-scale and micro-scale phenomena developed within a macroscopic framework to accurately predict uni-axial failure and complex impacts. The complex interdependencies of these two damage mechanisms create a requirement for competitive and cumulative evolution in constitutive solutions.

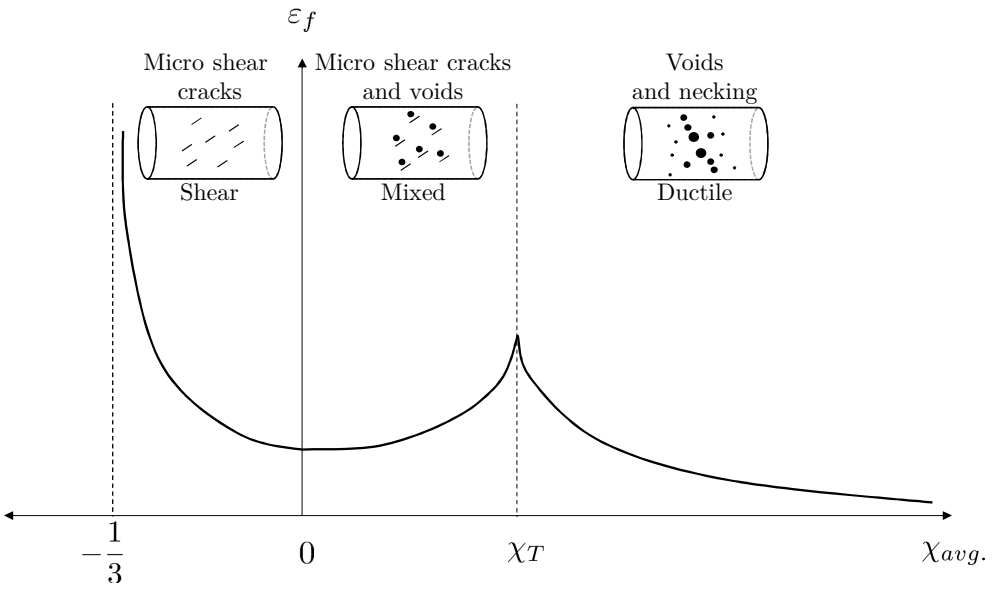


Figure 3.9: Generalised average stress triaxiality χ and failure strain ε_f locus with associated dominant damage mechanisms.

3.3 Plastic asymmetry and anisotropy

Industrial hexagonal close-packed (HCP) materials, such as titanium and magnesium, can seldom be assumed to be isotropic due to uni-directional twinning, for example [109]. In metal forming processes the yield point and subsequent plastic deformation were originally assumed to be isotropic and homogeneous in yield functions such as von Mises [110] and Tresca [111]. Extensive work conducted by Khan et al. [49, 112, 43, 113] not only illustrates the temperature and strain-rate dependency of Ti-6Al-4V but also the pressure sensitivity, often referred to as Strength Differential (SD) effect, in compression and tension.

3.3.1 Asymmetric deformation

In H.C.P. structures, such as titanium alloys, SD effects have been associated with deformation twinning which is a uni-directional mechanism. Previous investigators, such as Lee and Backofen, experimentally observed asymmetric yield points in biaxial tension and compression of Ti-6Al-4V. Linking macroscopic and microscopic phenomena, Hutchinson and Lowden [114] explored the influence of texture as a differential strengthening mechanism, which was found to significantly influence compression strength.

Cazacu's observations led to a proposed criterion for titanium alloys which is based upon the assumption that the observed SD effect is due to directionally sensitive twin evolution. This is contrary to Lowden and Hutchinson [114] who concluded that the asymmetric strengthening is not due to twinning. The strong SD effect observed in the c-axis was suggested to be due to $\langle c+a \rangle$ slip. Spitzig et al. [115] also observed a similar SD effect in polycrystalline aluminium alloys and steels without observing twinning. It was concluded that this effect was due to pressure on dislocation motion. Similarly, Neeraj et al. [116] noted a strong asymmetric effect in relation to $\langle c+a \rangle$ dislocation activity but concluded that the asymmetry could not be explained by this observation alone. Asymmetry in the CRSS of the $\langle a \rangle$-type slip was observed.

This led to the proposition that $\langle a \rangle$-type screw dislocation could lead to asymmetric propensity of cross-slip in the pyramidal plane, when in tension. There is no single mechanism which can be concluded upon in the literature to describe the observed asymmetric phenomena.

Numerically, various anisotropic criteria [48, 117, 118, 119, 120] based upon cubic materials exist which do not account for asymmetry in yielding. Cazacu and Barlat, for example, proposed a SD criterion based upon the earlier work of Hosford [119] which showed good agreement for highly asymmetric magnesium alloys. Nixon [121] also proposed a criterion for high-purity α-titanium; both studies where conducted at room temperature and under quasi-static conditions. However, Yoon [109] proposed a pressure sensitive criterion based upon Drucker-Prager's relation which was successfully applied to HCP materials magnesium and titanium. Whilst the physical mechanics of the phenomena remain undefined, the observable mechanism remains evident and subsequent numerical solutions should focus on simply reproducing the macroscopic behaviour.

3.3.2 Anisotropic deformation

Anisotropy is by definition crystallographic. One main advantage of macroscopic anisotropic constitutive modelling is the retention of textural data without resorting to computationally expensive crystal plasticity models [122]. This is essential for large-scale simulations which are becoming an increasing requirement from industry. The effects of anisotropy at different rates has been studies my many authors. Quasi-static anisotropic behaviour of Ti-6Al-4V has been extensively studied by Khan et al., however less data exists during shock loading. Burkins et al. [123] performed several ballistic plate impact tests and showed significant reductions in the V_{50} ballistic limit when varying the thermo-mechanical processing routes, and hence the microstructural texture. Failure was characterised by plugging and mixed-mode failure (bulging, delamination, shearing and spallation). The influence of annealing above the β-

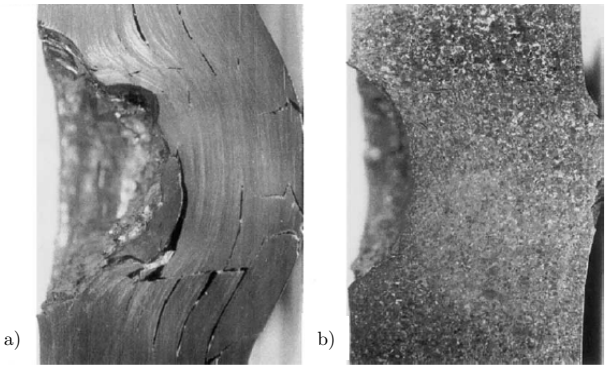


Figure 3.10: Fragment Simulating Projectile (FSP) impact cross-section in Ti-6Al-4V annealed below a) and above b) the β transus.

transus can be seen in Figures 3.10 a) and Figure 3.10 b) respectively.

Kad et al. [124] simulated the plugging response due to shear banding in two-dimensional polycrystalline aggregates. Their results indicate that misorientation of the basal slip to the shearing axis are the dominant factor affecting ballistic material response. Millett [38] also found that the shear strength of a material changes when shocked in the basal direction when compared to the tangential directions. This demonstrates that texture dependency exists at ballistic strain-rates. In order to simulate full three-dimensional sub-component impact events, computational lean solutions are required in combination with the aforementioned strain-rate, temperature dependencies and multiple damage mechanisms.

Numerical approximations on a macroscopic scale of the influences of texture have been proposed by a range of authors. Theories proposed by Hill [48, 125], Barlat and Lian [126] and Karafillis and Boyce [120] has been extensively studied and developed within the literature. All of these fundamental formulations utilise the associated flow rule, whereby the yield function and plastic flow rule are combined. Lademo et al. [127] proposed that the associated flow rule alone was unable to describe anisotropic plastic flow adequately, therefore suggesting a non-associated flow rule. Similarly, Stoughton and Yoon [128] observed similar deteriorations in accuracy attributed to kinematic effects due to the associated approach. Wu [129] expanded the classical

Hill formulation to include kinematic hardening which introduces directionality of the plastic strain-rate without introducing a non-associated flow rule suggested by Lademo [127] and Stoughton [130]. Other investigators [131, 132, 133] also combined anisotropy with mixed non-linear kinematic and isotropic hardening variables within the associated flow rule context. However, all of these contributors have concentrated on deep-drawing or bending tests at lower strain-rates. They have neglected the influence of damage, which is a necessity to describe both softening at high strain-rates and failure. More recently Khan [112] proposed a yield function with temperature and strain-rate dependence and the effects of anisotropic and asymmetric yielding, which was based on his previous experimental work. However, high strain-rates were not considered, neither were the effects of damage and kinematic hardening.

3.4 Summary

This chapter has focussed on the physcial mechanisms associated with deformation of Ti-6Al-4V at high strain-rates. Numerically, several authors have used the ISV approach to simulate individual phenomena observable at the macroscopic scale, which have been identified as relevant to high strain-rate deformation. However, none have combined all of these effects within a single constitutive framework.

- The fundamental concepts of continuum mechanics and the finite element method have been briefly discussed and their use identified as key tools within the field of solid mechanics.

- The contributions of numerous authors have illustrated the capability of the constitutive and Internal State Variable approaches to accommodate a wide variety of deformation mechanisms and length scales whilst maintaining computational accuracy and efficiently.

- The literature has demonstrated the importance and interdependencies of multiple ductile deformation mechanisms such as void growth and shear strain.

- Directionality during plasticity - in terms of anisotropy and asymmetry - are critical for describing textural effects during industrial manufacture and processing in Ti-6Al-4V.

- Key physical phenomena required to characterise the ductile deformation of titanium alloys during impact and high strain-rates have been identified. Figure 3.11 provides a visual representation of the required capabilities and their numerical solutions within the literature.

The capabilities described do not exist within a single constitutive framework. This provides a challenge and an opportunity to address within this research project.

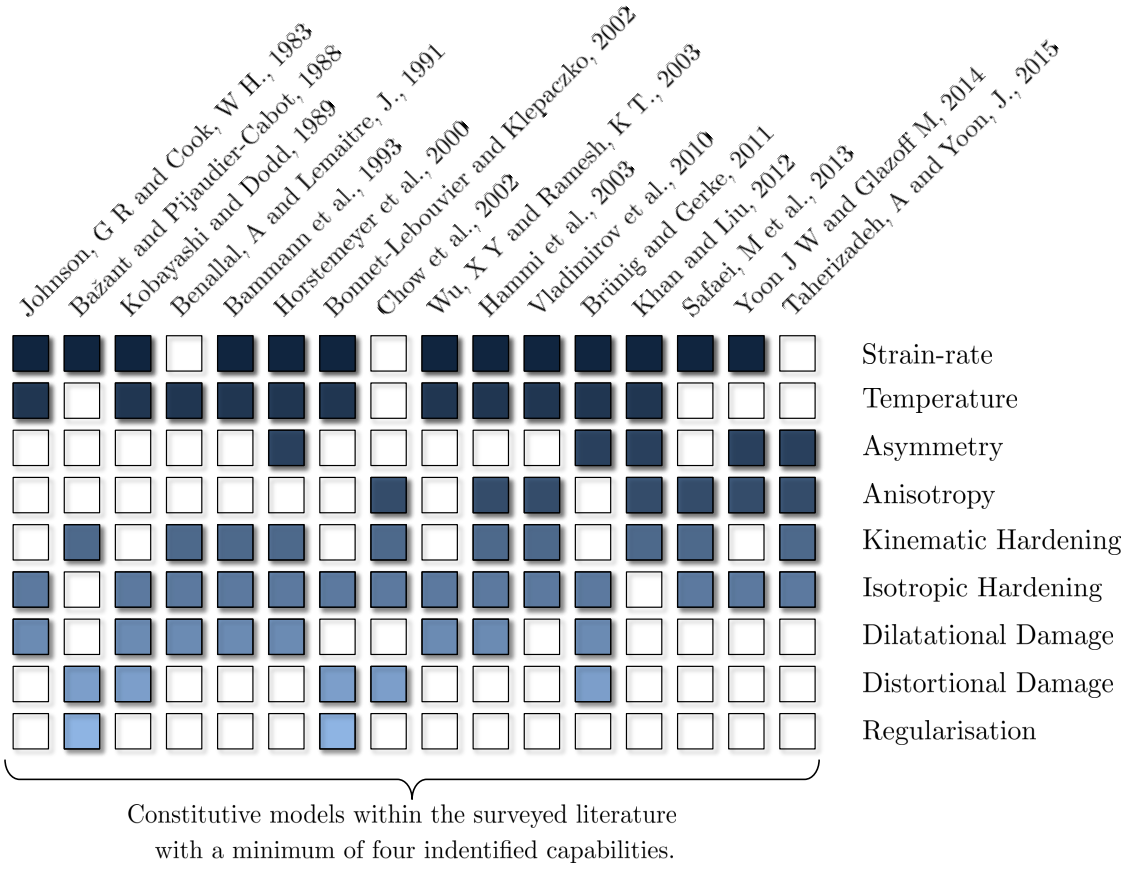


Figure 3.11: Constitutive modelling solutions corresponding to identified capability requirements.

Chapter 4

Experimental Support

The material responses under loading conditions relevant to this research are discussed during this chapter. The experimental techniques used and, the high strain-rate data produced for Ti-6Al-4V will form the foundation of numerical development validation exercises.

4.1 Uni-axial loading experiments

The experimental data described throughout this research was completed in-house, as part of ongoing parallel industrial projects performed by post-doctoral researchers within the Impact Engineering Team. The accumulated data is presented for validation purposes, where appropriate. The experimental datasets used to support the numerical constitutive developments and validations use small-scale uni-axial specimens. Small-scale uni-axial specimens increase repeatability by isolating certain failure modes and minimising the variability of influences at the boundary conditions. Specimen designs which produce well defined stress-strain states in predefined locations allow for repeatability and comparability. Depending on the complexity of a given experiment, multiple trials were conducted to account for the microstructural variation within the material.

The primary purpose of this research is to focus on high strain-rate thermo-mechanical behaviour, using split-Hopkinson bar and ballistic techniques.

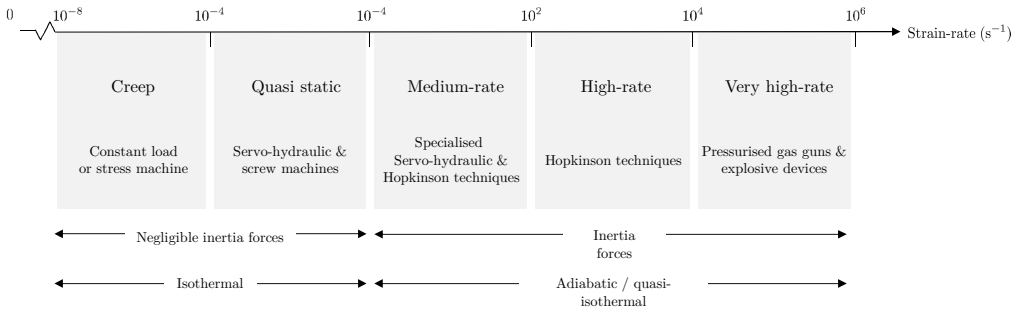


Figure 4.1: Typical experimental techniques for a range of strain-rates.

4.1.1 Split-Hopkinson bar

Material properties which include yield strength, ductility, ultimate strength and strain-rate sensitivity are used to characterise materials such as plastics, ceramics and alloys such as titanium. These properties are know to be time dependent, therefore efforts to experimental quantify these macroscopically observed effects at high strain-rates are required.

The original work of John Hopkinson and his son, Bertram Hopkinson has been extended by other investigators, such as Kolsky and Davies, who developed the now familiar concept of the split-Hopkinson pressure bar (SHPB). In addition to the classical compression testing pressure bar, which shall be described below, there are variants which allow for tension, torsion, reverse loading and various simultaneous combinations. Data produced during high strain-rate testing is typically applied to constitutive modelling problems, which require highly robust material models for complex large-scale simulations such as:

- Crashworthiness analyses in the automotive industry requires a minimum performance to protect human life.
- Blade-off and containment analyses within the aerospace industry, in the event of sudden and catastrophic foreign object damage such as bird ingestion.
- Gas turbine component failure due to erosion or fatigue and the subsequent ingestion or containment challenges.

- Civil applications in the event of earthquake or extreme weather conditions which endanger the dynamic structural integrity of load bearing engineering structures.

- Many industrial manufacturing processes such as friction welding, forging, machining and shot peening involve complex dynamic thermo-mechanical effects.

- The defeat of projectiles in defence applications or the deformation control of materials due to highly energetic material detonation.

Classical SHPB theory

The fundamentals of SHPB theory shall be discussed as the basis for later work. At impact, stress-wave excitations travel longitudinally along the incident bar, whilst the specimen is held in contact between the input bar and transmitted bar. The stress-wave is partially transmitted through the specimen and into the transmitted bar, and partially reflected. The corresponding incident ε_i, transmitted ε_t and reflected ε_r strains are shown in Figure 4.2 and Figure 4.3.

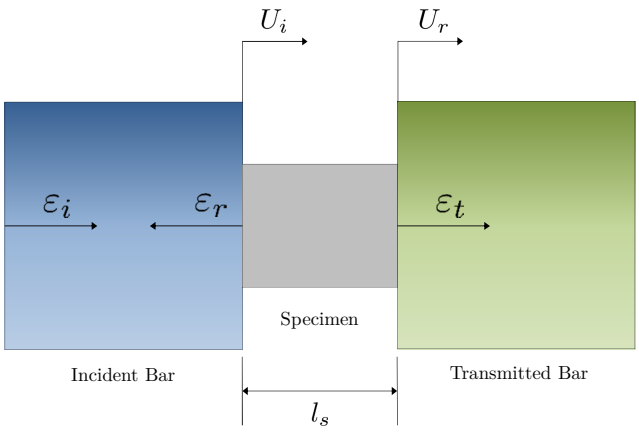


Figure 4.2: Specimen, incident and transmitted bar interfaces.

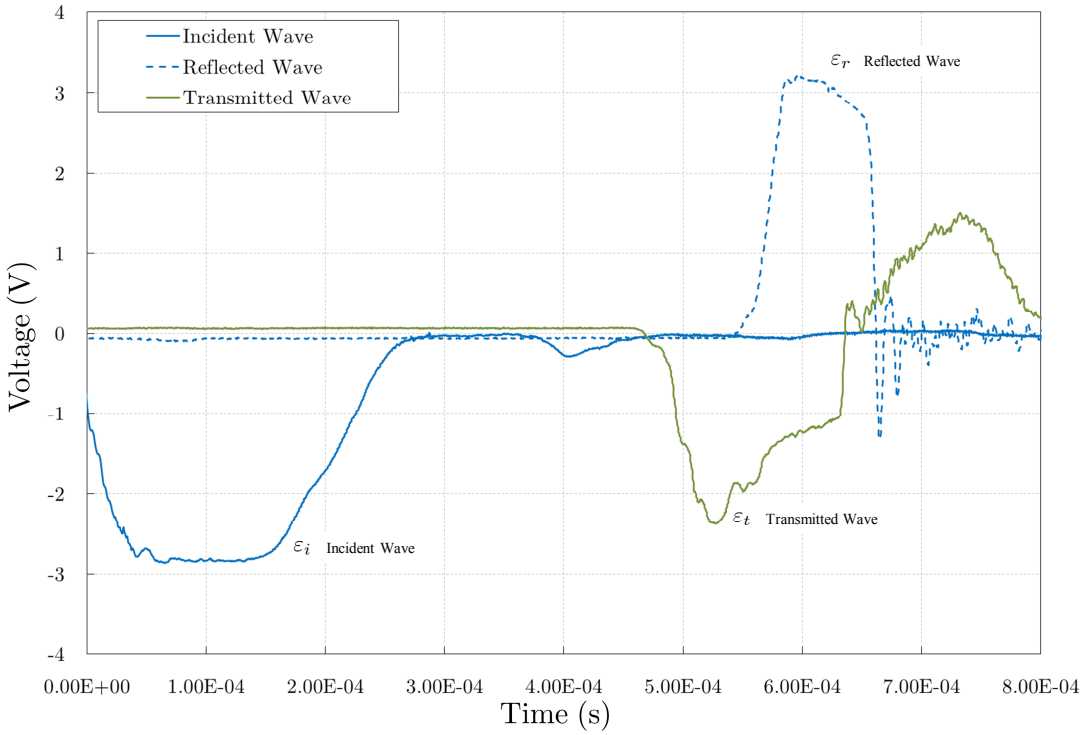


Figure 4.3: Strain gauge signals demonstrating the individual signals received during a SHPB experiment.

The solution for calculating displacement u from wave theory can be written as follows

$$u = f(z - c_m t) + g(z + c_m t) = u_i + u_r, \tag{4.1}$$

where f and g are functions describing the incident (u_i) and reflected (u_r) wave shapes, z is a known point in the bar and c_m is the wave speed in the bar material. Strain-rate calculations are required to quantify and compare rate sensitivities and various thermo-mechanical properties. These are derived by differentiating equation (4.1) with respect to z as follows

$$\varepsilon = f' + g' = \varepsilon_i + \varepsilon_r, \tag{4.2}$$

the velocities $(\dot{u})$ can then be obtained by differentiating equation (4.2) with respect to time (t) for the incident $(\dot{u}_i)$ and reflected $(\dot{u}_r)$ velocities as follows

$$\dot{u}_i = c_m(-f' + g') = c_m(-\varepsilon_i + \varepsilon_r), \tag{4.3}$$

$$\dot{u}_r = -c_m \varepsilon_t. \tag{4.4}$$

The strain-rate in the test specimen $\dot{\varepsilon}$ is given as:

$$\dot{\varepsilon} = \frac{(\dot{u}_i - \dot{u}_r)}{l_s} = \frac{c_m}{l_s}(-\varepsilon_i + \varepsilon_r + \varepsilon_t), \tag{4.5}$$

where l_s is the instantaneous length of the specimen. The variables $\dot{u}_i$ and $\dot{u}_r$ are the velocities at the bar-specimen interfaces. Equations (4.3) and (4.4) are valid at any value of z along their respective bars. The corresponding forces within the incident and reflected bars are

$$F_i = AE(\varepsilon_i + \varepsilon_r), \tag{4.6}$$

$$F_t = AE\varepsilon_t, \tag{4.7}$$

where A is the cross-sectional area of the pressure bar and E is the Young's modulus of the bar. The engineering stress ($\sigma = F/A_0$) is calculated in association with the original area, A_0.

Whilst the volume remains the same for incompressible solid, i.e. $A_0 l_0 = A_t l_t$, strain can be calculated from either the length or area. Consequently, the true stress can be calculated from the strain-gauge signal as follows:

$$\sigma_{tr} = \frac{A_0 E \varepsilon_t}{A_t}. \tag{4.8}$$

where A_t is the specimen cross-sectional area at time t. Further detailed explanations of dynamic testing procedures and theories can be found in [134].

SHPB apparatus

In brief, the split-Hopkinson pressure bar (Figure 4.4) features a striker which excites an elastic incidence stress-wave. The experimental apparatus consists of the following apparatus and arrangement:

- The input and output bars are required to be symmetrical and straight for alignment purposes to avoid buckling.
- Alignment is ensured with a system of fixtures and bearings. This allows the bars to move with minimal resistance in the longitudinal direction, in relation to the direction of travel of the striker.
- The striker bar is typically accelerated by releasing a valve between two adjacent chambers, one of which is filled with pressurised gas. This allows for predictable control of the striker velocity.
- Strain-gauges on both input and output bars measure the elastic response and are used to infer the elastic-plastic response of the specimen.
- High-speed data acquisition equipment is used to capture strain-gauge data and optically measurements at the surface with Digital Image Correlation (DIC) software.

For classical SHPB theory to be valid elasticity is assumed to remain in the incident and transmitted bars throughout testing. Therefore, high strength materials such as maraging steel and nickel superalloys are common candidate bar materials. This allows for higher stresses to be attained within the specimen, without causing

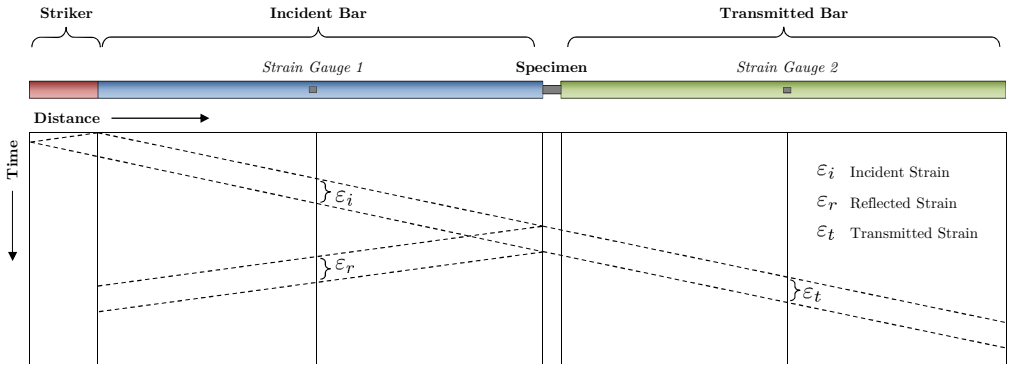


Figure 4.4: Schematic diagram of split-Hopkinson pressure bar arrangement and Lagrangian diagram illustrating stress wave propagation.

yielding in the bars material. Nickel-base superalloys also retain their elastic limit at high temperatures, which is important if the specimen needs to be heated.

The length (l) and diameter (d) ratio of the pressure bars should exceed 20:1 in order to achieve wave separation for data analyses. The bar diameter is also affected by the strain-rate required in the specimen; ultra-high strain-rates can be achieved with smaller diameter bars [134]. Finally, the length of the striker determines the total amount of strain via the length of the incident wave. The incident bar length must also be, at least, double the length of the incident wave, to eliminate wave interaction during data collection. The length of the bars is then also directly related to strain gauge position, such that wave interferences are avoided.

The bars should be supported but allowed to move in the direction of wave propagation, the support structure should also align the bars to a high tolerance. The bars should be physically straight to avoid boundary conditions which violate the one-dimensional wave propagation assumption, to maintain uniform propagation in accordance with the theory. Violation of these conditions can lead to noise in the received signal and bending forces in the bars.

The striker material is commonly identical to the incident bar and of the same diameter. Moreover, the length is determined by the desired length of the incident wave. In addition, accelerating the striker bar with compressed gas, as opposed to explosive charges, is preferable due to excitations within the striker prior to impact [134].

IEL testing facility

Fortunately, the Impact Engineering Laboratory has extensive in-house testing facilities, which include various testing apparatus and data acquisition techniques were used to obtain the uni-axial data presented herein.

- Zwick 250: Quasi-static electric screw-driven loading rig, equipped with a 20kN load cell. High definition telecentric camera systems were used to capture high

definition images for post processing. The cross-head velocities were $v_t \approx 8 \cdot 10^{-3}$mm/s in tension and $v_t \approx 2.5 \cdot 10^{-3}$mm/s in compression.

- In-house SHCB: Compression split-Hopkinson bar features a compressed gas chamber controlled striker ($v \approx 10$ m/s). Calibrated strain gauges located on the loading bars were used to calculate strain and forces. For verification, the SIMX16 an ultra high-speed camera was used to verify strain estimates.

- In-house SHTB: Tensile split-Hopkinson bar features a compressed gas chamber controlled striker ($v \approx 20$m/s). Calibrated strain gauges located on the loading bars were used to calculate strain and resisting force. For verification, the SIMX16 ultra high-speed camera was used to verify strain measurements.

Both high strain-rate and medium strain-rate tensile tests were performed on the customised Hopkinson bar apparatus which allows for a large range of strain rates due to the length of the incident and transmitted bars [135].

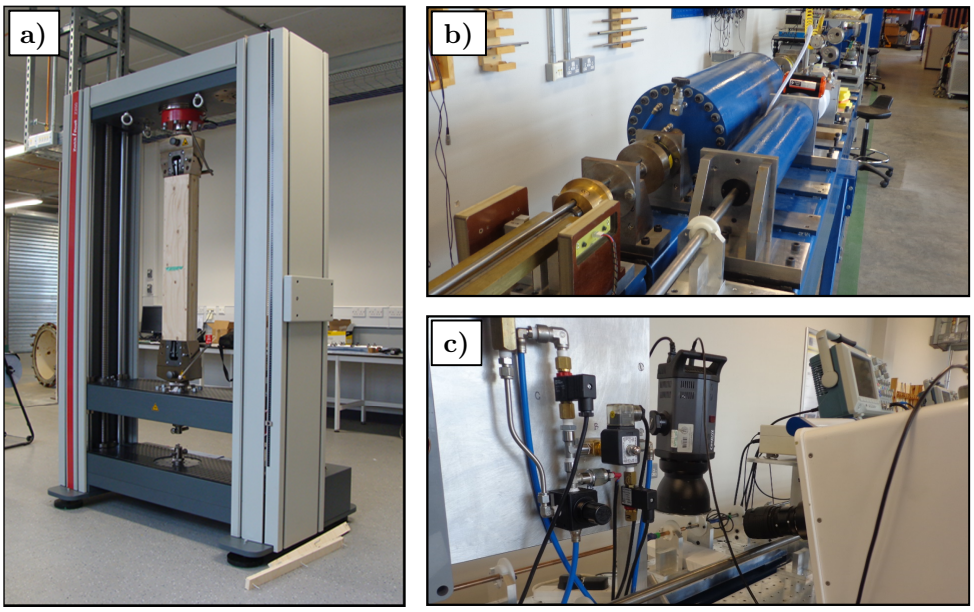


Figure 4.5: Experimental apparatus: a) Electrically screw driven ZWICK 250, b) Tension and compression Hopkinson bars, c) SIMX16 ultra high-speed camera.

Specimen design

The same specimen geometries were used for all strain-rates, to maintain comparability and consistency in terms of boundary conditions effects. Small scale specimens are used due to the strain-rate which is required during dynamic testing. Critical dimension schematics are shown below for repeatability and further discussion. The tensile specimen has a threaded section on either end, this corresponds to a female threaded hole in both the incident and transmitted bars. The engagement of the threads are accounted for during experimental post-processing, and plasticity is assumed to be confined to the gauge section.

The small-scale compression specimen (shown in Figure 4.7) is used extensively and during simulations. The experiments detailed during this chapter use the compression dog-bone configuration, shown in Figure 4.8. The reason for this specimen design was the avoidance of boundary conditions effects at interfaces. The limitation of this particular design is the initiation of failure at the fillet-shoulder interface. Overall, the specimen design is not critical for comparative numerical purposes.

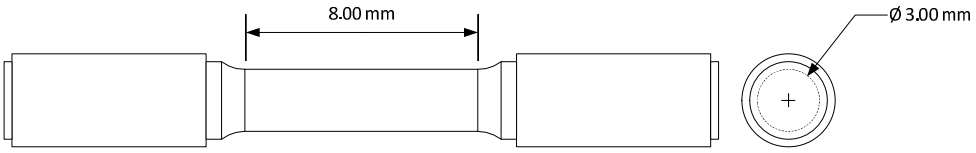


Figure 4.6: Tensile specimen at various strain rates, including critical dimensions.

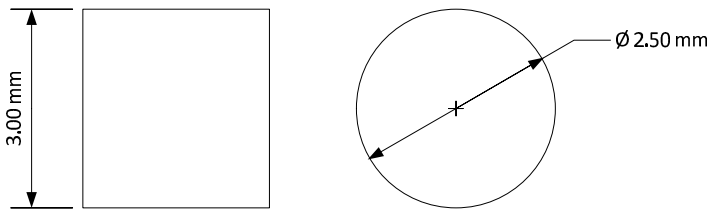


Figure 4.7: Compression specimen at various strain rates, including critical dimensions.

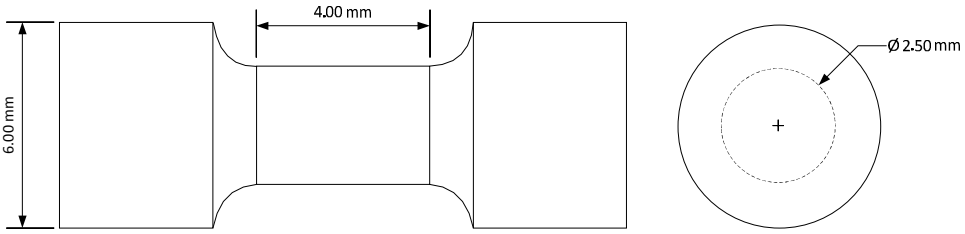


Figure 4.8: Compression dog-bone specimen at various strain rates, including critical dimensions.

High strain-rate validation

In order to assess the validity of the high strain-rate testing apparatus used within this chapter, dynamic force equilibrium within the specimen is required. This ensures deformation is uniform across the specimen and initial inertia effects are overcome. This condition is critical for split-Hopkinson bar experimentation, and allows for comparison of stress-strain responses across multiple strain-rates. Force histories in the specimen can be derived from the strain histories at the strain gauges, shown in Figure 4.4. The duration of time period prior to dynamic force equilibrium is determined by the specimen geometry and speed of sound within the material (c_m), this can be equated below

$$\frac{\pi \, l_s^t}{c_m}, \tag{4.9}$$

where l_s^t is the total length of the specimen, and not simply the gauge length. As a 'rule of thumb', dynamic equilibrium is usually within the region of 3 - 5 reverberations of the stress wave within the specimen [134]. This corresponds to an analytical approximation for dynamic equilibrium of $33\mu s$ in tension and $13\mu s$ in compression, for the geometries illustrated in Figure 4.6 and Figure 4.8. These estimations can be used to verify experimental observations by plotting the force histories and corresponding strain-rate histories, as shown in Figure 4.9 and Figure 4.11.

Figure 4.9 shows input and output bar force histories in tension. Dynamic equilibrium is assumed to have been reached at approximately 35 μs, which corresponds to a strain of 0.25% as calculated from the strain history provided in Figure 4.10.

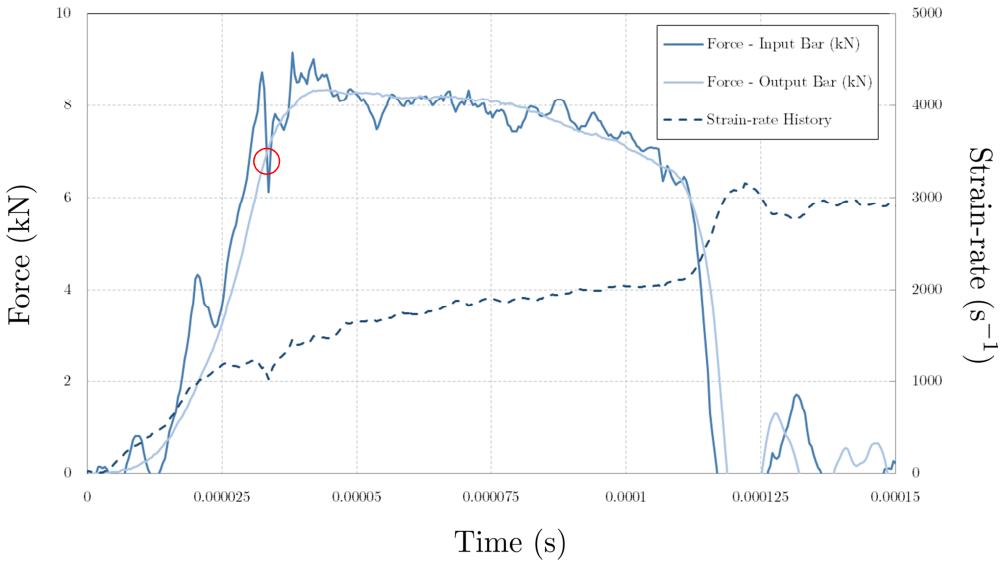


Figure 4.9: Input and output bar forces achieved in tension, with corresponding stain-rate history.

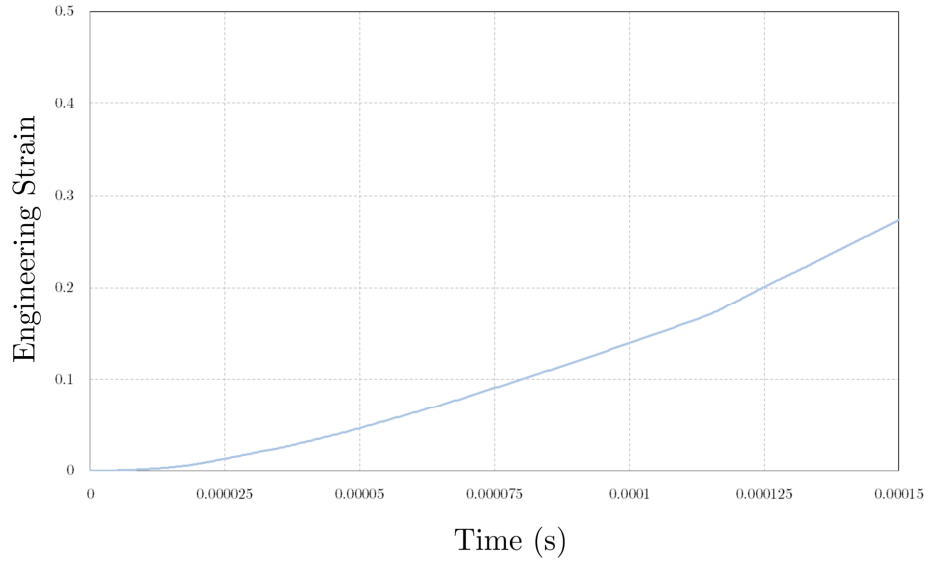


Figure 4.10: Strain history tension of Ti-6Al-4V during high strain-rate tensile deformation.

Similarly, Figure 4.11 shows input and output bar force histories in compression.

Dynamic equilibrium can be assumed to have been reached at approximately 30 μs which corresponds to a strain of 0.33%, which is calculated from the strain history provided in Figure 4.12.

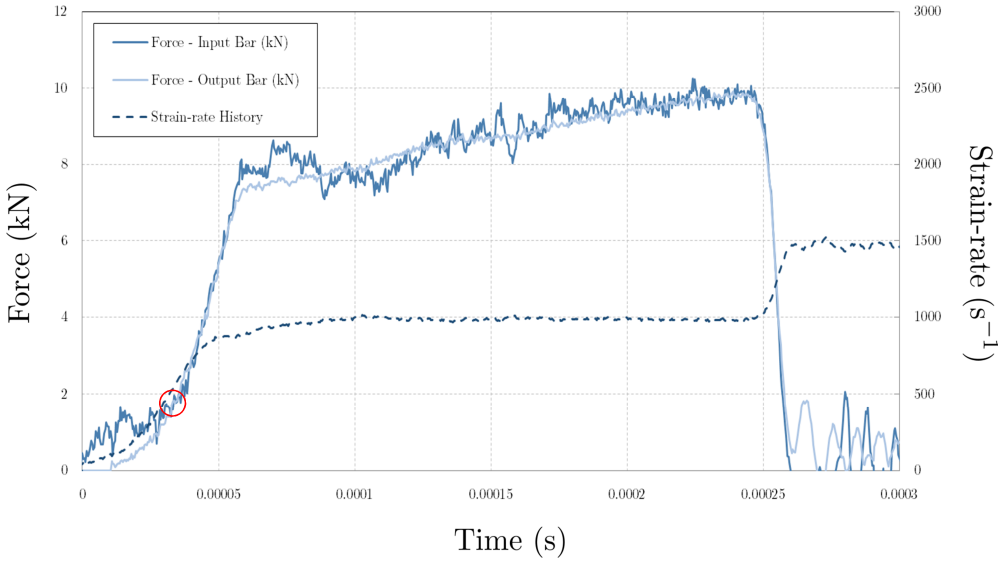


Figure 4.11: Input and output bar forces achieved in compression, with corresponding stain-rate history.

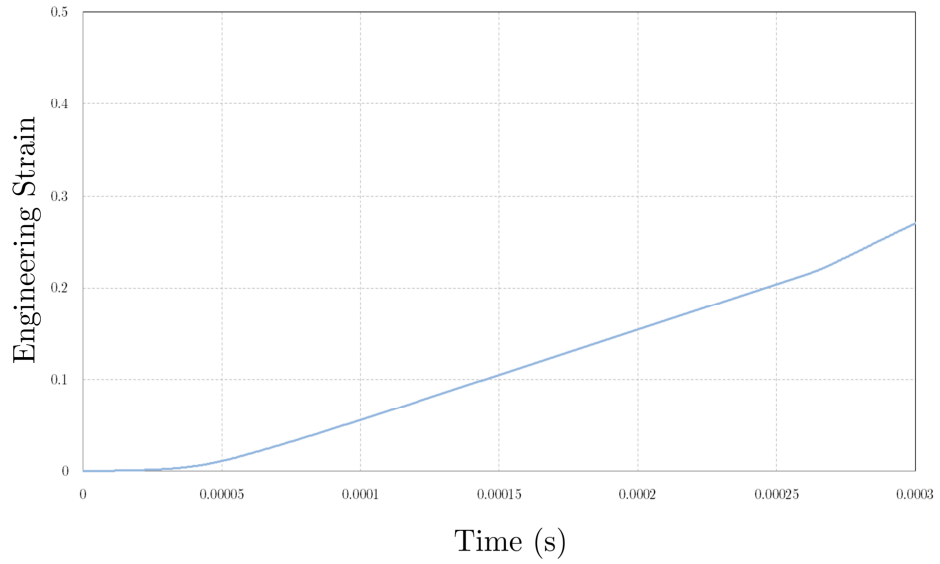


Figure 4.12: Strain history tension of Ti-6Al-4V during high strain-rate compressive deformation.

The time taken to achieve dynamic force equilibrium for both tension and compres-

sion was within an acceptable range when comparing the analytical approximation and experimental observation. For both tension and compression it can, also, be assumed that the dynamic equilibrium has been achieved as the strain-rates, beyond equilibrium and prior to failure, are approximately constant. This indicated that the measured dynamic stress, strain and strain-rates quantities are valid for the experimental arrangements used during this chapter.

4.1.2 Rate sensitivity

As discussed, strain rate sensitivity based upon dislocation theory has been studied for many years and is integral to characterising titanium alloys. The observed strain-rate sensitivity illustrates the sources of motivation in aerospace design to utilise this observable characteristic. Whilst the current research focus is high strain-rate applications, correct numerical representation of titanium alloy deformation mechanisms requires strain-rate sensitivity capability.

The experimental results presented here have been completed within the Impact Engineering Laboratory at the University of Oxford as part of a larger and ongoing industrial collaboration to characterise various titanium alloys, including Ti-6Al-4V.

Tensile results

It is clearly demonstrated in Figure 4.13 that Ti-6Al-4V shows a strong strain rate dependency. This is characterised by an increased yield strength and reduced elongation to failure at higher rates of strain.

From Figure 4.14 a larger amount of necking is observed when compared to Figure 4.15. This is reflected in the elongation prior to failure illustrated in Figure 4.13. From Figure 4.13 two distinctions can be made when comparing strain-rate flow stress characteristics.

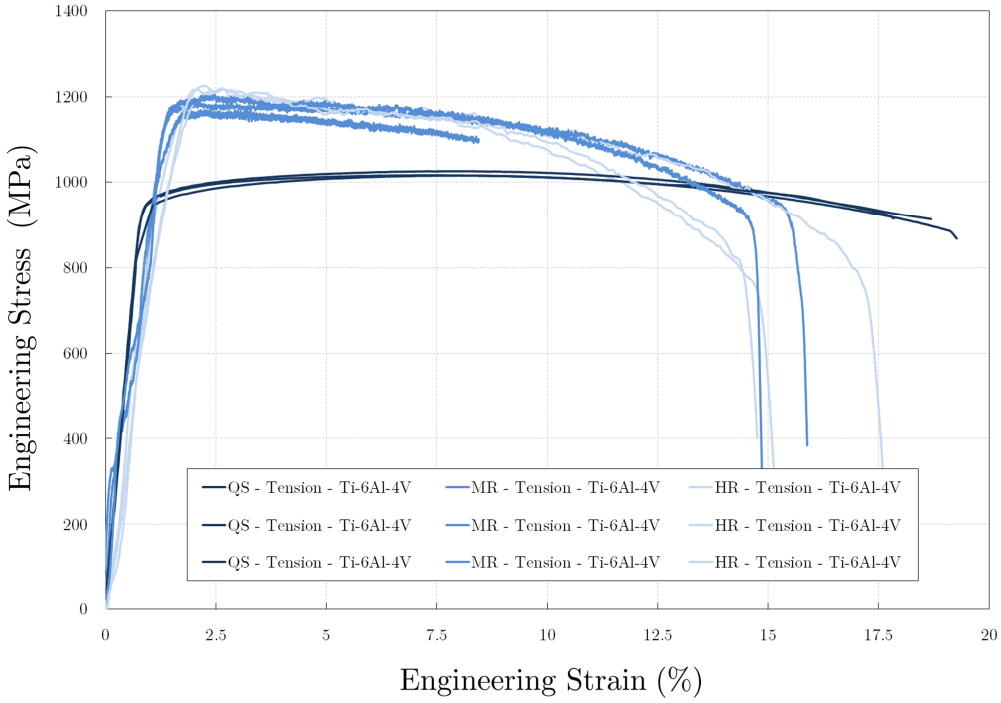


Figure 4.13: Observed macroscopic tensile flow-stress strain-rate sensitivity of Ti-6Al-4V.

Firstly, there is an increase from ~ 920 MPa, in the quasi-static regime, to $\sim$ 1140 MPa in the high strain-rate regime. There was a negligible difference in yield point ranging from medium strain-rates to high strain-rates. In addition, the strain to failure also varies depending on strain-rate. This is due to strain hardening effects in relation to the increased applied stresses required to provide sufficient energy with which dislocations can overcome barriers to their motion. The engineering strain to failure for quasi-static tests is elevated when compared to higher rates of strain. This relationship can also be roughly applied to high and medium strain-rate tests, although the result scatter gives a lower level of confidence. This is partially due to the occurrence of shear banding and influence of thermal softening during plastic deformation which exceed the influence of strain hardening [136]. It should also be noted that the failure plane in tension differs between tests and the point of localisation also differs. This is likely due to the microstructure and internal defects, which act as stress raisers.

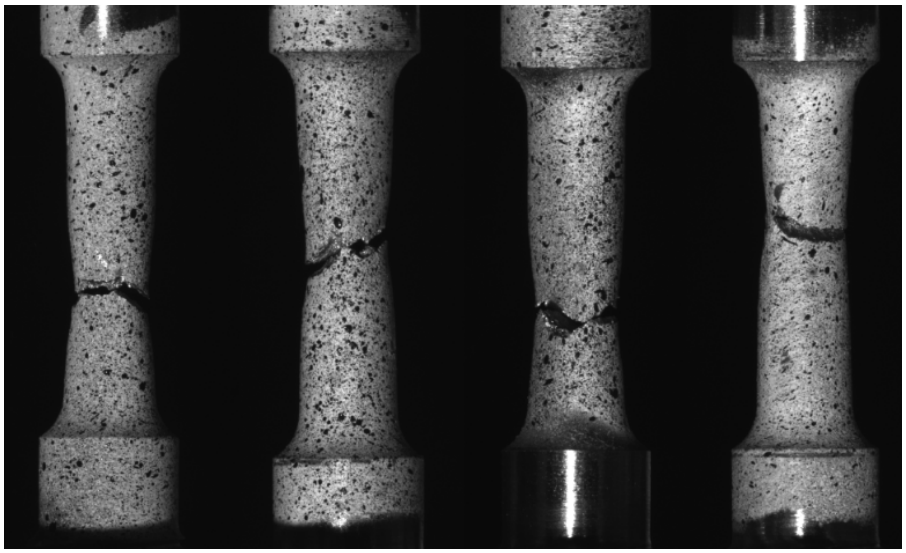


Figure 4.14: Quasi-statically loaded tensile specimens at the point of fracture.

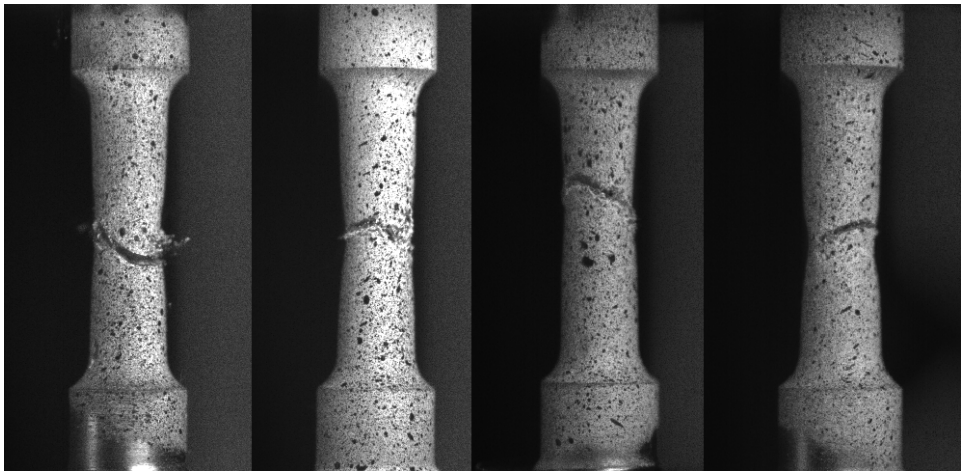


Figure 4.15: High strain-rate loaded tensile specimens at the point of fracture.

Compressive results

Similarly, during compression Ti-6Al-4V also displays strain-rate sensitivity in the form of yield strength increase and ductility decrease at elevated rates of strain.

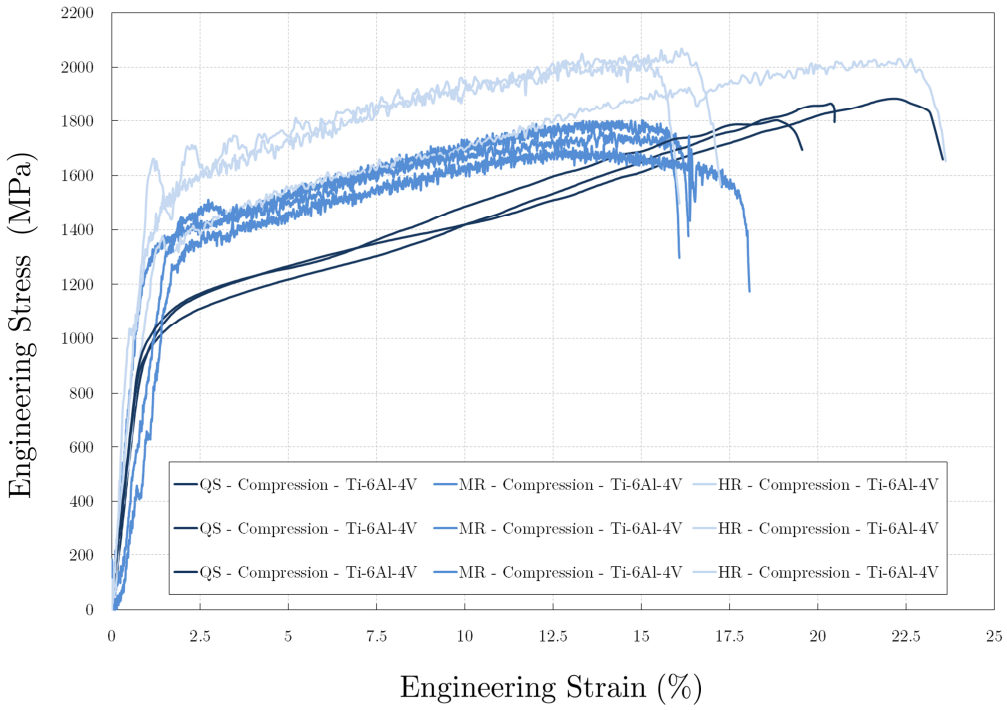


Figure 4.16: Observed macroscopic compressive flow-stress strain-rate sensitivity of Ti-6Al-4V.

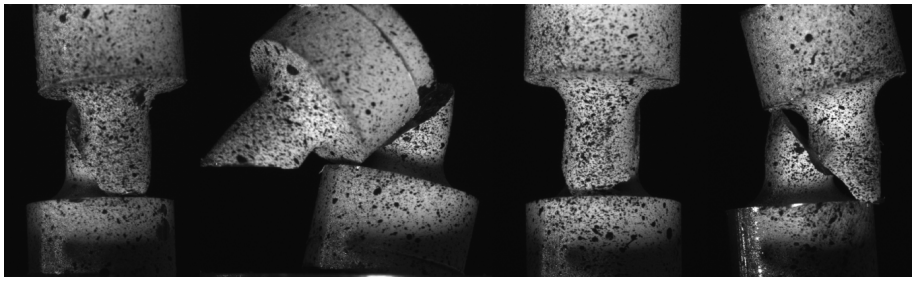


Figure 4.17: Quasi-statically loaded compression specimens at the point of fracture.

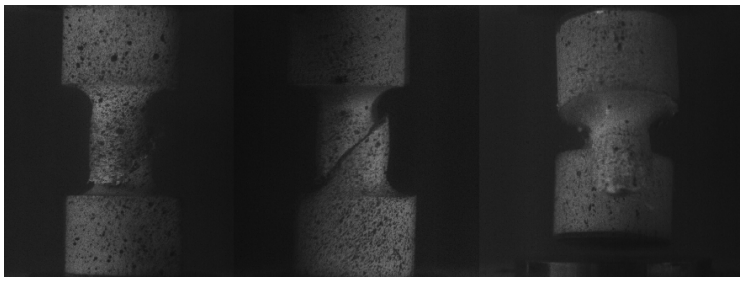


Figure 4.18: High strain-rate loaded compression specimens at the point of fracture.

The cylindrical dog-bone specimen geometry was chosen for compression to eliminate complexities at the boundary conditions, due to the influence of friction. Less can be derived from these images, however during quasi-static loading in Figure 4.17 evidence of bending or buckling can be seen. In both cases the fracture is characterised by the typical 30° shear plane, in relation to the loading axis.

Rate sensitivity summary

In conclusion, it has been clearly demonstrated that Ti-6Al-4V shows a dramatic difference in flow stress under varying rates of strain. It has also been demonstrated that the failure mode in tension and compression differ; compression is notably characterised by a distinct shear fracture plane whilst tension is more difficult to generalise. This is an area which can be explored in more detail numerically during inelastic deformation and failure. Noise in the flow curves can be attributed to instrumentation and sampling rates.

4.1.3 Directionality trends

Tensile specimens were machined from a section of fan systems containment casing in both the axial and tangential orientations, with respect to the rolling direction. The aim of this exercise was to establish the degree of anisotropic behaviour and any predictable trends which are predictable numerically. This analysis was performed for tensile specimens at three different strain-rates.

Quasi-static results (Figure 4.19) indicate a small degree of observable anisotropic trend behaviour in both yield strength and flow stress. Specimens machined for tensile loading in the axial direction, in relation to ring rolling, demonstrate a small increase in tensile yield and a marked decrease in the stress and strain at failure. Strain to failure scatter is within the region of 2.5% for both orientations; however, a distinct trend can be seen whereby specimens axially loaded in the direction tangential to rolling fail at larger strains and yield at a lower point. For clarity, Figure 4.20 displays two tests which demonstrate this trend.

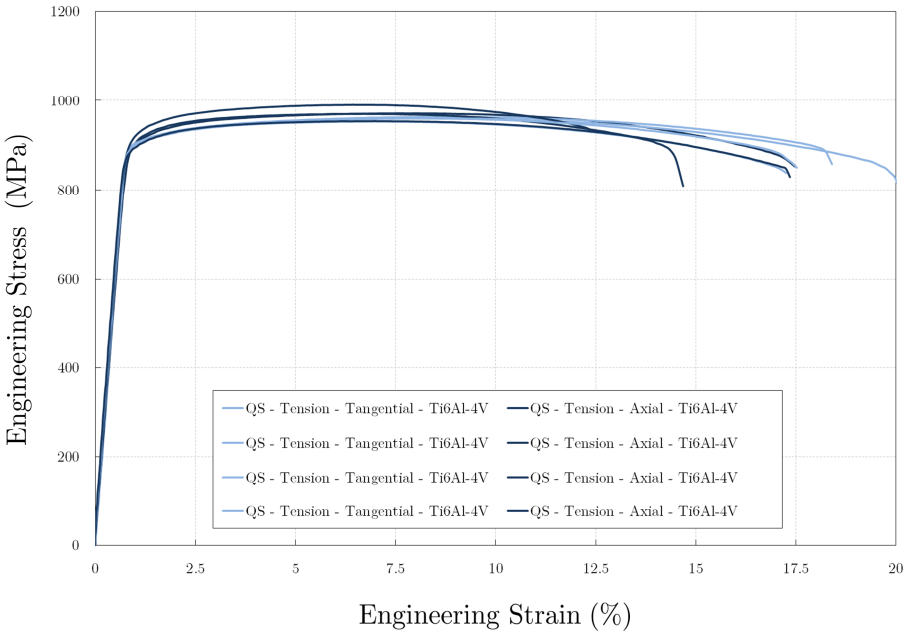


Figure 4.19: Quasi-static macroscopically observed tangential and axial flow-stress discrepancy trends.

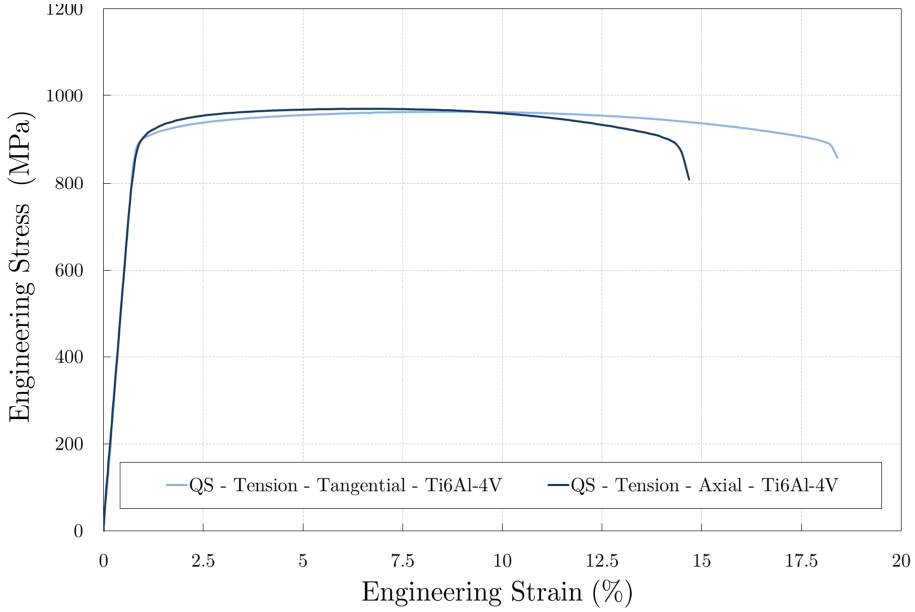


Figure 4.20: Yield stress and flow stress behaviours for quasi-static tangential and axial tension.

At medium strain-rates the influence of directional yield strength can no longer be clearly identified in all experiments, as illustrated in Figure 4.21. However, the flow-stress relationship evident at quasi-static strain-rates remains. The scatter in terms of

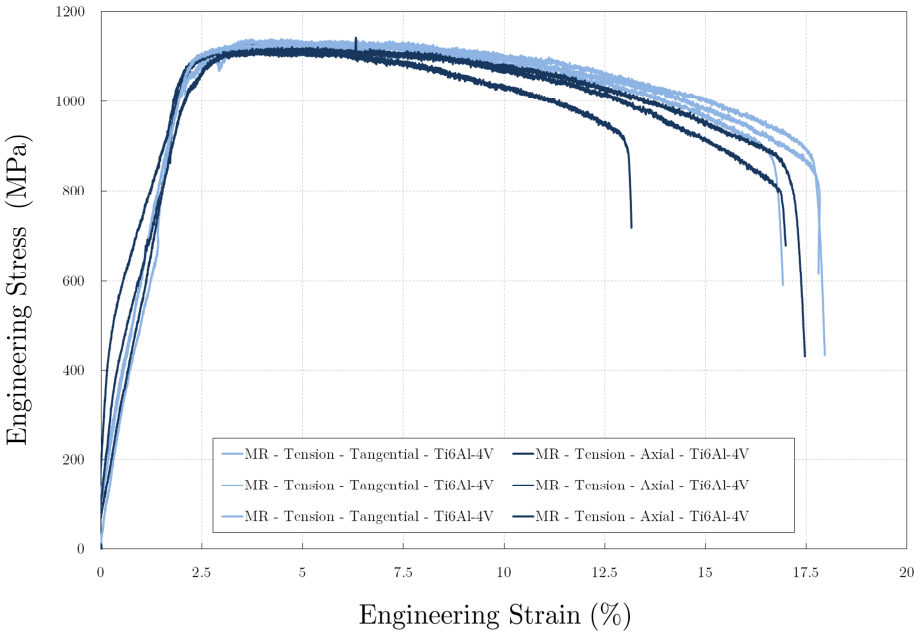


Figure 4.21: Medium strain-rate macroscopically observed tangential and axial flow-stress discrepancy trends.

strain to failure and stress at failure is larger for the axial direction $\sim 5\%$. Excluding potential anomalous results the trend remains apparent - tangential strain to failure and stress immediately prior to failure exceed their axial counterparts. Reduction of results demonstrates the described trend in Figure 4.20.

Finally, the comparison between axial and tangential specimen orientations at high strain-rates is compared in Figure 4.23. Whilst a similar trend can be identified, clear definition of the yield strength discrepancies for all tests falls within scatter. This is expected as yield stress during high strain-rate experiments are difficult to define. Again, the strain to failure scatter in the axial direction is approximately 5%. The axial test which failed at the largest accumulated strain ($\sim 18.5\%$) also features the lowest yield strength, which warrants further investigation. Potential causes of the anomalous yield behaviour could be due to variability of the pulse shaper used, the application of silicon grease and inhomogeneity within the material. Another factor effecting the reliability of the yield at higher strain-rates is the so-called Pochhammer-Chree oscillations [137]. Overall, the maximum variation of yield stress remains low,

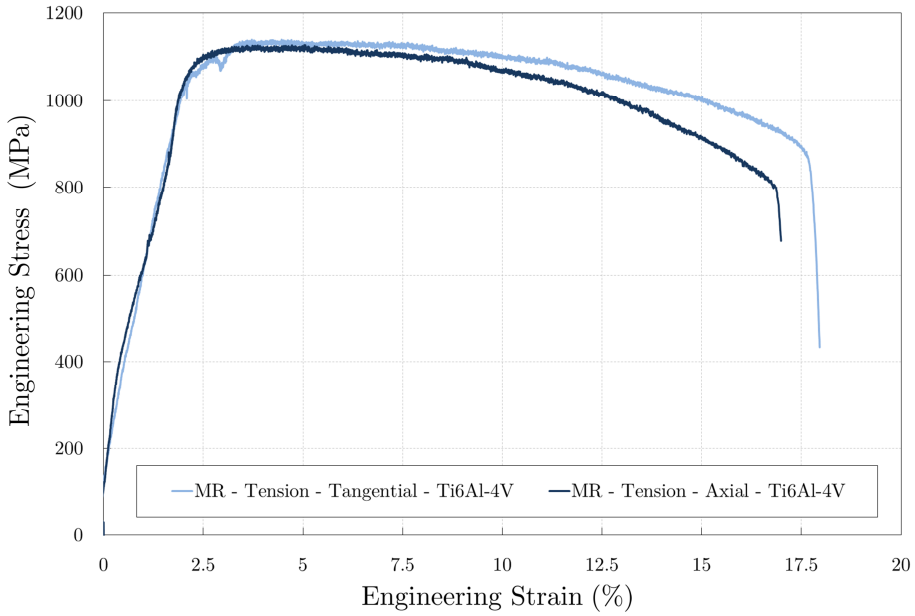


Figure 4.22: Yield stress and flow stress behaviours for medium-rate tangential and axial tension.

within 20 MPa, which is a highly reliable result for most purposes. Once again, a reduced set of experimental curves illustrates the trends observed at each strain rate, whereby the axial yield exceeds the tangential equivalent and failure occurs at lower total strains (see Figure 4.24).

Directionality summary

In order to make a confident assessment based upon directionality, further analysis of the microstructural evolution is required and diameter of the specimen gauge section neck region at failure is required, to calibrate the Lankford parameters, discussed in Chapter 7. However, from the macroscopically observed results presented here, it is clear that the tangential specimens persistently display both increased strain to failure and stress immediately prior to failure at all three strain rates examined. It can also be inferred that the yield strength in the axial direction marginally exceeds that of the tangential, accounting for scatter induced at higher strain-rates. The role of anisotropy has been demonstrated and can be quantified, within a margin of scatter, for uni-axial tension at three strain-rates.

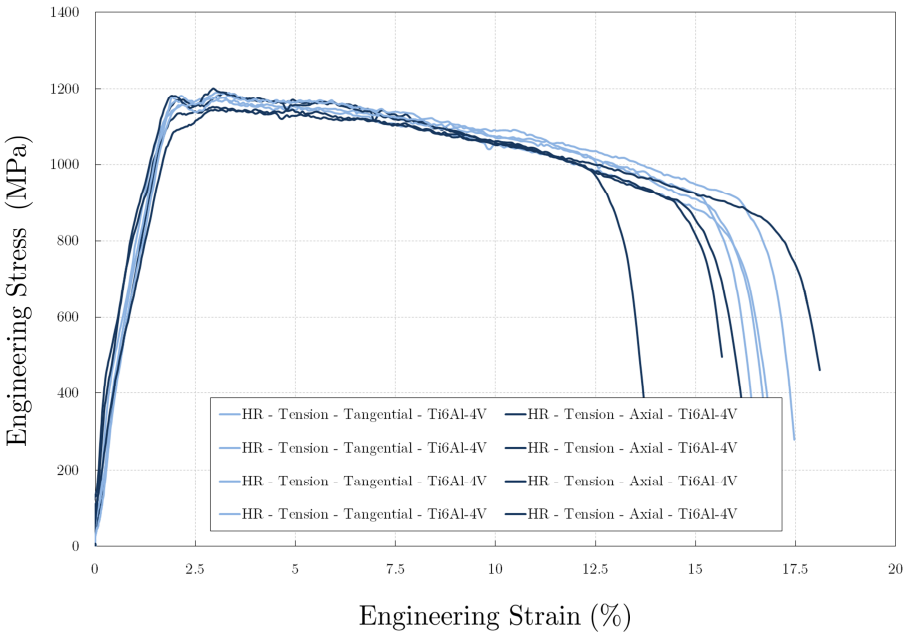


Figure 4.23: High strain-rate macroscopically observed tangential and axial flow-stress discrepancy trends.

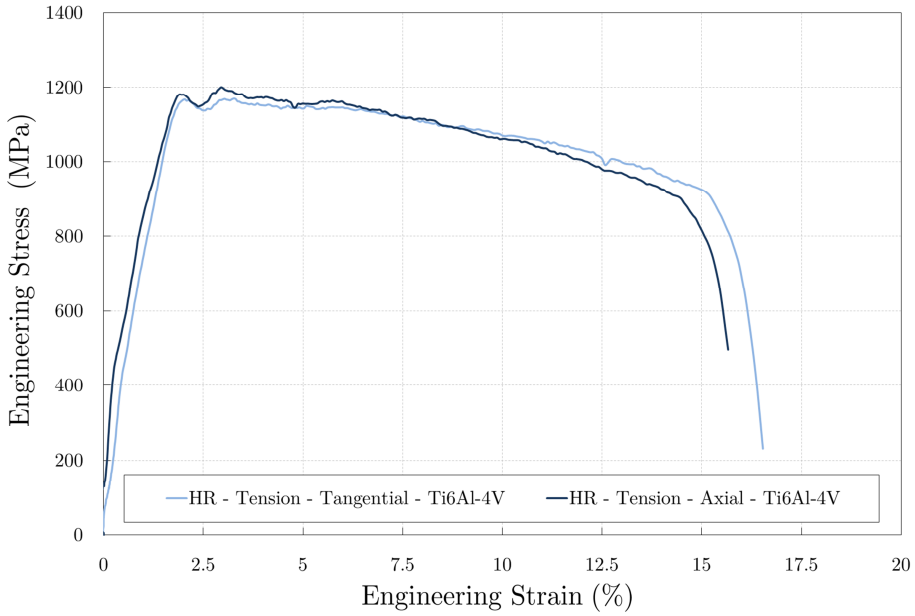


Figure 4.24: Yield stress and flow stress behaviours for high-rate tangential and axial tension.

Since these experimental specimens were machined from an industrial component, this provides motivation for constitutive modelling efforts to include an anisotropic capability. The degree of anisotropy demonstrated here is marginal but this presents

an opportunity to examine the influence of texture design within components, if the modelling capability allows.

4.2 Ballistic testing

Simple uni-axial testing is far removed from the reality of blade release and containment, therefore sub-component scale tests have been proposed. The resulting plate impact test has been used to assess the material behaviour at greater strain rates and with more realistic boundary conditions to those experienced during the aforementioned high strain-rate uni-axial events. Similarly, the experimental data described throughout this research was also completed in-house as part of a series of parallel industrial projects performed by post-doctoral researchers. The accumulated data is simply presented for validation purposes, where appropriate.

Data extracted from plate impacts tests aims to establish the ballistic limits achieved by a given alloy, in this case Ti-6Al-4V. The window of ballistic limit velocities is based upon the fastest trial which results in no rear-face cracking (i.e. failure) and slowest trials which results in failure (i.e. penetration and macroscopically observable rear-face cracking). The initial velocity range between penetration and non-penetration trials were incrementally reduced for the given number of available specimens. The failure mechanisms are difficult to quantify in isolation, in order to define material properties. This test can also be used for comparative studies between different alloy chemistries and manufacturing routes. Care has been taken to ensure that variables have been eliminated where possible, for example the preparation of the projectile and optimisation of the intended velocity at impact.

4.2.1 Pressurised gas-gun apparatus

Pressurised gas-guns allow for higher velocities to be achieved and therefore higher strain rates. The strain rates achieved in the plate impact tests described below are of the order $10^3\text{s} - 10^4\text{s}$. The gas-gun design used features a two-stage mechanism,

whereby pressure is increased and then released rapidly which accelerates the projectile.

Nitrogen gas is used to pressurise up to ~ 5.0 bar; for higher velocities Helium gas can also be used. The rapid release of pressure is achieved by rupturing a brass diaphragm of ≈ 0.10 mm thickness. The gas enters the barrel and accelerates a polymer sabot which contains the projectile. Immediately prior to the projectile departing the barrel, the brittle polymer sabot impacts a tubular steel component which strips the sabot from the projectile.

Digital image acquisition

Two high speed cameras were used to capture the impact events from both the side and rear perspectives. The Photron camera captures 30,000 frames per second with a 10.1μs exposure time with a resolution of 640x376 pixels. The Phantom camera captures 37,000 frames per second a 7μs exposure time with a resolution of 256x256 pixels. Apparatus arrangements can be seen in Figure 4.25.

Velocity of the projectile prior to impact was calculated via an oscilloscope and known light curtain positions whilst the projectile travels down the barrel. This measurement was verified with the use of a high speed camera and DIC software which tracks different points to establish an average, shown in Figure 4.26.

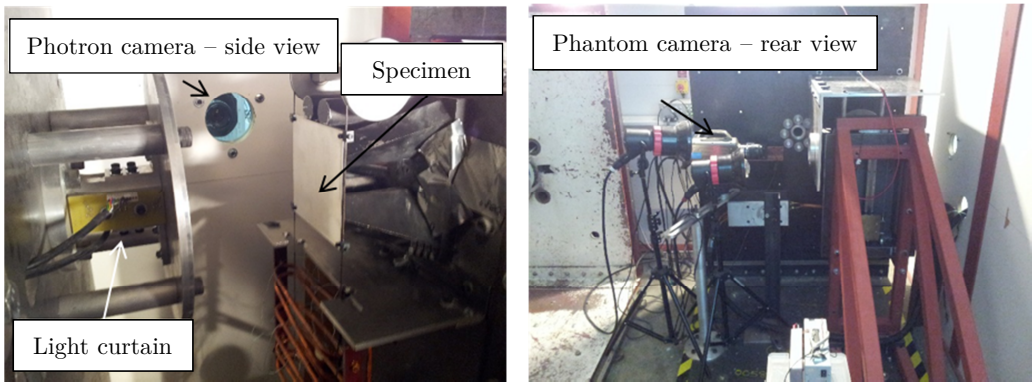


Figure 4.25: In-house ballistic gas-gun apparatus with multiple camera arrangement.

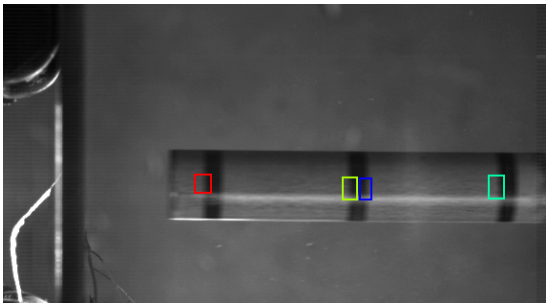


Figure 4.26: Digital image processing with in-house motion tracking software.

Specimen geometry and fixture

Figure 4.27 highlights the critical dimensions of the plate impact specimen geometry. The projectile is assumed to impact the plate normal to the surface of the plate. If there is a distinct and obvious angle of yaw at impact then the test is discarded. The plate is suspended and placed in contact with four spherical steel ball-bearings, which are rigidly held in place.

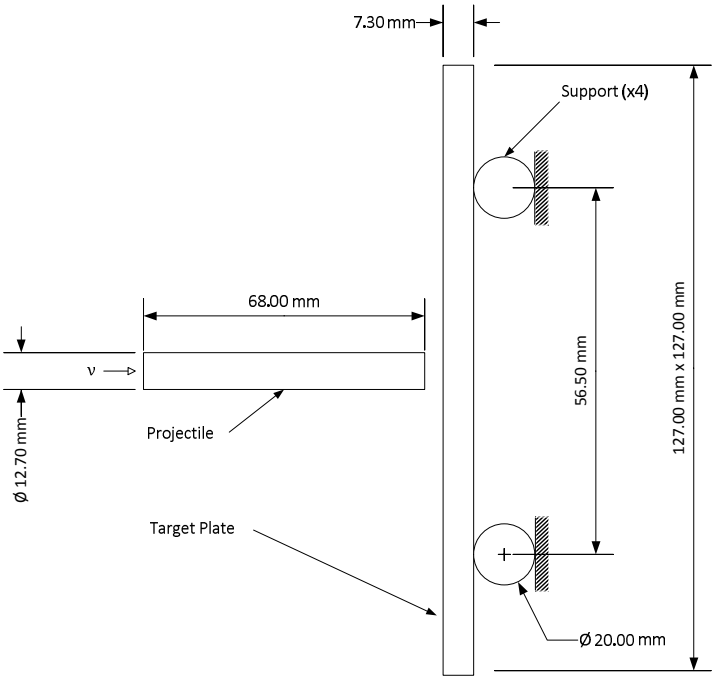


Figure 4.27: Flat-nosed, normal impact experimental arrangement with critical dimensions.

A combination of light curtain and DIC techniques are used to establish the velocity of the projectile immediately prior to impact. Inspection of the plate after impact is conducted to determine whether failure has occurred; this is defined as macroscopically observable cracking on the rear-face of the plate. Further analysis of the rebound and residual velocities of the projectile can be extracted if required. The suspension of the plate was achieved by drilling four evenly spaced holes and rigidly attaching four brackets which are then attached to wires running parallel to the vertical edge of the specimen.

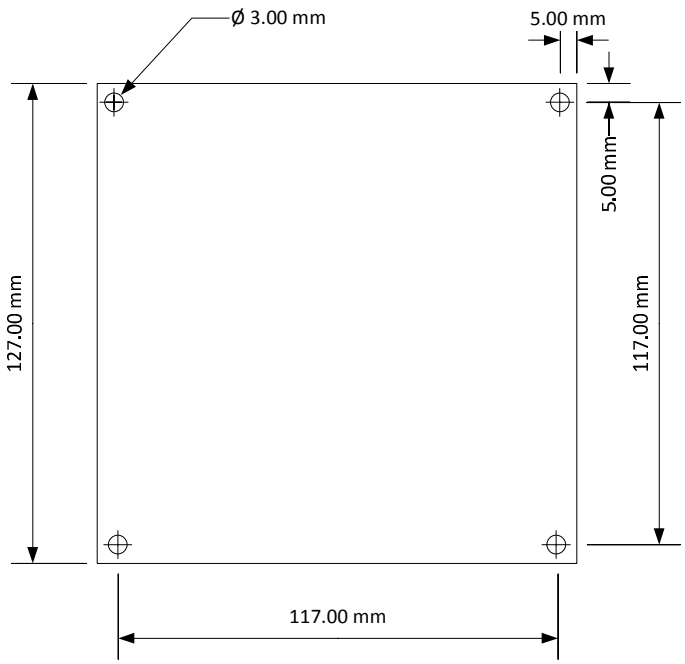


Figure 4.28: Plate preparation for the applied fixture technique with drilled hole positioning and dimensioning.

4.2.2 Plate impact

Still images taken during penetration are shown in Figure 4.29. It can be seen that considerable plastic bulging deformation is evidenced by the large deflection of the rear face during impact, prior to plugging failure. The ballistic test results are illustrated in a reduced format for the chosen alloys tested (see Table 4.1).

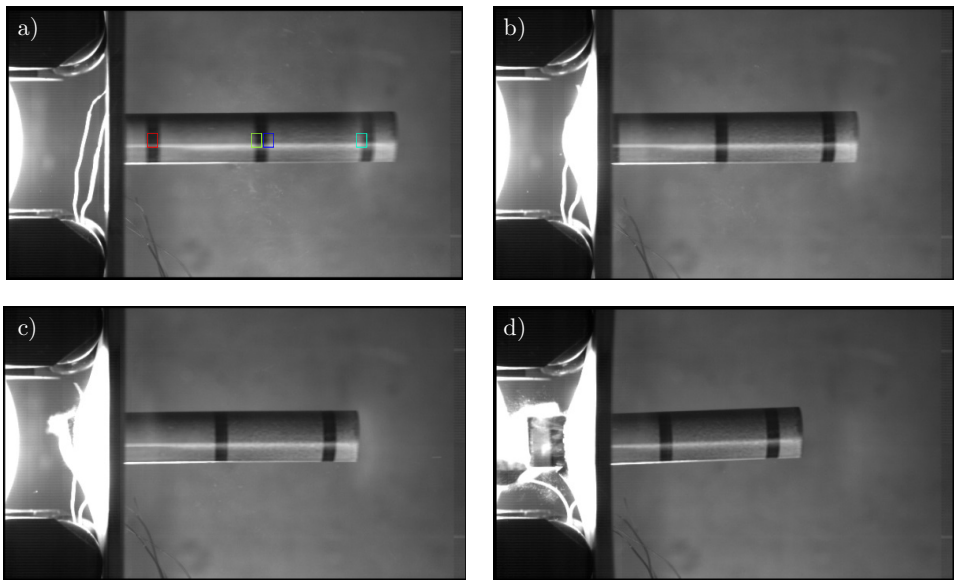


Figure 4.29: Flat-nosed, normal impact image stream illustrating penetration and plugging failure.

For example, the ballistic limit range of Ti-6Al-4V (I) was determined to be between 125.1 m/s and 142.4 m/s. This provides an upper limit and lower limit for numerical simulations, for validation exercises. Further testing would be required to reduce the velocity range, however a single resultant velocity value does not correspond with the sensitivity observed in the literature around the ballistic limit.

The primary mode of failure during these experiments is shear plugging formation, as discussed in Chapter 3. Plugging consists of a circular portion of plate which is

Table 4.1: Experimental ballistic plate impact impact results summary, flat-nosed projectile, Ti-6Al-4V.

Velocity *(m/s)*	**Initial Velocity** *(m/s)*	**Resultant Velocity** *(m/s)*	**Penetration** (Yes/No)	**Alloy Identifier**
160	159.4	105.6	Yes	J
142	142.4	80.1	Yes	J
123	123.2	N/A	No	J
134	133.6	15.5	Yes	J
142	142.2	83.4	Yes	I
125	125.1	N/A	No	I

ejected ahead of the projectile. The plug diameter is approximately equal to the projectile.

Ballistic summary

The ballistic limit has been established for Ti-6Al-4V within an acceptable range for numerical modelling validations. The mode of failure across all specimens is common and reproducible which indicates the validity of the test for comparative purposes when examining other alloy chemistries and manufacturing methods.

4.3 Summary

This chapter provides the support for numerical developments at both high strain-rates and ballistic strain-rates.

- The experimental campaign discussed above demonstrates the behaviour of high strain-rate Ti-6Al-4V, in terms of yield stresses and strain to failure envelopes, for tension and compression.
- The presence of directionality effects have also been demonstrated at all three rates of strain. This highlights clear objectives for constitutive solutions and reaffirms findings in the literature relating to anisotropy and dynamic phenomena.
- The establishment of the ballistic limit provides a metric for validation purposes at the sub-component level, which introduces multi-axial and increased strain-rate characteristic for benchmarking.
- Using this data, representative numerical benchmarks may be produced for both calibration and virtual testing to exploit variables such as angle of attack, plate thickness or path-mass and texture orientation.

Chapter 5

Constitutive Modelling

This chapter introduces the macroscopic physically-based numerical modelling approach, and the underlying constitutive framework of equations. Numerical implementation algorithms are presented for reference and further constitutive developments discussions. The associated limitations of the constitutive model are presented, based upon uni-axial and plate impact benchmarking scenarios. Finally, a mesh insensitivity algorithm is then proposed with validation exercises to demonstrate the improved capability.

5.1 Macroscopic numerical model

As discussed in chapter 3, computational cost is important for industrial applications. Therefore, the field of physically-based modelling was chosen to maximise accuracy and minimise computational expense. The baseline framework chosen for development was an isotropic, hypo-elastic, visco-plastic, damage model based upon ISV theory, known as the BCJ model or Sandia Damage Model. This has been implemented within commercial codes such as LS-DYNA and in-house code DEST.

The BCJ model was originally developed by Bammann, Chiesa and Johnson, at Sandia National Laboratories. This physically-based, time and temperature dependent plasticity model is based on classical deviatoric J_2 plasticity theory. Internal State Variable (ISV) theory was utilised to introduce strain-rate dependent and temperat-

ure dependent history effects. The damage evolution criterion was later introduced by Bammann and Aifantis [74] to account for inhomogeneity associated with the reality of ductile failure. This development introduced a scalar damage variable which acts to degrade the elastic modulus, based upon the void growth model proposed by Cocks and Ashby [138].

Multiplicative decomposition is used to differentiate between the deformation contributions related to the elastic, deviatoric plastic and volumetric plastic deformations. Deviatoric deformations are a consequence of dislocations in the cell walls and cell interiors, the mathematical basis for these approximations were outlined by Bammann and Aifantis [66, 42]. Localised heat generation - caused by plastic deformation - evolves independently of damage and diminishes both the yield and hardening variables, thus shrinking the yield surface. This is especially poignant in titanium alloys as the Young's modulus has been shown to reduce by 20 GPa when the bulk temperature increases from room temperature $\sim 273°C$ to 315°C [71]. The void growth criterion represents porosity, evolution of this parameter degrades the elastic modulus. A finite element is considered failed when it can no longer resist further imposed deformation, at either a critical damage threshold or an effective plastic strain. At this point the element is removed from further computations and the remaining forces are redistributed to the surrounding elements.

The strain-rate and temperature capabilities of this constitutive framework are beneficial for applications ranging from deep-drawing/forming, cyclic deformation, and dynamic ballistic events. Developments based upon this model have been numerous, yet concentrated within a small circle of investigators, related to the original developments. Bammann [61, 66, 65, 74, 139, 140] and associative authors [141, 142, 59, 143] form the principle core of published efforts using the BCJ framework. The framework described within this thesis has been implemented within LS-DYNA and DEST explicit finite element codes. This implementation forms the basis of the described developments discussed during this thesis.

5.1.1 Constitutive equations

The following constitutive equations have been implemented within commercial finite element code, LS-DYNA, as a user-defined material model. Development of the constitutive model was performed within the in-house development environment - DEST. The constitutive relations described herein are identical across all platforms.

Kinematics

The kinematics are based upon the multiplicative decomposition of the total deformation gradient $\boldsymbol{F}$, into elastic and inelastic parts. This accommodates large strain formulations, as shown below in equation (5.1)

$$\boldsymbol{F} = \boldsymbol{F}^e \boldsymbol{F}^i, \tag{5.1}$$

where $\boldsymbol{F}^e$, is the elastic deformation gradient in an initial stress-free configuration $\mathscr{B}_0$. The inelastic part of the deformation gradient $\boldsymbol{F}^i$ is given by

$$\boldsymbol{F}^i = \boldsymbol{F}^v \boldsymbol{F}^p, \tag{5.2}$$

where the deformation gradient $\boldsymbol{F}^p$, relates to a continuous distribution of dislocations and a permanent isochoric distortional shape change. $\boldsymbol{F}^v$ represents a continuous distribution of voids, which cause a permanent volumetric dilatational change. This decomposition is illustrated in Figure 5.1 as a function of the total deformation gradient $\boldsymbol{F}$.

To establish an explicit representation of $\boldsymbol{F}^v$, Bammann and Aifantis [66] found porosity to be a convenient and continuous measure of damage, as this directly relates to distribution of voids. If changes in volume dV correspond to the multiplicative decomposition cycle in Figure 5.1, then it can be assumed that $dV_0 = dV_1$ from $\mathscr{B}_0$ to $\mathscr{B}_1$, as there is no volume change. Similarly, dV_2 then corresponds to configuration $\mathscr{B}_2$. Moreover, by introducing dV_v, which corresponds to a portion of total elementary volume in $\mathscr{B}_2$ due to voids, then the following relationships are determined

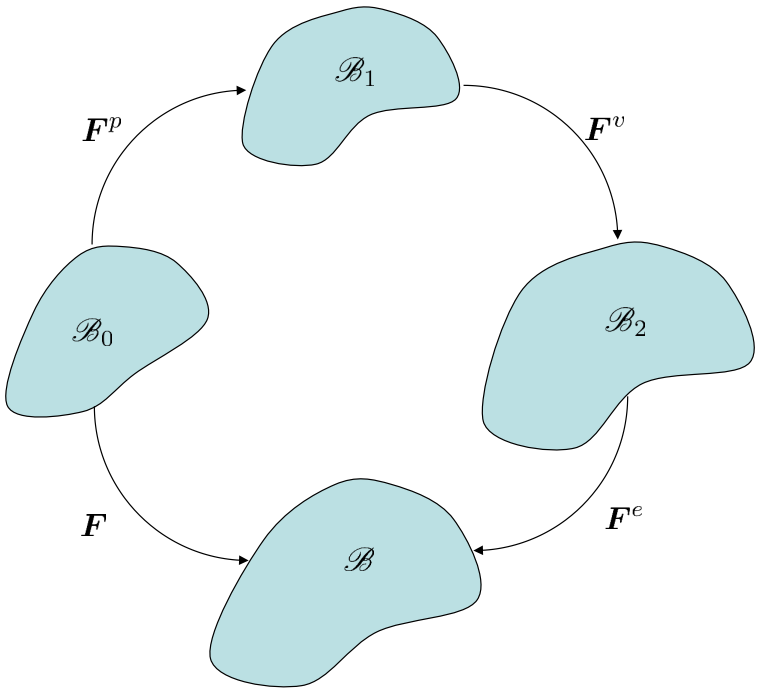


Figure 5.1: Kinematics of dilatational and distortional plastic material in terms of deformation gradient components.

$$\det \boldsymbol{F}^v = \frac{dV_2}{dV_0}, \qquad dV_2 = dV_0 + dV_v, \qquad D_v = \frac{dV_v}{dV_2}, \tag{5.3}$$

since damage D_v can be expressed as a ratio of the change in volume, in the elastically unloaded state, $\mathscr{B}_2$ then $D_v = dV_1/dV_2$ can be assumed as follows

$$dV_0 = (1 - D_v)dV_2, \tag{5.4}$$

which leads to a definition of the Jacobian J, which is determined by the damage parameter D_v, as follows

$$J = \det \boldsymbol{F}^v = \frac{1}{(1 - D_v)}. \tag{5.5}$$

Assuming dilatational damage D_v is isotropic, the volumetric part of the deformation gradient is determined below

$$\boldsymbol{F}^v = \frac{1}{(1 - D_v)^{1/3}} \boldsymbol{I}. \tag{5.6}$$

The constitutive relations developed and implemented during this thesis are given in an explicit rate-form, and therefore require definitions in terms of the velocity gradient, denoted by $\boldsymbol{L}$

$$\boldsymbol{L} = \boldsymbol{L}^e + \boldsymbol{L}^p + \boldsymbol{L}^v \equiv \dot{\boldsymbol{F}}^e \boldsymbol{F}^{e-1} + \boldsymbol{F}^e \dot{\boldsymbol{F}}^p \boldsymbol{F}^{p-1} \boldsymbol{F}^{e-1} + \dot{\boldsymbol{F}}^v \boldsymbol{F}^{v-1}. \tag{5.7}$$

The total velocity gradient $\boldsymbol{L}$ can be decomposed into symmetric ($\boldsymbol{d}$) and skew symmetric ($\boldsymbol{w}$) components, further decomposition into elastic ($\boldsymbol{d}^e$) and dilatational plastic ($\boldsymbol{d}^v$) and distortional plastic ($\boldsymbol{d}^p$) components form the following relationship

$$\boldsymbol{L} = \boldsymbol{d} + \boldsymbol{w} = \begin{cases} \boldsymbol{d} = \boldsymbol{d}^e + \boldsymbol{d}^v + \boldsymbol{d}^p, \\ \boldsymbol{w} = \boldsymbol{w}^e + \boldsymbol{w}^v + \boldsymbol{w}^p, \end{cases} \tag{5.8}$$

in relation to equation (5.6) the corresponding volumetric part of the velocity gradient $\boldsymbol{L}_v$ assumes the following rate form

$$\boldsymbol{L}_v \equiv \dot{\boldsymbol{F}}^v \boldsymbol{F}^{v-1} = \frac{\dot{D}_v}{3(1-D_v)} \boldsymbol{I}, \tag{5.9}$$

since there is no volumetric component of the spin tensors, i.e. $\boldsymbol{w}^v = 0$, then $\boldsymbol{L}^v \equiv \boldsymbol{d}^v$ and the volumetric component is given as

$$\boldsymbol{d}^v = \frac{\dot{D}_v}{3(1-D_v)} \boldsymbol{I}, \tag{5.10}$$

this provides a direct relation between damage D_v and the volumetric rate of deformation $\boldsymbol{d}^v$. This relationship shall be assumed during the following constitutive description.

Thermodynamics

The thermodynamics of internal state variable theory, developed by Coleman and Gurtin [144], were utilised by Bammann, Chiesa and Johnson et al. [42] to form the thermodynamic framework of the current implementation, in the natural configuration. The free energy Ψ is assumed to be function of the elastic strain energy

$\bar{\boldsymbol{E}}_e$, temperature θ, temperature gradient $\nabla\theta$, and internal state variables motivated by dislocations in cell structures $\bar{\boldsymbol{A}}$, cell interiors $\bar{\boldsymbol{K}}$, and voids $\bar{\boldsymbol{\Phi}}$, denoted in an intermediate configuration and presented below

$$\Psi = \hat{\Psi}\left(\bar{\boldsymbol{E}}_e, \theta, \nabla\theta, \bar{\boldsymbol{K}}, \bar{\boldsymbol{A}}, \bar{\boldsymbol{\Phi}}\right). \tag{5.11}$$

It then follows that the Clausius-Duhem inequality can be written as follows

$$\dot{\Psi} + S\dot{\theta} + \frac{1}{\bar{\rho}}\bar{\sigma}^T \cdot \bar{\boldsymbol{L}} - \frac{\bar{\boldsymbol{q}} \cdot \nabla\theta}{\bar{\rho}\theta} \geq 0, \tag{5.12}$$

where S is the entropy, $\bar{\sigma}$ is the Cauchy stress in the intermediate configuration, $\bar{\boldsymbol{q}}$ is heat flux and $\bar{\rho}$ is the density in an intermediate configuration. By taking the time derivative of the above equation and then linearising with respect to elastic strain, the elastic law can be obtained, in equation (5.16). The conjugate thermodynamic Cauchy stress $\boldsymbol{\sigma}$ and the dislocation related variables $\boldsymbol{\kappa}$ and $\boldsymbol{\alpha}$ associated with the developed constitutive model are described below

$$\boldsymbol{\sigma} = \bar{\rho}\boldsymbol{F}^e \frac{\partial\Psi}{\partial\bar{\boldsymbol{E}}_e}(\boldsymbol{F}^e)^T \tag{5.13}$$

$$\boldsymbol{\alpha} = \bar{\rho}\boldsymbol{F}^e \frac{\partial\Psi}{\partial\bar{\boldsymbol{A}}}(\boldsymbol{F}^e)^T \tag{5.14}$$

$$\boldsymbol{\kappa} = \bar{\rho}\boldsymbol{F}^e \frac{\partial\Psi}{\partial\bar{\boldsymbol{K}}}(\boldsymbol{F}^e)^T \tag{5.15}$$

where $\boldsymbol{\alpha}$ is a tensor related to dislocations of slip systems in the cell structures interiors, $\boldsymbol{\kappa}$ is related to dislocation substructures, such as cell walls averaged over several grains. These form the micromechanical and physical basis of the evolution equations described during this chapter. Further detailed descriptions can be found in the literature [42, 141], for the purposes of this research development shall begin from the hypoelastic law in the following section.

Hypoelastic law

Elastic laws are used to model the small strain deformation consistent with reversibility and, therefore, energy dissipations of zero. Temperature changes can also be neglected during these elastic deformations. The hypoelastic law takes the following form

$$\overset{\nabla}{\boldsymbol{\sigma}} = \lambda(1-D_v)\,\mathrm{tr}[\boldsymbol{d}^e]\boldsymbol{I} + 2\mu(1-D_v)\boldsymbol{d}^e - \frac{\dot{D}_v}{1-D_v}\boldsymbol{\sigma}, \tag{5.16}$$

where $\overset{\nabla}{\boldsymbol{\sigma}}$ is the objective Cauchy rate of stress. Symbols λ and μ are the Lamé's constant and shear modulus, given below

$$\lambda = \frac{\nu E}{(1+\nu)(1-2\nu)}, \tag{5.17}$$

$$\mu = \frac{E}{2(1+\nu)}, \tag{5.18}$$

where E in the Young's Modulus, ν is the Poisson's Ratio. The classical Jaumann rate is used, as illustrated in equation (5.19). Fortunately, the energy balance errors associated with the lack of work-conjugacy in the Jaumann rate of Cauchy stress - highlighted most recently by Bažant [145] - can be deemed negligible as inelastic incompressibility of metals is assumed.

$$\overset{\nabla}{\boldsymbol{\sigma}} = \dot{\boldsymbol{\sigma}} - \boldsymbol{w}^e\boldsymbol{\sigma} + \boldsymbol{\sigma}\boldsymbol{w}^{\boldsymbol{e}} \tag{5.19}$$

Yield function

The yield function (Φ) is a variation of classical J_2 plasticity with the addition of isotropic (κ) and kinematic ($\boldsymbol{\alpha}$) hardening, which allows for the modification of the yield surface. When $f = J(\boldsymbol{\sigma}' - \boldsymbol{\alpha}) - \kappa \leq 0$ the yield function is assumed in the following form:

$$\Phi = \bar{\xi} - \kappa - \beta(\dot{\varepsilon}, \theta, D_v), \tag{5.20}$$

where κ denotes the isotropic scalar hardening variable and $\bar{\xi}$ denotes the magnitude of the kinematic hardening tensor $\boldsymbol{\xi}$, as follows

$$\bar{\xi} = \sqrt{\boldsymbol{\xi} : \boldsymbol{\xi}}, \tag{5.21}$$

the non-linear kinematic hardening tensor, originally proposed by Chaboche [146], is formulated below

$$\boldsymbol{\xi} = \boldsymbol{\sigma}' - \frac{2}{3}\boldsymbol{\alpha}. \tag{5.22}$$

The influences of temperature and rate dependency within the yield function $\beta(\bar{d}, \theta, D_v)$ are given in equation (5.23), where $Y(\theta)$, $V(\theta)$ and $f(\theta)$ are the temperature dependent yield functions and D_v is the scalar dilatational damage parameter related to void growth, as follows

$$\beta = (1 - D_v)\left[V(\theta)\sinh\left(\frac{\bar{d}}{f(\theta)}\right) + Y(\theta)\right]. \tag{5.23}$$

Plastic flow-rule

Assuming the yield function (5.20) is exceeded, i.e. $\Phi > 0$, the plastic flow-rule then applies, whereby the inelastic volumetric part $\boldsymbol{d^v}$ of the velocity gradient $\boldsymbol{L}$ is given by

$$\boldsymbol{d}^v = \frac{\dot{D}_v}{3(1 - D_v)}\mathbf{I}, \tag{5.24}$$

and the distortional plastic $\boldsymbol{d}^p$ component, or 'flow-rule', is given in the following form

$$\boldsymbol{d}^p = f(\theta)\sinh\left[\frac{\bar{\xi} - \kappa - Y(\theta)(1 - D_v)}{V(\theta)(1 - D_v)}\right]\frac{\boldsymbol{\xi}}{\bar{\xi}}. \tag{5.25}$$

Inelastic flow is further defined by three groups of Arrhenius functions which describe yielding and hardening evolution with respect to temperature. The equations below

define the initial yield response and evolution mechanisms based upon temperature increase, due to plasticity

$$V(\theta) = c_1 \exp\left[-\frac{c_2}{\theta}\right], \tag{5.26}$$

$$Y(\theta) = c_3 \exp\left[\frac{c_4}{\theta}\right], \tag{5.27}$$

$$f(\theta) = c_5 \exp\left[-\frac{c_6}{\theta}\right], \tag{5.28}$$

where $V(\theta)$ is the rate dependence of yielding, $Y(\theta)$ is the rate independent yield and $f(\theta)$ is the rate dependent yield transition. The objective material parameters (c_n) are established via a combination of experimental measurements, inverse modelling and equivalent techniques [147, 148].

Hardening laws

The kinematic (5.29) and isotropic hardening (5.34) variables are shown in the usual hardening-minus-recovery rate format. The kinematic hardening tensor $\boldsymbol{\alpha}$ is convected to maintain objectivity

$$\overset{\nabla}{\boldsymbol{\alpha}} = h(\theta)\boldsymbol{d}^p - [r_d(\theta)\bar{d} + r_s(\theta)]\bar{\alpha}\boldsymbol{\alpha}, \tag{5.29}$$

$$\overset{\nabla}{\boldsymbol{\alpha}} = \boldsymbol{w}^e\boldsymbol{\alpha} + \boldsymbol{\alpha}\boldsymbol{w}^{\boldsymbol{e}}, \tag{5.30}$$

where $r_s(\theta)$ and $r_d(\theta)$ are the static and dynamic and temperature dependent functions describing the diffusion-controlled recovery rates, whilst $h(\theta)$ represents the associated kinematic hardening, formulated below

$$r_d(\theta) = c_7 \ \exp\left[-\frac{c_8}{\theta}\right], \tag{5.31}$$

$$h(\theta) = c_9 \ \exp\left[\frac{c_{10}}{\theta}\right], \tag{5.32}$$

$$r_s(\theta) = c_{11} \exp\left[-\frac{c_{12}}{\theta}\right]. \tag{5.33}$$

Isotropic static $R_s(\theta)$ and dynamic $R_d(\theta)$ recovery and the hardening $H(\theta)$ parameters are incorporated into the isotropic hardening description κ, given in the hardening-minus-recovery rate formulation

$$\dot{\kappa} = H(\theta)\bar{d}^p - [R_d(\theta)\bar{d} + R_s(\theta)]\kappa^2, \tag{5.34}$$

where respective isotropic hardening parameters are given in a temperature dependent form

$$R_d(\theta) = c_{13}\exp\left[-\frac{c_{14}}{\theta}\right], \tag{5.35}$$

$$H(\theta) = c_{15}\exp\left[\ \frac{c_{16}}{\theta}\right], \tag{5.36}$$

$$R_s(\theta) = c_{17}\exp\left[-\frac{c_{18}}{\theta}\right]. \tag{5.37}$$

The effective plastic flow $\bar{d}^p$, effective von Mises strain-rate $\bar{d}$ and back-stress $\bar{\alpha}$ are given in equations (5.38 - 5.40);

$$\bar{d}^p = \sqrt{\tfrac{2}{3}\boldsymbol{d}^p : \boldsymbol{d}^p}, \tag{5.38}$$

$$\bar{d} \ = \sqrt{\tfrac{2}{3}\boldsymbol{d} : \boldsymbol{d}}, \tag{5.39}$$

$$\bar{\alpha} \ = \sqrt{\tfrac{3}{2}\boldsymbol{\alpha} : \boldsymbol{\alpha}}. \tag{5.40}$$

Damage laws

The deformation and failure mechanisms of Ti-6Al-4V operate on a micromechanical length scale. Physically-based modelling attempts to capture these effects on a macroscopic scale. Discrepancies in the length-scales considered lead to losses of homogeneity across the RVE, damage mechanics attempt to address these limitation motivated by physical observations and approximations.

Cocks and Ashby's [73] solution for spherical void growth in rate dependent plastic materials was suggested as an extension to the classical continuum damage mechanics approach, this focused on the mechanistic aspects of void growth. Most notably, triaxiality χ_v was coupled with diffusional growth and power-law creep growth in a

consistent manner. Whilst this approach relies upon the assumption that voids grow spherically, Rice and Tracey [149] demonstrated that this assumption is valid as shape change contributions are outweighed by volumetric change contributions, which are effectively spherical.

The Cocks and Ashby damage law was implemented into the aforementioned framework by Bammann and Aifantis [74]. The implemented damage growth law $\dot{D}_v$ is given in the following rate form

$$\dot{D}_v = \chi_v \left[\frac{1}{(1-D_v)^m} - (1-D_v) \right] \left[\bar{d}^p \right]. \tag{5.41}$$

The mechanistic approach of coupling diffusional and power-law creep growth results in an accelerated void growth under high triaxiality conditions. The formulation of triaxiality is given below

$$\chi_v = \sinh \left[\frac{2(2m-1)p_t}{(2m+1)\sigma_{ef}} \right], \tag{5.42}$$

where $p_t = \min\{0, p\}$ which limits pressure (p) to be non-zero in tension only, σ_{ef} is the scalar effective von Mises stress below

$$\sigma_{ef} = \sqrt{\tfrac{3}{2}\boldsymbol{\sigma}' : \boldsymbol{\sigma}'}. \tag{5.43}$$

Adiabatic effects

The empirical assumption that 90% of plastic work is dissipated as heat is applied to represent temperature influences leading to localised softening. Whilst the proportionality can be modified, the relationship is currently as follows

$$\vartheta \frac{\Delta\gamma}{\bar{\xi}} (\boldsymbol{\sigma} : \boldsymbol{\xi}), \tag{5.44}$$

$$\vartheta = \left(\frac{0.9}{\rho C_v} \right), \tag{5.45}$$

where ρ and C_v are the density and specific heat of the chosen material, and $\Delta\gamma$ is the plastic multiplier increment.

Loading/unloading conditions

Finally, the yield surface obeys the loading/unloading conditions developed by Kuhn and Tucker [150], in the standard form

$$\varrho \leq 0, \quad \dot{\mathscr{F}} \geq 0, \quad \dot{\mathscr{F}}\varrho = 0. \tag{5.46}$$

5.1.2 Constitutive implementation

Discretised constitutive equations are given during this section. The following algorithmic developments have been written in a vectorised FORTRAN programming routine, within LS-DYNA explicit finite element analysis code. Equivalent algorithms, written in C-programming language have also been developed and implemented in the in-house development software - DEST.

Step 1. Trial elastic assumptions

Trial values of the deviatoric stress $\boldsymbol{\sigma}'$ tensor and the hardening variables are calculated assuming purely elastic deformation. Subscript $n+1$ denotes an updated value at time-step $t+1$, the current value is denoted by $n+1/2$ and n denotes the variable at the previous time-step t.

$$\boldsymbol{\sigma}'^{\text{trial}}_{n+1} = \boldsymbol{\sigma}_n \left[\frac{\dot{D}_v}{1-D_v}\right]_n + 2\mu(1-D_v)_n\, d_{n+1/2} + 3\lambda(1-D_v)_n\, \text{tr}\left[d_{n+1/2}\right]\boldsymbol{I} - p_{n+1}\boldsymbol{I}, \tag{5.47}$$

where pressure, the Lamé's constant and shear modulus are given below

$$p_{n+1} = \frac{1}{3}\text{tr}\left[\boldsymbol{\sigma}^{trial}_n\right]\left[\frac{\dot{D}_v}{1-D_v}\right]_n + 3\lambda(1-D_v)_n\, \text{tr}\left[d_{n+1/2}\right]\Delta t. \tag{5.48}$$

$$2\mu = \frac{2E}{2(1+\nu)}, \tag{5.49}$$

$$3\lambda = \frac{E}{(1-2\nu)}. \tag{5.50}$$

To calculate the trial state variables, the recovery-minus-hardening form is assumed as follows

$$\boldsymbol{\sigma'}_{n+1}^{\text{trial}} = \boldsymbol{\sigma}_n - p_{n+1}\boldsymbol{I}, \tag{5.51}$$

$$\boldsymbol{\alpha}_{n+1}^{\text{trial}} = \boldsymbol{\alpha}_n - \left[1 - \left(r_s + r_d\, \bar{d}_{n-1/2}\right) \bar{\alpha}\boldsymbol{\alpha}\, \Delta t\right], \tag{5.52}$$

$$\kappa_{n+1}^{\text{trial}} = \kappa_n - \left[1 - \left(R_s + R_d\, \bar{d}_{n-1/2}\right) \kappa^2\, \Delta t\right], \tag{5.53}$$

Step 2. Elastic assumption evaluation

The elastic assumption is now checked against the yield function by substituting equation (5.21) and (5.23) into (5.20). If $\Phi^{\text{trial}} \leq 0$ then the elastic assumption is correct for $n+1$. However, if $\Phi^{\text{trial}} > 0$ then plastic deformation has occurred and the state variables need to be returned to the newly calculated yield surface.

$$\Phi_{n+1}^{\text{trial}} = \bar{\xi}_{n+1}^{\text{trial}} - \sqrt{\frac{2}{3}}\left[\kappa_{n+1}^{\text{trial}} + \beta_{n+1}\right] \tag{5.54}$$

Step 3. Visco-plastic multiplier

The consistency condition $\dot{\Phi} = 0$ is then used to determine $\Delta\gamma$. The resulting linear algebraic equation (5.55) can then be inserted into equations (5.56), (5.57) and (5.58) to update the state variables.

$$\Delta\gamma_{n+1} = \frac{\Phi_{n+1}^{\text{trial}}}{2\mu + \frac{2}{3}(h+H)} \tag{5.55}$$

Step 4. Solution dependent variable correction

Here the radial return method, originally proposed by Krieg and Kreig [151], is applied to return the stresses. Plastic strain is assumed constant over the time-step to maintain equilibrium. The following state variables are then updated as follows

$$\boldsymbol{\sigma}'_{n+1} = \boldsymbol{\sigma}'^{\,\text{trial}}_{n+1} - 2\mu\Delta\gamma\mathbf{n}, \tag{5.56}$$

$$\boldsymbol{\alpha}_{n+1} = \boldsymbol{\alpha}^{\,\text{trial}}_{n+1} - h\Delta\gamma\mathbf{n}, \tag{5.57}$$

$$\kappa_{n+1} = \kappa^{\,\text{trial}}_{n+1} - H\sqrt{\tfrac{2}{3}}\Delta\gamma, \tag{5.58}$$

where the unit-vector of effective stress for radial return is assumed to be linear over the current time-step and is given as follows (5.59),

$$\mathbf{n}_{n+1} = \frac{\xi}{\bar{\xi}}. \tag{5.59}$$

Step 5. Adiabatic thermal effects

Finally, the empirical assumption states that 90% of plastic work-done is dissipated through generation of heat. Thermal effects of θ then influence the yield, hardening and recovery functions in the following time-step

$$\theta_{n+1} = \theta_n + \vartheta\,\frac{\Delta\gamma_{n+1}}{\bar{\xi}^{\text{trial}}_{n+1}}\left(\boldsymbol{\sigma}_n : \boldsymbol{\xi}^{\text{trial}}_{n+1}\right), \tag{5.60}$$

$$\vartheta = \left(\frac{0.9}{\rho C_v}\right), \tag{5.61}$$

where C_v is the specific heat material parameter for constant volume and ρ is the material density.

5.1.3 Constitutive parameters

The material parameters which are required by the user are contained within Table 5.1. Certain parameters can be defined from experimental observations, however some require alternative approaches such as inverse modelling. The parameters shown here were partially defined using an in-house optimiser routine within DEST [147].

Table 5.1: Material parameters for the BCJ damage model, developed in LS-DYNA.

ID	Description	Units	HR Value
E	Young's modulus	GPa	$1.08\text{x}10^{5}$
v	Poisson's ratio	-	0.3
ρ	Density	kgm^{-3}	$4.43\text{x}10^{-9}$
θ	Initial temperature	K	293.0
D_0	Initial damage (porosity)	-	0.0032
c_1	Yield rate dependence $V(\theta)$	MPa	25.0
c_2	$V(\theta)$ temperature dependence modulus	K	-20.0
c_3	Yield rate dependence $Y(\theta)$	MPa	$4.30\text{x}10^{2}$
c_4	$Y(\theta)$ temperature dependence	K	$2.60\text{x}10^{2}$
c_5	Rate dependence transition $f(\theta)$	MPa	1.0
c_6	$f(\theta)$ temperature dependence	K	$1.80\text{x}10^{2}$
c_7	Dynamic recovery, kinematic hardening r_d	MPa	0.2
c_8	r_d temperature dependence	K	1.0
c_9	Kinematic hardening modulus h	MPa	$2.50\text{x}10^{3}$
c_{10}	h temperature dependence	K	8.0
c_{11}	Static recovery, kinematic hardening r_s	$\text{MPa}^{-1}\text{s}^{-1}$	$1.0\text{x}10^{-3}$
c_{12}	r_s temperature dependence	K	$1.0\text{x}10^{-3}$
c_{13}	Specific heat C_v	$\text{kJkg}^{-1}\text{K}^{-1}$	0.331
c_{14}	Void growth damage m	-	1.1
c_{15}	Shear damage exponent n	-	1.1
c_{16}	Shear damage denominator N	-	12.0
c_{20}	Dynamic recovery, isotropic hardening R_d	MPa	$1.0\text{x}10^{-3}$
c_{21}	R_d temperature dependence	K	$1.0\text{x}10^{-3}$
c_{22}	Isotropic hardening modulus H	MPa	$2.50\text{x}10^{3}$
c_{23}	H temperature dependence	K	8.0
c_{24}	Static recovery, isotropic hardening R_s	$\text{MPa}^{-1}\text{s}^{-1}$	$1.0\text{x}10^{-3}$
c_{25}	R_s temperature dependence	K	$1.0\text{x}10^{-3}$
c_{26}	Volumetric regularisation *vcl*	-	1.0
c_{27}	Distortional regularisation *dcl*	-	1.0
c_{30}	Volumetric damage limit *vdl*	-	0.99
c_{31}	Distortional damage limit *ddl*	-	0.99
c_{32}	Combined total damage limit *cdl*	-	0.99
c_{33}	Effective plastic strain limit *epl*	-	0.5
c_{40}	Angle of friction φ	$^{\circ}$	30.0
c_{41}	Cohesive intercept c	MPa	100.0
c_{42}	Asymmetric hardening a	-	0.0
c_{43}	Asymmetric hardening b	-	0.0
c_{50}	Lankford coefficient r_{00}	-	1.0
c_{51}	Lankford coefficient r_{90}	-	1.0
c_{52}	Lankford coefficient r_{45}	-	1.0

For the purposes of developing a benchmarking procedure, the parameters in Table 5.1 will be used. Several material parameters can be derived from experimental testing, more details can be found in [139] whilst brief calibration and identification procedures are detailed in the following section.

Yield parameters

The yield point Y and elastic modulus E can be measured from true stress - true strain uni-axial data at a given strain-rate and for a given temperature, assuming symmetry and isotropic at this point. When plotting true stress - true strain, the values of $Y(\theta)$, $V(\theta)$ and $f(\theta)$ can be determined empirically, as illustrated in Figure 5.2.

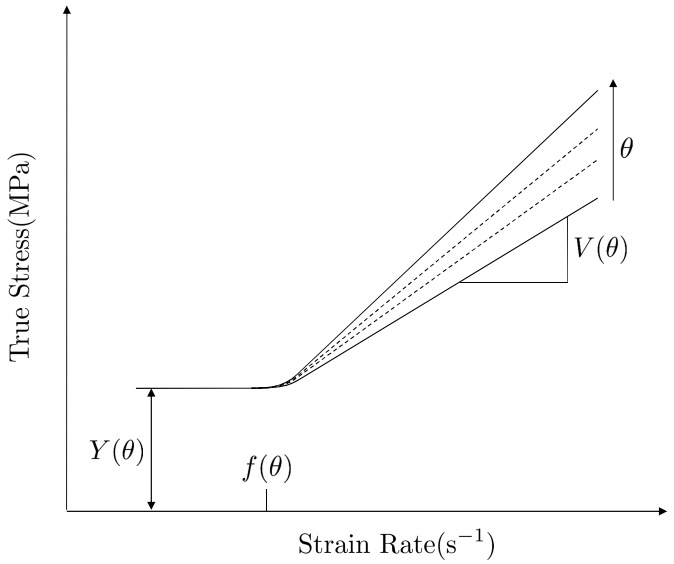


Figure 5.2: Empirical yield function parameter schematic.

The tests required to experimentally characterise these functions fully would involve uni-axial tension, compression and torsion at various strain rates, in addition to upper and lower temperature bounds, for extrapolation purposes. Considering the yield function $Y(\theta)$, the parameters c_3 and c_4 from equation (5.62) can be determined if two yield stresses Y_1, Y_2 are known, at two extreme and opposite temperatures.

$$Y(\theta)_n = c_3 \exp\left[-\frac{c_4}{\theta_n}\right] \tag{5.62}$$

The following procedure can also be applied to $V(\theta)$ and $f(\theta)$ to establish their respective c_n constants, as follows

$$c_4 = \frac{\theta_1\theta_2}{\theta_1 - \theta_2}\ln\left(\frac{Y_1}{Y_2}\right), \tag{5.63}$$

$$c_3 = Y_1 \exp\left[-\frac{c_4}{\theta_1}\right], \tag{5.64}$$

then by inserting equation (5.63) into (5.64) we can find the following

$$c_3 = Y_1 \exp\left[-\frac{\theta_2}{\theta_2 - \theta_1}\ln\left(\frac{Y_1}{Y_2}\right)\right]. \tag{5.65}$$

This model also reduces to a simple rate and/or temperature independent model by setting c_1, c_2, c_4 and c_6 to zero.

Hardening parameters

The hardening moduli (h and H) can also be approximated manually from true stress - true strain flow stress curves. However this can be highly subjective and therefore inverse modelling or alternative approaches are advisable due to the number of parameters.

If we consider isothermal conditions, i.e. constant true strain-rate, and initially ignore the recovery terms, the model reduces to bilinear plasticity and the hardening slope in the plastic region can be approximated as $h + H$. Due the implementation method, the slope of the stress-strain curve in the plastic regime can be described in equation (5.66) and is illustrated in Figure 5.3.

$$\frac{d\sigma}{d\varepsilon} = \frac{E(H+h)}{E+H+h} \tag{5.66}$$

Hardening and the relationship between h and H can be partially be determined by observing kinematic hardening, known as the Bauschinger effect.

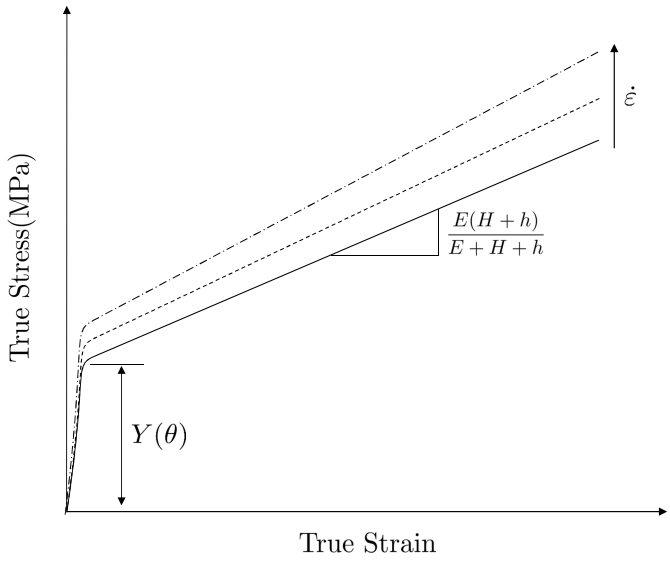


Figure 5.3: Rate dependence of yield stress, assuming no influences of recovery term ($R_s = R_d = r_s = r_d = 0$), resulting in bilinear hardening.

Recovery parameters

The saturation stress σ_{sat} is the point at which hardening approaches zero ($h \to 0, H \to 0$), on the stress-strain curve. At this point we can use equation (5.67) to investigate the relationship between dynamic and thermal (static) recovery.

$$\sigma_{sat} = \beta + \sqrt{\frac{h\dot{\varepsilon}}{r_s}} + \sqrt{\frac{H\dot{\varepsilon}}{R_s}}, \tag{5.67}$$

where

$$\beta(\theta, \dot{\varepsilon}) = Y(\theta) + V(\theta)\sinh^{-1}\left[\frac{\dot{\varepsilon}}{f(\theta)}\right]. \tag{5.68}$$

The above is derived by integrating uni-axial definitions of the strain-rate and hardening rates. Further detailed analyses of the influences of both the static and dynamic recovery terms, for a simplified uni-axial case subjected to various strain-rate effects, are discussed in [139].

Parameter fitting tool

An inverse modelling tool exists within the DEST development environment [147], this provides a fully customisable method of optimising parameters for constitutive

modelling. This inverse tool uses only physically meaningful data to efficiently optimise objective parameters and assess their stability based upon parameter sensitivity. This method was partially utilised in Table 5.1.

An alternative tool, developed by Horstemeyer et al. [152, 148], features a coupled MATLAB and ABAQUS approach, with detailed user instructions. Further modifications to this tool to accommodate constitutive developments are prohibited by copyright. However, a significant number parameters described during this thesis can be optimised using this tool.

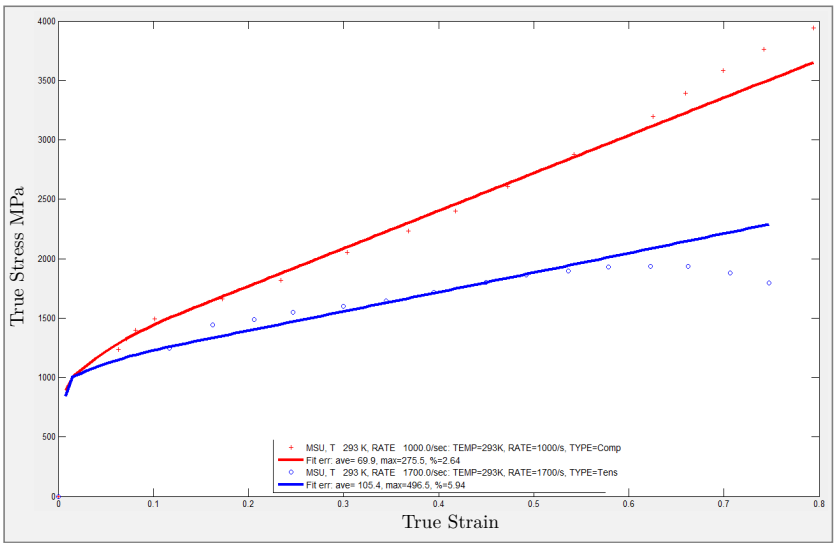


Figure 5.4: Parameter optimisation tool for the BCJ model.

Data taken from Figure 4.16 and Figure 4.13 were used to demonstrate the parameter optimisation capabilities, shown in Figure 5.4. The point data represents uniaxial experimental data in true stress σ_{true} and true strain $\varepsilon_{\text{true}}$. This data has been derived from the engineering stress σ_{eng} and engineering strain ε_{eng} data obtained and presented in Chapter 4.

$$\sigma_{\text{true}} = \sigma_{\text{eng}}(1+\varepsilon_{\text{eng}}) \tag{5.69}$$

$$\varepsilon_{\text{true}} = \ln(1+\varepsilon_{\text{eng}}) \tag{5.70}$$

These assumptions are only reliable prior to necking, after this point stress becomes non-uniform in the gauge length and the true stress - true strain relationship requires DIC processing. Figure 5.4 demonstrates the capabilities of the fitting tool until the point of localisation, when the experimental points and fitting curves diverge. At this point calibration of the damage parameter is required.

5.2 Uni-axial benchmark

The inherent limitation of finite elements is the mesh density required to capture deformation during plasticity. A point is reached in static problems whereby upon increasing the mesh density the accuracy plateaus and convergence is assumed. This process can be computationally expensive and is ultimately unreliable during dynamic problems. It can be clearly demonstrated that coarse meshes over-predict the stiffness of the mechanical response, when unable to geometrically predict necking deformation, whilst fine meshes under-predict the same material response. In dynamic simulations this phenomena is called the vanishing energy effect. Freund and Wu [153] showed that a perfect one-dimensional material can experience strain localisation, which is similar to that characterised by shear banding deformation. This was expanded upon by Bazant and Belytschko, who found that the strain softening area reduces to an infinitely thin plane - at which point the strain becomes infinite and the energy dissipation reduces to zero [154]. Both studies illustrate that an element subjected to high shear strain deformation would result in a tangent modulus (G_t) which approaches zero. This would then result in a wave speed (c_t) which also approaches zero, thus effectively becoming unable to communicate time dependent boundary data.

$$c_t = \sqrt{\frac{G_t}{\rho}}. \tag{5.71}$$

Static mesh convergence studies are also unreliable during dynamic problems. Needleman [155] highlighted the concerns relating to the lack of a material length

scale, and the fact that simple phenomenological relationships cannot describe the material behaviour within narrow bands of localised strain. It can be clearly demonstrated that a coarse mesh may over-predict the stiffness of the mechanical response as a consequence of being unable to geometrically predict necking deformation.

5.2.1 Tensile sensitivity

To demonstrate the developed capabilities, a simple uni-axial tension benchmark was applied in DEST development code. The mesh density was varied in the longitudinal direction to demonstrate and isolate the beneficial influence in the longitudinal direction.

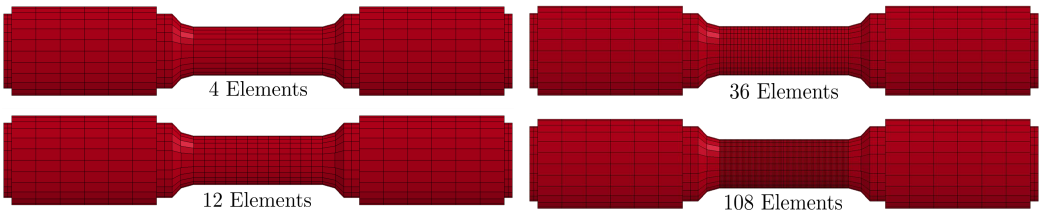


Figure 5.5: Mesh discretisation in the longitudinal direction.

An intentionally large discrepancy between the mesh densities was applied to assess the boundaries of the technique, beyond which the precepts of the FE approach are violated. The example meshes are displayed in Figure 5.5. As discussed, mesh refinement during dynamic simulations can either over-predict or under-predict the mechanical behaviour of a material response during evolution.

In Figure 5.6, divergence away from the experimental solution is observed as a consequence of insufficient localisation capabilities during damage accumulation. The separation of solutions occurs at a certain point during softening, which ultimately effects the failure prediction. Uni-axial tension simulations in Figure 5.6 illustrate the mesh sensitivity effect, this occurs during softening and coincides with experimentally observed damage localisation and experimental data deviation from fitting curves in

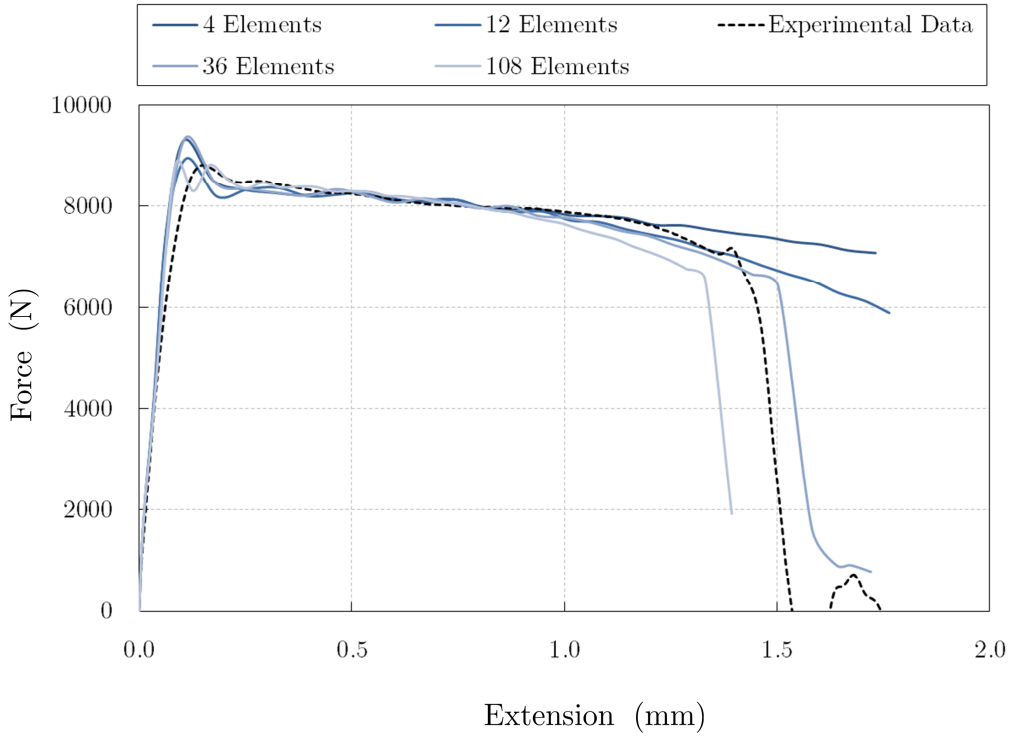


Figure 5.6: Numerical versus experimental data demonstrating the effect of uni-axial mesh sensitivity in tension at high strain-rates.

Figure 5.4. Liao [97] also observed this phenomena during high strain-rate torsion, this confirms the logical hypothesis that localisation effects also occurs due to shear strain localisation, which shall be addressed in the following developments described in section 5.6.

5.3 Multi-axial ballistic benchmark

One of the goals of this research is to enhance simulation accuracy and reliability through a detailed understanding of impact phenomena and the consequences which arise during simulation. The work of Børvik [95] has illustrated that a transition between plate bending and pure shear exists in steel plates. This is yet to be determined in titanium. However, from the experimental campaign thus far both bending and shear plugging have been observed. This indicates that both shear and tensile strains are present in the plate thickness tested. It should also be noted that the

mesh density used by Børvik was extremely high compared to industrial mesh size limitations, considered during this project. Mesh instabilities under the influence of shear strain and high mesh densities required during similar simulations, provide a rationale for further study of mesh sensitivity effects before constitutive benchmarks can be performed accurately. The plate impact study - described in section 4.2.1 - has been used extensively within industry and provides relevant data for benchmarking. In addition to validation exercises, the following parametric study shall highlight limitations and hence opportunities for constitutive developments.

5.3.1 Numerical model

Firstly, a numerical representation of the impact experiment was created within LS-DYNA, shown in Figure 5.7. An initial velocity was applied to the projectile at all nodal points. Half geometry support spheres were used and rigidly constrained on their rear face. Both the support spheres and the projectile were assumed to be almost rigid, therefore an elastic steel model was used during the following parametric study. Whilst geometrically axisymmetric, the full plate impact geometry was simulated to compare against and capture any asymmetries during plug formation when anisotropy is introduced.

The constitutive model chosen in the uni-axial study was retained here, due to the strain-rate and temperature dependency capabilities. These results will be compared against the constitutive developments described in later chapters. Element erosion is defined by plastic strain accumulation only. The mesh density of the plate and projectile were varied in the lateral and axial directions, in a parametric manner, depicted in Figure 5.8. As damage is expected to be highly localised, the mesh density is higher only at the impact location, which reduces computational cost. Mesh densities of 0.5 mm, 1.0 mm and 2.0 mm are indicative of the length, width and depth of elements at the impact location. Similarly, projectile meshes were simultaneously varied in axial and radial directions.

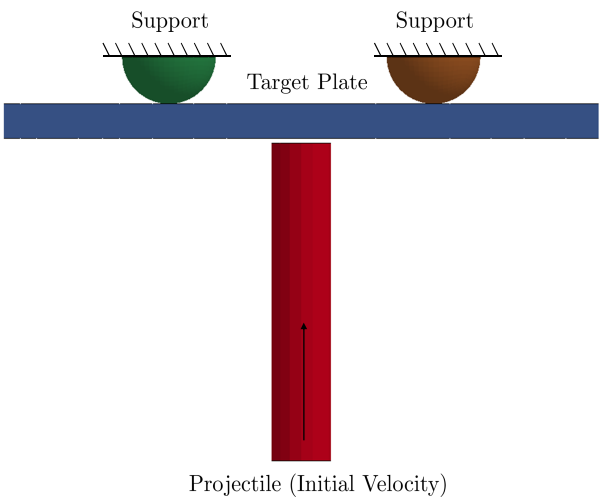


Figure 5.7: Plate impact numerical benchmark arrangement.

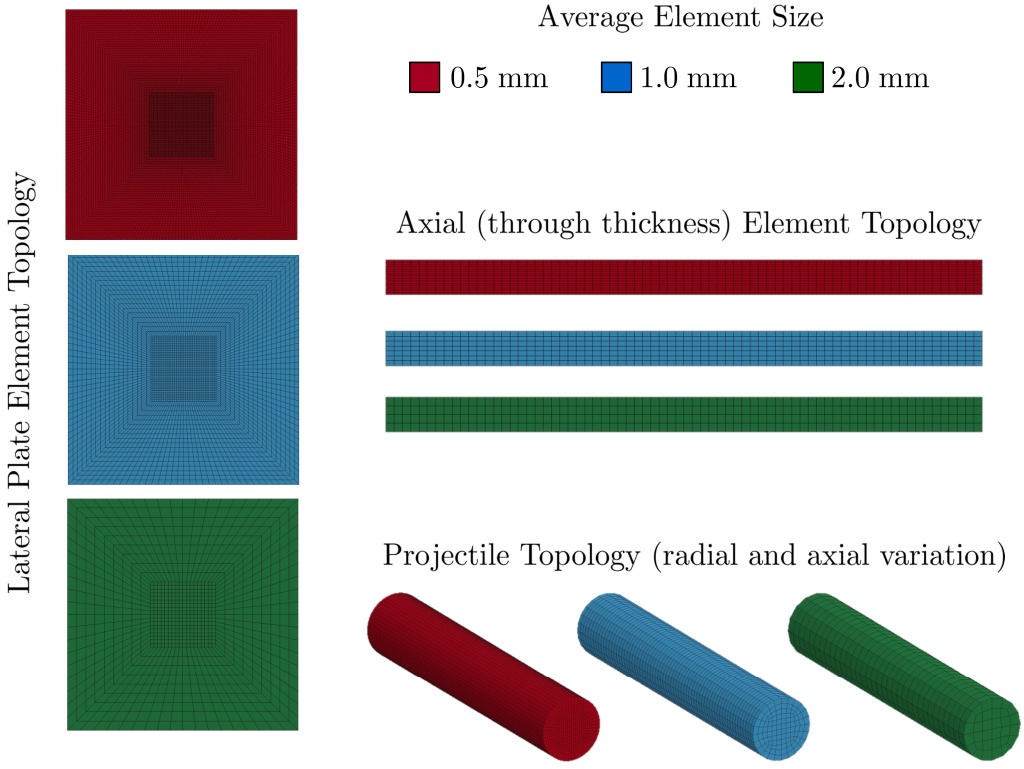


Figure 5.8: Parametric mesh adaptations in both target plate and projectile.

5.3.2 Ballistic limit simulation

For the purpose of assessing the influence of mesh dependence during impact, the benchmark arrangement utilises data from Table 4.1. The ballistic limit was established within the range of 125 m/s to 142 m/s. These two velocities were prescribed to the benchmark simulation projectile, the results can be seen in Figures 5.9 and 5.10.

As discussed within Chapter 3, titanium displays a sensitivity around the ballistic limit, this is reflected in the established ballistic limit range. This is also influenced by multiple failure modes present in plates of this approximate thickness. In general, the ballistic benchmark simulation is able to reproduce the ballistic limit reasonable well. The mesh density is approximately four times finer than the that of an ideal large-scale industry simulation. This poses a challenge for newly proposed constitutive modelling solutions when also attempting to reproduce accurate damage evolution via void growth in a predominantly shear damage regime. It is likely that the plastic strain to failure flag was triggered due to element aspect ratio deformation before damage accumulation approaches the corresponding failure limit.

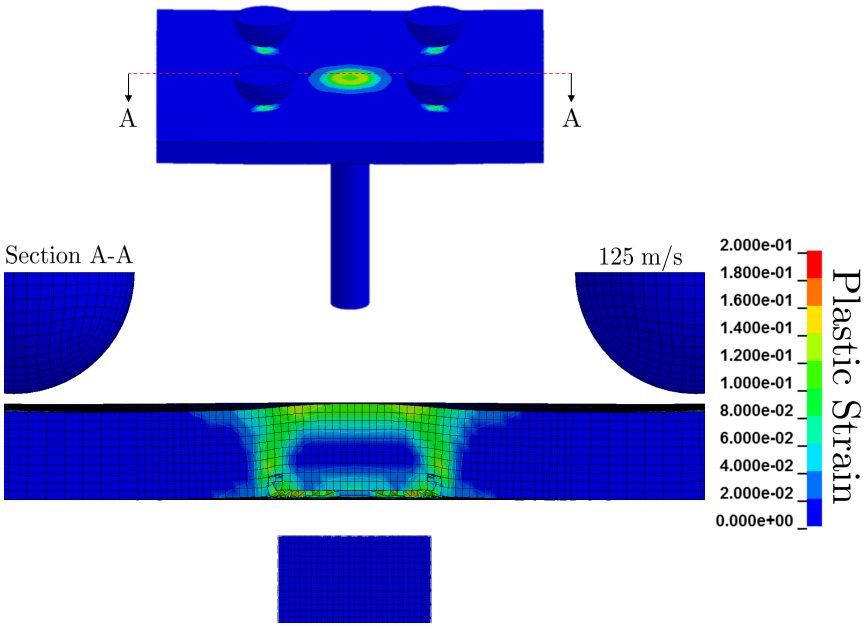


Figure 5.9: Cross-section view of 125m/s impact event at $t = 300.0\mu$s.

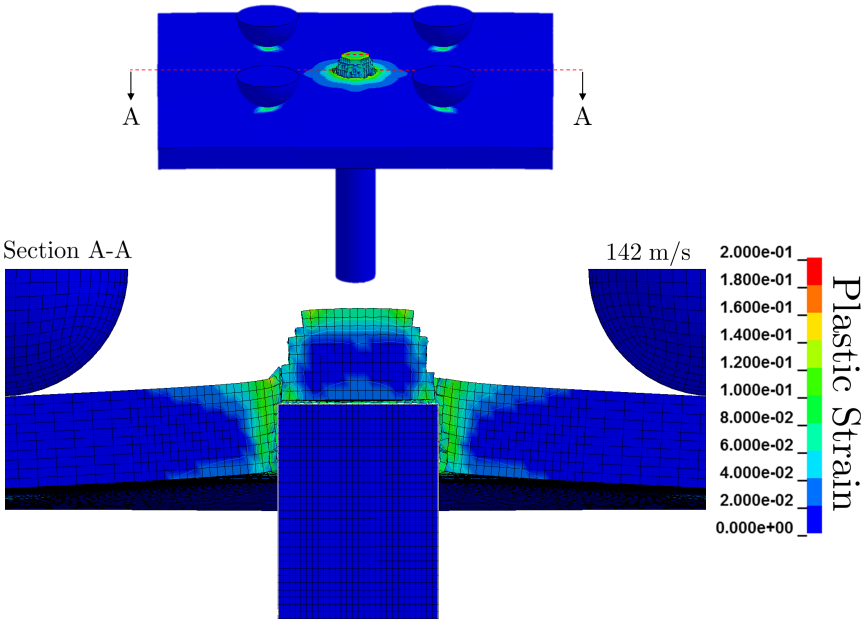


Figure 5.10: Cross-section view of 142m/s impact event at $t = 300.0\mu$s.

5.4 Parametric ballistic study

During this parametric study the mesh sensitivity of the plate and projectile shall be evaluated, leading to ballistic limit predictions. This is motivated by the high mesh densities which were necessary during the work of Børvik and Hopperstad [95]. Multiple shear and bending modes during failure are observed in plate thickness of 7.3 mm, this also presents a complex numerical challenge for the current scalar damage mechanisms within the commercial software.

5.4.1 Plate mesh sensitivity

The upper ballistic limit of 142 m/s, which was established in Chapter 4, has been applied during this numerical study, unless otherwise stated. The element size ($l = w = h$) in Figure 5.11 are measured at the impact location; the lateral and axial element sizes are varied to evaluate the mesh sensitivity implications.

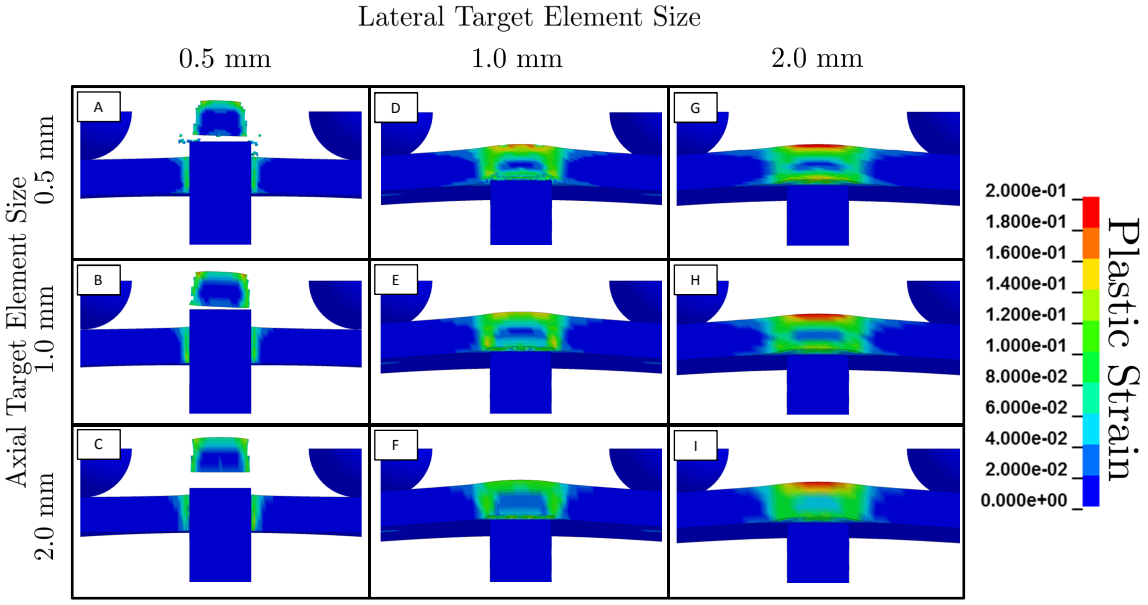


Figure 5.11: Cross-section view of lateral and axial target plate mesh density variation matrix trials.

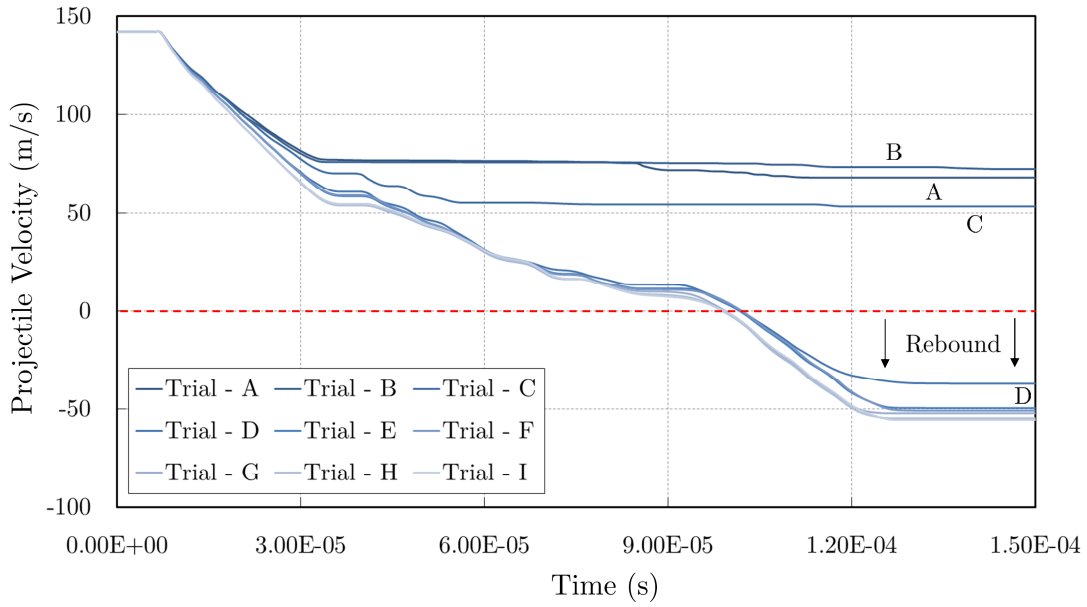


Figure 5.12: Axial velocity profiles of plate mesh variation.

From Figure 5.11 we can see that plugging penetration can be reproduced by maintaining a relatively high lateral mesh density. This indicates that smaller elements accumulate damage more rapidly, as one might expect. However, when varying

the axial mesh density no plugging occurs. Clearly, lateral mesh densities dominate plugging predictions, whilst axial mesh densities have a marginal effect on projectile residual velocities (~ 20m/s), as shown in Figure 5.12.

From Figure 5.13 it can be shown that the peak stress observed at, or close to, the edge of the projectile diminish in coarser meshed targets. The inability to localise stress in larger elements is also reflected in the accumulated plastic strain and, hence, element failure. Element failure is defined by plastic strain accumulation which, in the current material model, is also associated with damage; this indicates that damage accumulation is also mesh sensitive. Therefore, this presents a calibration challenge unless element sizes remain regular, which is unlikely during meshing of complex industrial components.

It is clear that any constitutive model developments should address the localisation limitation, the appropriateness of the failure flags and the evolution of the single damage mode. All of these studies demonstrate that the current commercially avail-

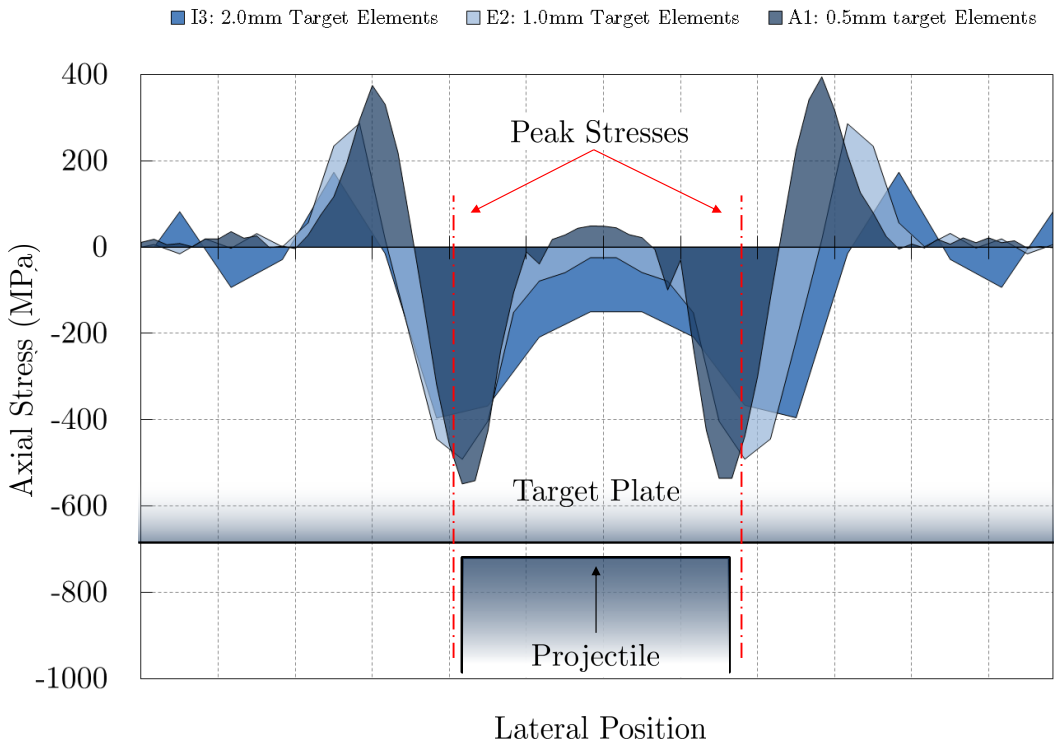


Figure 5.13: Peak target plate stress concentrations in the lateral position.

able constitutive solution fails to predict plug formation failure when element sizes increase beyond ~ 0.5mm.

5.4.2 Projectile mesh sensitivity

To assess whether stress localisation is effected by the projectile mesh density a similar study was conducted on meshes A (0.5mm in lateral and axial directions), E (1.0mm in lateral and axial directions) and I (2.0mm in lateral and axial directions) in Figure 5.11, as a reduced but representative sample. The average global mesh density was then varied ($0.5\text{mm}, 1.0\text{mm}$ and 2.0mm) to form the matrix in Figure 5.14. This indicates that projectile mesh variations make little difference compared to target plate mesh densities. Small variation in the residual velocities are observed when projectile mesh densities are varied; Figure 5.15 illustrates that varying the projectile mesh density results in a ~ 20m/s variation in residual velocity.

Whilst projectile mesh densities influence the solution, target mesh has a greater

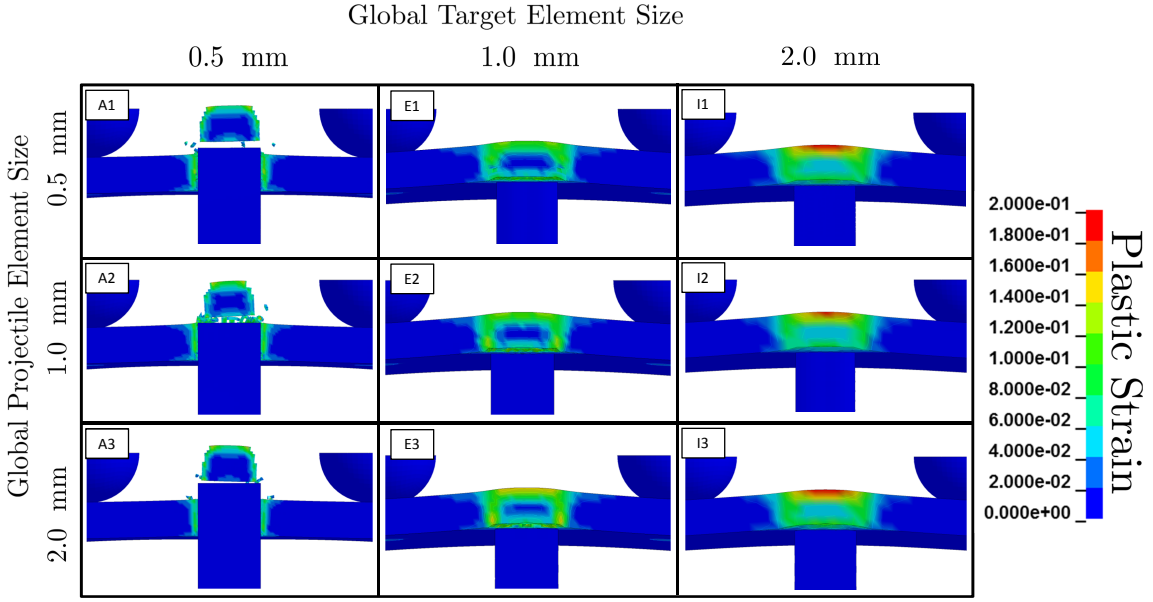


Figure 5.14: Cross-section view of projectile mesh density and lateral target plate mesh density variation matrix.

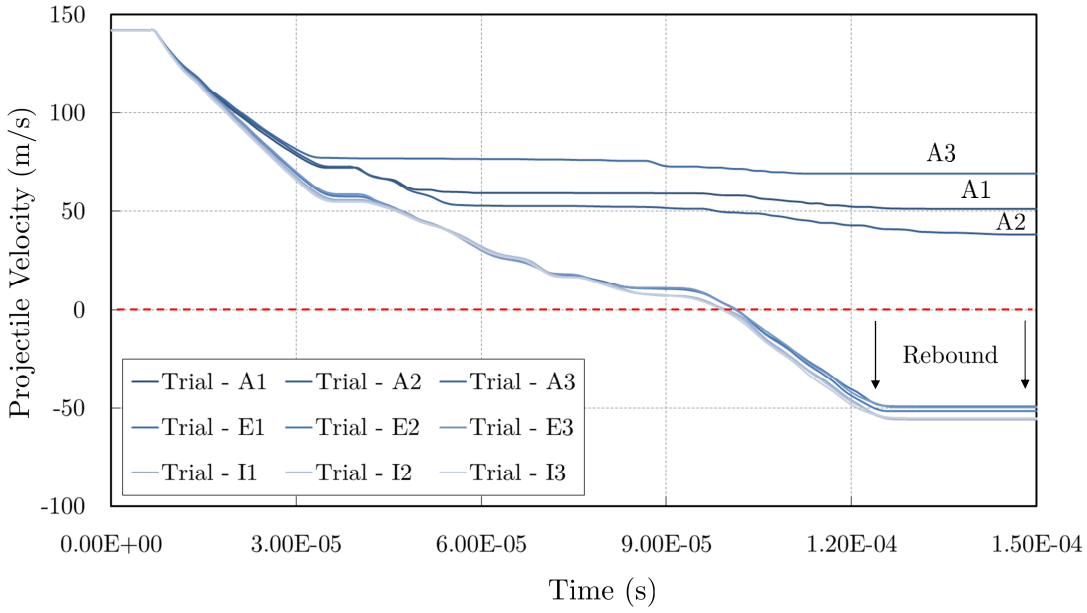


Figure 5.15: Axial velocity profiles of projectile mesh and plate mesh variation.

influence on the overall solution. This is most clearly demonstrated in A3, E3 and I3 from Figure 5.14 which reflect a similar response as A, E and I in Figure 5.11.

5.4.3 Projectile velocity study

Thus far the initial velocity has been maintained at the ballistic limit, 142 m/s, however no penetration is observed for larger target plate elements. Caution should be taken during ballistic limit estimation when using commercial software. Without foreknowledge of the mesh sensitivity, the apparent numerical ballistic limit predictions may be erroneous. To assess the potential error, the fine-scale (A1), medium-scale (E1), and coarse-scale (I1) mesh configurations have been used with increasing initial velocities, until plugging was achieved.

From Figure 5.16, plugging is only observed when the initial velocity is increased $\sim 13\%$ beyond the experimentally established limit, which is accurately predicted numerically for element sizes of 0.5mm. Trials 1 and 2 either rebounded or decelerated to almost zero, as illustrated in Figure 5.17. Experimentally, titanium should experience failure sensitivity around the ballistic limit, meaning zero residual velocity

is unlikely to occur. Similarly, the same initial velocity study was conducted for the coarse mesh variant, I3 in Figure 5.14.

Once again, the velocity required to achieve plug formation exceeds that obtained experimentally, with an element size of 0.5 mm. Figure 5.18 indicates that an increase in the initial velocity of $\sim 40\%$ is required to achieve plug formation. Figure 5.19 also highlights the positive residual velocity achieved as a consequence of penetration.

To conclude, the lack of mesh sensitivity and accurate damage accumulation have resulted in significant errors in the numerically predicted ballistic limits, based upon the currently available commercial constitutive model. Velocity trials are summarised in Figure 5.20, full plug formation and residual velocity cross-section views are highlighted in red. Due to the expense of experimental testing numerical estimations are an important tool but caution should be taken when using commercially available constitutive material models which do not feature mesh sensitivity reduction techniques or appropriate damage accumulation.

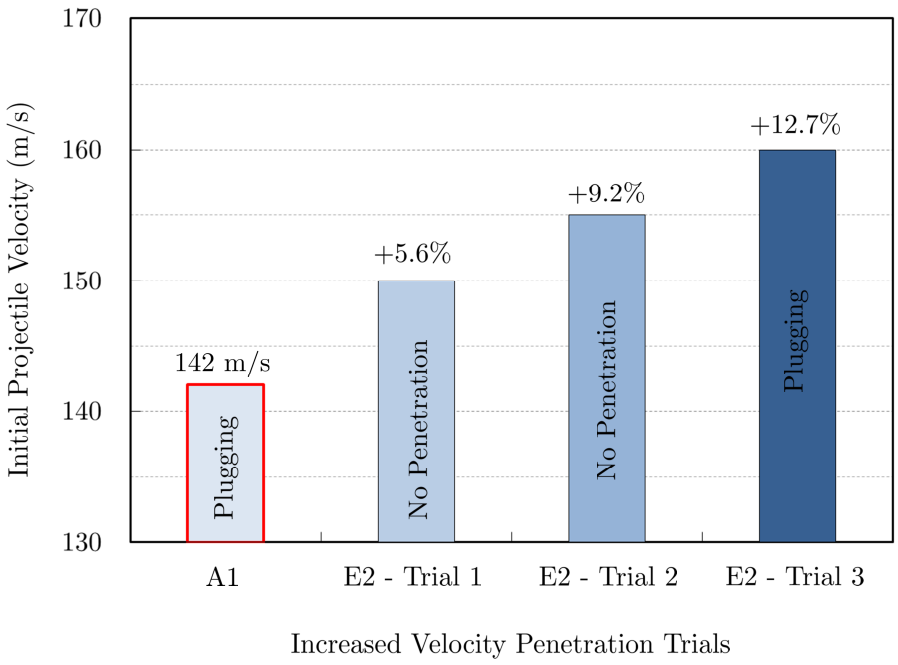


Figure 5.16: Increased velocity trials of E2 mesh configuration, from Figure 5.14.

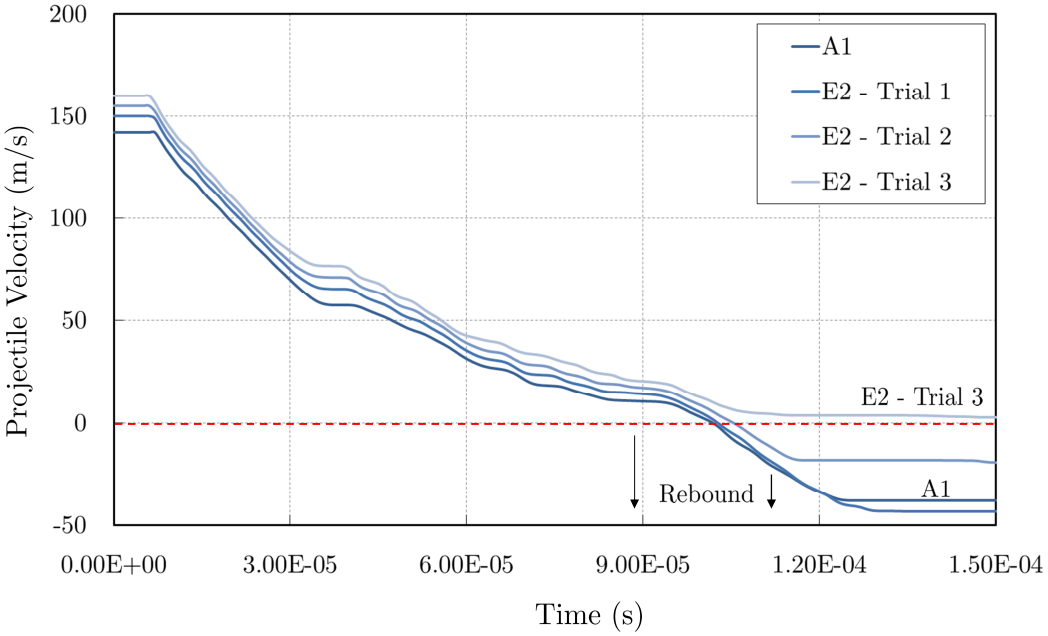


Figure 5.17: Residual velocities for E2 mesh configuration when varying initial velocity.

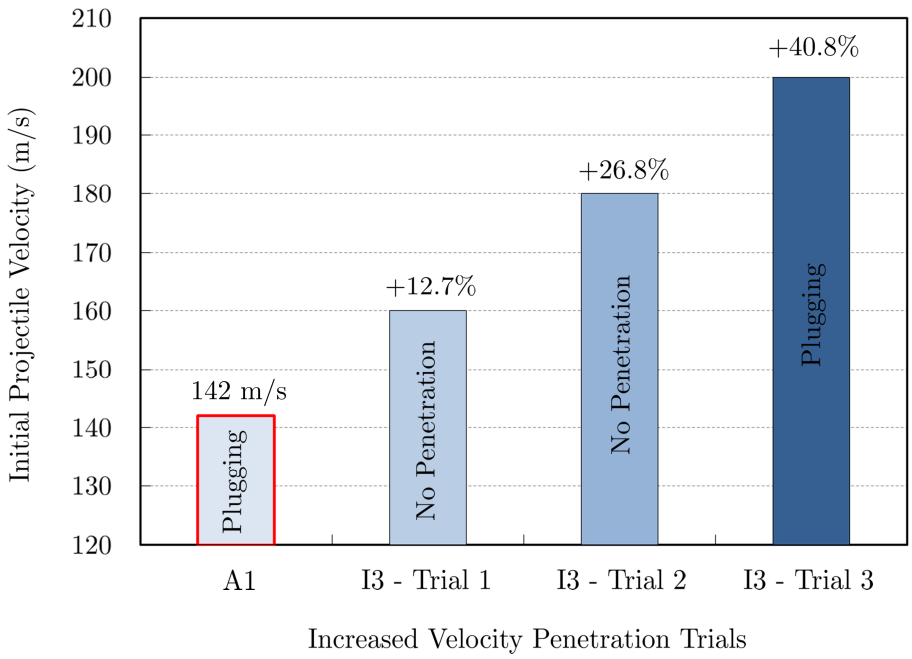


Figure 5.18: Increased velocity trials of I3 mesh configuration, from Figure 5.14.

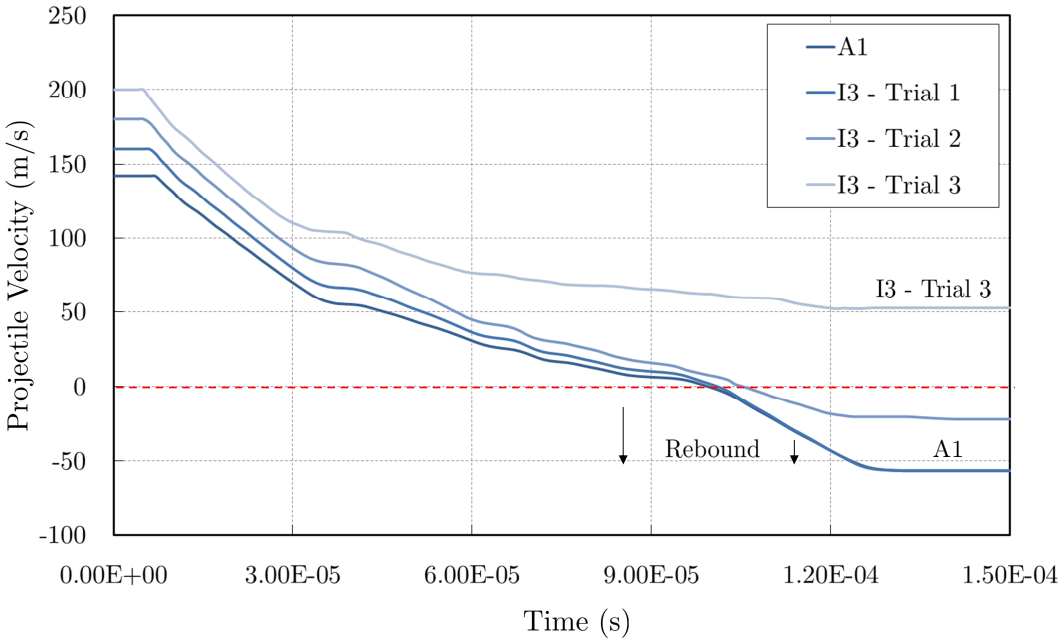


Figure 5.19: Residual velocities for I3 mesh configuration when varying initial velocity.

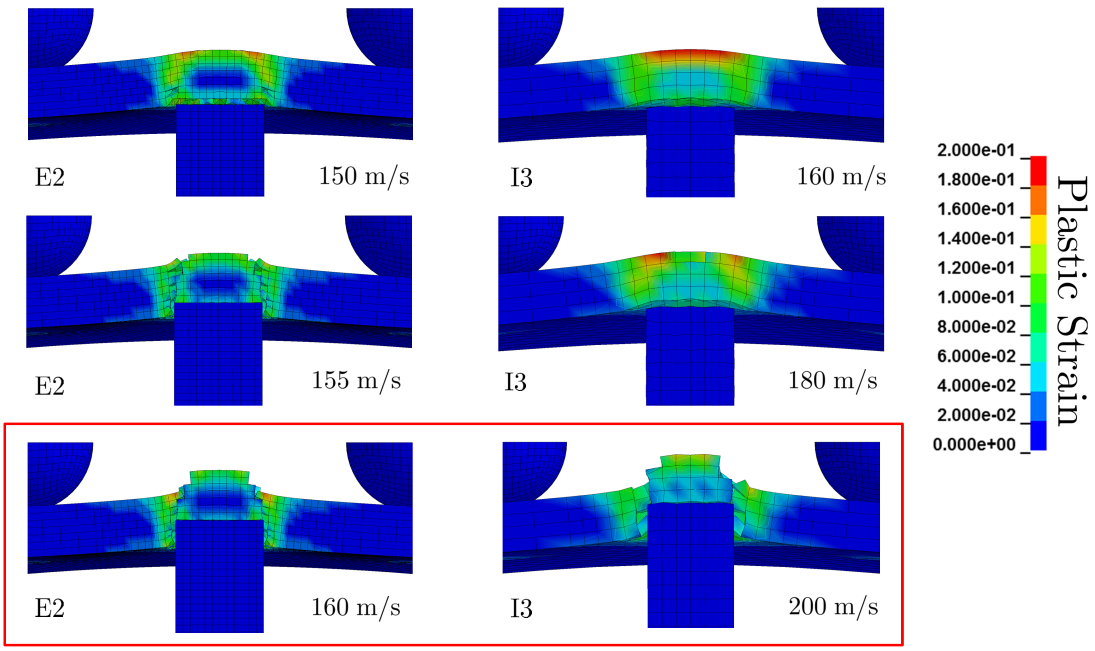


Figure 5.20: Plug formation for E2 and I3 mesh configurations when subjected to increased impact velocities.

5.5 Summary

The uni-axial simulation results in Figure 5.6 highlight that the macroscopic model is highly sensitive to the discretisation density. This indicates that homogeneity cannot be assumed within the element. It is therefore proposed that alleviation of this phenomena, especially pertinent at high strain-rates, is required regardless of the applicability of the damage mechanism. The parametric ballistic impact study also demonstrates that damage accumulation and localisation is highly mesh sensitive, which can lead to significantly misleading component strength assumptions. Plate impact experiments demonstrate that the shear failure mechanism is dominate for the geometries and velocities discussed. This highlights another key limitation of the current commercial framework, which features a single damage law related to void growth. Regardless of the applicability of the damage law, the localisation instabilities remain a challenge which needs to be alleviated. One such development is discussed in more detail during the following section.

5.6 Mesh insensitivity technique

Mesh sensitivity has clearly been demonstrated to significantly influence the establishment of uni-axial flow curves, numerical ballistic limits and realistic plug formation. During impact, mesh densities of 0.5 mm were found to accurately capture the plug formation and ballistic limit, when calibrated accordingly. However, increasing the mesh toward the industrial minimum of 2.0 mm results in an overestimation of the ballistic limit. The danger exists that homogeneity can not be assumed to be maintained within an element, thus violating the basic principles of continuum mechanics the finite element method. A lack of any localisation criteria in larger elements was found to be the cause of this error, as a consequence of a lack of ellipticity. This leads to the boundary value problem being ill-posed and therefore becoming highly mesh dependent. De Borst and Crisfield [156] outline several approaches which maintain

ellipticity, some being more suitable the present research, such as spatial averaging and stress evolution dependence on the strain gradient.

5.6.1 Regularisation implementation

A technique has been proposed which aims to alleviate the mesh sensitivity limitations within the current implementation by, introducing a length scale based upon element characteristic length. By using the characteristic length of each element individually the damage can then be assumed to evolve over an area, rather than a volume. Physically, this area represents the surface of an emerging discontinuity, such as the coalescence of voids to form a crack plane prior to failure.

The developments proposed here attempt to introduce a length scale and simultaneously enhance the constitutive relations by coupling the damage term. This maintains the capabilities of the existing framework whilst providing an enhanced localised softening capability with user-defined control. The damage growth rate exponent function m can be directly defined or implicitly defined via the below relationship

$$m = c_{25}\, l_{cr.I} + c_{14}, \tag{5.72}$$

where the parameters c_{14} and c_{25} can be determined by inverse techniques described within section 5.1.3 with initial starting values of $c_{14} = 1.1$ and $c_{25} = 1.0$, the latter can be increased to amplify the characteristic length damage evolution rate scaling effect. This technique is valid for all element sizes assuming the kinematics of deformation can be sufficiently captured. For example, large elements which cannot capture the deformation kinematics during necking would not benefit from this technique. Similarly, element sizes which approach the grain or crystalline scales would also not benefit from this technique, as the physics of deformation are not captured in this macroscopic approach. These are both consequential limitations of the FE approach without dynamic re-meshing or alternative techniques.

The assumption is made that during tensile loading dilatational damage evolution

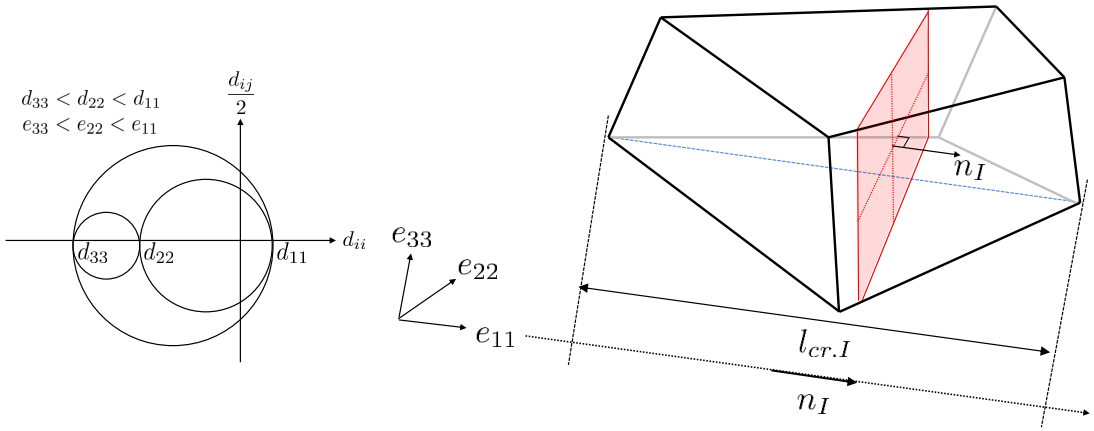


Figure 5.21: Dilatational damage mode specific planes of emerging discontinuities with associated element characteristic length depictions.

is dominant and damage is primarily due to void growth. Similarly, we assume that distortional damage will be dominant during for shear strain deformation. The orientation of this plane of emerging discontinuities is based upon element characteristic element lengths, which are related to the damage mode specific strain direction, as illustrated in Figure 5.21. A theoretical area of emerging discontinuities is calculated using the element characteristic length $l_{cr.I}$, which is defined as the largest projection of the element space diagonal onto the largest principal rate-of-deformation vector, specific to the damage mode n_I. These are defined by the eigenvalues d_{ii} and eigenvectors e_{ii} of the rate-of-deformation tensor.

$$n_I = e_I, \tag{5.73}$$

The resulting theoretical plane of discontinuities is assumed to correspond with physical fracture planes based upon void growth prior to coalesce and planar slip in the form of prevailing dislocation planes during failure.

Dilatational damage is characterised by a plane of emerging discontinuities oriented normal to the direction of largest principal rate of deformation. Damage accu-

mulates until a failure flag is activated, the element is then assumed to be unable to provide any stiffness and is therefore removed from the calculation using the element erosion technique.

The drawback of element erosion and localisation planes at oblique angle to the mesh boundaries are discussed by Needleman [155]. This is being considered in parallel with this research, and addresses aspects of this inherent FE limitation. The current element erosion technique is known to be non-physical as failure is localised on a plane of discontinuities rather than an element volume. The element erosion technique is most accurate when predicting crack propagation for the initial element removed from computation. Beyond this point the crack tip is blunted and stress state may change. Furthermore, the remaining forces are simply redistributed to the surrounding elements, this can cause non-realistic boundary conditions and internal force distributions.

5.6.2 Regularisation validation

To reiterate, minimisation of the vanishing energy effect during dynamic simulations is achieved by developing the regularisation technique coupled with damage, within the current framework.

Uni-axial validation

After implementation and activation of the regularisation algorithm, the accumulation of damage can be adjusted to compensate for the size of an element. The characteristic length is used as a scaling factor which directly provides a relative length-scale specific to the damage mode. The influence of the characteristic element length can also be scaled, and when combined with damage growth-rate control, via the exponent m, this provides a diffusive or concentrated effect related to the fracture energy release rate, or damage growth-rate control. The uni-axial tensile effect can be seen in Figure 5.22.

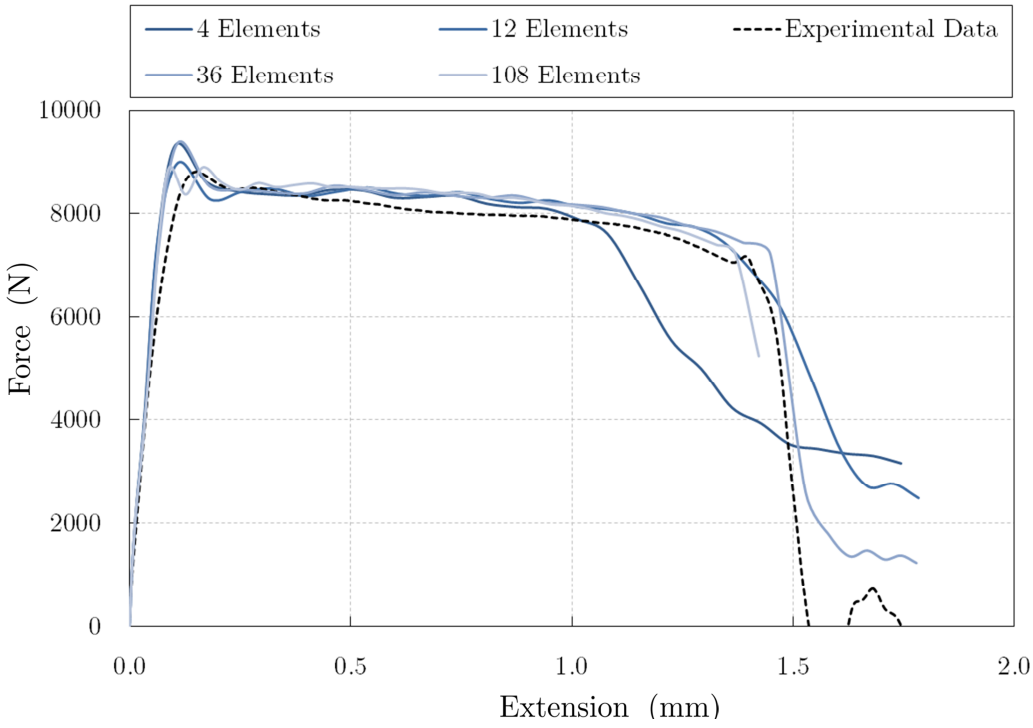


Figure 5.22: Results of uni-axial mesh in-sensitivity in tension at high strain-rates.

The developed regularisation technique enables a range of mesh densities to reproduce similar plastic flow responses. However, inherent limitations due to an inability to represent the necking phenomena are highlighted when severely reducing the axial mesh density in the gauge section. This demonstrates that whilst the influence of damage can be controlled, this does not replace the need for a mesh which can represent the desired physical deformation phenomena. Neglecting this requirement results in an abuse of the fundamental finite element concept.

Multi-axial ballisitc validation

An extensive study of the influence of mesh density during impact has been described earlier in this chapter.

Figure 5.23 compares the commercial formulation (Cases: A, B and C) with the enhanced constitutive model (Cases: D, E and F) for an initial velocity of 142 m/s with the developed damage mechanism coupled with regularisation. Plugging pen-

etration is achieved in all cases for the newly proposed constitutive model (Cases: D, E and F). The sub-component benchmark can therefore be used for further calibration exercises with a greater degree of mesh insensitivity, when compared to the commercially available solution. Simple metrics such as resultant projectile velocity can be achieved in case E, for example. However, the physical meaningfulness of the results remains a concern when attempting to represent highly localised phenomena. Ultimately, the localisation of coarse elements in case F further demonstrates the inherent limitations of the finite element failure technique, when using classical element erosion and coarse meshes.

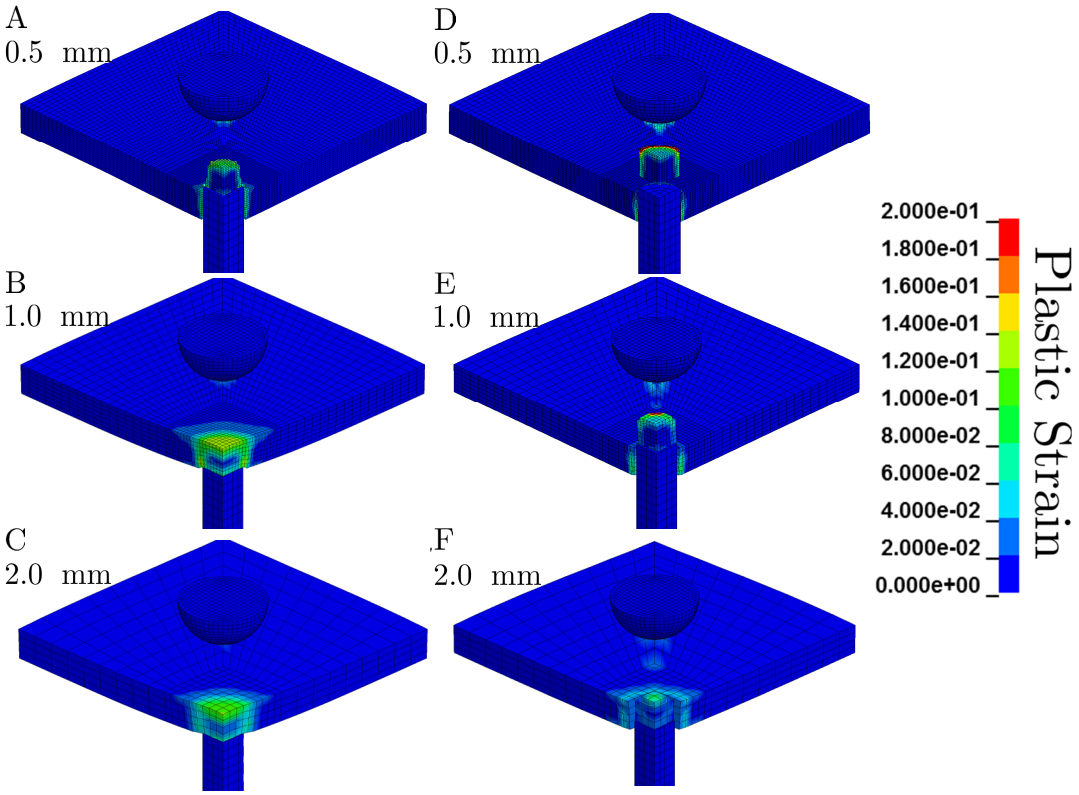


Figure 5.23: Quarter geometry ballistic limit impact simulations depicting plastic strain accumulation across multiple mesh densities. No Regularisation: A, B and C. Regularisation: D, E and F.

5.7 Summary

As a result of the findings and proposed developments, the following conclusions can be drawn

- The constitutive framework which has been developed inherently features the relevant strain-rate and temperature dependencies, in addition to dilatational void growth.

- Empirical methods for parameter identification have been presented, where possible. Parameter optimization tools have been identified for the BCJ constitutive framework, in addition to general purpose tools which exist internally within DEST and commercially within LS-OPT, and Isight, for example.

- Mesh sensitivity, perpendicular to the direction of projectile travel, has been shown to be critical to failure predictions. The margin of potential error has been demonstrated as approximately 40%, when compared to the numerically optimised benchmark. The inability to localise damage correctly has led to erroneous element erosion characteristics and over-predictions of ballistic limits when varying mesh density without the proposed regularisation technique.

- An additional length-scale has been introduced which controls the fracture energy release rate is based upon element characteristic lengths. This length-scale is associated with the prescribed directionality of damage. Control of the damage evolution rates are also a capability maintained within this proposed technique.

- The proposed coupled regularisation technique development provides a significant mesh sensitivity reduction improvement; the potential computational cost reduction, compared to re-meshing, are also highly valuable for industrial applications.

This provides an additional degree of confidence when considering the unavoidable influence of mesh density. The benefit during impact has also been demonstrated due to plug formation in coarse meshes, which was previously not possible. Caution should be taken as this numerical technique still requires a certain degree of mesh granularity, albeit significantly lower than the commercially available solutions.

The work of Børvik [95] observed the combination of shear and tensile rupture during plate impact deformation. Within the wider literature, two forms of failure mechanisms exist in ductile deformation, void growth and shear failure. These both exist simultaneously in both uni-axial tension and compression. This indicates that a single damage mode - void growth - is not sufficient to represent the complexities of localised plate impact. An opportunity, therefore, exists to enhance the current framework to include the effect of shear damage coupled with the regularisation technique developed during this chapter.

Chapter 6

Isotropic Damage Developments

The following constitutive development introduces a distinct shear damage capability fully coupled within the previously developed mesh sensitivity reduction framework. These developments have been demonstrated against the uni-axial and impact benchmarks previously studied.

6.1 Isotropic damage developments

From the literature several macroscopic mechanisms and phenomena have been identified as relevant to the deformation of titanium alloys at high strain-rates (Figure 3.11). Within an isotropic framework, the theoretical motivations, numerical developments and their applications shall be discussed during this chapter.

As discussed during Chapter 2 and Chapter 3 a single damage mechanism is an insufficient representation of failure. To demonstrate the limitations of the commercial solution a simple uni-axial compression benchmark is used.

Uni-axial testing forms the basis of alloy characterisation in many applications. Improving the simulated fidelity of uni-axial specimen deformation and failure mechanisms is also of fundamental importance, as shown in Figure 6.1. Here failure initiates centrally and propagates radially until fracture. Regardless of the enabled regularisation techniques, this does not reflect reality and provides further motivation for further constitutive developments.

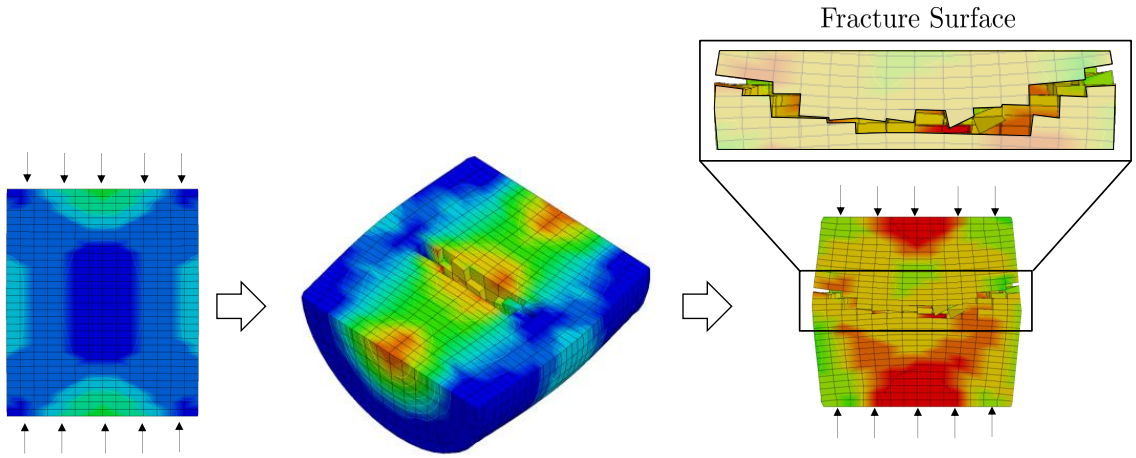


Figure 6.1: Central element erosion resulting in non-physical fracture during uni-axial compression at high strain-rates.

6.1.1 Constitutive equations

From a physical perspective, the literature clearly demonstrates the importance of shear failure in uni-axial loading cases. It has also been demonstrated that a single damage law is insufficient to characterise failure in uni-axial compression, for example. Therefore, a second damage mode, associated with shear strain, has been proposed based upon Lemaitre's 'unified damage law', which is used throughout continuum mechanics and has been applied to other dynamic impact scenarios [72]. This additional damage law is coupled with the localisation technique described in section 5.6. The plane of emerging discontinuities represent the shear band, or strain localisation plane, which forms a narrow band of highly concentrated plastic flow, typically in the order of microns. Physically, this phenomenon is characterised by a collection of dislocations which activate within a small area. Increased localised temperatures are due to plastic deformations and their inability to dissipate heat to the surrounding material during high strain-rate events, such as those of interest.

Distortional damage potential

The strain equivalence principle for linear thermo-elastic isotropic damage yields the following elastic potential function Ψ_e.

$$\rho\Psi_e = \frac{1+\nu}{2E}\frac{\sigma_{ij}\sigma_{ij}}{1-D_d} - \frac{\nu}{2E}\frac{\mathrm{tr}(\sigma_{ii})^2}{1-D_d} + q_v(T-T_{ref})\mathrm{tr}(\sigma_{ii}), \tag{6.1}$$

where σ_{ij} is the Cauchy stress in Einstein notation, q_v denotes the thermal expansion coefficient, E the Young's modulus, ν the Poisson's ratio and T is temperature in Kelvin. The energy density release rate Z can be written as follows

$$Z = \rho\frac{\partial\Psi^*}{\partial\sigma_{ij}} = \frac{\tilde{\sigma}_{ef}^2\chi_d}{2E}, \tag{6.2}$$

where χ_d represents triaxiality, σ_h is the hydrostatic stress, $\bar{d^p}$ is the effective plastic flow and σ_{ef} is the effective von Mises Cauchy stress

$$\tilde{\sigma}_{ef} = \frac{\sigma_{ef}}{1-D_d}, \tag{6.3}$$

$$\chi_d = \frac{2}{3}(1-\nu) + 3(1-2\nu)\left(\frac{\sigma_h}{\tilde{\sigma}_{ef}}\right)^2, \tag{6.4}$$

$$\dot{D}_d = \left(\frac{Z}{N}\right)^n \bar{d^p}. \tag{6.5}$$

Distortional damage law

This additional damage mechanism describes the influence of shear within the bulk and can be described in the one-dimensional rate form, where $\chi_d = 1$ in equation (6.6), for a uni-axial case

$$\dot{D}_d = \left[\frac{(1+\nu)\sigma_{ef}^2}{2E(1-D_d)^2 N}\right]^n \left[\bar{d^p}\right], \tag{6.6}$$

E is the Young's Modulus, ν is the Poisson's ratio, and the user-defined parameters n and N are constants which determine the shear damage evolution rate.

Multi-mode damage coupling

As the surrounding matrix undergoes comparatively low homogeneous flow, the regularisation technique limits the influence of damage evolution to the surrounding

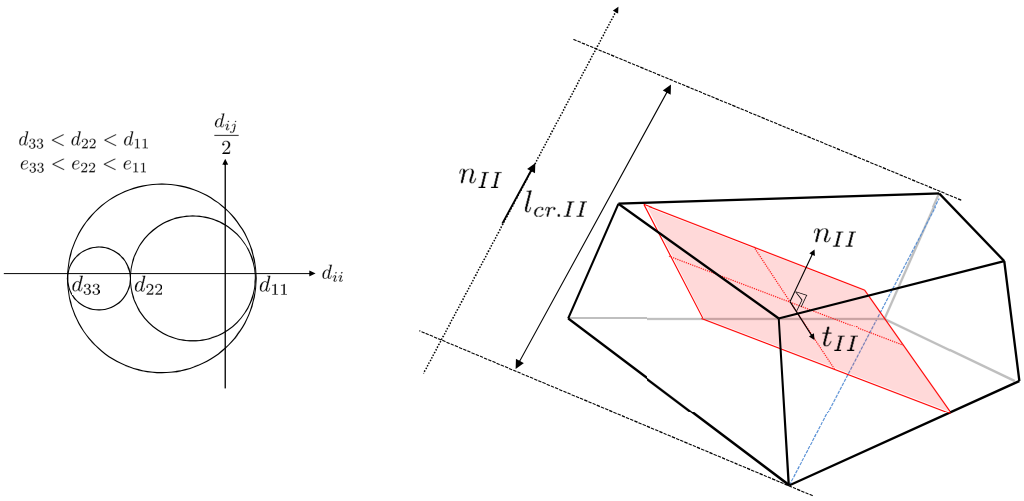


Figure 6.2: Distortional damage mode specific planes of emerging discontinuities with associated element characteristic length depictions.

material by increasing c_{26}. Initial values are assumed ($c_{15} = 1.1$, $c_{26} = 1.0$) and similar parameter fitting techniques to those described in section 5.6 can be applied. Several loading conditions, i.e. tension, torsion and compression, are required to capture the appropriate influence of each individual damage mode. Mesh sensitivity control has been coupled with the new damage exponent n as follows

$$n = c_{26}\, l_{cr.II} + c_{15}, \tag{6.7}$$

where $l_{cr.II}$ is the element characteristic length specific to the damage mode; distortional damage is characterised by a similar plane of emerging discontinuities parallel to the direction of maximum rate of shear strain deformation, t_{II}. This theoretical plane of emerging discontinuities is shown in Figure 6.2.

$$t_{II} = \frac{e_{11} - e_{33}}{|e_{11} - e_{33}|} \quad n_{II} = \frac{t_{11} \times e_{22}}{|t_{11} \times e_{22}|} \tag{6.8}$$

As discussed, the subsequent internal length scale generated is damage mode specific. As such, an element which is subjected to distortional strain components alone would evolve distortional damage D_d only. Similarly, the opposite would be true if

tri-axial conditions were achieved. In practice, both of these conditions rarely occur, therefore, a single damage mode which utilises the mesh insensitivity and localisation technique remains insufficient. By coupling the two damage evolution laws with the regularisation technique the evolution both damage mechanisms are independent to each other. Evolution of one damage parameter will not depend upon the other, as they are both coupled to different deformation vectors. However, as both damage laws influence the elements total damage D_t, damage will cumulatively accumulate until a failure flag is activated. This cumulative and competitive damage evolution mechanism has been developed and illustrated in section 6.2.

As illustrated in the literature, shear failure is dominant in both compression and impact, for certain geometries and velocities. This development therefore provides a critical improvement, in terms of realistic damage accumulation capabilities. This also provides the ability to form preferential damage accumulation if a requirement is identified and justifiable. Whilst sharing information between the element and the constitutive model is not ideal, this development provides a marked improvement, and also opportunities for further element failure techniques to be developed, which utilise this theoretical plane of discontinuities.

Multi-mode damage formulation

These two mechanisms will be shown to cumulatively damage the element until a predefined value of effective plastic strain or damage D_v, D_d, D_t is reached, thus triggering the element erosion technique. The two singular damage thresholds D_v, D_d and cumulative D_t damage thresholds can trigger element failure

$$D_t = D_v + D_d. \tag{6.9}$$

Upon failure flag activation the associated element is assumed to be obsolete and is therefore removed from the calculation. This technique is known to be non-physical as failure is localised on a plane of discontinuities rather than an element volume.

For clarity, we can express the multi-mode damage terms within the stress tensor (6.10) as follows

$$\overset{\nabla}{\boldsymbol{\sigma}} = \lambda(1-D_v)\,\mathrm{tr}[\boldsymbol{d}^e]\boldsymbol{I} + 2\mu(1-D_v)(1-D_d)\boldsymbol{d}^e - \frac{\dot{D}_v}{1-D_v}\boldsymbol{\sigma}, \tag{6.10}$$

The influence of distortional damage has been assumed to only effect the isochoric part of the stress tensor, associated with the shear modulus. The yield criterion takes the following form

$$\Phi = \bar{\xi} - \kappa - \beta(\bar{d}, \theta, D_v, D_d), \tag{6.11}$$

where the isotropic hardening and temperature dependent yield stress functions are incorporated within the following current yield stress function

$$\sigma_y = (1-D_v)(1-D_d)\left[V(\theta)\sinh\left(\frac{\bar{d}}{f(\theta)}\right) + Y(\theta)\right] + \kappa. \tag{6.12}$$

The implementation of the radial return and plastic multiplier increment remains as described in Chapter 5. Further discussion during this chapter shall pertain to the implementation and illustration of the independent nature of the damage evolution and localisation.

6.1.2 Constitutive implementation

The newly developed multi-mode damage mechanism described above has been implemented within the commercial LS-DYNA Explicit software and in-house development code DEST. An overview of the implementation formulations are described for completeness.

Step 1. Trial elastic assumptions

The deviatoric trial Cauchy stress tensor $\boldsymbol{\sigma}'^{trial}$ is evaluated with the combined influence of both dilatational and distortional damage modes which individually influence bulk and shear moduli, respectively.

$$\boldsymbol{\sigma}'^{\,\text{trial}}_{n+1} = \boldsymbol{\sigma}_n \left[\frac{\dot{D}_v}{1-D_v}\right]_n + 2\mu(1-D_v)_n(1-D_d)_n\, d_{n+1/2} + 3\lambda(1-D_v)_n \,\text{tr}\left[d_{n+1/2}\right] \boldsymbol{I} - p_{n+1}\boldsymbol{I}, \tag{6.13}$$

Pressure at t_{n+1} does not include the influence of both damage terms, for example. Distortional damage D_d results in a shape change and therefore is assumed not to influence hydrostatic components. The multi-mode damage development stress tensor (6.13) requires updating, based upon the deviatoric stress tensor from the previous step, shown below

$$\boldsymbol{\sigma}'^{\,\text{trial}}_{n+1} = \boldsymbol{\sigma}_n - p_{n+1}\boldsymbol{I}, \tag{6.14}$$

$$p_{n+1} = \frac{1}{3}\text{tr}\left[\boldsymbol{\sigma}_n^{trial}\right]\left[\frac{\dot{D}_v}{1-D_v}\right]_n + 3\lambda(1-D_v)_n \,\text{tr}\left[d_{n+1/2}\right]\Delta t. \tag{6.15}$$

Step 2. Elastic assumption evaluation

The multi-mode damage elastic assumption is now checked against the yield function, if $\Phi^{\text{trial}} > 0$ then plastic deformation has occurred.

$$\Phi^{\text{trial}}_{n+1} = \bar{\xi}^{\text{trial}}_{n+1} - \sqrt{\frac{2}{3}}\left(\kappa^{\text{trial}}_{n+1} + \beta_{n+1}\right) \tag{6.16}$$

It should also be noted that the implementation of the hyperbolic portion of the deviatoric plastic flow rule (β), in equation (5.23), has been converted to a logarithmic formulation, for computational efficiency

$$\beta = V(\theta)\text{sinh}^{-1}\left[\frac{\bar{d}_{n+1/2}}{f(\theta)}\right] = V(\theta)\ln\left[\frac{\bar{d}_{n+1/2} + \sqrt{\bar{d}^{\,2}_{n+1/2} + f(\theta)^2}}{f(\theta)}\right]. \tag{6.17}$$

Step 3. Visco-plastic multiplier

The newly developed visco-plastic multiplier increment ($\Delta\gamma$) is used to update the internal state variable $\boldsymbol{\alpha}$ and κ, and to return the trial elastic stress increment back to the newly calculated yield surface.

$$\Delta\gamma_{n+1} = \frac{\Phi^{\text{trial}}_{n+1}}{(1-D_v)(1-D_d)2\mu + \frac{2}{3}(h+H)} \tag{6.18}$$

Step 4. Solution dependent variable correction

The new plastic multiplier increment is introduced as follows

$$\boldsymbol{\sigma}'_{n+1} = \boldsymbol{\sigma}'^{\,\text{trial}}_{n+1} - 2\mu\Delta\gamma\mathbf{n}, \tag{6.19}$$

$$\boldsymbol{\alpha}_{n+1} = \boldsymbol{\alpha}^{\,\text{trial}}_{n+1} - h\Delta\gamma\mathbf{n}, \tag{6.20}$$

$$\kappa_{n+1} = \kappa^{\,\text{trial}}_{n+1} - H\sqrt{\tfrac{2}{3}}\Delta\gamma, \tag{6.21}$$

where the unit vector of effective stress for radial return is assumed to be linear over the current time-step and is given as follows (6.22).

$$\mathbf{n}_{n+1} = \frac{\xi}{\bar{\xi}} \tag{6.22}$$

Step 5. Adiabatic thermal effects

The empirical assumption that 90% of plastic work done is dissipated through generation of heat, using the modified $\Delta\gamma_{n+1}$

$$\theta_{n+1} = \theta_n + \vartheta\,\frac{\Delta\gamma_{n+1}}{\bar{\xi}^{\text{trial}}_{n+1}}\left(\boldsymbol{\sigma}_n : \boldsymbol{\xi}^{\text{trial}}_{n+1}\right), \tag{6.23}$$

$$\vartheta = \left(\frac{0.9}{\rho C_v}\right). \tag{6.24}$$

6.2 Isotropic damage validation

During this section the implemented dilatational (void growth) and distortional (shear strain) damage terms, active during uni-axial experiments, shall be evaluated. During development, both dilatational and distortional damage can initiate element erosion, in addition to their combined influence and plastic strain.

6.2.1 Tensile damage evolution

An initial dilatational damage is assumed to be present which represents defects or flaws in the material. Initial growth is gradual, based on diffusion, whilst at high stresses and temperatures the rapid power-law growth increases damage accumulation towards failure ($D_v \rightarrow 1$). As expected, dilatational damage initiates element erosion from the longitudinal and radial centre of the gauge section (① in Figure 6.4) which are incrementally depicted in Figure 6.3.

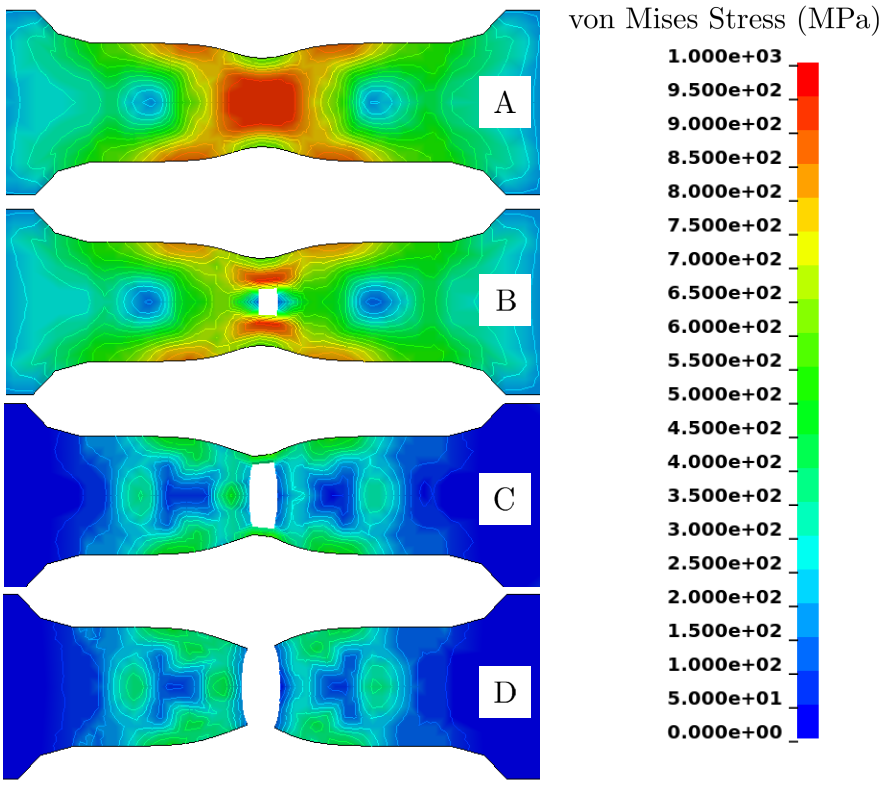


Figure 6.3: Stress contours and erosion of the central element via dilatational damage growth and necking due to distortional damage.

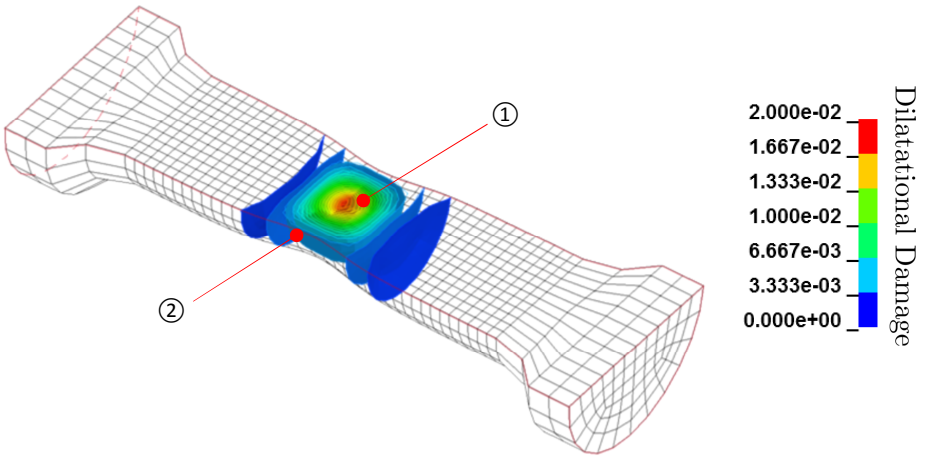


Figure 6.4: Dilatational damage contours of high strain-rate uni-axial tension specimen during plasticity, prior to element erosion.

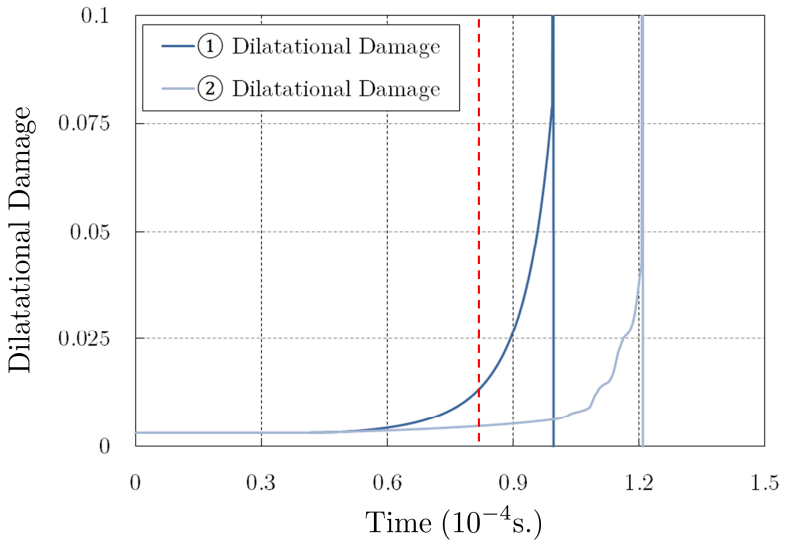


Figure 6.5: Dilatational damage of high strain-rate uni-axial tension specimen during plasticity, prior to element erosion.

Distortional damage is also present at surface of the specimen neck in Figure 6.6 at location ②, and Figure 6.7. However, failure is ultimately characterised by sudden catastrophic failure due to void growth, this can be seen in Figure 6.5 as damage rapidly increases until failure. Distortional damage migrates away from ① during necking, causing the apparent plateau of the damage evolution in Figure 6.7. It should be noted that localisation of distortional damage is also influenced by geo-

metric necking, this indicates that mesh densities which are unable to capture this deformation mode cannot evolve damage sufficiently. When distortional damage does not trigger failure independently, a single row of surface elements remain on the failure plane, as shown in C from Figure 6.3. Here the stress state becomes tensile and dilatational damage dominates, as shown Figure 6.5. These complexities during localised deformation demonstrably capture the importance of combined dilatational and distortional damage modes.

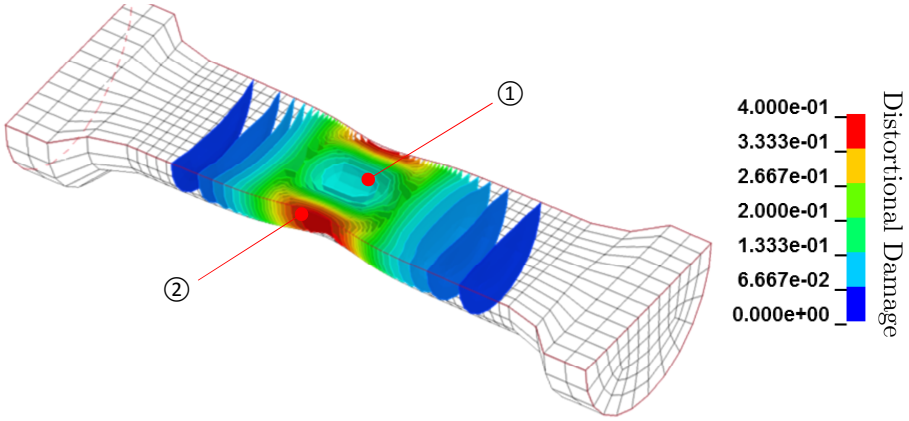


Figure 6.6: Distortional damage contours of high strain-rate uni-axial tension specimen during plasticity, prior to element erosion.

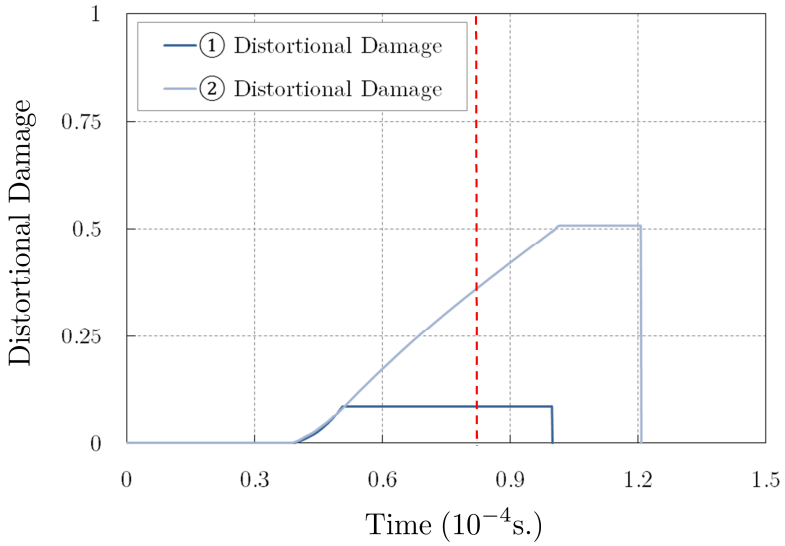


Figure 6.7: Distortional damage of high strain-rate uni-axial tension specimen during plasticity, prior to element erosion.

6.2.2 Tensile damage summary

The influence of shear strain, and hence distortional damage D_d, cannot be ignored. Whilst dilatational damage D_v dominates in this loading condition, distortional damage significantly contributes towards final failure when necking occurs. The newly developed constitutive model, described herein, is able to firstly differentiate and secondly capture these two competing mechanisms. In reality, this is reflected in cup-and-cone failure, which is often seen in tensile failure. Mesh densities adopted within industry are likely to exceed those needed to explicitly depict failure patterns due to micromechanical heterogeneities within an element. However, even in comparatively large elements the accumulation of both damage modes can be observed. This motivates further investigation, when simulating complex structures where prediction of failure modes becomes difficult.

6.2.3 Compressive damage evolution

Uni-axial compression simulations also activate both damage modes. Distortional damage localises on the typical shear failure plane at 30° with respect to the axial loading direction. This dominates the fracture pattern observed in Figure 6.8.

Dilatational damage is active in the centre of the specimen due to lateral tension which contributes towards localised softening, as shown in Figure 6.11. This coincides with the literature. In addition, dilatational damage is present in elements associated with the failure plane (Figure 6.9). However, distortional damage is an order of magnitude greater than dilatational damage during compression, as shown in Figures 6.10 and 6.12. Interestingly, both damage modes are active at both ① and ② as opposed to distinct regions during tension.

Lee also postulated [78] that both damage modes are active during uni-axial compression. Distortional and dilatational damage are observed in areas associated with the failure plane, this further demonstrates the importance of the multi-mode damage approach to represent complex failure scenarios. The combined effect of the multi-

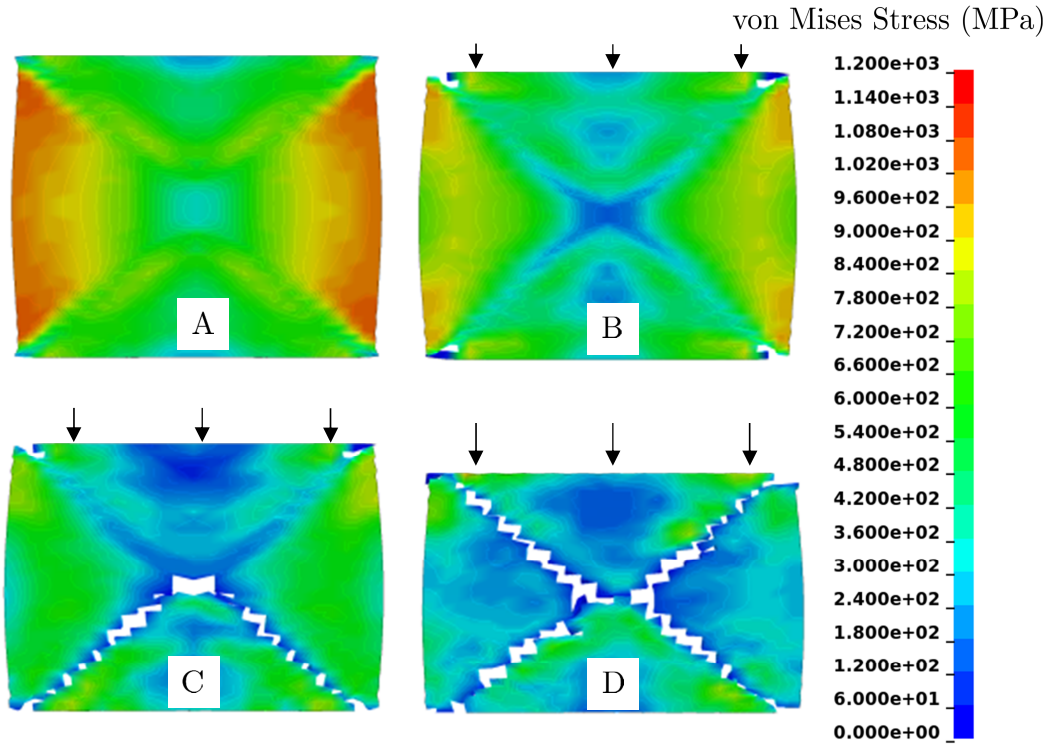


Figure 6.8: Stress contours and erosion on the 30° plane via distortional damage.

mode damage mechanism and the regularisation algorithm enables an improved strain localisation capability in multi-axial three-dimensional systems.

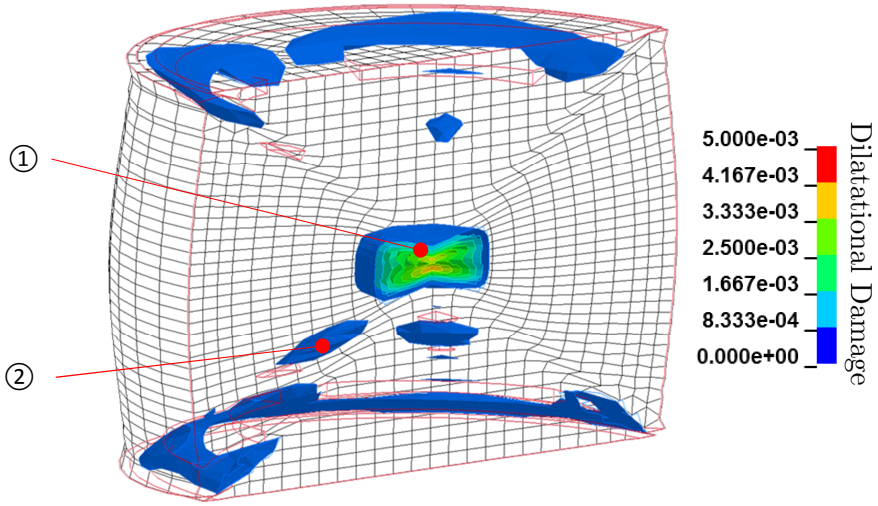


Figure 6.9: Dilatational damage contours of high strain-rate uni-axial compression specimen during plasticity, prior to element erosion.

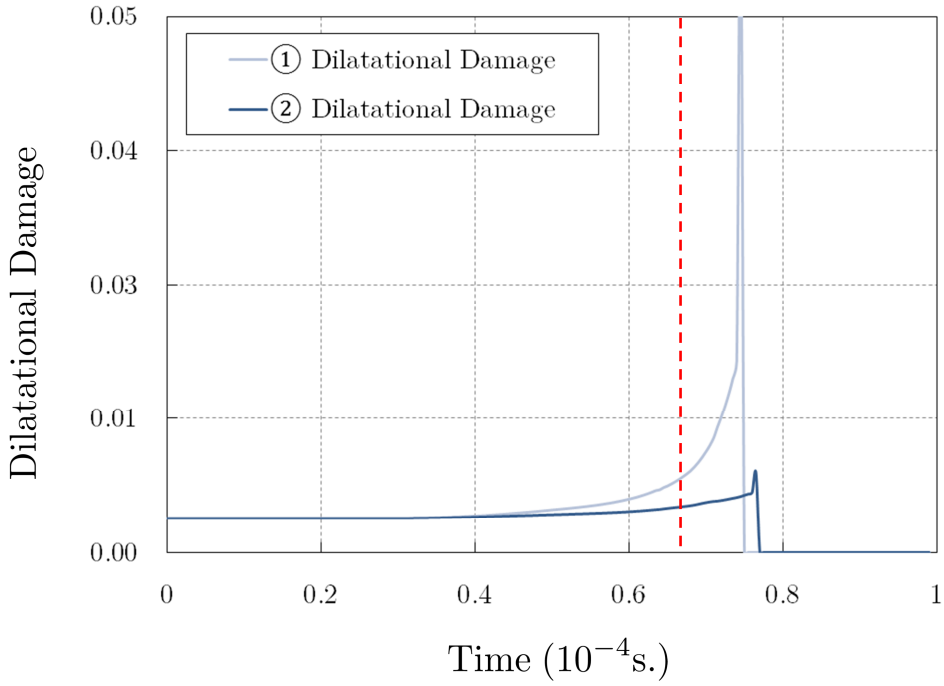


Figure 6.10: Dilatational damage of high strain-rate uni-axial compression specimen during plasticity, prior to element erosion.

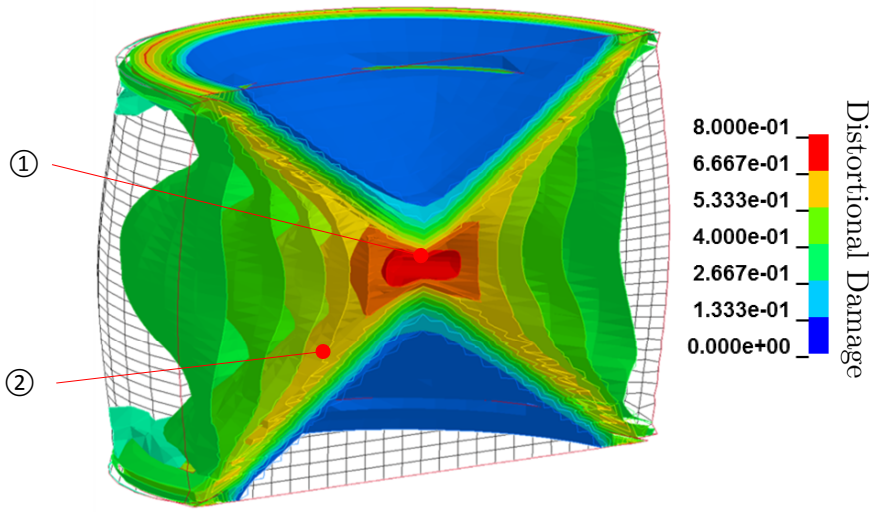


Figure 6.11: Distortional damage contours of high strain-rate uni-axial compression specimen during plasticity, prior to element erosion.

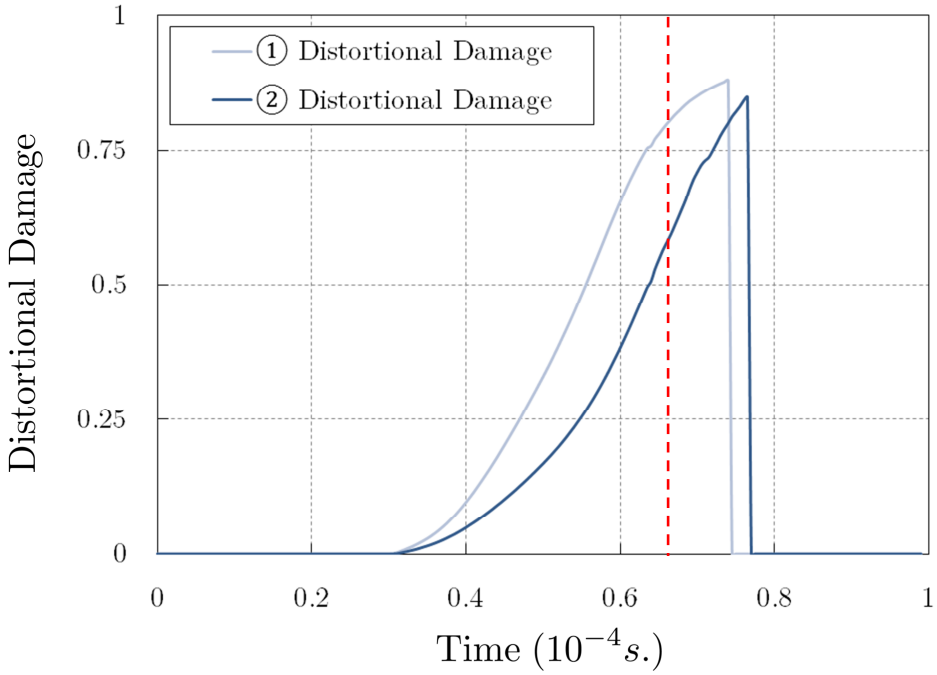


Figure 6.12: Distortional damage evolution of high strain-rate uni-axial compression specimen during plasticity, prior to element erosion.

6.2.4 Compressive damage summary

It is clear that distortional damage D_d is dominant in compression; the localisation of damage on the corresponding shear failure plane is also clearly demonstrated. An important factor to note is that failure is characterised by a conical plane of failure. This is due to the idealised and perfectly uniform conditions during isotropic deformation. In reality, imperfections within the material and effects of the boundary conditions result in a single prevailing failure plane. In order to introduce aspects of these physical imperfections, non-symmetric and non-isotropic yielding are required. In an isotropic case the benefit of localising distortional damage remains intuitively self-evident and is clearly demonstrated.

6.2.5 Plate impact damage evolution

Beyond the SHPB strain-rates, the performance of the constitutive model at ballistic strain rates has been assessed against the experimentally established ballistic

limit and previous numerical studies in Chapter 5. The value of the sub-component simulation is to demonstrate the applicability of the shear damage mode during plug formation, as observed during experimentation. The ballistic limit was experimentally established to be between 125m/s - 142m/s. Experimentally, failure is classified as an observable crack of length > 0.5mm on the target rear-face. Numerically, this corresponds to a single element failure, for the highest mesh density topology simulated. Good correlation between experimental and numerical ballistic limits has been demonstrated. At impact velocities < 125 m/s no element removal is observed, as shown in Figure 6.13. Conversely, rear-face failure and full plug formation are observed at velocities ≥ 142 m/s, as shown in Figure 6.14. Experimentally, shear failure has been shown to dominate during plate impact, the present constitutive developments have demonstrated that distortional damage, as opposed to dilatational damage, is the primary damage mechanism contributing towards failure. This is clearly demonstrated at probe locations in the failure region (Figures 6.15 and 6.17).

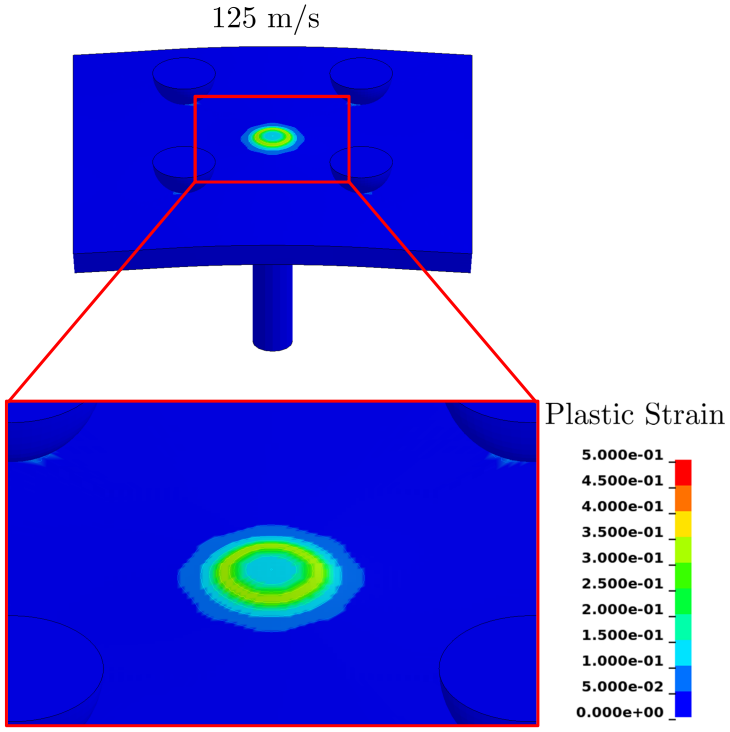


Figure 6.13: Isometric view of target plate rear face with initial velocity of 125 m/s

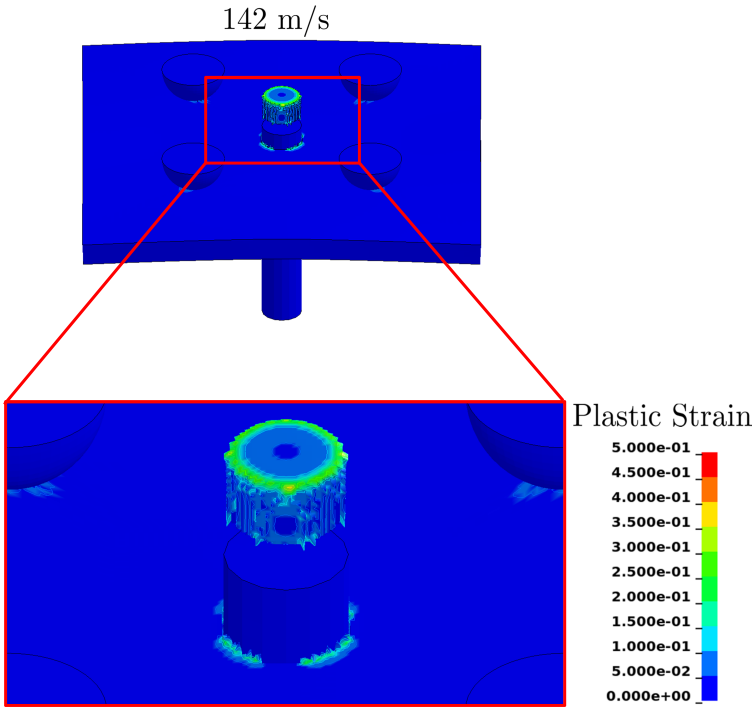


Figure 6.14: Isometric view of target plate rear face with initial velocity of 142 m/s

The damage growth rates of each damage mechanism can be seen in Figure 6.16 and Figure 6.18. Both shear and normal stress states are present, the competitive and cumulative damage evolution is facilitated by the multi-mode development. When damage is based upon the stress states present, dilatational damage has little influence beyond initial impact, this corresponds to experimental findings in the literature (Chapter 2) and experiments during Chapter 4, which are based upon the plate impact experiments performed within the Impact Engineering Laboratory.

When comparing the modified constitutive development results in Figure 6.19, with previous impact simulations in Figures 5.9 and 5.10, the plug formation is far more regular and uniform. During experimentation, the regular failure path is indicative of shear-band failure. Similarly, minimal element failure was observed at the lower bound of the ballistic limit, however from the literature we know that the propensity to failure remains high when shear damage initiates. Therefore, greater damage would be expected, as shown in Figure 6.19. This indicates that the newly

developed shear damage algorithm is far more applicable for impact localisation scenarios.

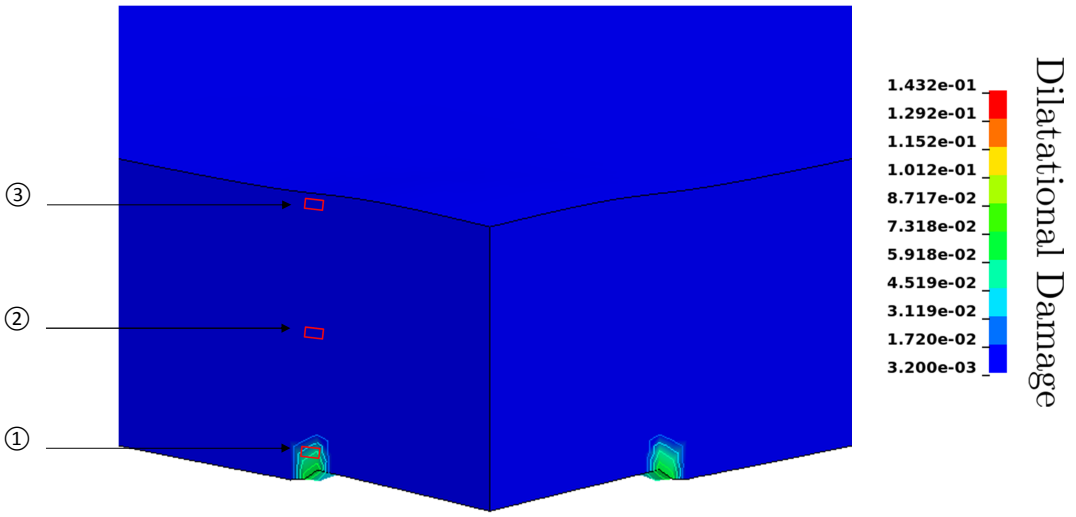


Figure 6.15: Quarter cross-section view of target plate impact at 142 m/s, contours of dilatational damage.

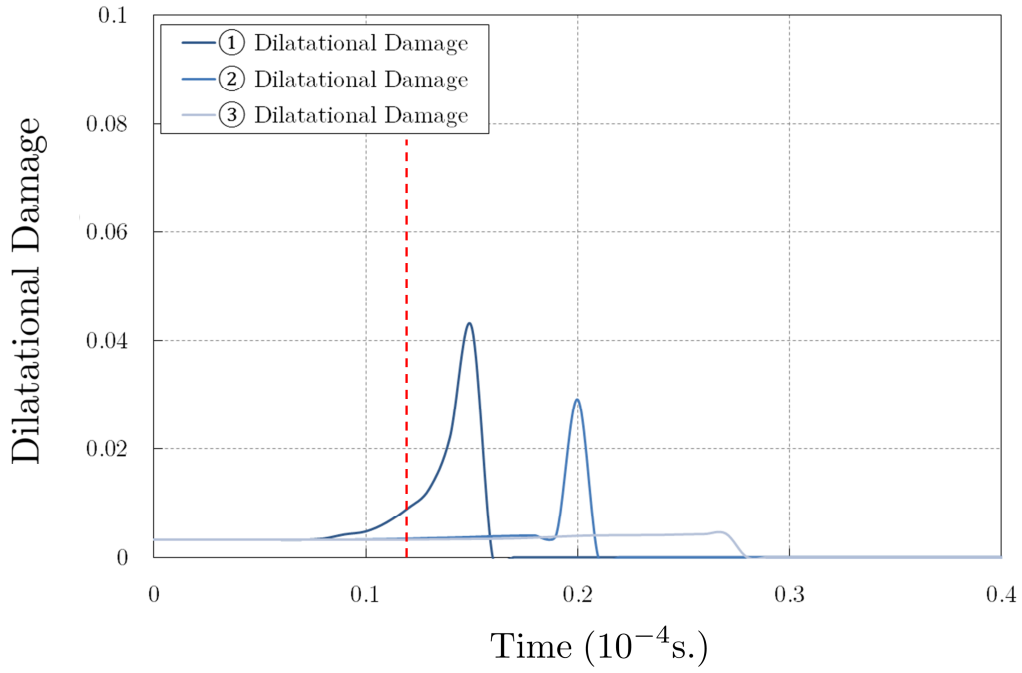


Figure 6.16: Probe dilatational damage evolution at 142 m/s, from Figure 6.15.

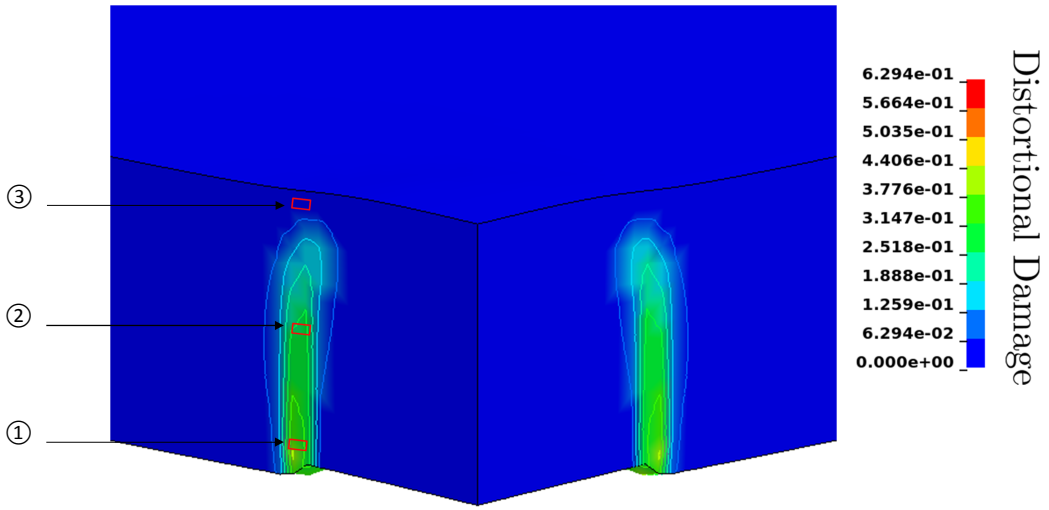


Figure 6.17: Quarter cross-section view of target plate impact at 142 m/s, contours of distortional damage.

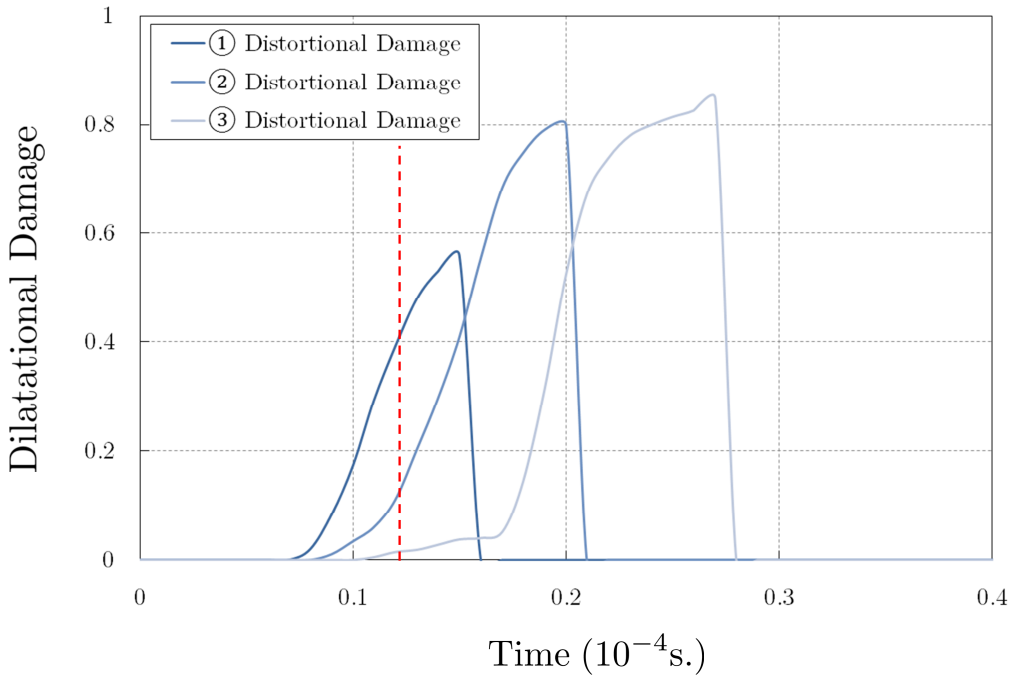


Figure 6.18: Probe distortional damage evolution at 142 m/s, from Figure 6.17.

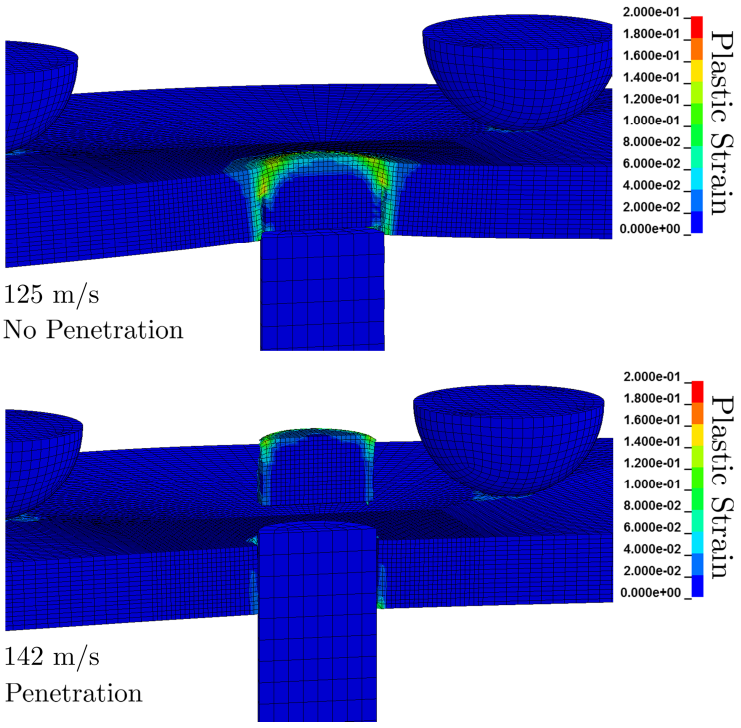


Figure 6.19: Element failure characteristics surrounding the ballistic limit.

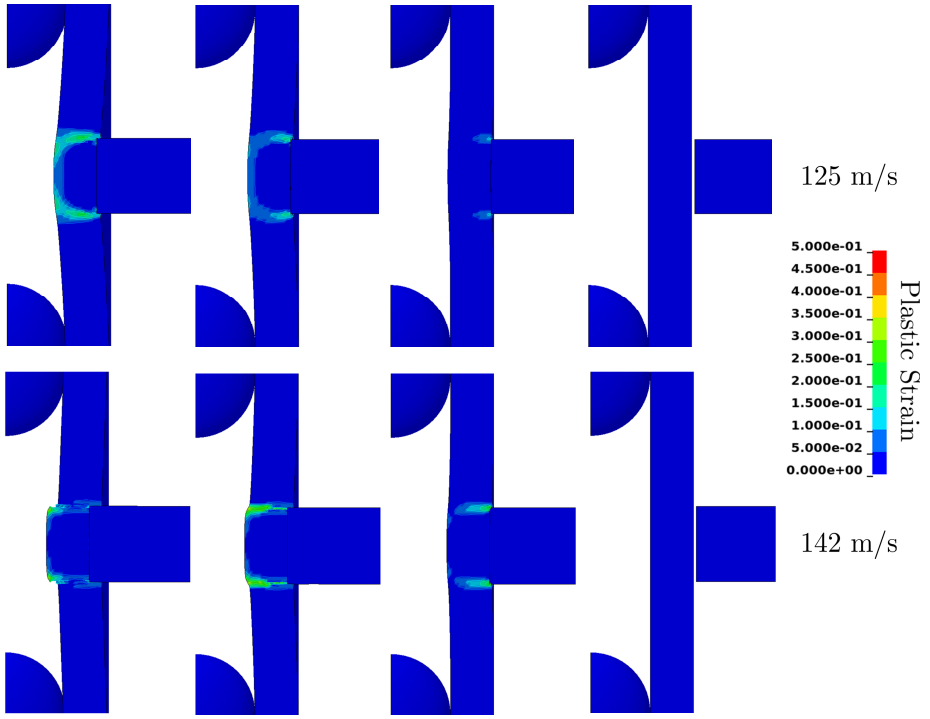


Figure 6.20: Element failure and plastic strain localisation at upper and lower bounds of the ballistic limit range.

The literature has indicated that shear band formation is strain-rate sensitive; previous numerical impact simulations in Chapter 5 did not demonstrate sufficient damage localisation at the lower ballistic limit, or sensitivity to strain-rate. Firstly, Figure 6.19 indicates further sensitivity at lower impact velocities, secondly Figure 6.20 indicates that damage localises to a greater degree at the upper ballistic limit.

6.2.6 Plate impact damage summary

Unlike the uni-axial benchmarks, the plate impact benchmark shows a strong distortional damage evolution preference. It has been clearly demonstrated that the distortional damage growth rate is far higher than the dilatational counterpart, this corresponds to the literature and experiential observations. This provides a mechanism to characterise failure due to shear band formation, as damage growth rates and localisation can be controlled and modified based upon experimental observations. The regularity of the plug formation with the newly developed multi-mode damage algorithm demonstrates that element failure is no longer artificially influenced by void growth as a softening mechanism, which deviates from the prescribed shear band failure plane. The rapid distortional damage evolution and magnitude of accumulated damage during impact reflects the sensitivity observed during impact experiments, which is characterised by sudden catastrophic failure.

6.3 Summary

The importance of multiple damage modes has been clearly demonstrated in uni-axial simulations and plate impact studies.

- The stress-state dependent damage evolution assumption has been proven to be an accurate approximation. This is reflected in appropriate damage localisation regions in all benchmarks, which combines the regularisation technique and introduces a length scale dependent upon damage directionality.

- Cumulative and competitive damage evolution has been demonstrated in both tension and compression. This has also been shown to influence deformation mechanisms such as necking and shear localisation. These observations have also validated theoretical assumptions from the literature regarding stress states and their associated damage modes.

- Development and implementation of both dilatational and distortional damage have provided the ability to simulate accurate damage accumulation in failure mode specific scenarios. This improvement has been clearly demonstrated in uni-axial tension, compression and impact damage accumulation.

- The relevance of the newly proposed shear mechanism has also been demonstrated during plate impact, which is highly preferential to shear failure corresponding to experimental findings within the literature and during in-house testing.

The wider literature and EBSD plots produced by TIMET of a typical RVE (Figure 2.6) illustrate that Ti-6Al-4V is both asymmetric and anisotropic. The above formulations, do not take into account either pressure dependencies or macroscopic anisotropic effects caused by initial textures [43, 113, 157, 51]. These are both relevant in an industrial material and hence require a constitutive framework which encapsulates these capabilities. These developments are detailed in Chapter 7.

Chapter 7

Non-Isotropic Constitutive Developments

Building upon the framework described in Chapter 6, the present research is extended to include the influence of asymmetric and anisotropic plastic deformation. The constitutive developments will be described and validated against in-house experimental data.

7.1 Asymmetric developments

The Strength Differential (SD) effect is characterised by a flow stress which differs in tension and compression. Historically, this was assumed to be associated with plastic dilatancy (microvoid formation) via the normality rule due to the small but observable plastic volumetric expansion, as discussed by Casey and Sullivan [158]. However, Richmond and Spitzig [115] experimentally demonstrated that the Strength Differential effect is also related to the influence of pressure on dislocation motion. Yoon [109] also indicated that uni-directional twin formation may also contribute to a strength differential effect. The source of this phenomena has not been clearly defined at the point of writing; regardless, the macroscopic behaviour can be represented numerically.

Numerically, these effects cannot be represented by only J_2 yield functions, as with von Mises, unless there is an initial non-zero stress imposed externally, which

is typically a technique used when representing a bulk residual stress [159]. Drucker and Prager introduced the influence of the hydrostatic stress I_1, which modifies the classical von Mises yield surface to form a conical yield surface with a single apex point. The Drucker-Prager criterion has been used for many materials, including titanium, to predict the macroscopically observed discrepancies between tensile and compressive yielding [157, 160]. The yield surface is symmetric around the hydrostatic axis which results in a return vector perpendicular to the trial stress yield surface, assuming the time-step remains sufficiently small.

7.1.1 Constitutive equations

The classical Drucker-Prager yield function takes the following form

$$f(\sigma_{ij}) = \sqrt{J_2(\boldsymbol{\sigma}')} + \eta p(\boldsymbol{\sigma}) - \zeta = 0, \tag{7.1}$$

where the material parameters η and ζ are defined in equation (7.1) and formulated below, with respect to user-defined parameters φ and c which represent the friction angle and cohesive intercept shown in Figure 7.1.

$$\eta = \frac{2\sin(\varphi)}{\sqrt{3}(3 \pm \sin(\varphi)}, \tag{7.2}$$

$$\zeta = \frac{6\,c\cos(\varphi)}{\sqrt{3}(3 \pm \sin(\varphi)}. \tag{7.3}$$

Asymmetric yield

From equation (5.20) and (7.1 - 7.3) the pressure sensitive yield function within the BCJ framework takes the following form

$$\Phi(\boldsymbol{\sigma}', \boldsymbol{\alpha}, \boldsymbol{d}, \theta, D_v, D_d) = \bar{\xi} + \eta p(\boldsymbol{\sigma}) - \zeta - \kappa - \beta = 0, \tag{7.4}$$

the variable β is formulated below with the inclusion of multi-mode damage as previously described

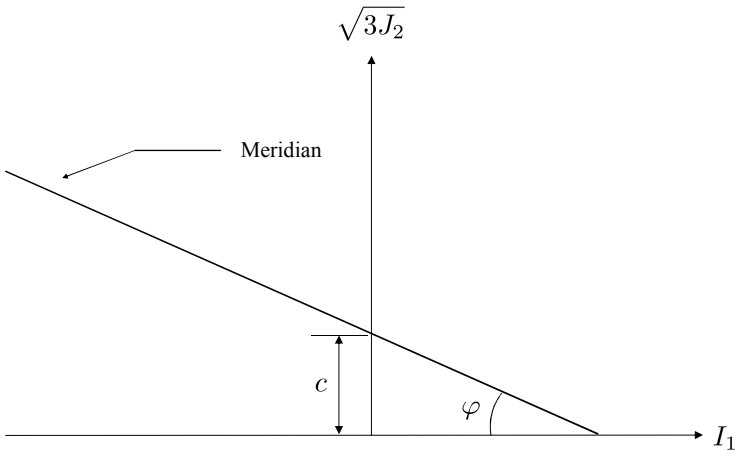


Figure 7.1: Two dimensional representation of Drucker-Prager parameters and conical yield surface.

$$\beta = (1 - D_v)(1 - D_d)\left[V(\theta)\sinh\left(\frac{\bar{d}}{f(\theta)}\right) + Y(\theta)\right]. \tag{7.5}$$

Asymmetric yielding in Ti-6Al-4V is not as pronounced as other alloys, however the capability has been demonstrated, as shown in section 7.3.

Asymmetric hardening

Modification of equation sets (5.31) and (5.35) to include the deviatoric stress invariants creates differential hardening rates depending of the stress state present [142, 141]. The corresponding formulations are described below

$$r_d(\theta) = c_7\left[1 - a\left(\frac{4}{27} - \frac{J_3^2}{J_2^3}\right) - b\left(\frac{J_3}{J_2^{3/2}}\right)\right]\exp\left[-\frac{c_8}{\theta}\right], \tag{7.6}$$

$$h(\theta) = [c_9 - c_{10}\,\theta]\left[1 - a\left(\frac{4}{27} - \frac{J_3^2}{J_2^3}\right) - b\left(\frac{J_3}{J_2^{3/2}}\right)\right], \tag{7.7}$$

$$r_s(\theta) = c_{11}\exp\left[-\frac{c_{12}}{\theta}\right]. \tag{7.8}$$

$$R_d(\theta) = c_{13}\left[1 - a\left(\frac{4}{27} - \frac{J_3^2}{J_2^3}\right) - b\left(\frac{J_3}{J_2^{3/2}}\right)\right]\exp\left[-\frac{c_{14}}{\theta}\right], \tag{7.9}$$

$$H(\theta) = [c_{15} - c_{16}\,\theta]\left[1 - c_{26}\left(\frac{4}{27} - \frac{J_3^2}{J_2^3}\right) - c_{27}\left(\frac{J_3}{J_2^{3/2}}\right)\right], \tag{7.10}$$

$$R_s(\theta) = c_{17} \exp\left[-\frac{c_{18}}{\theta}\right], \tag{7.11}$$

where J_2 and J_3 are the deviatoric stress invariants, and a and b are material parameters determined from different stress states. Similar formulations of the yield parameters exist, these use additional constants which cannot be derived experimentally. Therefore, it was decided that the extension to the von Mises formulation, adapted from equation (7.4), was more desirable. This further facilitates anisotropic developments based upon the quadratic Hill formulation which is also a von Mises extension (as described in section 7.2.1).

7.1.2 Constitutive implmentation

The asymmetric development described above has been implemented within the commercial LS-DYNA Explicit software and in-house development code DEST. A brief overview of the algorithmic structure concerning the constitutive developments is described within this section.

Step 1. Trial elastic assumptions

The multi-mode damage trial elastic assumption formulation remains unchanged from Chapter 6, as does the pressure formulation, they are merely included here for completeness.

$$\boldsymbol{\sigma}'^{\text{trial}}_{n+1} = \boldsymbol{\sigma}_n \left[\frac{\dot{D}_v}{1-D_v}\right]_n + 2\mu(1-D_v)_n(1-D_d)_n\, d_{n+1/2} + 3\lambda(1-D_v)_n \,\text{tr}\left[d_{n+1/2}\right]\boldsymbol{I} - p_{n+1}\boldsymbol{I}, \tag{7.12}$$

$$p_{n+1} = \frac{1}{3}\text{tr}\left[\boldsymbol{\sigma}_n^{trial}\right]\left[\frac{\dot{D}_v}{1-D_v}\right]_n + 3\lambda(1-D_v)_n \,\text{tr}\left[d_{n+1/2}\right]\Delta t. \tag{7.13}$$

The asymmetric development influences the trial state variables relating to deviatoric stress and the hardening and recovery function updates, which incorporate the stress state dependent developments described in equation sets (7.6) and (7.9).

$$\boldsymbol{\sigma'}_{n+1}^{\text{trial}} = \boldsymbol{\sigma}_n - p_{n+1}\boldsymbol{I}, \tag{7.14}$$

$$\boldsymbol{\alpha}_{n+1}^{\text{trial}} = \boldsymbol{\alpha}_n - \left[1 - \left(r_s + r_d\, \bar{d}_{n-1/2}\right) \bar{\alpha}\boldsymbol{\alpha}\, \Delta t\right], \tag{7.15}$$

$$\kappa_{n+1}^{\text{trial}} = \kappa_n - \left[1 - \left(R_s + R_d\, \bar{d}_{n-1/2}\right) \kappa^2\, \Delta t\right]. \tag{7.16}$$

This development, therefore, combines the multi-mode damage evolution together with an asymmetric description of yield described below.

Step 2. Elastic assumption evaluation

As described in Chapter 5, the elastic assumption is checked against the newly proposed yield function which features the asymmetric evolution depicted in Figure 7.1 and equation (7.4). This is given in an updated and discretised form below

$$\Phi_{n+1}^{\text{trial}} = \bar{\xi}_{n+1}^{\text{trial}} - \sqrt{\frac{2}{3}}\left[\kappa_{n+1}^{\text{trial}} + \beta_{n+1} - \eta\, p\left(\boldsymbol{\sigma}_{n+1}^{\text{trial}}\right) + \zeta\right]. \tag{7.17}$$

The influences of temperature and strain-rate dependency are retained from the previously implemented formulations in equation set (5.26).

Step 3. Visco-plastic multiplier

If yielding occurs, i.e. $\Phi^{\text{trial}} > 0$ from equation (7.17), the plastic multiplier increment is re-evaluated. The resulting visco-plastic multiplier increment is then used within equations (7.19), (7.20), (7.21)

$$\Delta\gamma_{n+1} = \frac{\Phi_{n+1}^{\text{trial}}}{(1-D_v)(1-D_d)2\mu + \frac{2}{3}(h+H)} \tag{7.18}$$

Step 4. Solution dependent variable correction

Due to the elliptical nature of the newly developed asymmetric yield surface the radial return method is assumed to be valid for the correction of the solution dependent variables, as the return vector is assumed to act in the direction of effective

stress, due to the relatively small asymmetry in titanium and other metallic alloys. The following relationships are applied if plastic yielding occurs

$$\boldsymbol{\sigma}'_{n+1} = \boldsymbol{\sigma}'^{\,\text{trial}}_{n+1} - 2\mu\Delta\gamma\mathbf{n}, \tag{7.19}$$

$$\boldsymbol{\alpha}_{n+1} = \boldsymbol{\alpha}^{\,\text{trial}}_{n+1} - h\Delta\gamma\mathbf{n}, \tag{7.20}$$

$$\kappa_{n+1} = \kappa^{\,\text{trial}}_{n+1} - H\sqrt{\tfrac{2}{3}}\Delta\gamma, \tag{7.21}$$

$$\mathbf{n}_{n+1} = \frac{\boldsymbol{\xi}}{\bar{\xi}}. \tag{7.22}$$

Step 5. Adiabatic thermal effects

The assumption remains, which states that 90% of plastic work done is dissipated through generation of heat. The effect of the variable θ influences the update of ISVs relating to yielding, hardening and recovery from equation sets (5.31) and (5.35)

$$\theta_{n+1} = \theta_n + \vartheta\frac{\Delta\gamma_{n+1}}{\bar{\xi}^{\text{trial}}_{n+1}}\left(\boldsymbol{\sigma}_n : \boldsymbol{\xi}^{\text{trial}}_{n+1}\right), \tag{7.23}$$

$$\vartheta = \left(\frac{0.9}{\rho C_v}\right), \tag{7.24}$$

where C_v is the specific heat material parameter for constant volume, and ρ is the material density.

7.1.3 Parameter identification

The friction angle and cohesive intercept can also be measured directly from experimental shear strength testing methods or via the following uni-axial tensile and compressive failure strength (σ_f^c, σ_f^t) relationships [56, 161]:

$$\varphi = \sin^{-1}\left(\frac{\sigma_f^c - \sigma_f^t}{\sigma_f^c + \sigma_f^t}\right), \tag{7.25}$$

$$c = \left(\frac{\sigma_f^c \sigma_f^t}{\sigma_f^c - \sigma_f^t} \right) \tan(\varphi), \tag{7.26}$$

where σ_f^c and σ_f^t represent the compressive and tensile yield strength of a material. Various other approach also exist to define the Drucker-Prager parameters. Alternatively, the BCJ-fitting [148] tool can be used to establish the hardening, recovery and asymmetry parameters within the constitutive framework described.

7.2 Anisotropic developments

It has been well established that crystalline and polycrystalline industrial alloys are intrinsically anisotropic as a result of texture evolution developed during manufacturing and forming processes [162, 122, 51]. The macroscopically observable anisotropic mechanical behaviour is due to directional dependencies of the elasticity tensor within HCP polycrystalline structures. Micro-mechanisms such as dislocations, twin formations and martensitic transformations contribute towards the macroscopic directional dependent deformation mechanisms such as yield strength, ductility, strain hardening, damage evolution and various thermal effects. Explicitly simulating the aforementioned micro-mechanical effects is beyond the scope of this research project. The current research provides an adaptable framework on the macroscopic scale which accounts for these phenomena.

Other investigators [131, 132, 133] have also combined anisotropy with mixed non-linear kinematic and isotropic hardening variables within the non-associated flow rule context. One drawback the non-associated flow rule has is the inability to maintain the temperature and strain-rate dependencies formulations already established in the yield function. Therefore, developments within this research shall surround the associated flow rule due to the simplicities of the quadratic Hill solution and given the complexities of the existing model. Moreover, due to the highly non-linear deformation considered during this research, maintaining the accuracy of the plastic strain has been prioritised over the simplification of initial yielding calibration against uni-axial

data.

Simulation of anisotropic effects has been highlighted as key to describe the deformation behaviour of industrial Ti-6Al-4V. The ISV framework provides the ability to incorporate phenomena over a wide range of length-scales whilst remaining computationally efficient. Solutions which consider physics-based material deformation phenomena are becoming an increasing necessity for highly specialised applications and bespoke material solutions.

7.2.1 Constitutive equations

Anisotropic developments have been implemented within the newly proposed constitutive framework described in Chapter 5 and Chapter 6. The following describes the constitutive equations and the numerical implementation required to enhance the solution beyond isotropic approximations.

To reiterate, tensor variables are represented in **boldface**. The yield function Φ combines an extended variation of J_2 plasticity with isotropic and kinematic hardening, strength differential effects, temperature and multiple damage modes, together with an associated quadratic Hill anisotropic yield criterion. The resulting yield function can be assumed to be in the following form:

$$\Phi(\boldsymbol{\sigma}', \boldsymbol{\alpha}, \boldsymbol{d}, \theta, D_v, D_d) = \bar{\xi} + \eta p(\boldsymbol{\sigma}) - \zeta - \kappa - \beta = 0. \tag{7.27}$$

As previously stated, $\boldsymbol{\xi}$ is represented as the difference between the deviatoric Cauchy stress tensor $\boldsymbol{\sigma}'$ and back stress tensor $\boldsymbol{\alpha}$ in equation (7.28)

$$\boldsymbol{\xi} = \boldsymbol{\sigma}' - \frac{2}{3}\boldsymbol{\alpha}. \tag{7.28}$$

Isotropic hardening is, again, denoted as the scalar variable κ and the yield surface threshold parameter denoted as β. The development of plastic anisotropy in the flow rule is introduced in the form of the Hill parameters F, G, H and L, M, N . The effective stress tensor $\boldsymbol{\xi}$ defines the size and shape of the six-dimensional stress-state

and the location of the centre of the yield surface to form an anisotropic yield surface with kinematic hardening. To achieve this, $\boldsymbol{\xi}$ in equation (7.28) is combined with the $\mathbf{P}$ matrix, as shown in equation (7.30), this introduces anisotropic evolution as follows

$$\mathbf{P} = \left(\frac{2}{3}\right) \begin{bmatrix} \text{H+G} & \text{-H} & \text{-G} & 0 & 0 & 0 \\ & \text{H+F} & \text{-F} & 0 & 0 & 0 \\ & & \text{F+G} & 0 & 0 & 0 \\ & & & \text{2N} & 0 & 0 \\ & \text{Sym.} & & & \text{2M} & 0 \\ & & & & & \text{2L} \end{bmatrix} \tag{7.29}$$

$$\bar{\xi} = \sqrt{\tfrac{3}{2}\boldsymbol{\xi}^T : \mathbf{P} : \boldsymbol{\xi}}. \tag{7.30}$$

The isotropic von Mises yield surface is recovered when the Hill parameters are F=G=H=0.5 and N=M=L=3F.

7.2.2 Consitutive implementation

The constitutive equations have been implemented into commercial LS-DYNA Explicit software as an extension of the proposed user-defined material model, described in Chapter 6.

Step 1. Trial elastic assumptions

Adoption of the quadratic formulation of Hill's anisotropy allows for the Cauchy trial stress tensor $\boldsymbol{\sigma}_{n+1}^{\text{trial}}$ to remain unchanged in the following form as developed in Chapter 6.

$$\boldsymbol{\sigma}_{n+1}^{\text{trial}} = \boldsymbol{\sigma}_n \left[\frac{\dot{D}_v}{1-D_v}\right]_n + 2\mu(1-D_v)_n(1-D_d)_n\, d_{n+1/2} + 3\lambda(1-D_v)_n \,\text{tr}\left[d_{n+1/2}\right]\boldsymbol{I} - p_{n+1}\boldsymbol{I}, \tag{7.31}$$

the pressure formulation also remains unchanged from Chapter 5 as follows,

$$p_{n+1} = \frac{1}{3}\text{tr}\left[\boldsymbol{\sigma}_n^{trial}\right]\left[\frac{\dot{D}_v}{1-D_v}\right]_n + 3\lambda(1-D_v)_n \,\text{tr}\left[d_{n+1/2}\right]\Delta t. \tag{7.32}$$

Step 2. Elastic assumption evaluation

The elastic assumption is now checked against the new yield function (7.33) by substituting (7.30) into the previously developed asymmetric yield function (7.4). Once again, if $\Phi^{\text{trial}} \leq 0$ then the elastic assumption is correct for $n+1$. However, if $\Phi^{\text{trial}} > 0$ then plastic deformation has occurred and the following solution dependent variables require correction.

$$\Phi_{n+1}^{\text{trial}} = \bar{\xi}_{n+1}^{\text{trial}} - \sqrt{\frac{2}{3}}\left[\kappa_{n+1}^{\text{trial}} + \beta_{n+1} - \eta\, p\,\left(\boldsymbol{\sigma}_{n+1}^{\text{trial}}\right) + \zeta\right]. \tag{7.33}$$

Step 3. Visco-plastic multiplier

The new visco-plastic multiplier function includes the new yield function (7.33), which informs the update of the solution dependent variables (7.36), (7.37) and (7.38).

$$\Delta\gamma_{n+1} = \frac{\Phi_{n+1}^{\text{trial}}}{(1-D_v)(1-D_d)2\mu + \frac{2}{3}(h+H)} \tag{7.34}$$

Step 4. Solution dependent variable correction

The newly formulated anisotropic unit vector incorporates Hill's parameters via the $\mathbf{P}$ matrix in equation (7.29), as shown below

$$\mathbf{n}_{n+1} = \frac{1}{\bar{\xi}_{n+1}}\mathbf{P}\boldsymbol{\xi}_{n+1}. \tag{7.35}$$

Plasticity is assumed constant over the time-step to maintain equilibrium, the radial return ($\mathbf{n}$) is assumed in alignment with the direction of the effective stress. The following hardening parameters include the new unit vector (7.35) and plastic multiplier (7.34).

$$\boldsymbol{\sigma}'_{n+1} = \boldsymbol{\sigma}'^{\,\text{trial}}_{n+1} - 2\mu\Delta\gamma\mathbf{n} \tag{7.36}$$

$$\boldsymbol{\alpha}_{n+1} = \boldsymbol{\alpha}^{\,\text{trial}}_{n+1} - h\Delta\gamma\mathbf{n} \tag{7.37}$$

$$\kappa_{n+1} = \kappa^{\,\text{trial}}_{n+1} - H\sqrt{\tfrac{2}{3}}\Delta\gamma \tag{7.38}$$

Step 5. Adiabatic thermal effects

The assumption remains which states that 90% of plastic work done is dissipated through generation of heat. The effect of temperature variable θ influences the update of ISV's relating to yield (5.26), hardening and recovery from equation sets (5.31) and (5.35)

$$\theta_{n+1} = \theta_n + \vartheta\,\frac{\Delta\gamma_{n+1}}{\bar{\xi}^{\text{trial}}_{n+1}}\left(\boldsymbol{\sigma}_n : \boldsymbol{\xi}^{\text{trial}}_{n+1}\right), \tag{7.39}$$

$$\vartheta = \left(\frac{0.9}{\rho C_v}\right), \tag{7.40}$$

where C_v is the specific heat material parameter for constant volume and ρ is the material density.

7.2.3 Parameter identification

The yield surfaces presented in Figures 7.10 - 7.13 apply arbitrary parameters to demonstrate the capabilities of the algorithm. The quadratic Hill (1948) parameters can be solved via the stress-based or r-ratio approaches. Examples of these can be found throughout the literature [163, 164, 165]. The process described during this section uses a combination of both

$$\mathrm{F} = \frac{1}{2}\left(\frac{1}{R_{22}^2} + \frac{1}{R_{33}^2} - \frac{1}{R_{11}^2}\right), \tag{7.41}$$

$$\mathrm{G} = \frac{1}{2}\left(\frac{1}{R_{33}^2} + \frac{1}{R_{11}^2} - \frac{1}{R_{22}^2}\right), \tag{7.42}$$

$$\mathrm{H} = \frac{1}{2}\left(\frac{1}{R_{11}^2} + \frac{1}{R_{22}^2} - \frac{1}{R_{33}^2}\right), \tag{7.43}$$

$$\mathrm{L} = \frac{3}{2\,R_{23}^2}, \tag{7.44}$$

$$\mathrm{M} = \frac{3}{2\,R_{31}^2}, \tag{7.45}$$

$$\mathrm{N} = \frac{3}{2\,R_{12}^2}, \tag{7.46}$$

the values of R_{ij} are stress ratios relating to the corresponding axial and co-axial directions. The yield stress ratios can be determined from the following plastic strain ratio relationships

$$R_{22} = \sqrt{\frac{r_{90}(r_0+1)}{r_0(r_{90}+1)}}, \tag{7.47}$$

$$R_{33} = \sqrt{\frac{r_{90}(r_0+1)}{(r_0+r_{90})}}, \tag{7.48}$$

$$R_{12} = \sqrt{\frac{3(r_0+1)r_{90}}{(2r_{45}+1)(r_0+r_{90})}}, \tag{7.49}$$

where $R_{11} = 1$ is assumed and for convenience $R_{11} = R_{13} = R_{23} = 1$ are also commonly assumed. The associated r_0, r_{90} and r_{45} values can be calculated using the Lankford coefficient [166] as follows

$$r = \frac{\varepsilon^{\alpha}}{\varepsilon^{\beta}} = \frac{\ln(r_f^{\alpha}/r_0)}{\ln(r_f{}^{\beta}/r_0)}, \tag{7.50}$$

where, r_f^{α} and r_f^{β} correspond to the major and minor radii of the failed specimen, r_0 represents the initially measured specimen radii which is assumed to be circular. An illustration of this technique is presented in Figure 7.2.

Alternatively, Yan et al. [167] proposed an inverse method for calibration of the yield parameters. This technique and similar can be used in conjunction with larger numbers of material parameters.

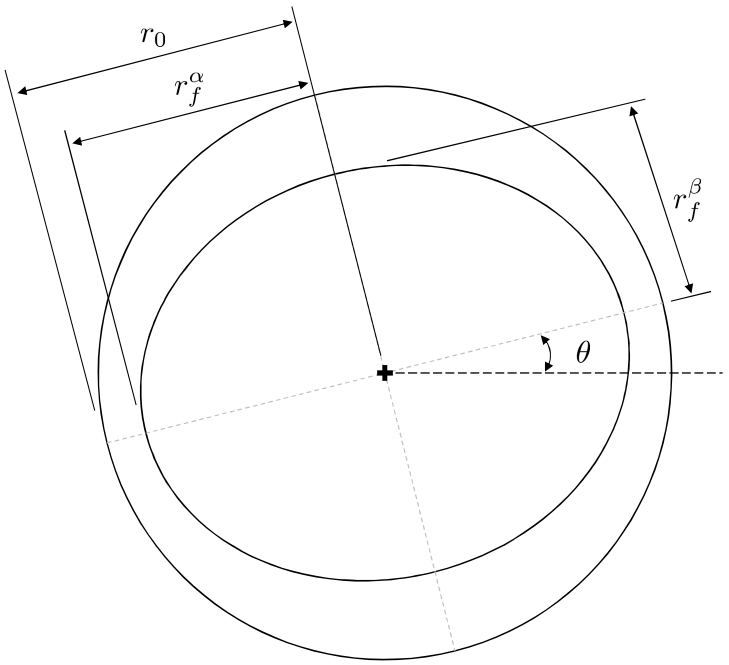


Figure 7.2: Original circular and elliptical failure profile of a specimen with Lankford parameters.

7.3 Asymmetric validation

The SD effect has been observed in metallic systems including carbon steels, titanium, aluminium, magnesium and nickel-based super alloys [168, 159]. It is therefore necessary plot the yield surface effects. Titanium alloys show minimal SD effects when compared with other alloys [114] unless highly textured.

7.3.1 Asymmetric yield surface

For the purposes of demonstrating the ability of the constitutive model to predict SD effects, the observable yield point was estimated in Figure 7.5, from uniaxial tension and compression data at high strain-rates and room temperature. The strength-differential or pressure-dependent parameters are demonstrated in Figures 7.3 and 7.4. Whilst the strength differential effects may remain small in titanium alloys, evidence has shown that it remains a capability which is required. Beyond the scope of titanium alloys, the ability to simulate SD, or pressure dependent, behaviour remains important for other alloy systems.

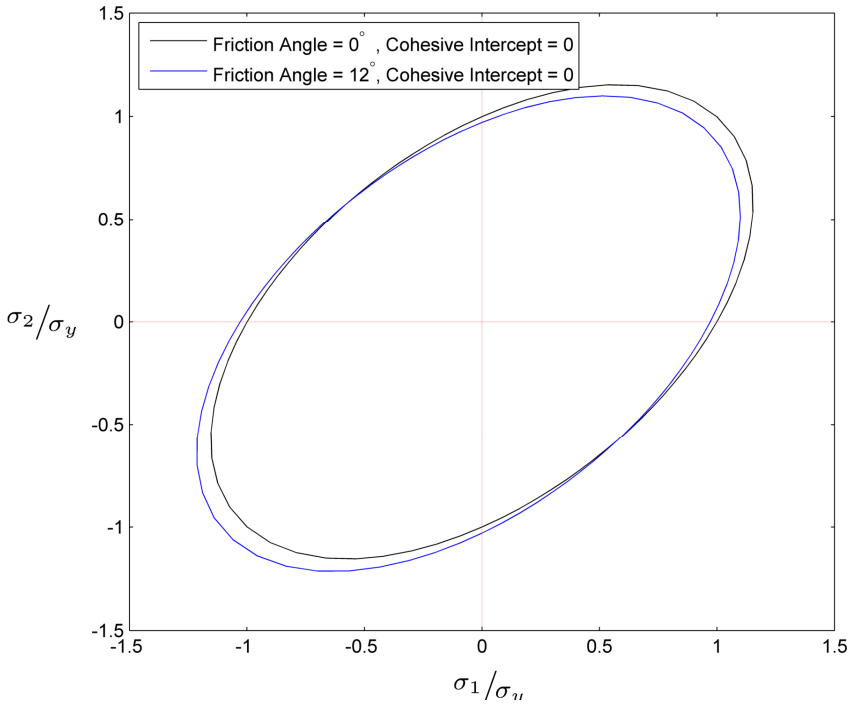


Figure 7.3: Normalised influence of the Drucker-Prager friction angle φ on the initial yield surface in principal stress space.

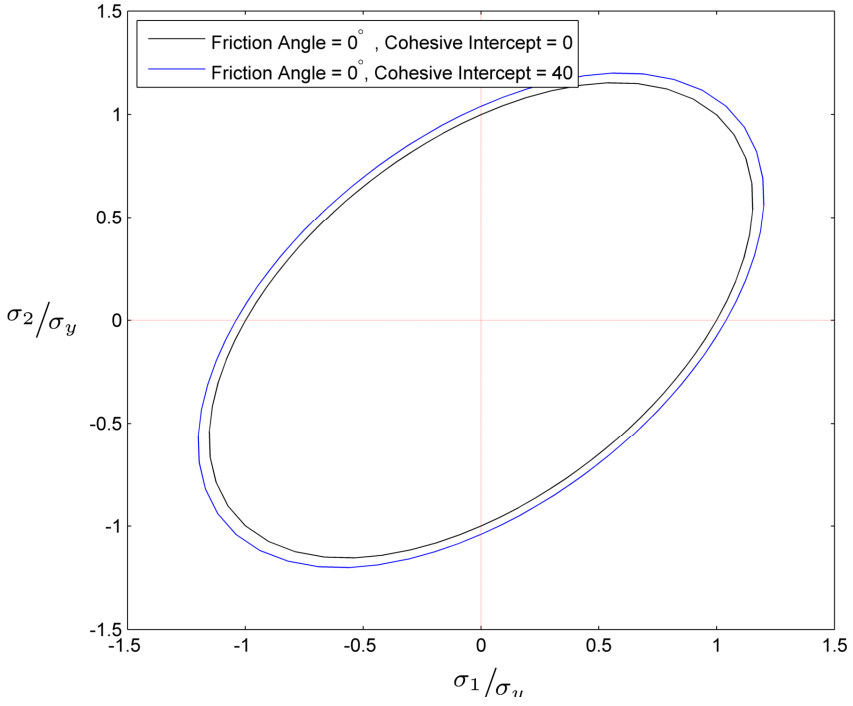


Figure 7.4: Normalised influence of the Drucker-Prager cohesive intercept c on the initial yield surface in principal stress space.

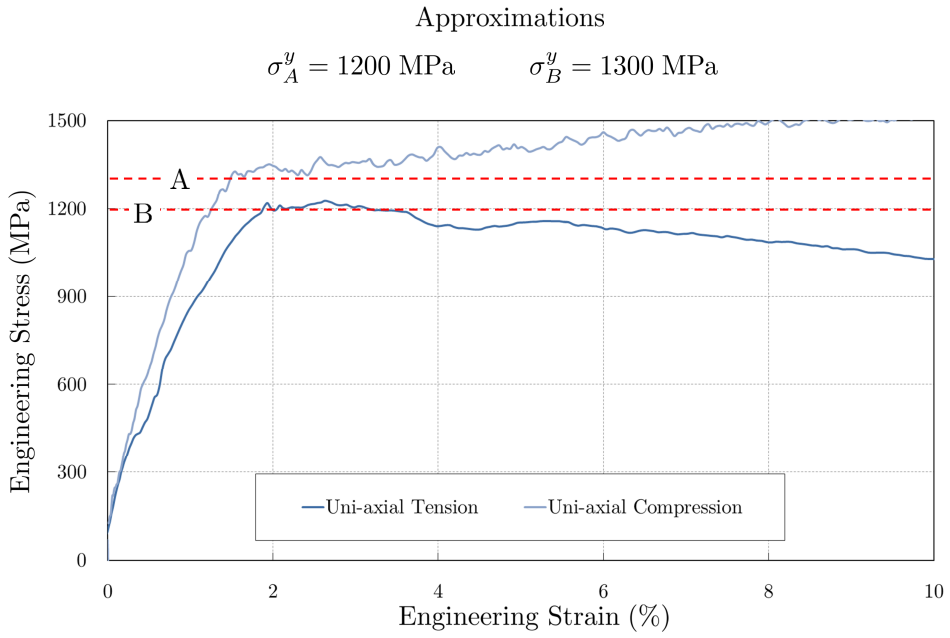


Figure 7.5: Experimentally obtained SD effect of absolute uni-axial tension and compression data for Ti-6Al-4V at high strain-rates.

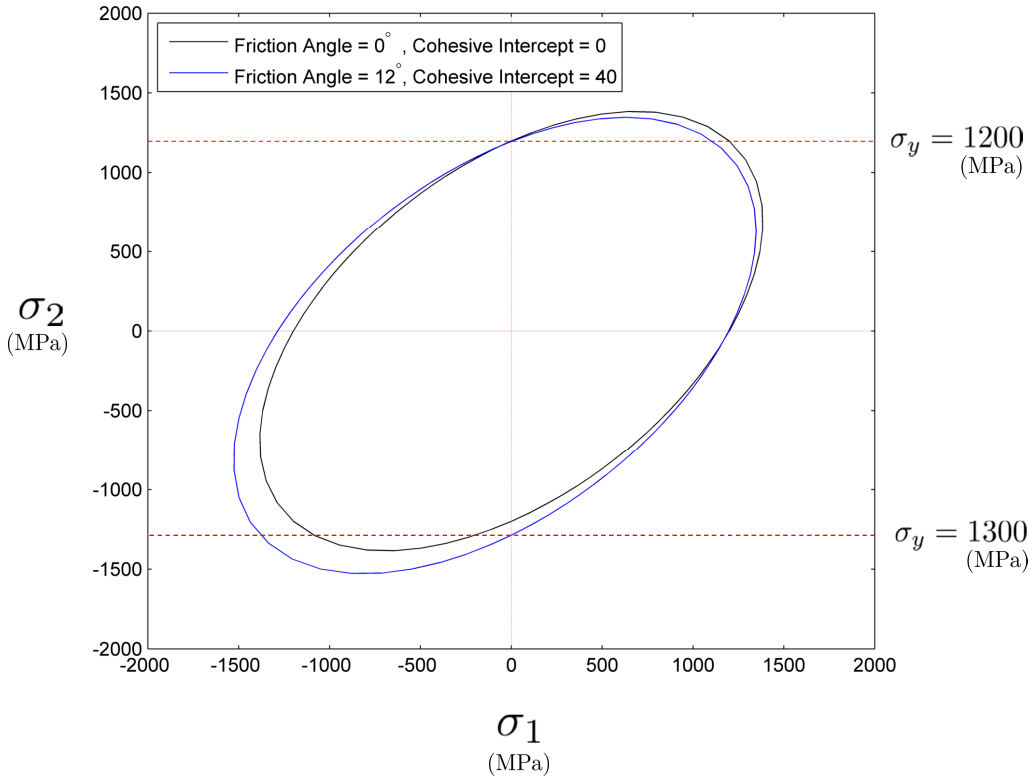


Figure 7.6: Strength Differential (SD) capabilities for initial yield strength in two-dimensional principal stress space for Ti-6Al-4V at high strain-rates.

It should be noted that the quantifiable magnitude of the observed SD effect may be influenced by yield point estimation, phase changes during deformation at high temperatures, thermal contractions in the candidate material, Bauschinger effects during cyclic loading and residual stress (macro- and micro-scale) as a consequence of thermo-mechanical manufacturing routes. Combinations of all of these factors may influence definition of the observable magnitude. For illustration purposes, 100 MPa was assumed, this is reflected in Figures 7.5 and 7.6.

7.4 Anisotropic validation

Experimental data obtained during Chapter 4 and data within the literature have identified an anisotropic requirement for titanium alloys. The ISV approach has been demonstrated as an appropriate method for the numerical development of plastic anisotropy. The implementation of one such approach within the newly proposed constitutive framework described within Chapter 5 and Chapter 6 has been completed within this chapter. The capability of the developments are demonstrated in an idealised case for an initial yield surface, based upon experimentally obtain data. Deviation from the isotropic strength in one or more anisotropic directions is depicted on the σ_1 - σ_2 plane in the form of yield surface evolution. The boundaries of this algorithm were also established to be within those required for ductile metallic systems. Finally, a method describing the identification of the Hill parameters (F, G, H, L, M ,N) from simple tension tests in three orientations has been proposed.

As discussed in Chapter 4, an anisotropic trend exists in the flow stress response of materials loaded in axial and tangential orientations. The yield strength during axial testing, in general, exceeds that of the tangential specimens. In addition, the strain to failure of the tangential experiments exceeds the axial equivalent experiments. The magnitude of these characteristics is marginal in the Ti-6Al-4V alloy under investigation. This trend is also difficult to define accurately at high strain-rates. However, the ability of the algorithm and parameter identification technique can be demonstrated

practically from available data.

7.4.1 Anisotropic yield surfaces

Visualisation of full anisotropic six-dimensional hypersurface is a challenge. For our purposes, two-dimensional projections are created by fixing the remaining dimensions.

The isolated influence of Hill's anisotropic parameters F, G, and H have been demonstrated in Figure 7.7, Figure 7.8 and Figure 7.9, respectively. These have been produced in accordance with the yield criteria established in equation (7.33) and normalised against tensile yield σ_y which is assumed to be axial yield from Figure 4.24. If we consider the three normal principal stresses aligned with directions of anisotropy, we can demonstrate the relationship between parameters F, G, and H, and their effect on a normalised yield surface on the $\sigma_1 - \sigma_2$ plane. Here $\sigma_1 = \sigma_{xx}$, $\sigma_2 = \sigma_{yy}$ and $\sigma_3 = \sigma_{zz}$, and $\sigma_y = \sigma_1$ which is the yield stress in the tensile axial orientation.

Figure 7.10 compares the variation of σ_2 yield strength on the $\sigma_1 - \sigma_2$ plane against the isotropic yield surface C, where F = G = H = 0.5. Yield surfaces A and B demon-

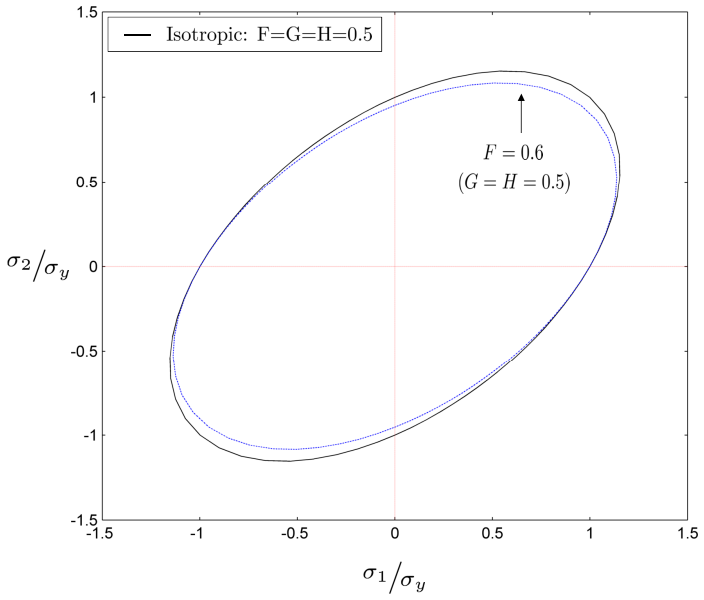


Figure 7.7: Normalised yield locus evolution of anisotropic Hill parameter F, in isolation.

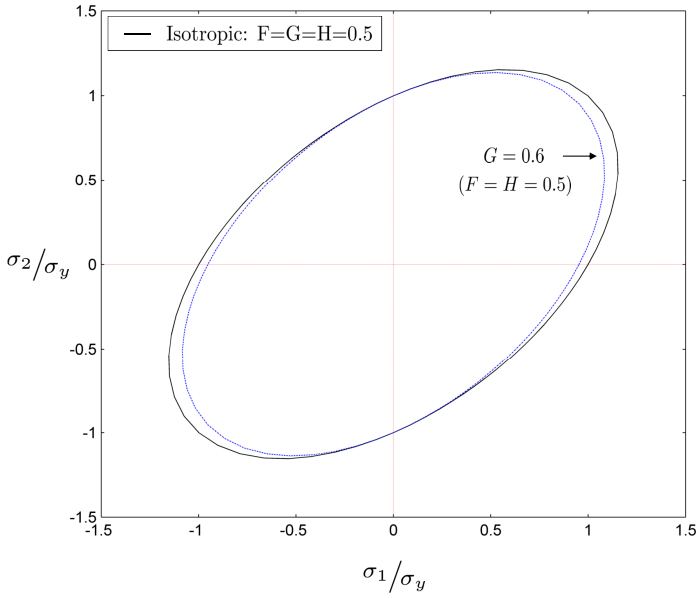


Figure 7.8: Normalised yield locus evolution of anisotropic Hill parameter G, in isolation.

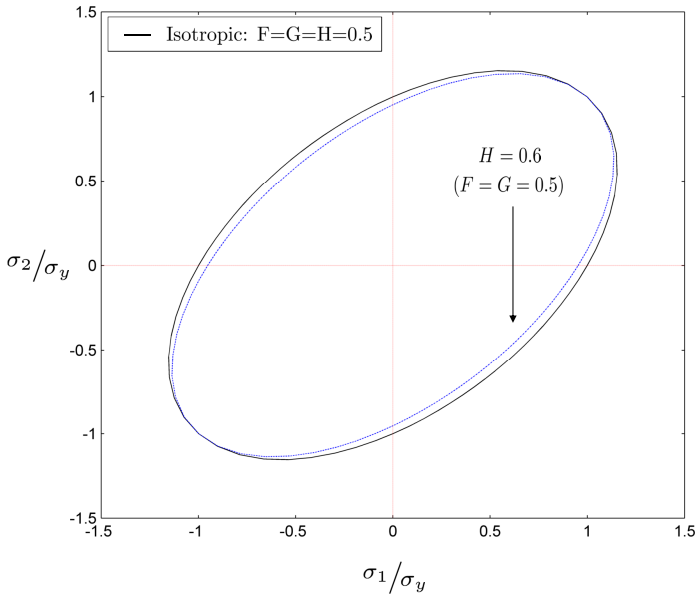


Figure 7.9: Normalised yield locus evolution of anisotropic Hill parameter H, in isolation.

strate an increased σ_2 yield whilst maintaining isotropic yield in the σ_1 and σ_3 directions when $\sigma_2 = 0$ and $\sigma_1 = \sigma_2$ conditions are valid, respectively. When $\sigma_2 \neq 0$ and $\sigma_1 \neq \sigma_2$ and as σ_2 decreases, the ellipsoidal yield surface is accompanied by a corresponding radial expansion in the σ_1 component. This expansion becomes unbounded, shown in yield surface E, at certain point which indicates that the quadratic Hill formulation can only be used within certain limits.

To maintain isotropic conditions when $\sigma_2 = 0$ and $\sigma_1 = \sigma_2$ the associated Hill parameters have to satisfy and accumulated unity condition. The linear relationship between the opposing parameters can be seen in Figure 7.11. The influence of the σ_3 component is also displayed on the $\sigma_1 - \sigma_2$ plane in Figure 7.12. As the influences of the σ_3 yield in reduced the yield surface experiences biaxial compression until the solution becomes unbounded as the yield surface expands in the pure shear direction ($\sigma_1 = -\sigma_2$). The parallel lines in Figure 7.10 and Figure 7.12 represent an unbounded yield surface. This occurs if the yield strength in one direction is double that of an opposing normal direction , i.e. tension versus compression. This is highly unlikely to happen in ductile metallic materials, but should be noted. A linear relationship between opposing Hill parameters observed in Figure 7.11 are similarly observed for transversal direct stress variation in Figure 7.12. The parameter F varies with the G, in opposition to H.

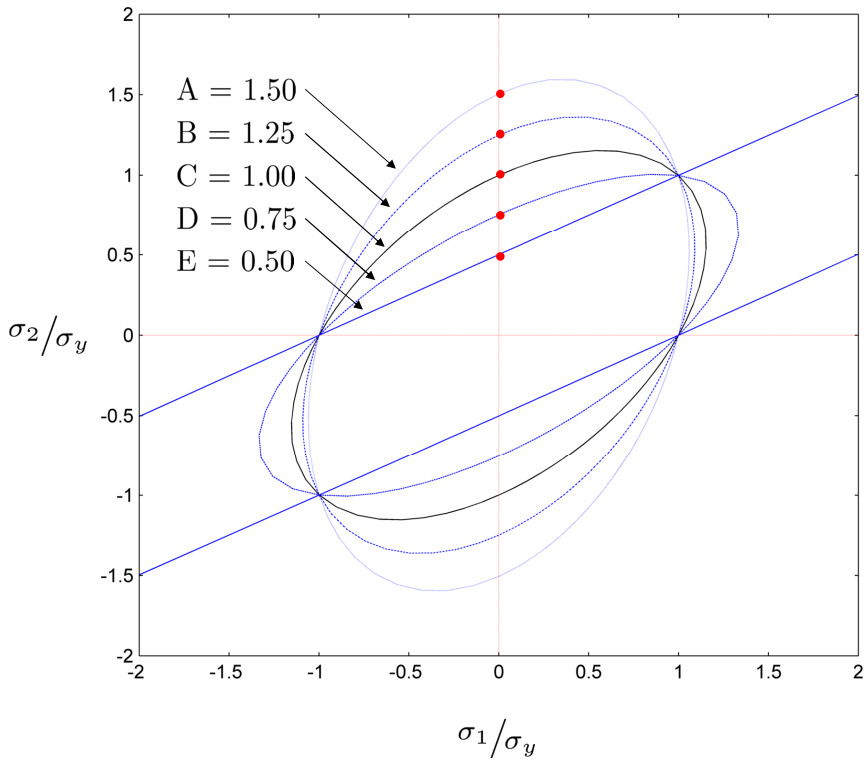


Figure 7.10: Hill yield surface due to variation of the orthotropic direct stress σ_2.

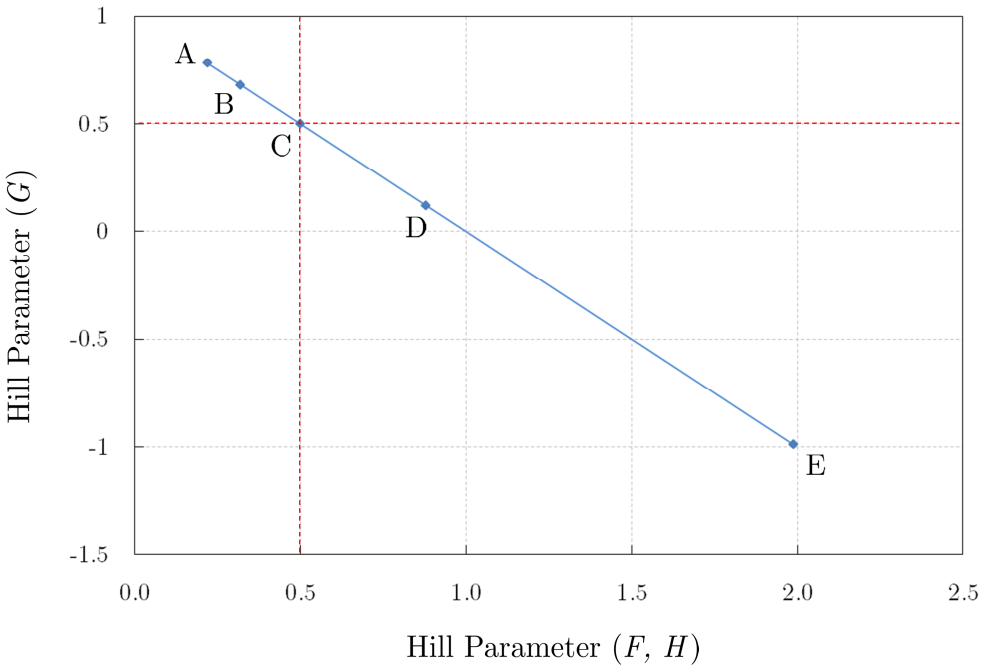


Figure 7.11: Parameter variation relationship for isolated direct stress evolution.

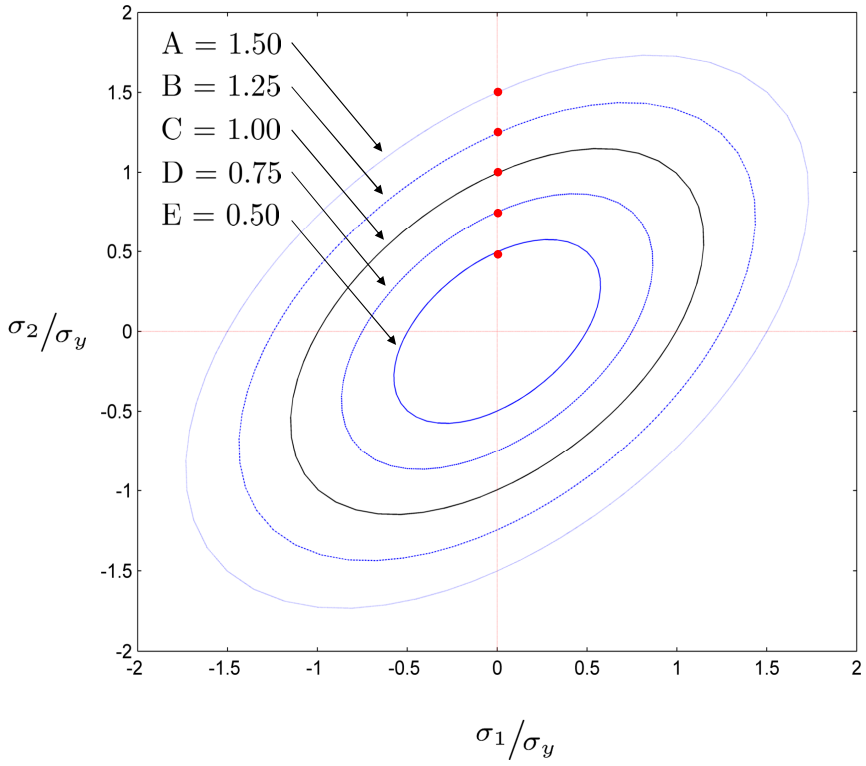


Figure 7.13: Effect of shear stress on the Hill yield surface.

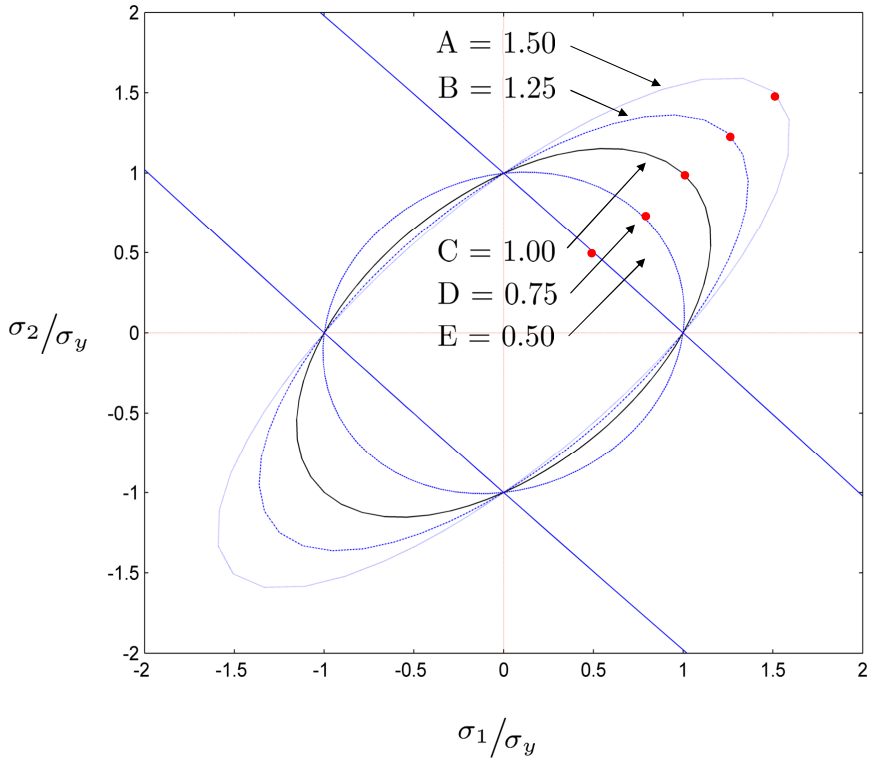


Figure 7.12: Hill yield surface due to variation of the orthotropic transversal stress σ_3.

There has been no influence of shear stresses in Figures 7.10 and 7.12. As shear stress increases an isotropic reduction of the yield surface is observed, as shown in Figure 7.13. To achieve an isotropic increase of reduction of the yield surface the anisotropic Hill parameters are related as follows: F = G = H.

7.4.2 Anisotropic evolution

As discussed in Chapter 4, an anisotropic trend exists in the flow stress response of materials loaded in axial and tangential orientations. The yield strength during axial testing, in general, exceeds that of the tangential specimens. In addition, the strain to failure of the tangential experiments exceeds the axial equivalent experiments. The magnitude of these characteristics is marginal in the Ti-6Al-4V alloy under investigation. This trend is difficult to define accurately at high strain-rates. However, the ability of the algorithm and parameter identification technique can be

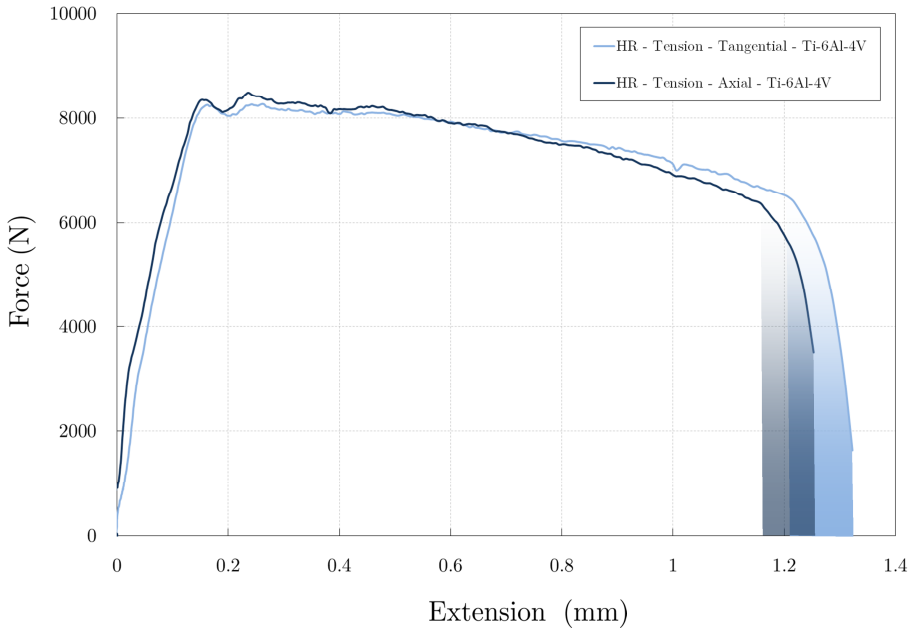


Figure 7.14: Load-Extension plots of selected axially and tangentially loaded experimental tension specimens at high strain-rates.

demonstrated practically from available data.

For post-processing purposes the results found in Figure 4.24 have been converted to load-displacement, as shown in Figure 7.14.

To demonstrate the ability of the constitutive model both isotropically and anisotropically, the above data set is used as a reference. The axial data is assumed to be numerically isotropic ($F = G = H = 0.5$) to isolate the influence of the anisotropic material parameters. The shaded regions in Figure 7.14 represent the experimental envelope of failure for numerical purposes, as failure occurs rapidly.

Firstly, post-processing of data available from the tangential tensile experiment chosen in Figure 7.14 was conducted for benchmarking purposes. Strain accumulation and localisation at the surface and centre of the specimen necked region can be seen in Figure 7.15. This was achieved by a speckling technique and Digital Image Correlation (DIC) in commercial software - ARAMIS. Several data points were evaluated in the necked region to estimate the area reduction during deformation. In Figure 7.16 two

parallel lines are illustrated from which the resultant reduction in area was calculated, as shown in Figure 7.17, combined with the corresponding engineering strain.

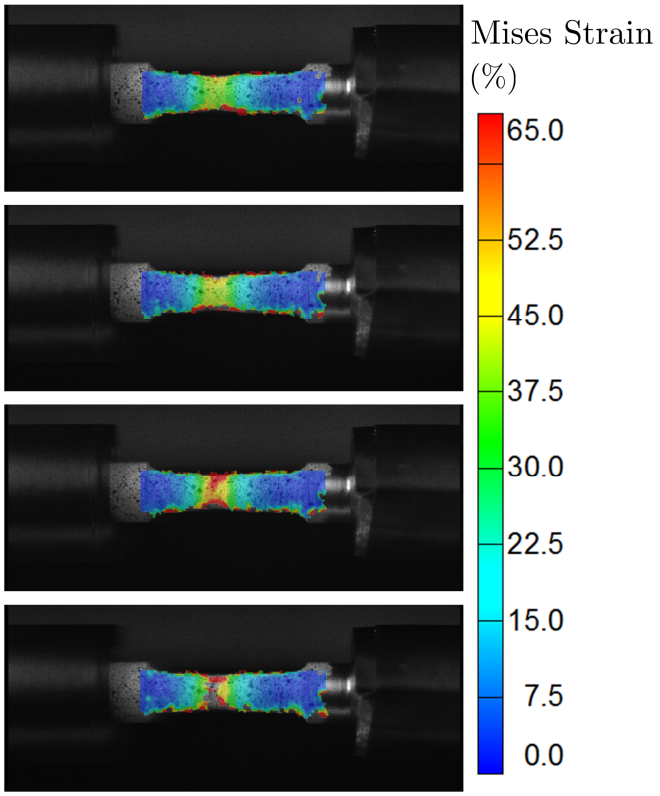


Figure 7.15: Selected frames during high strain-rate deformation of tangential tension experiments, evaluated using DIC.

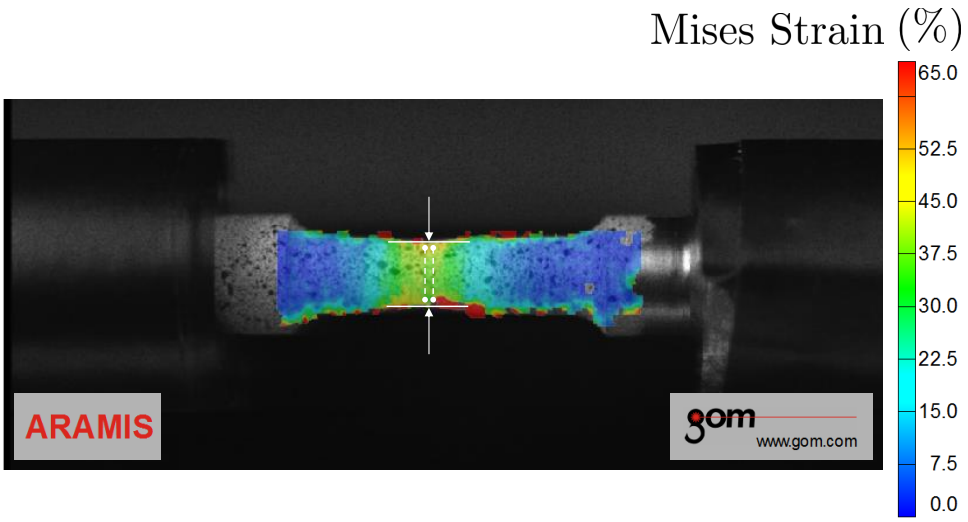


Figure 7.16: Area reduction measurement in a one-dimension based upon DIC particle tracking.

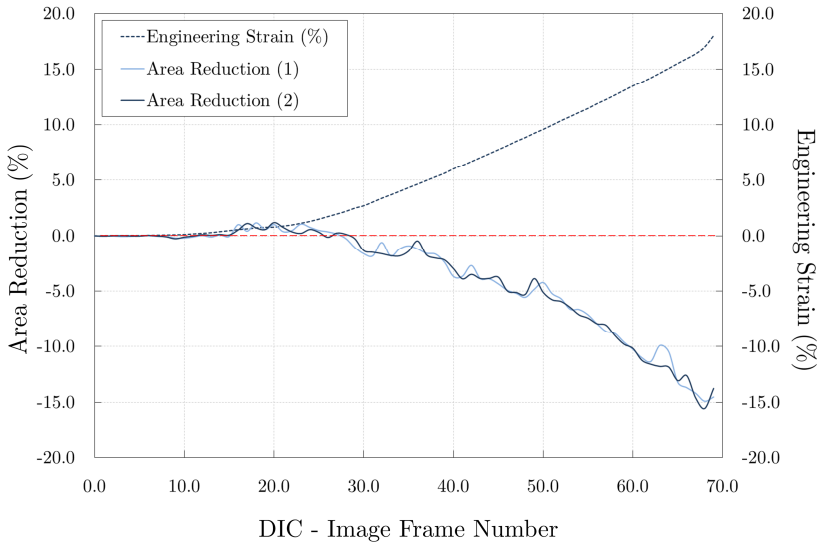


Figure 7.17: Evolution of the reduction of area and engineering strain during deformation via. Digital Image Correlation.

At failure the area of reduction calculated was $\sim 15\%$. This allows for the estimation of the Lankford parameter r_f^{α}, which in this case represents the minor radii based upon the anisotropic affect discussed later in this section. To assess the effect of the opposing r_f^{β} Lankford parameter - and in the absence of multiple DIC camera angles data - multiple simulations were conducted to determine the likely major radii. The resultant r_f^{β} parameter is illustrated in Figure 7.18.

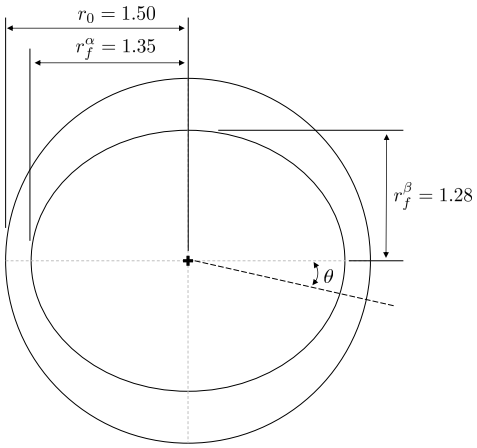


Figure 7.18: Lankford parameters estimation based upon a numerical and experimental approach.

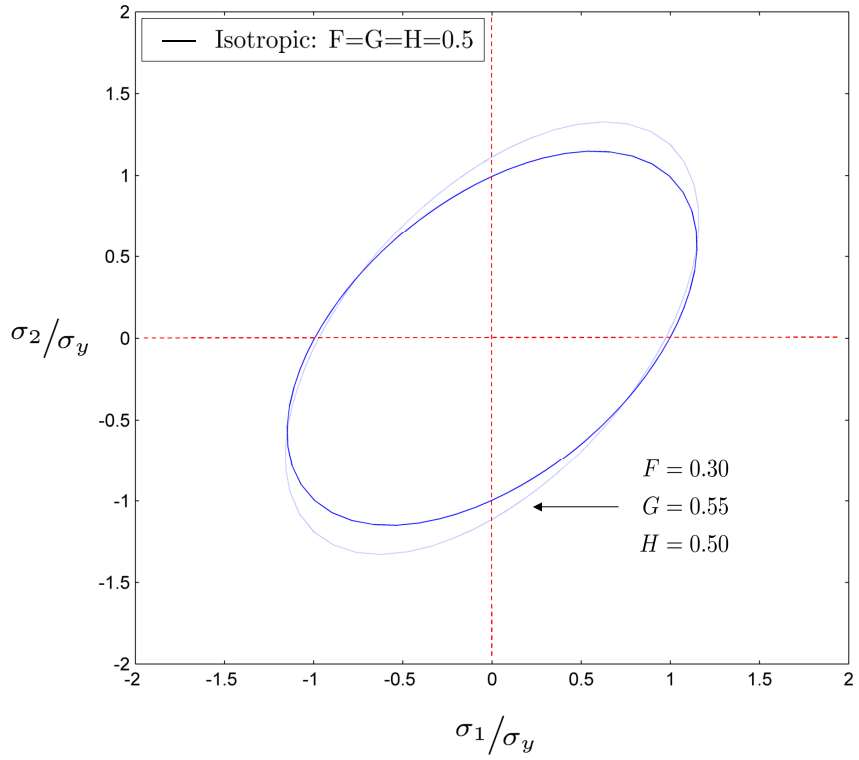


Figure 7.19: Resultant yield surface of high strain-rate Ti-6Al-4V in the tangential direction.

For further alloy characterisation, accurate measurements of the major r_f^{α} and minor r_f^{β} radii are required at failure and ideally during deformation. This would require both physical measurements and DIC techniques to asses the anisotropic behaviour from multiple orientations simultaneously [169]. In addition, further experiments are required to better quantify the yield point and failure strain trends. The resulting Lankford parameters used to obtain the anisotropic behaviour in Figure 7.20 are shown in Figure 7.19. Verification of the yield surface based upon multi-axial experimental data was unavailable; however, the normalised yield surface highlights the importance of representing materials and components as non-isotropic, and as a consequence of processing routes.

Validation of the parameter identification process and the anisotropic developments based upon high strain-rate deformation have been demonstrated in Figure 7.20. Modification of the anisotropic parameters enables a similar trend to be estab-

lished numerically. As discussed, the axial case is treated as isotropic. The anisotropic yield strength, flow stress and strain to failure - within the established envelopes - are replicated numerically. Figures 7.21 and 7.22 compare the experimentally obtained results in Figure 7.14 with the numerically obtained results in Figure 7.20. The yield stress, flow stress and strain to failure for the anisotropic (tangential) data have been successfully replicated. The simulated results fail within the shaded envelope defined by the experimental results. The yield strengths and the associated trend established in section 4.1.3 are also maintained numerically. This trend is characterised by a reduced yield stress and increased failure stress, as expected.

The model used to establish the results found in Figure 7.21 and Figure 7.22 incorporates the developments described in Chapters 5, 6 and 7. The oscillations are attributed to the post-processing method at the specimen boundary conditions and the effect of spurious wave reflections at the free end. Overall, there appears to be good agreement between the experimental results obtained in Chapter 4 and numerical approximations.

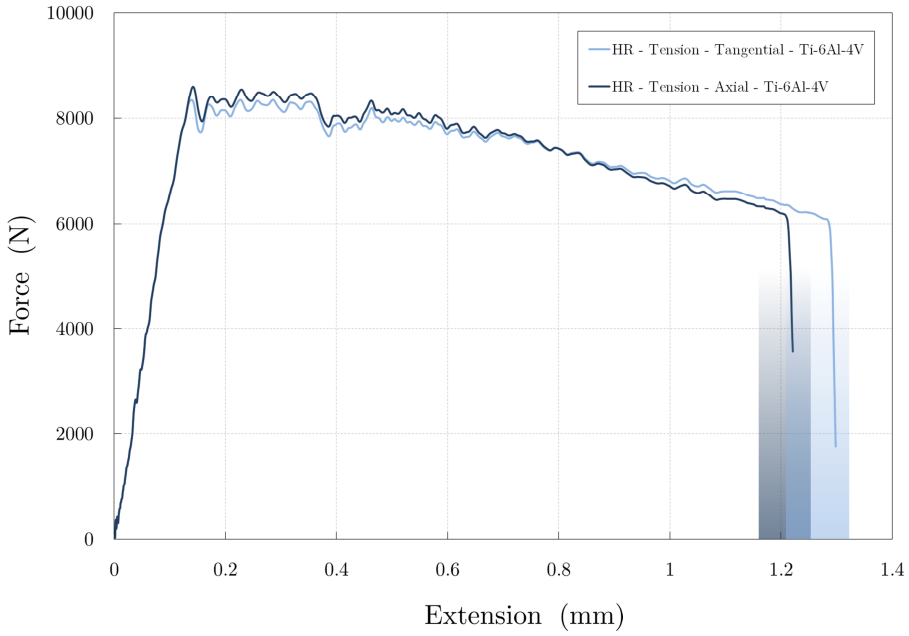


Figure 7.20: Numerical approximation of high strain-rate axial and tangential tensile experiments.

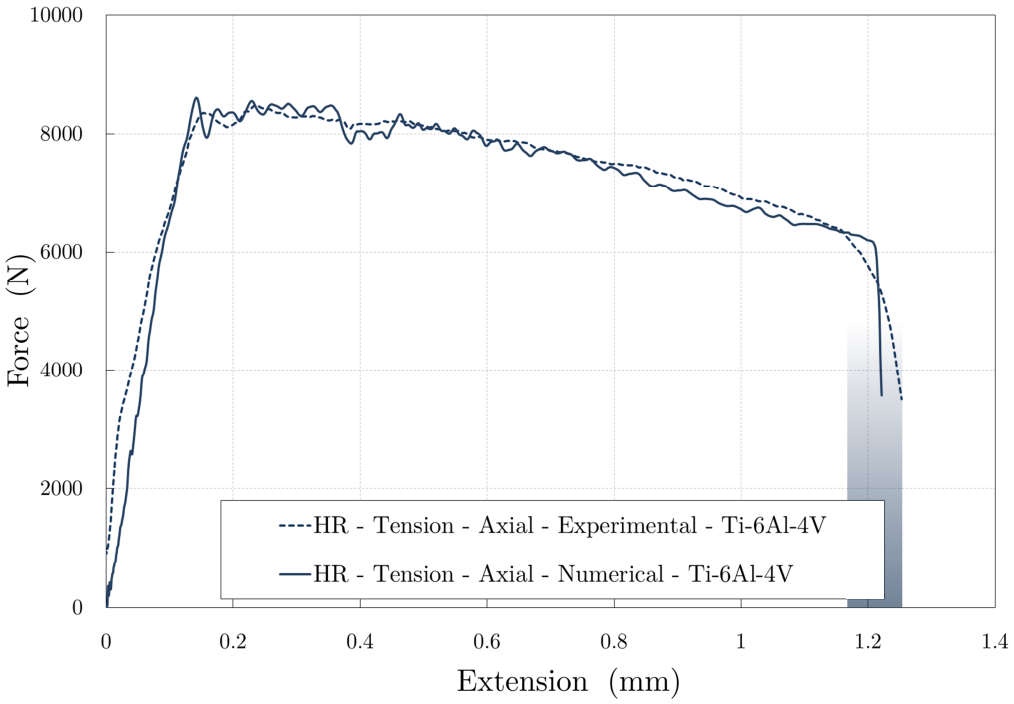


Figure 7.21: Numerical approximation of high strain-rate axial orientation tensile experiments.

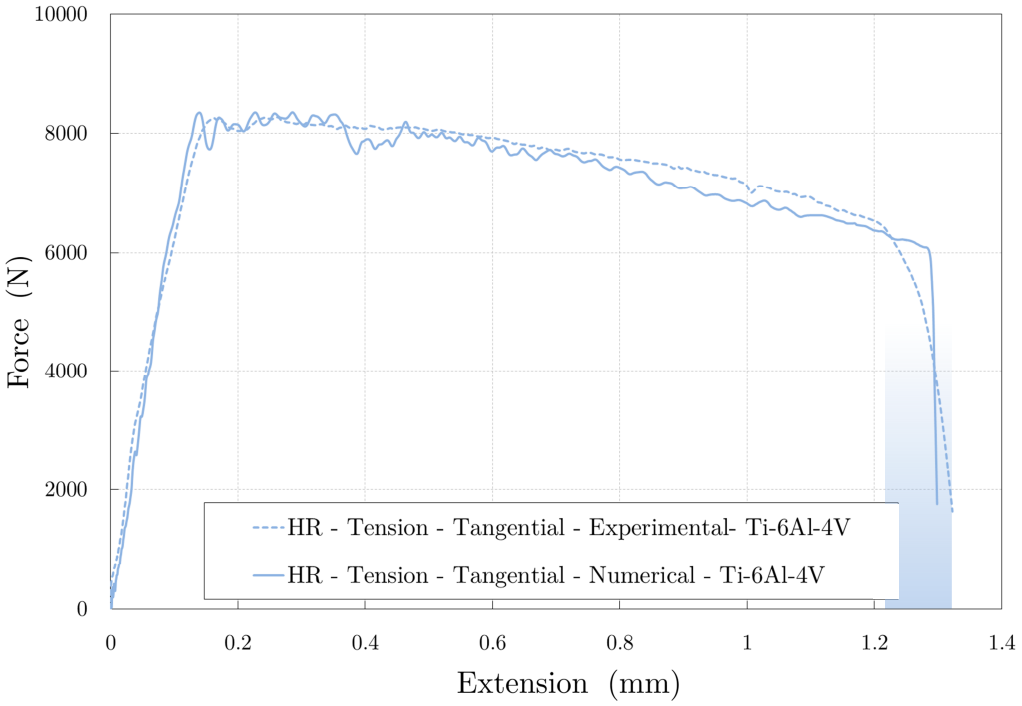


Figure 7.22: Numerical approximation of high strain-rate tangential orientation tensile experiments.

7.5 Summary

The development of an integrated strength differential mechanism has been successfully demonstrated through the resultant yield surface evolution. Yield strength control is achieved via two user-defined parameters which can be calibrated from uni-axial tests. In addition, the constitutive framework proposed within Chapter 5 and Chapter 6 has been expanded to include full anisotropy. This development is essential for modelling titanium alloys and industrial processing routes, such as ring rolling and cooling rates in the microstructure.

- HCP materials have been shown to exhibit differential strength effects in titanium alloys. This macroscopic behaviour has been successfully developed within the existing framework. This has been demonstrated based upon uni-axial data for Ti-6Al-4V. This provides the ability to control the influence of asymmetry in yielding and plastic evolution individually.

- Anisotropic enhancements have been developed within the newly proposed constitutive framework. The additional developments combine the existing asymmetric, multi-mode damage and mesh insensitivity capabilities together with the visco-plastic temperature dependencies.

- The influence of the individual Hill parameters on a two-dimensional yield surface have been demonstrated. The limitations of this algorithm have also been established when the strength of a material in one orthogonal direction exceeds twice that of the remaining orthogonal directions. In ductile metallic materials this condition is unlikely, but care should be taken.

- A methodology has been established to determine the anisotropic parameters from uni-axial tests, using both physical measurements and DIC techniques. An example has been demonstrated to establish the required parameters using DIC software at high strain-rates.

Chapter 8

Conclusions

To conclude, a discursive overview of this research projects activities is presented, followed by a list of key contributions made to the field and the associated benefits and applications of this research. As a consequence of the developments made further work is suggested that would compliment the research described herein.

8.1 Summary

This projects aim was the *Development of Improved Numerical Techniques for High Strain Rate Deformation Behaviour of Titanium Alloys*. To fulfil this aim a comprehensive search of the literature was performed, thus providing a 'bottom up' approach to the subsequent research based on physical metallurgical phenomena. A clear distinction was made that any numerical solution to be developed would be aimed at an industrial application, and would therefore be required to remain computational efficient. This defined the macroscopic approach described throughout this research.

The identified physical phenomena associated with high strain-rate deformation of Ti-6Al-4V and the corresponding numerical solutions proposed by various authors exposed gaps in the literature. No numerical solution featured all the identified relevant phenomena at the marcoscopic scale.

An appropriate constitutive framework was established which featured strain-rate

and temperature dependencies. This framework was implemented within commercial and in-house software packages. Limitations of the implemented framework were demonstrated during parametric numerical studies of uni-axial and impact scenarios. These shortcomings corresponded with a lack of functionality in areas identified in the literature from a physical metallurgy perspective.

Development of multi-mode damage, asymmetry, anisotropy, localisation and mesh insensitivity capabilities addressed these shortcomings and have been successfully implemented and demonstrated through this research.

8.2 Contributions

A list of the key conclusions and contributions made during this research are listed below:

- A comprehensive survey of the existing literature has been completed within Chapter 2, this has highlighted a series of physically observable phenomena at the macroscopic scale, which are relevant to high strain-rate deformation of Ti-6Al-4V. Numerical solutions which correspond to the identified physical phenomena have been developed within a single consistent constitutive framework. A summary of these phenomena can be found in Figure 8.1.

- A series of numerical studies, including software verification and validation benchmarks for both uni-axial and sub-component plate impact benchmarks have been established and validated against experimental data. These benchmarks have highlighted the limitations of commercial constitutive models in areas of mesh sensitivity (section 5.5) and accurate damage accumulation (section 6.3). Techniques and benchmarks have also been established that allow for rationalisation of experimental testing during development and characterisation exercises (section A.4).

- A multi-mode damage algorithm has been developed. The influences of dilatational and distortional damage have been coupled with a mesh sensitivity reduction and localisation technique (section 6.3). This facilitates competitive and cumulative damage evolution within the existing strain-rate and temperature dependent framework.

- Failure due to shear has been demonstrated, based upon the literature and in-house experiments. The newly developed damage accumulation and evolution algorithm has been demonstrated in uni-axial and plate impact benchmarks (section 6.2.5). This provides an enhanced capability which can both accurately represent damage accumulation whilst minimising the errors associated with irregular or inappropriately mesh geometries.

- A method has been developed which combines asymmetric (section 7.3) and anisotropic yielding and plastic evolution (section 7.4). This has been fully integrated within the multi-mode damage framework. This provides an ability to represent macroscopically observable non-isotropic affects of twin formation and texture, for example. Combined experimental and numerical techniques were used to assess the applicability of the techniques for Ti-6Al-4V and to propose methods for parameter identification.

- Industrial alloys clearly demonstrate both asymmetric and anisotropic behaviours at high strain-rates. Experimental data has been used to demonstrate the newly developed constitutive capabilities (section 4.1.3). Uni-axial data has been accurately represented in terms of yielding and plastic deformation (section 7.4.2).

- The developed marcoscopic model addresses and combines the macroscopic phenomena identified within a single constitutive framework, as is illustrated in Figure 8.1. This provides a tool for industrial applications which enables strain-rate and temperature scenarios to be captured and the influences of pressure

dependencies, texture, and competing failure mechanisms. The constitutive algorithm has been delivered to industry for integration within their numerical library, providing additional insight into experimentally observed phenomena.

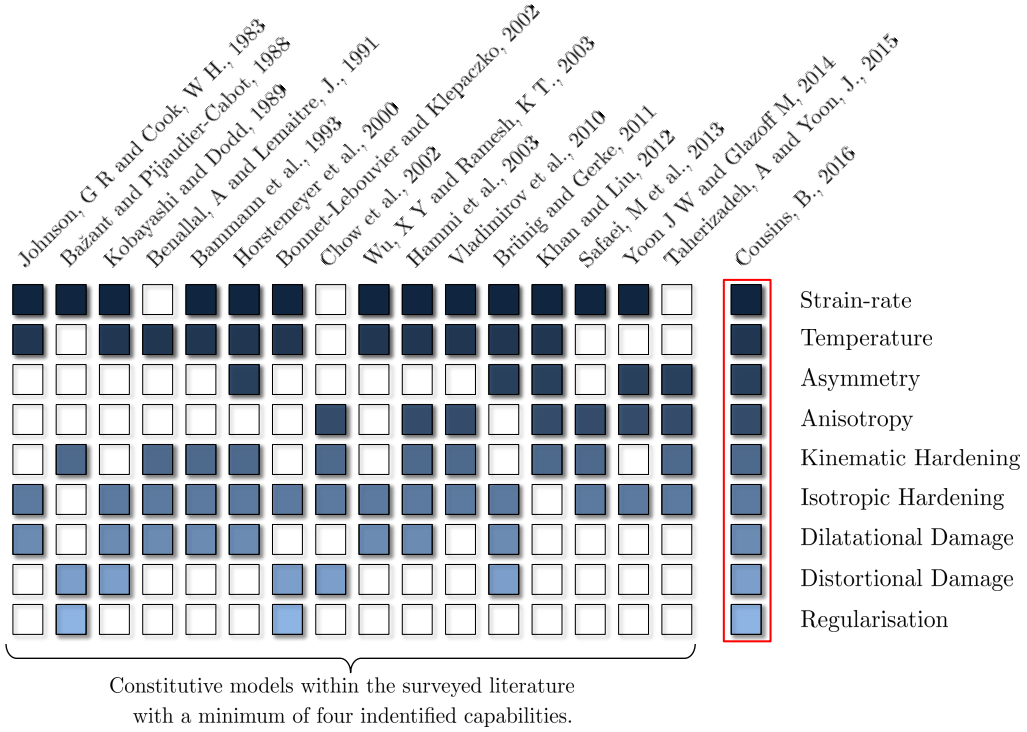


Figure 8.1: Constitutive modelling features developed and implemented during this research.

8.3 Future work

This research has exposed areas of research in associated fields which would further compliment this research. These have been briefly list below for further consideration:

- Element failure techniques within classical continuum mechanics poses a persistent challenge when considering element erosion. Development of novel element splitting techniques which utilise the planes of emerging discontinuities - established within this research - would provide a significant improvement, whilst retaining computational efficiency.

- Crystal plasticity modelling would provide further micro-mechanical data which

could be used to calibrate individual macroscopic parameters within the existing framework.

- Application of multi-scale coupling validation and calibration capabilities. This 'bottom up' approach would create physically based macroscopic solution relating visco-plastic, thermo-mechanical and textural phenomena.

Appendix A

Numerical Support

This research spans a variety of software platforms, which will be discussed in terms of their relevance. The benchmark simulations used throughout this research will be evaluated in terms of numerical reliability and applicability. The justifications and reasons for the assumptions made shall be discussed in terms of their implications.

A.1 Software platforms

Three main software platforms - commercially available ABAQUS and LS-DYNA, and in-house development code DEST - were used during this research for various specialised purposes. The product of this research has been made compatible with all of these platforms in a vectorised form for explicit computations. This adds to the applicability of the developments made and enables further developments beyond this research.

A.1.1 DEST

DEST is an in-house development code which was originally developed as a Discrete Element Method (DEM) solver, by Professor Nikica Petrinic [170]. The flexibility of the integrated programming environment enabled an expansion of the original implementation to integrate a Finite Element Method (FEM) solver, as discussed in Chapter 2. The unique DEM and FEM coupling within DEST has been described by other authors [171] but shall not be utilised during this project. The computational

speed of DEST exceeds that of commercial codes and due to constant developments remains far more applicable for development exercises. The benefit of access to the source-code during development is unparalleled compared to commercial software. Further DEST developments related to element failure techniques, which closely relate to aspect of this work, would not have been possible in commercial codes.

Whilst DEST remains faster than both LS-DYNA and ABAQUS, the parallelisation of the code is still in development; this limits the scalability of the solver for large-scale industrial simulations. However, another major advantage of the DEST platform is the use of open source libraries which enables the use of well established MPI libraries, for example, to facilitate rapid developments.

A.1.2 LS-DYNA

Within industry LS-DYNA is commonly used to solve dynamics FEM problems. The user-defined material sub-routine was used extensively during this project for validation against development platform - DEST, and for post-processing of larger benchmarking simulations. Versions were developed in parallel for both Windows and LINUX operating systems for validation and post-processing of data. The extensive library of material models and customised tools within LS-DYNA is an important benefit to the platform. This enables the evaluation of developments against alternative approaches, and other developments within the literature.

Access to variables beyond those common for constitutive modelling is limited and documentation to understanding their implications elsewhere during computation is limited. The documentation and support which is available for developers is constantly being improved and upgraded. The user community is extremely narrow in comparison to other commercial codes, however many publications and specialised conferences exist as sources of reference.

A.1.3 ABAQUS

The commercial platform, ABAQUS, is used widely throughout industry and all levels of academia. Similarly to LS-DYNA, the limited access to source code is a constraint. ABAQUS does provide extensive documentation but ultimately limits the developer compared to DEST. For the purposes of this research ABAQUS was used for two reasons, firstly a third-party MATLAB-based parameter identification tools was used which accesses an ABAQUS VUMAT (Vectorised User Material) routine. This approach was chosen in the interests of time and to provide a tool which can be utilised outside of the Impact Engineering Laboratory. Secondly, crack propagation using techniques such as XFEM allow for future comparisons with techniques being developed within DEST development environment.

A.2 Uni-axial simulations

During the development of a constitutive model, it is infeasible to perform analysis and pre/post-processing of full split-Hopkinson bar simulations. Therefore it is essential to reduce the size of the simulation problem whilst maintaining the boundary conditions, thus ensuring a representative benchmark for validation exercises.

The imposed boundary conditions of an entire tensile split-Hopkinson bar experiment will be examined with an aim to simplify the representation required whilst maintaining the repeatability of results observed at the specimen. Split-Hopkinson bar apparatus developed by Sivasubramaniam Sathianathan [29] during an investigation into the dynamic Bauschinger effect have been used for simulation purposes.

A.2.1 Split-Hopkinson Tension Bar

The reverse loading split-Hopkinson bar apparatus has been modified to perform monotonic tension only. This shall provide an initial starting point for the following numerical investigation, which aims to provide justification for the reduction of components necessary to reproduce stress and strain responses at the specimen gauge

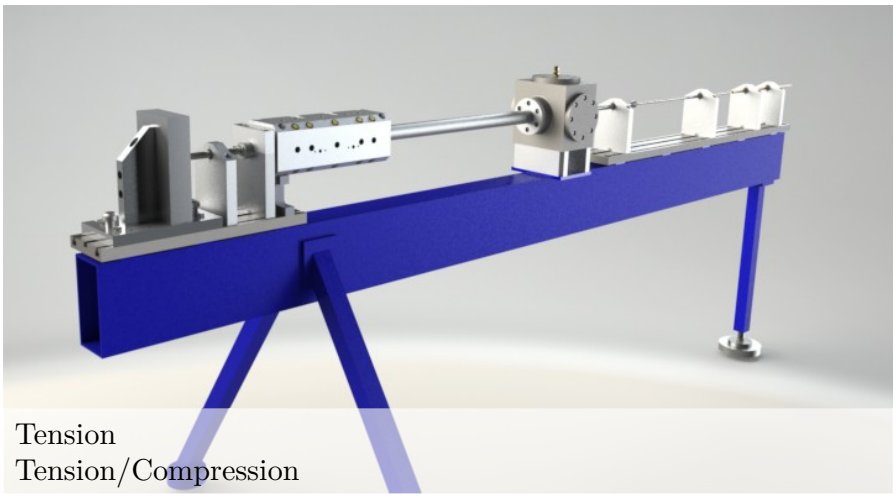


Figure A.1: High strain-rate apparatus split-Hopkinson Tension-Compression and/or Tension bar.

section. The experimental set-up is illustrated in Figure A.1.

All components of the apparatus in Figure A.2 are Ti-6Al-4V except the transmitted bar, which is Phosphor-Bronze. This is due to the reduced magnitude of the transmitted signal. The striker tube is free to move longitudinally along the external surface of the loading bar. Connection of all other components are achieved with screw-threads. A schematic representation of Figure A.1 is illustrated in Figure A.2. This initial configuration shall form the basis for further detailed discussion.

The above arrangement was simulated in LS-DYNA. Inter-connection of components were established using a combination of 'tied contacts' and 'automatic surface-

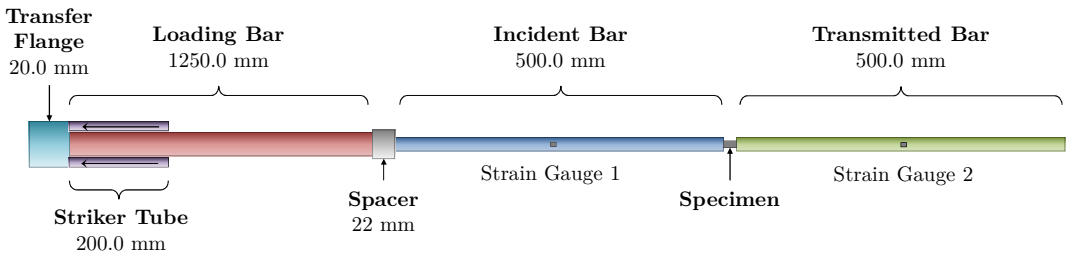


Figure A.2: High strain-rate apparatus numerical schematic of split-Hopkinson tension bar.

to-surface' contacts. The striker tube was provided an excitation with the 'initial velocity' boundary condition applied globally; this assumes a constant velocity at impact. Experimentally, the bars are supported on nylon bushes to minimise friction. Numerically, zero friction is assumed and translational motion perpendicular the axial wave propagation is restricted. No other boundary conditions were applied for the full SHTB arrangement.

The bars and other components are assumed to remain elastic. This is to satisfy the split-Hopkinson bar theory, discussed earlier section 4.1.1. The material model chosen for the plastic response of the specimen was the Bammann-Chiesa-Johnson model [42]. This was chosen for future comparisons during constitutive developments. Calibration of this material model is not required as data obtained from specimens are used for validation of the boundary conditions and component rationalisation only. Data was collected at both the nodes and elements to establish boundary condition information. This will be discussed in more detail during the following section.

A.2.2 Dispersions

In an ideal case, the wave speed is calculated assuming uni-axial stress in a slender bar (A.1). In reality the influence of inertia and wave interaction with free surfaces have been observed, this is called dispersion.

$$c_m = \sqrt{\frac{E}{\rho}}. \tag{A.1}$$

The nodal velocities in Figure A.5 demonstrates the increase in longitudinal wave speed due to the free end. The analytical solution for this effect is described in equation (A.2), from classical split-Hopkinson bar theory to satisfy the zero stress condition at the free-end and maintain equilibrium and compatibility conditions.

$$v = \frac{v_i - v_r}{\rho c_m} \tag{A.2}$$

Variable v_i is the incident wave velocity and v_r is the reflected wave velocity. The

influences of the free-end can be seen in Figure A.3. Probe 1 is located furthest from the specimen, whilst probe 3 is much closer. At probe 1 the incident pulse duration rise and fall is observed; the duration of the pulse at probe 2 is reduced because of its proximity to the free-end. The pulse duration is further reduced at probe 3, and the velocity is doubled according to equation (A.2) before the incident pulse falls.

A comparison of the velocity pulse magnitude at the strain gauge location and the specimen are shown in Figure A.5. Further effects of dispersions are related to relative wave speeds in the non-longitudinal directions. The Pochhammer-Chree solution indicates that higher frequency stress waves (i.e. non-longitudinal) propagate slower than lower frequency waves; the relationship is shown in Figure A.4.

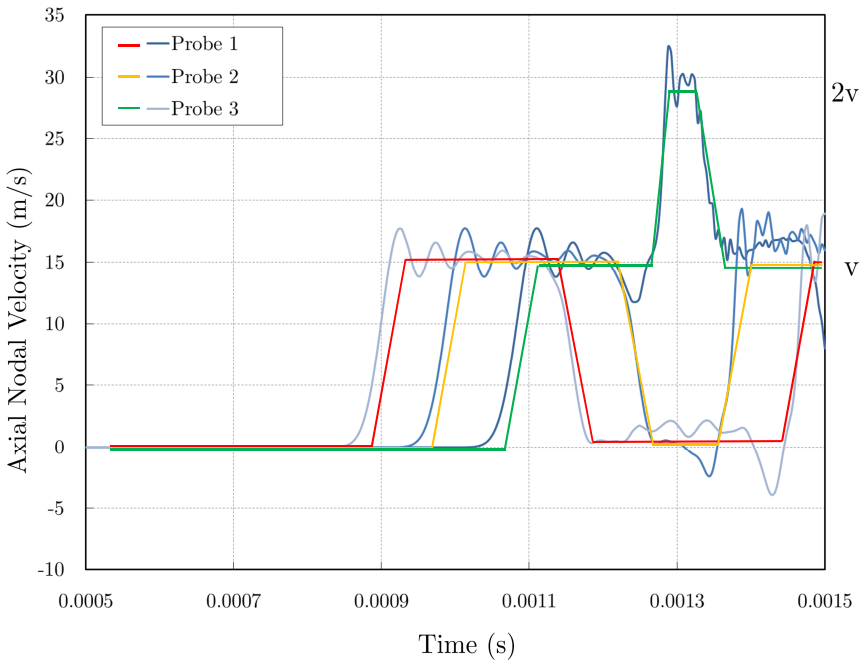


Figure A.3: Free-end particle velocities, incremental influences at incident bar probe locations approaching the specimen.

The parameter c_p in Figure A.4 is the plastic wave speed of wave components of chosen frequencies. Parameter c_e is the elastic bar wave speed (A.1), A is the circular cross-sectional area of the bar and Λ is the wave length [172]. The oscillations also observed in Figure A.5 are a consequence of individual wave speeds travelling at

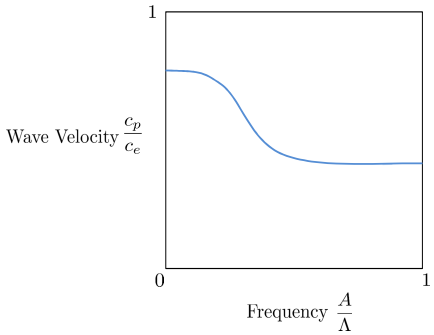


Figure A.4: Wave dispersion schematic relationship due to high frequency component propagation velocity discrepancy.

different velocities. The theoretical idealised trapezoidal wave is superimposed. The influence of the free-end and the associated velocities observed in the specimen display almost zero duration at the incident velocity, rather an immediate increase due to the effect of the free-end.

Follansbee and Frantz extensively studied this effect [172]. The following example Fourier transform $f(t)$ can estimate wave speed at a given position z, due to dispersions as follows

$$f(t) = \frac{A_0}{2} + \sum_{n=1}^{\infty} D_n \cos(n\omega_0 t - \delta), \tag{A.3}$$

where A_0 and D_n are constants, and the phase angle δ is given below

$$\delta = \frac{n\omega_0 z}{c_l}\left(\frac{c_l}{c_n} - 1\right), \tag{A.4}$$

where c_n and c_l are the wave propagation velocities of the frequency component $n\omega_0$, and the longitudinal velocity. By adjusting the phase angle, the dispersion can be corrected as follows

$$\delta = \delta_0 + \frac{n\omega_0 \Delta z}{c_l}\left(\frac{c_l}{c_n} - 1\right) \tag{A.5}$$

where δ_0 corresponds to the phase angle z_0, whilst the phase angle at $z = z_0 + \Delta z$.

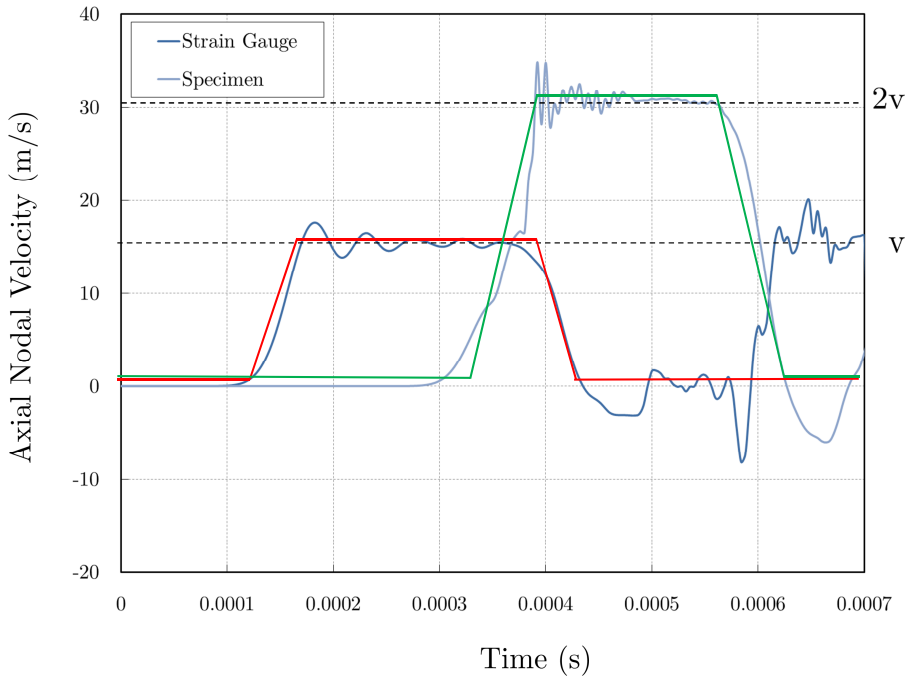


Figure A.5: Axial nodal velocities at cross-sectional positions at the strain gauge and within the specimen, from section A.3.4.

A.3 Component rationalisation

During each trial, locations within the gauge section were chosen within the specimen. The von Mises stress at these positions was compared for each of the following rationalisation phases.

- SHTB-1: Full split-Hopkinson tension bar apparatus.
- SHTB-2: Incident and transmitted bars. Full bar lengths.
- SHTB-3: Incident and transmitted bars, shortened to strain gauge positions.
- SHTB-4: Incident bar, shortened to strain gauge positions.
- SHTB-5: Specimen only.

The progression between each trial shall be examined during this chapter. Assumptions made shall be stated and the von Mises stress evaluated at the probe

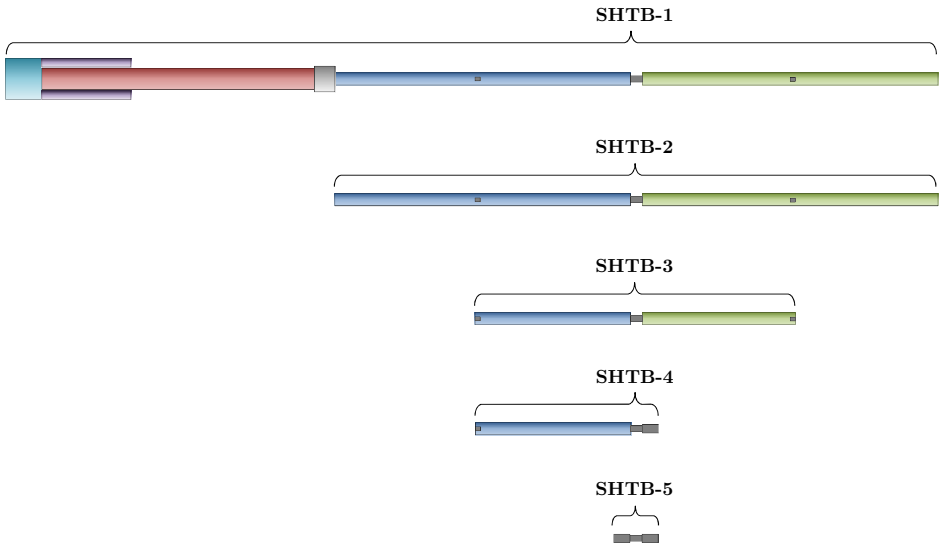


Figure A.6: Numerical modelling apparatus reduction for component rationalisation phases.

locations. Figure A.6 illustrates the numerical set-up for each phases. Boundary conditions shall be discussed during individual sub-sections.

A.3.1 SHTB - 1

Naturally, full representation of the experimental set-up is preferable, however the data in Table A.1 clearly demonstrates the computational time savings possible. For clarity the stress wave initiation is demonstrated in Figure A.7. The corresponding compressive and tensile axial waves are shown in Figure A.8.

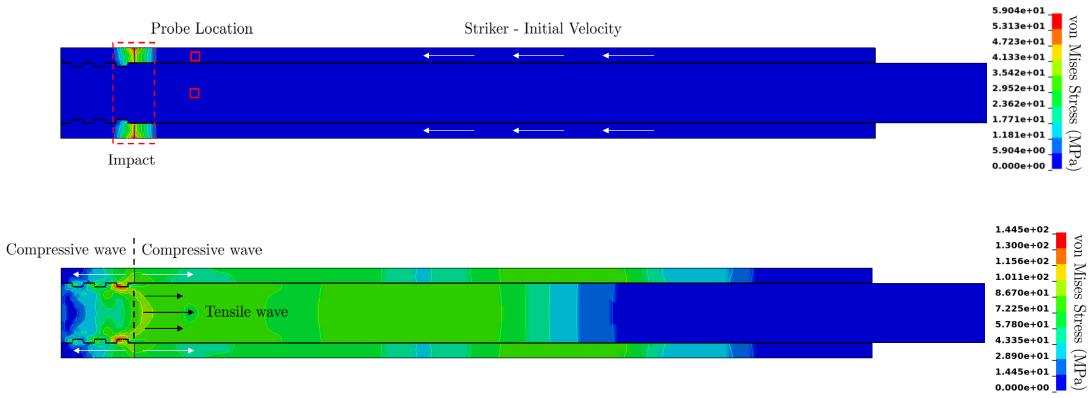


Figure A.7: Cross-section view of striker, transfer flange and loading bar assembly and impact stress wave excitation.

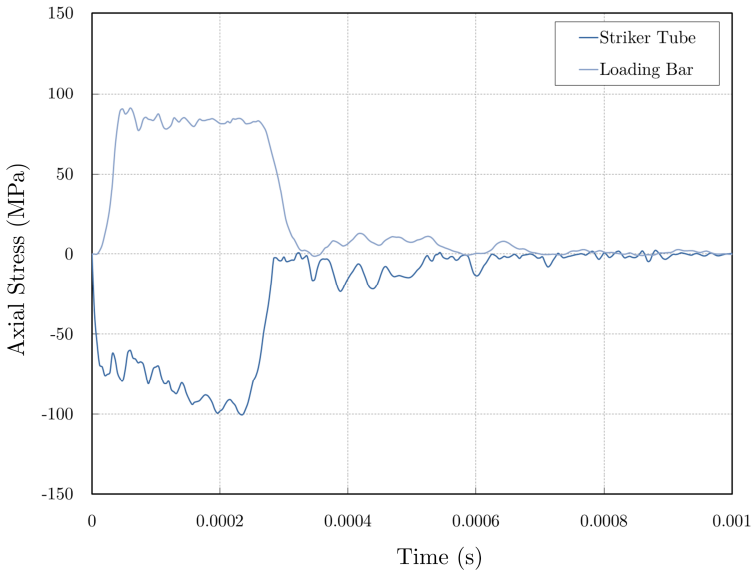


Figure A.8: Tensile and compressive wave excitation in the loading bar and striker, respectively.

The tensile stress wave then travels longitudinally down the axis of the loading bar into the spacer and eventually into the incident bar. The wave propagation can be seen in Figure A.9. The axial stress wave decays in magnitude due to dispersions during propagation, this is demonstrated by comparing the loading bar stress wave in Figure A.8 and Figure A.10. The effects of dispersions and joined components are of interest when simulating specimen-only configurations.

As the stress wave propagates into the smaller diameter incident bar the amplitude of the stress wave is magnified, as demonstrated in Figure A.10. For clarity, a

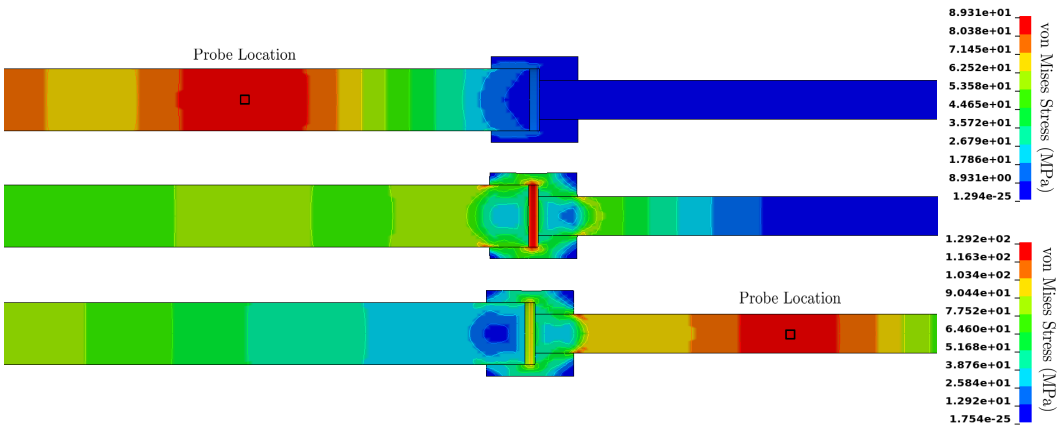


Figure A.9: Cross-section view of tensile wave propagation between loading bar and incident bar.

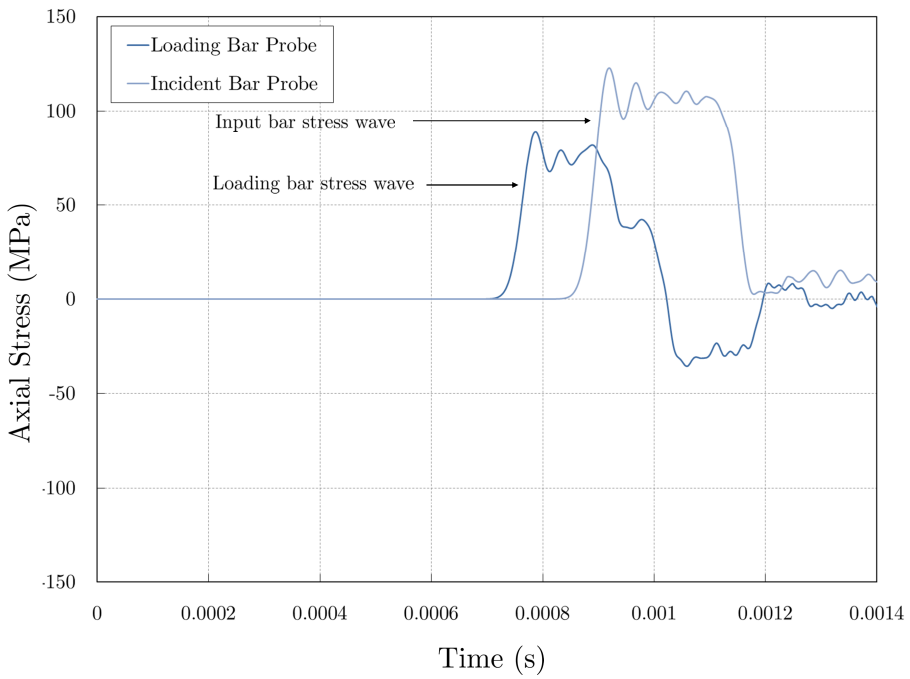


Figure A.10: Tensile wave propagation and amplification between loading bar and incident bar.

comparison of axial stress wave amplitude and the period, due the reflections, can be seen in Figure A.11. During experimental post-processing the wave separation is an important factor to calculate the resultant stress-strain response.

Finally, the von Mises stress in the specimen is plotted in Figure A.13 and contours of plastic strain are seen in Figure A.12. The lack of observed softening in the specimen (Figure A.13) is a post-processing artefact when displaying stress at a single element in the gauge section. The chosen element is also located at the point of theoretical peak stress. Experimentally, the average is calculated whilst numerically it is possible to evaluate stresses at any point in the bulk. Regardless of the peak stress in Figure A.13, the corresponding yield stress in the literature and that experimentally measured in Chapter 4 are well aligned. It should be noted that the specimen geometry used during this chapter differs from that of the previous chapters, the reverse loading specimens typically used during dynamic reverse loading have a shorter gauge section length.

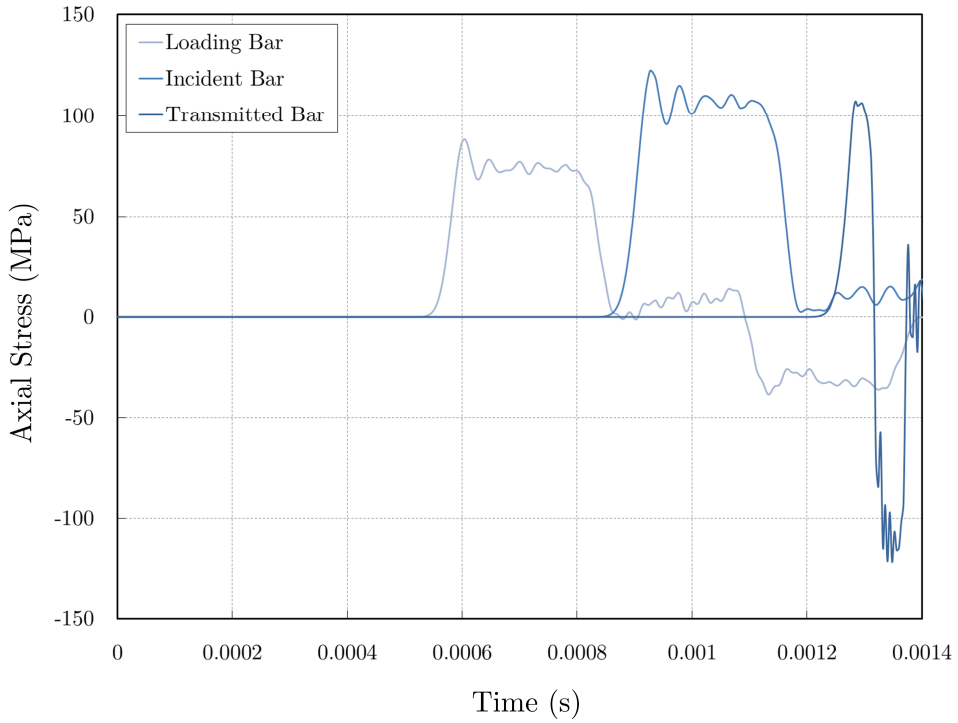


Figure A.11: Comparative wave propagation amplitudes in the loading bar, incident bar and transmitted bars.

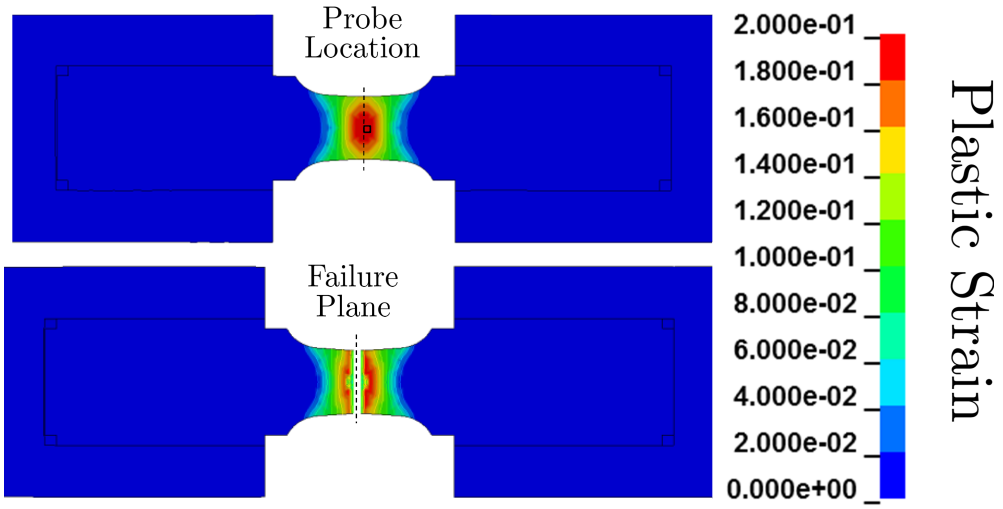


Figure A.12: Cross-section view of plastic strain contours and fracture due to element erosion during plastic deformation.

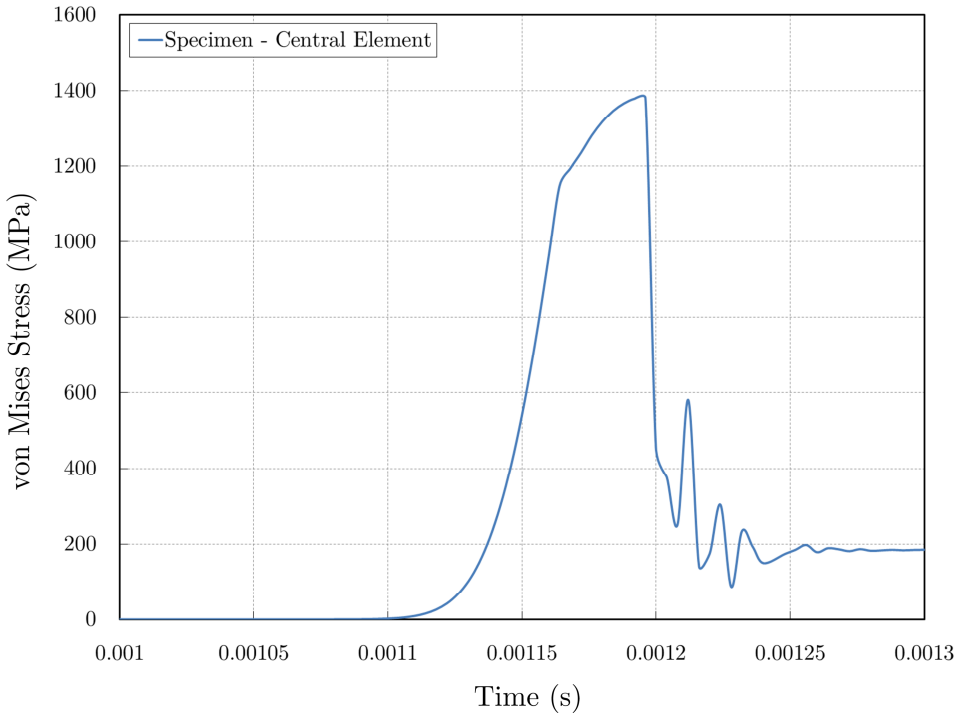


Figure A.13: High strain-rate response of Ti-6Al-4V specimen in a single element.

A.3.2 SHTB - 2

The first rationalisation simply eliminates the striker, loading bar and spacer. Velocity boundary conditions at the spacer-incident contact interface were applied to the reduced geometry. The location of these nodes can be seen in Figure A.14.

The velocity profile in the longitudinal direction and lateral direction are shown

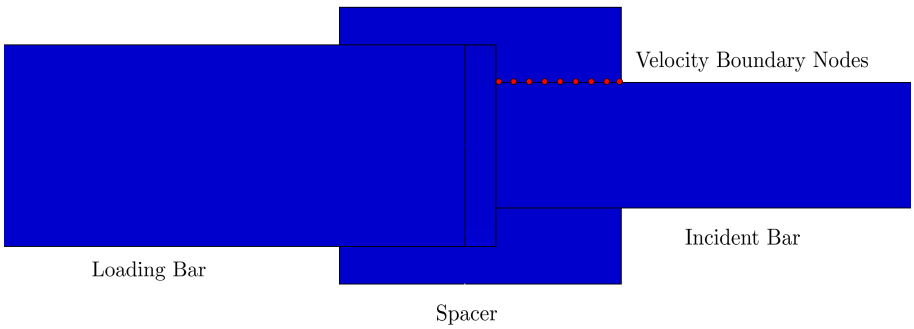


Figure A.14: Spacer-Incident bar contact interface nodal locations.

in Figure A.15 and Figure A.16, respectively. In the axial direction the velocities are almost identical across all nine nodes. This allows an average to be taken which can represent the boundary condition at the surface of the incident bar over the contact interface nodes. Velocities in the non-axial directions are displayed in Figure A.16: the magnitude of these velocities are an order of magnitude lower than that of the longitudinal direction. Therefore, it has been assumed that these non-axial velocities can be neglected during this phase. All other boundary conditions remain identical.

In summary, stress profiles at a known element during both A.3.1 and A.3.2 rationalisation phases are assumed equivalent. Figure A.17 demonstrates that the chosen velocity boundary conditions can be assumed to represent the full split-Hopkinson tension bar arrangement. The influence of non-axial velocities and reflections within the connected components can also be assumed to be negligible. This provides a computational benefit but remains too large for development benchmarking.

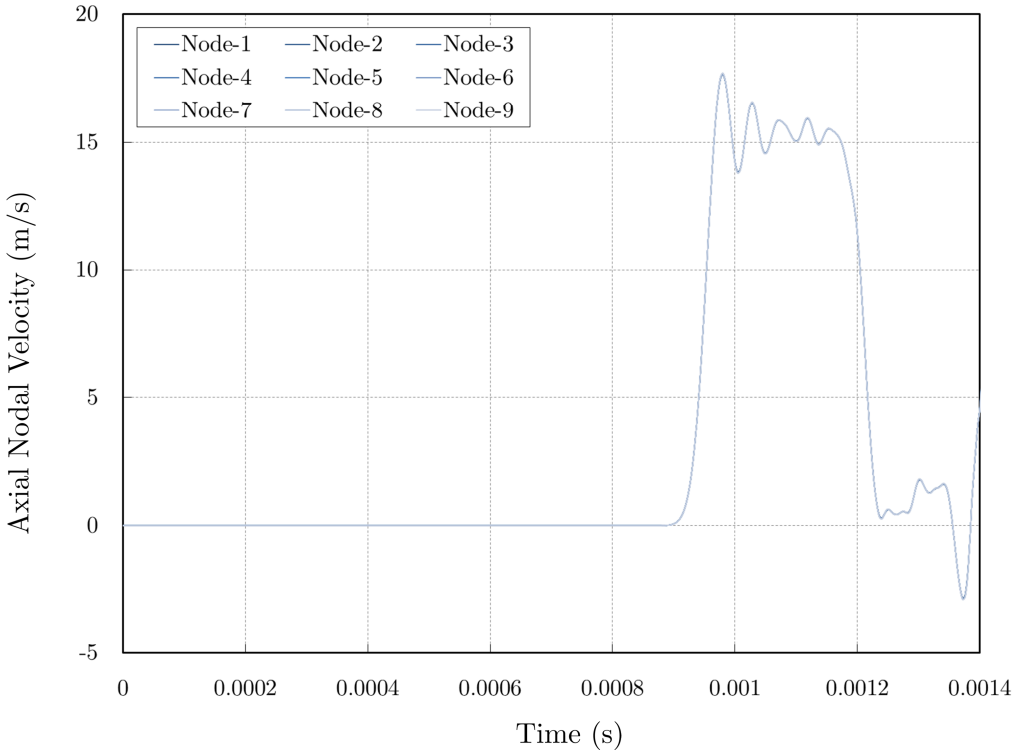


Figure A.15: Axial velocity at the contact interface nodes.

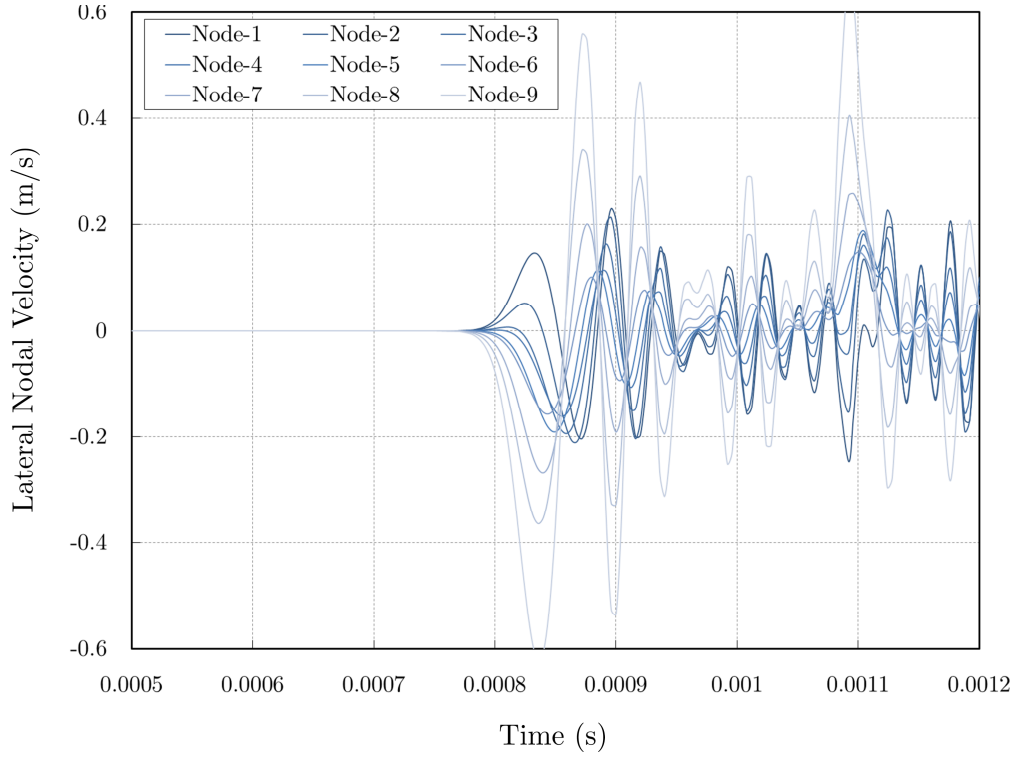


Figure A.16: Radial velocity at the contact interface nodes.

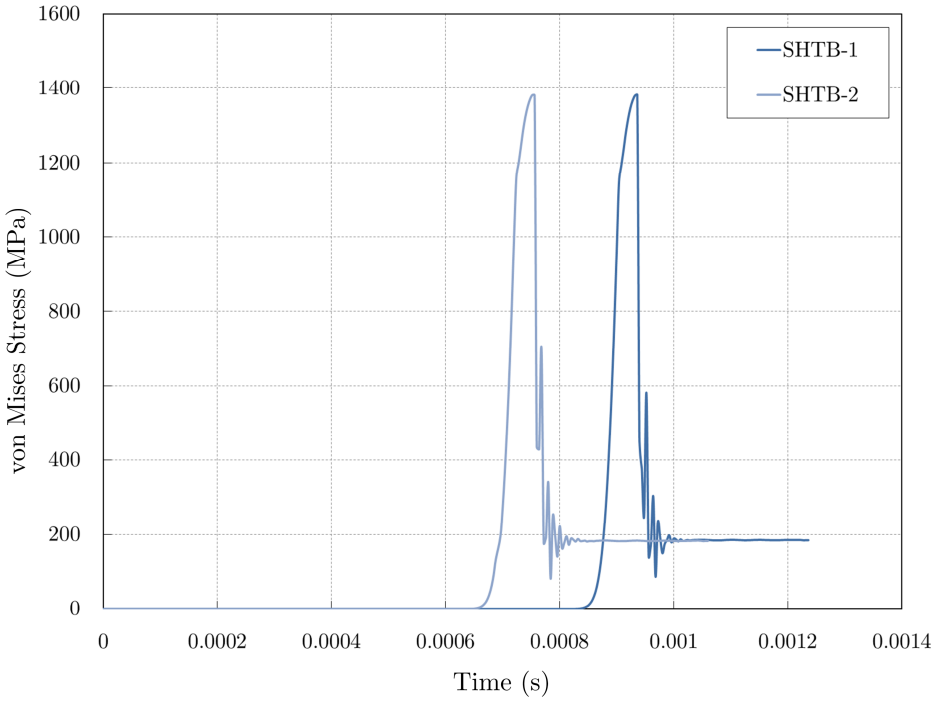


Figure A.17: SHTB - 2 Comparison: von Mises stress in specimen at a known element in the gauge section.

A.3.3 SHTB - 3

The next rationalisation phase aims to study the boundary conditions necessary at the strain gauge locations. This is critical as information gained through experimentation would inform the numerical model. To replicate this numerically the velocity - which can be derived from strain gauge data - was extracted at the surface of the bar in the location which the strain gauges are located. This was performed numerically from A.3.1 data.

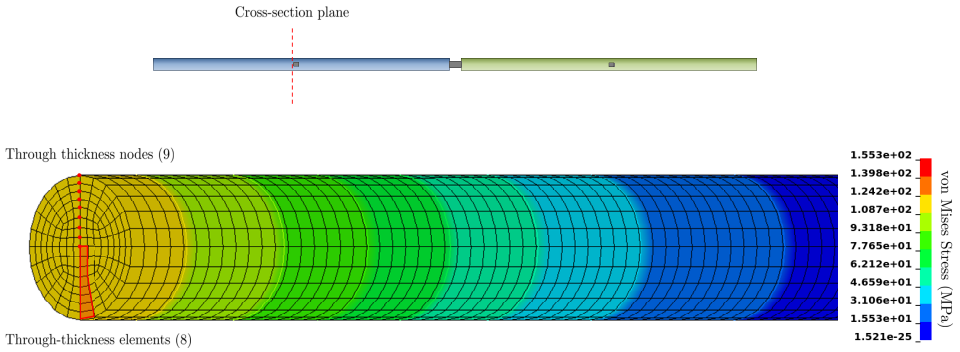


Figure A.18: Incident bar cross-section and probe locations from section A.3.2.

Numerically, the stress and velocity uniformity was examined through the bar cross-section (see Figure A.18). The results are described for all elemental and nodal values in Figures A.19 and A.20. The nodal and elemental values of axial velocity and von Mises stress are identical in the cross section, in accordance with SHPB theory. This verifies the assumption that the external quantities measured at the strain gauges can be applied to the entire cross section numerically by taking either an average or extrapolating experimental data. The resulting curve averages are shown in Figure A.21.

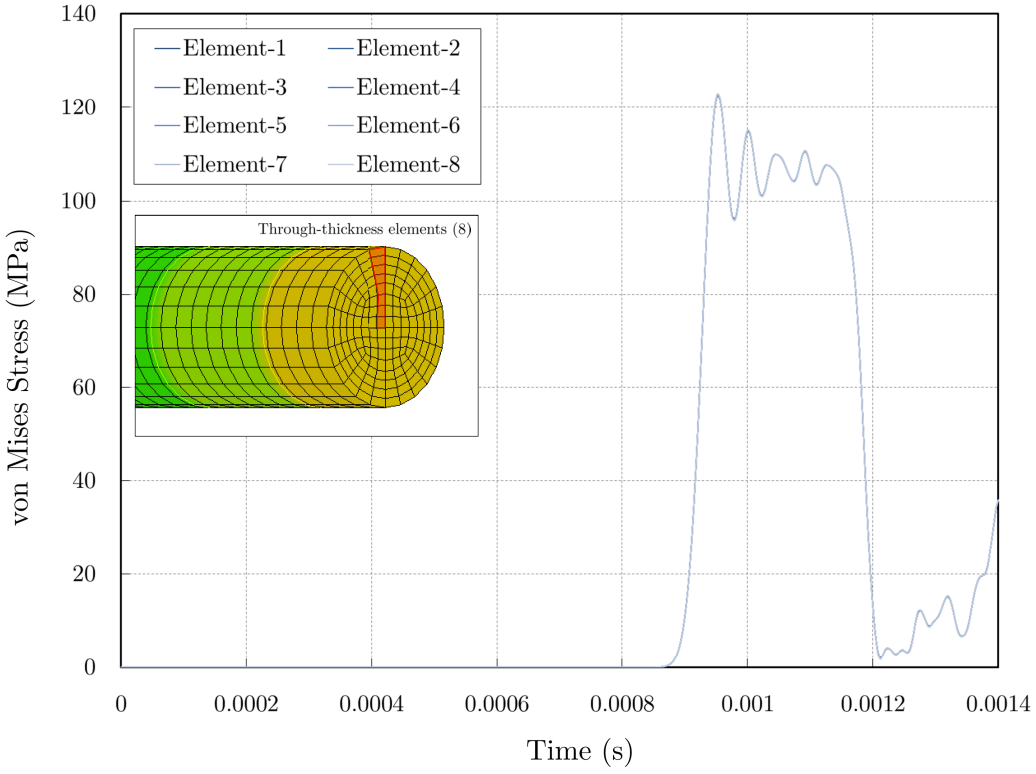


Figure A.19: Nodal velocity profile in the incident bar cross-section at strain gauge location.

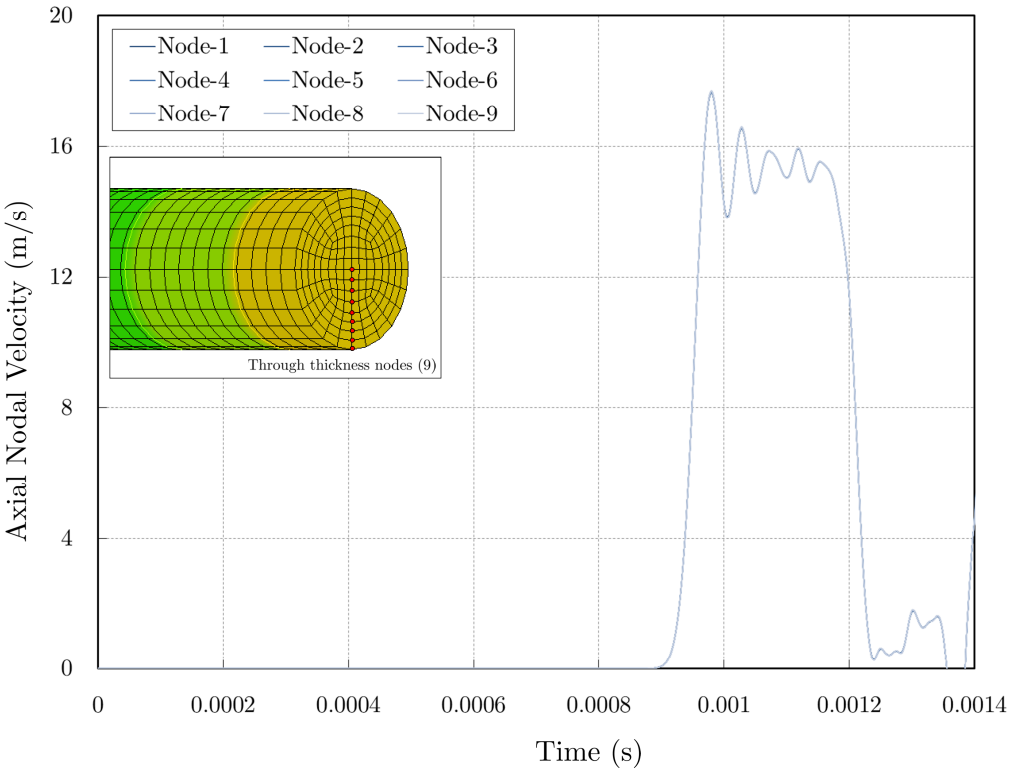


Figure A.20: Element von Mises incident bar stress profile cross-section at strain gauge location.

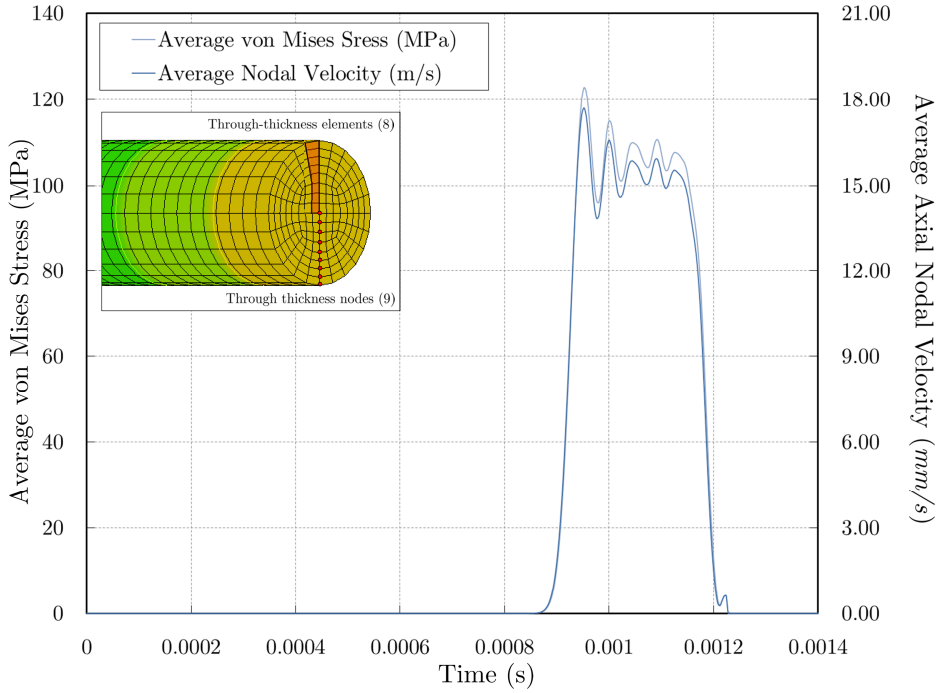


Figure A.21: Average von Mises and nodal velocity in the incident bar cross-section at the strain gauge location.

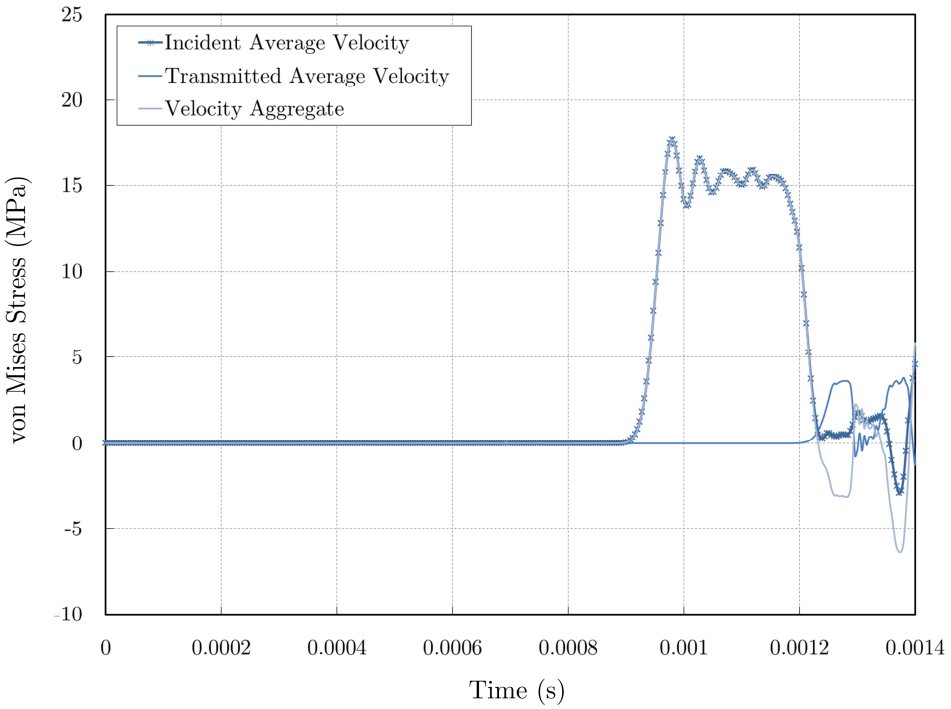


Figure A.22: Averaged axial aggregate velocity for fixed boundary condition single velocity input.

The boundary conditions have been modified to take into account the physically

reduced length of the bars. Firstly, non-reflecting boundary conditions were assumed at the strain gauge locations, this eliminates any fictitious reflections. Secondly, the velocity profile at the second strain gauge position was deducted from the first strain gauge position, resulting in an absolute velocity aggregate, as shown in A.22. Finally, a fixed boundary condition was applied to the transmitted bar free end. This verifies the the boundary conditions applied in the following section, A.3.4. The A.3.3 rationalisation phases has been verified against the previously measured specimen gauge section stress in Figure A.23. As expected, good agreement is found which provides evidence that a known excitation in the incident and transmitted bars can be directly applied to numerical computation on a reduced scale. Further rationalisation is required as computational time remains high and subject to bar lengths, which can vary depending on the apparatus [135].

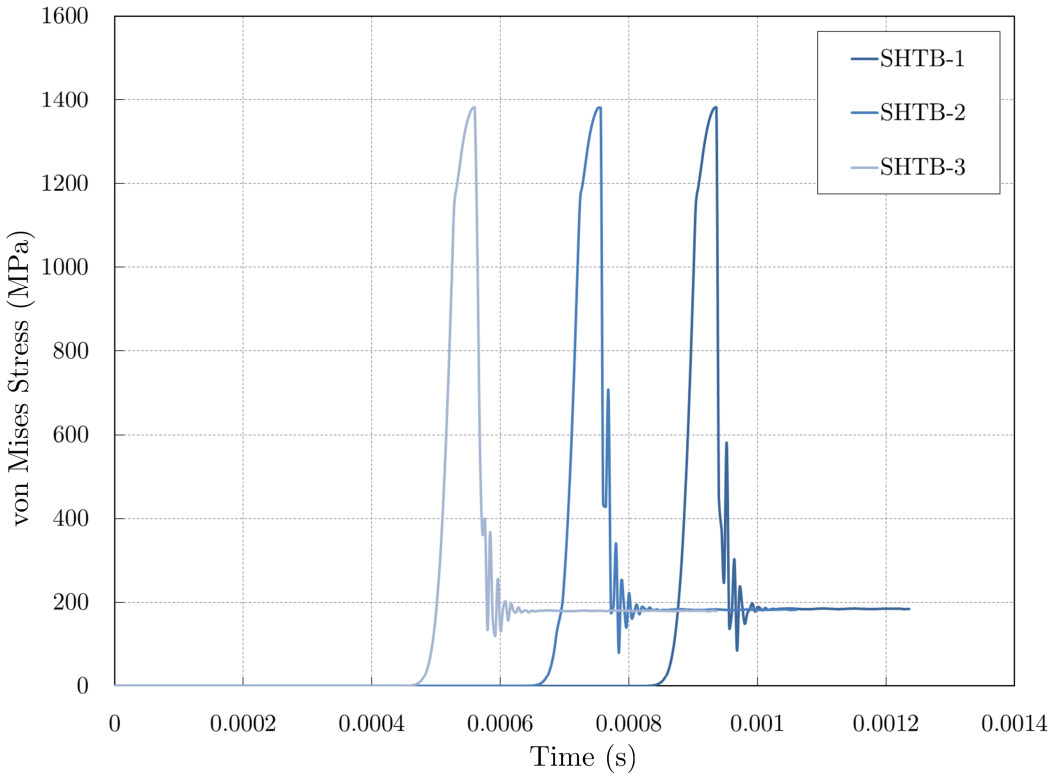


Figure A.23: SHTB - 3 Comparison: von Mises stress in specimen at a known element in the gauge section.

A.3.4 SHTB - 4

Similarly, the concept of applying a fixed and non-reflecting boundary condition allows an additional rationalisation phase to be achieved. The main advantage of this phase is the computational expense reduction. Firstly, the influence of the reflections surrounding the specimen and bar interface require assessment to quantify their contribution to stress in the specimen.

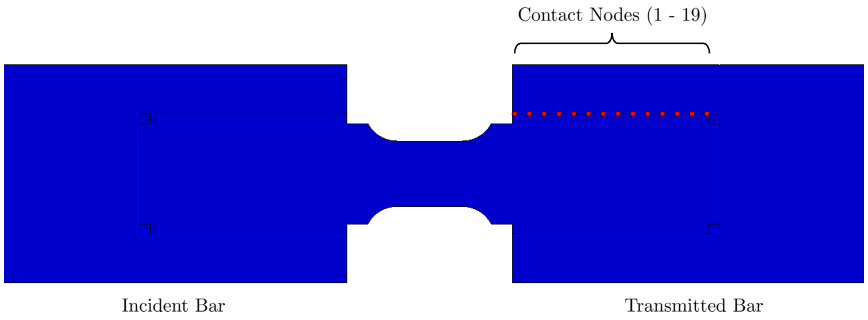


Figure A.24: Lateral nodal probes at the specimen-transmitted bar interface.

The lateral velocities at the interface are an order of magnitude smaller than those in the axial direction, this indicates that they can also be neglected, as previously assumed. To verify this assumption, the stress in the gauge section has also been compared in Figure A.26. This demonstrates that the full split-Hopkinson bar simulation can be reduced to a single portion of incident bar when the velocities recorded at the strain gauges are known.

In summary, it has been established that the full split-Hopkinson bar can be represented with an arbitrary portion of the incident bar and the specimen, when an excitation is known. The length of the incident bar required can be reduced by applying the velocity boundary condition and non-reflecting cross-sectional surfaces. However, the specimen only arrangement remains the ideal case. This shall be discussed in the following section.

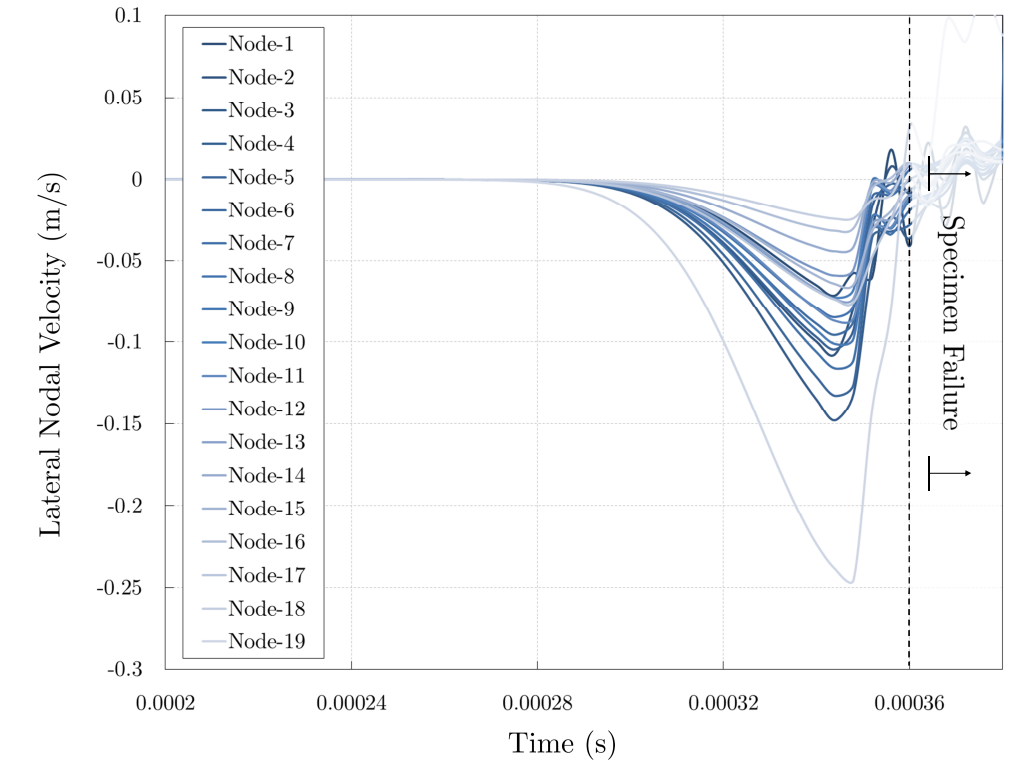


Figure A.25: Lateral nodal velocities at the specimen-transmitted bar interface.

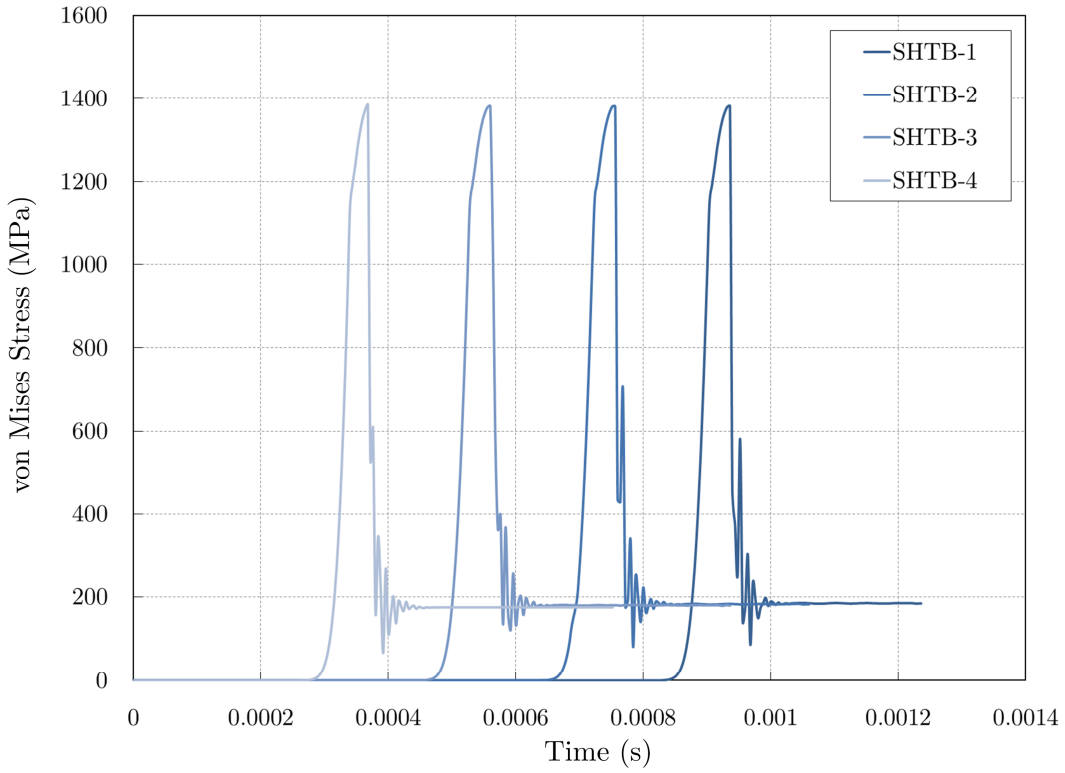


Figure A.26: SHTB - 4 Comparison: von Mises stress in specimen at a known element in the gauge section.

A.3.5 SHTB - 5

The specimen alone forms the final rationalisation phase. The fixed boundary condition is applied to the transmitted bar interface nodes of the specimen, whilst the aggregate velocity is applied directly to the incident bar interface nodes, as described in A.3.4. Predictably, stress measured in the gauge section correlates well with previous phases, as demonstrated in Figure A.3.5. This proves that the full split-Hopkinson bar simulations can be approximated with a single specimen. It has also been demonstrated that strain gauge data can be used similarly.

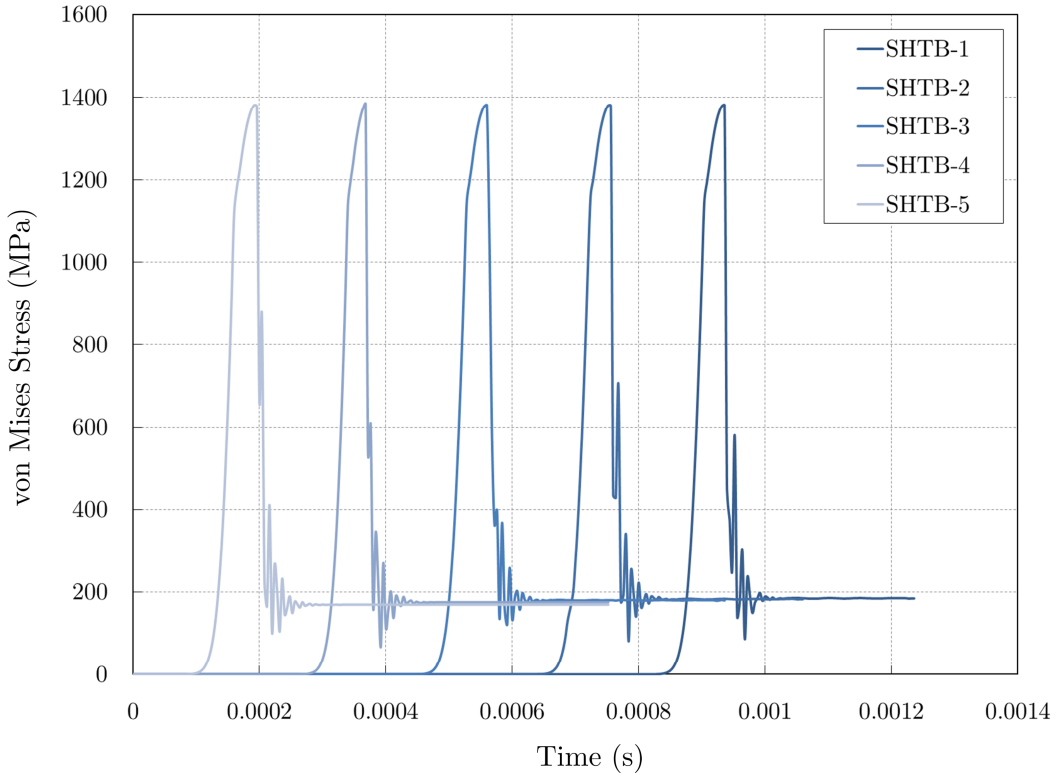


Figure A.27: SHTB - 5 Comparison: von Mises stress in specimen at a known element in the gauge section.

Simulating a full split-Hopkinson bar experiment to determine the boundary conditions is not feasible for calibration as plasticity will vary the transmitted velocity profile, however it may be argued that this is negligible. For monotonic high strain-rate testing and brittle failure, a single full simulation would provide an approximate

measure for all further simulations which could then be rationalised at a known gauge location, as described in A.3.3 and A.3.4.

However, when strain gauge data is only available at locations on the incident and transmitted bars, which require larger computations times due to the number of elements required, then simulating the specimen alone is required. Two options exist: firstly the arrangement described in A.3.4 would provide an approximate boundary condition for a range of experiments of similar inelastic behaviour. Secondly, the dispersion from strain gauge location to the specimen interface can be measured and calculated, which results in experiment specific approximations at the specimen-bar interface. This is preferable as it limits the computational expense required and utilises experimental data which can then be verified in multiple ways.

A.3.6 Computation time

Simulation time in Table A.1 clearly demonstrates the reduction in computational expense, which is achievable by applying rationalisation of components during benchmarking activities. This exercise provides additional confidence that reduced component simulations can be achieved whilst maintaining a representative approximation of the entire experimental arrangement.

Table A.1: Computational time reduction of SHTB simulations for a single CPU in explicit commercial software, LS-DYNA.

		Simulation Time		
Trial	**Number of Elements**	**Hours**	**Minutes**	**Seconds**
SHTB-1	502,363	12	25	1
SHTB-2	138,623	3	25	52
SHTB-3	121,151	1	30	24
SHTB-4	67,379	0	53	43
SHTB-5	13,607	0	14	10

A.4 Summary

To summarise, it has been proven that single specimen geometry is a feasible method for evaluating the split-Hopkinson bar experiment.

- It has been demonstrated that high strain-rate split-Hopkinson bar testing can be numerically represented by a series of greatly reduced geometries.
- This study has provided an incremental approach which enable the use of experimental data and numerical data to inform a reduced component model which captures the kinematics of the full-scale simulation, and ultimately reproduce the stress state within the specimen.
- Nodal velocities at the component surface have been shown to be a suitable boundary condition for such benchmarking, therefore creating a validated method for direct use of strain gauge data.
- For computational efficiencies, a single specimen geometry shall be used for further benchmarking exercises, thus reducing the computational time required by $\sim$ 12hrs. When multiple processors are used, the simulation times are reduced even further.

Figures A.28, A.29 and A.30 are schematic examples of the specimens geometries used during in-house high strain-rate testing. This chapter has provided justification for their application throughout this research.

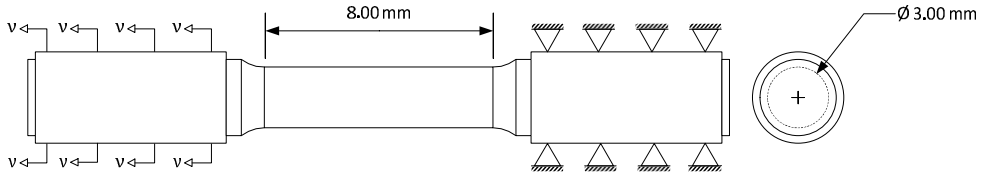


Figure A.28: Uni-axial high strain-rate dog-bone tensile specimen.

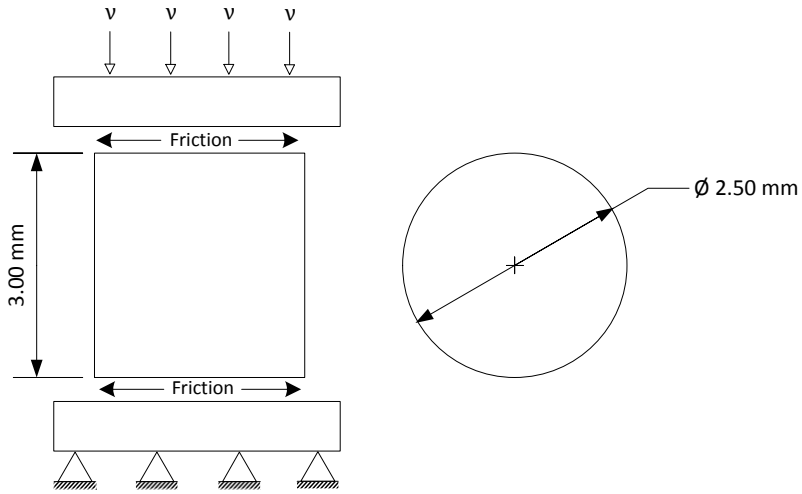


Figure A.29: Uni-axial high strain-rate compression specimen.

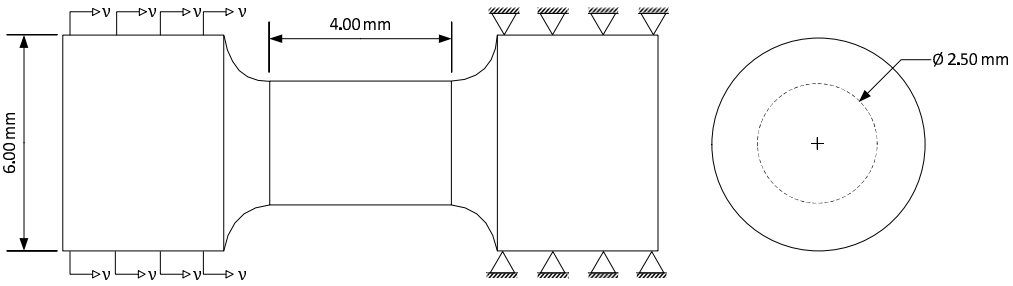


Figure A.30: Uni-axial high strain-rate dog-bone compression specimen.

References

[1] Holy Bible. New International Version. *Grand Rapids: Zondervan*, 1984.

[2] F Whittle. *Gas turbine aero-thermodynamics: with special reference to aircraft propulsion*. Elsevier, 2013.

[3] M P Boyce. *Gas Turbine Engineering Handbook*. 2006.

[4] Rolls-Royce Plc. *The Jet Engine*. Rolls Royce Technical Publication, 1996.

[5] H Richter. *Advanced Control of Turbofan Engines*. Springer Science & Business Media, 2011.

[6] A Linke-Diesinger. *Systems of commercial turbofan engines: an introduction to systems functions*. Springer Science & Business Media, 2008.

[7] M Mavromihales, J Mason, and W Weston. A case of reverse engineering for the manufacture of wide chord fan blades (WCFB) used in Rolls Royce aero engines. *Journal of Materials Processing Technology*, 134(3):279–286, 2003.

[8] Q He, H Xuan, L Liu, W Hong, and R Wu. Perforation of aero-engine fan casing by a single rotating blade. *Aerospace Science and Technology*, 25(1):234–241, 2013.

[9] K S Carney, C Lawrence, and D V Carney. Aircraft engine blade-out dynamics. In *Seventh international LS-DYNA users conference. Livermore CA, USA: Livermore Software Technology Corporation*, pages 14–17, 2002.

[10] S K Sinha and S Dorbala. Dynamic loads in the fan containment structure of a turbofan engine. *Journal of Aerospace Engineering*, 22(3):260–269, 2009.

[11] N F Knight Jr, Navin J, R E Lawson, and D R Ambur. Penetration simulation for uncontained engine debris impact on fuselage-like panels using LS-DYNA. *Finite Elements in Analysis and Design*, 36(2):99–133, 2000.

[12] D R Ambur, N Jaunky, R E Lawson, and N F Knight. Numerical simulations for high-energy impact of thin plates. *International Journal of Impact Engineering*, 25(7):683–702, 2001.

[13] M J Donachie. *Titanium: a technical guide*. ASM international, 2000.

[14] G Welsch, R Boyer, and E W Collings. *Materials properties handbook: titanium alloys*. ASM international, 1993.

[15] G Lütjering and J C Williams. *Titanium*, volume 2. Springer, 2003.

[16] R S Sandala. *Deformation Mechanisms of Two-Phase Titanium Alloys*. PhD thesis, The University of Manchester, 2013.

[17] S Zaefferer. A study of active deformation systems in titanium alloys: dependence on alloy composition and correlation with deformation texture. *Materials Science and Engineering: A*, 344(1):20–30, 2003.

[18] G Q Wu, C L Shi, W Sha, A X Sha, and H R Jiang. Effect of microstructure on the fatigue properties of Ti-6Al-4V titanium alloys. *Materials & Design*, 46(0):668–674, 2013.

[19] R M Miller, T R Bieler, and S L Semiatin. Flow softening during hot working of Ti-6Al-4V with a lamellar colony microstructure. *Scripta Materialia*, 40(12):1387–1393, 1999.

[20] J H Kim, S L Semiatin, and C S Lee. Constitutive analysis of the high-temperature deformation of Ti-6Al-4V with a transformed microstructure. *Acta Materialia*, 51(18):5613–5626, 2003.

[21] H Nasiri-Abarbekoh, R Abbasi, A Ekrami, and A A Ziaei-Moayyed. Notch-texture strengthening mechanism in commercially pure titanium thin sheets. *Materials & Design*, 55(0):683–689, 2014.

[22] M T Whittaker. Considerations in fatigue lifing of stress concentrations in textured titanium 6-4. *International Journal of Fatigue*, 33(10):1384–1391, 2011.

[23] H Nasiri-Abarbekoh, A Ekrami, and A A Ziaei-Moayyed. Effects of thickness and texture on mechanical properties anisotropy of commercially pure titanium thin sheets. *Materials & Design*, 44(0):528–534, 2013.

[24] A A Salem, S R Kalidindi, and R D Doherty. Strain hardening of titanium: role of deformation twinning. *Acta Materialia*, 51(14):4225–4237, 2003.

[25] G G Yapici, I Karaman, and H J Maier. Mechanical flow anisotropy in severely deformed pure titanium. *Materials Science and Engineering: A*, 434(1-2):294–302, 2006.

[26] G Lütjering. Influence of processing on microstructure and mechanical properties of (α+β) titanium alloys. *Materials Science and Engineering: A*, 243(1-2):32–45, 1998.

[27] W J Evans, J P Jones, and M T Whittaker. Texture effects under tension and torsion loading conditions in titanium alloys. *International Journal of Fatigue*, 27(10-12):1244–1250, 2005.

[28] H Iguchi, K Tanaka, and S Taira. Failure mechanisms in impact fatigue of metals. *Fatigue & Fracture of Engineering Materials & Structures*, 2(2):165–176, 1979.

[29] S Sivasubramaniam. *The development of reverse loading split Hopkinson pressure bar systems for the study of the dynamic Bauschinger effect.* PhD thesis, University of Oxford, Oxford, 2010.

[30] R A Claudio, C M Branco, E C Gomes, G F Harrison, and M R Winstone. Fatigue life prediction and failure analysis of a gas turbine disc using the finite-element method. *Fatigue & Fracture of Engineering Materials & Structures*, 27(9):849–860, 2004.

[31] A K Koul, N C Bellinger, and A Fahr. Damage-tolerance-based life prediction of aeroengine compressor discs: I. A deterministic fracture mechanics approach. *International Journal of Fatigue*, 12(5):379–387, 1990.

[32] A K Koul, N C Bellinger, and G Gould. Damage-tolerance-based life prediction of aeroengine compressor discs: II. A probabilistic fracture mechanics approach. *International Journal of Fatigue*, 12(5):388–396, 1990.

[33] J C Williams and E A Starke Jr. Progress in structural materials for aerospace systems. *Acta Materialia*, 51(19):5775–5799, 2003.

[34] B Cousins. The effects of damage on high pressure gas turbine disc alloys. Master's thesis, University of Birmingham, Birmingham, 2011.

[35] H Millwater, J Larsen, and R John. Effects of residual stresses on probabilistic lifing of engine disk materials. *Materials Science and Engineering: A*, (0):129–136, 2007.

[36] W Gambin. *Plasticity and textures.* Springer Science & Business Media, 2001.

[37] E Wielewski. *An investigation into the effects of microstructure and texture on the high strain rate behaviour of Ti-6Al-4V.* PhD thesis, University of Oxford, 2011.

[38] J C F Millett, G Whiteman, N K Bourne, and G T Gray. The role of anisotropy in the response of the titanium alloy Ti-6Al-4V to shock loading. *Journal of Applied Physics*, 104(7):73531, 2008.

[39] K Qin, L M Yang, and S S Hu. Interpretation of strain rate effect of metals. In *Dynamic Behavior of Materials, Volume 1*, pages 21–27. Springer, 2014.

[40] M N Shetty. *Dislocations and mechanical behaviour of materials*. PHI Learning Pvt. Ltd., 2013.

[41] H Zhan, D Kent, G Wang, and M S Dargusch. The dynamic response of a β titanium alloy to high strain rates and elevated temperatures. *Materials Science and Engineering: A*, 607:417–426, 2014.

[42] D J Bammann, M Chiesa, and G Johnson. Modeling Large Deformation and Failure in Manufacturing Process. *Theoretical and Applied Mechanics*, pages 359–376, 1996.

[43] A S Khan and S Yu. Deformation induced anisotropic responses of Ti-6Al-4V alloy. Part I: Experiments. *International Journal of Plasticity*, 38:1–13, 2012.

[44] S Seo, O Min, and H Yang. Constitutive equation for Ti-6Al-4V at high temperatures measured using the SHPB technique. *International Journal of Impact Engineering*, 31(6):735–754, 2005.

[45] P S Bate and D V Wilson. Analysis of the Bauschinger effect. *Acta Metallurgica*, 34(6):1097–1105, 1986.

[46] F Dunne and N Petrinic. *Introduction to computational plasticity*. Oxford University Press New York, 2005.

[47] I P Jones and W B Hutchinson. Stress-state dependence of slip in ti-6al-4v and other hcp metals. *Acta Metallurgica*, 29(6):951–968, 1981.

[48] R Hill. A theory of the yielding and plastic flow of anisotropic metals. In *Proceedings of the Royal Society of London A: Mathematical, Physical and Engineering Sciences*, volume 193, pages 281–297. The Royal Society, 1948.

[49] A S Khan, R Kazmi, and B Farrokh. Multiaxial and non-proportional loading responses, anisotropy and modeling of Ti-6Al-4V titanium alloy over wide ranges of strain rates and temperatures. *International Journal of Plasticity*, 23(6):931–950, 2007.

[50] M R Bache, W J Evans, V Randle, and R J Wilson. Characterization of mechanical anisotropy in titanium alloys. *Materials Science and Engineering: A*, 257(1):139–144, 1998.

[51] J Chakrabarty. Plastic Anisotropy. In *Applied Plasticity, Second Edition*, chapter 6, pages 405–477. Springer US, 2010.

[52] T Belytschko, W K Liu, and B Moran. Nonlinear Finite Elements for Continua and Structures, 2001.

[53] T Belytschko, W K Liu, B Moran, and K Elkhodary. *Nonlinear finite elements for continua and structures*. John Wiley & Sons, 2013.

[54] J L Chaboche. A review of some plasticity and viscoplasticity constitutive theories. *International Journal of Plasticity*, 24(10):1642–1693, 2008.

[55] N S Ottosen and M Ristinmaa. *The Mechanics of Constitutive Modeling*. Elsevier Science, 2005.

[56] E A de Souza Neto, D Peric, and D R J Owen. *Computational methods for plasticity: theory and applications*. John Wiley & Sons, 2011.

[57] G R Johnson and W H Cook. A constitutive model and data for metals subjected to large strains, high strain rates and high temperatures. In *Proceedings of*

the 7th International Symposium on Ballistics, volume 21, pages 541–547. The Netherlands, 1983.

[58] F J Zerilli and R W Armstrong. Dislocation mechanics based constitutive relations for material dynamics calculations. *Journal of Applied Physics*, 61(5):1816–1825, 1987.

[59] Y B Guo, Q Wen, and M F Horstemeyer. An internal state variable plasticity-based approach to determine dynamic loading history effects on material property in manufacturing processes. *International Journal of Mechanical Sciences*, 47(9):1423–1441, 2005.

[60] M F Horstemeyer and D J Bammann. Historical review of internal state variable theory for inelasticity. *International Journal of Plasticity*, 26(9):1310–1334, 2010.

[61] D J Bammann. An internal variable model of viscoplasticity. *International Journal of Engineering Science*, 22:1041–1053, 1984.

[62] J L Chaboche and G Rousselier. On the plastic and viscoplastic constitutive equations Part I: Rules developed with internal variable concept. *Journal of Pressure Vessel Technology*, 105(2):153–158, 1983.

[63] J L Chaboche. Continuum Damage Mechanics: Part I-General Concepts. *Journal of Applied Mechanics*, 55(1):59–64, 1988.

[64] J L Chaboche. Continuum damage mechanics: Part II-Damage growth, crack initiation, and crack growth. *Journal of Applied Mechanics*, 55(1):65–72, 1988.

[65] D J Bammann and G C Johnson. On the kinematics of finite-deformation plasticity. *Acta Mechanica*, 70(1-4):1–13, 1987.

[66] D Bammann and E Aifantis. A model for finite-deformation plasticity. *Acta Mechanica*, 69(1):97–117, 1987.

[67] E C Aifantis. The physics of plastic deformation. *International Journal of Plasticity*, 3(3):211–247, 1987.

[68] D C Stouffer and T L Dame. *Inelastic deformation of metals: models, mechanical properties, and metallurgy*. John Wiley & Sons, 1996.

[69] W Zhang and Y Cai. Review of Damage Mechanics. In *Continuum Damage Mechanics and Numerical Applications*, chapter 2, pages 15–57. Springer Berlin Heidelberg, 2010.

[70] L M Kachanov. Time of the rupture process under creep conditions. *Academy of Sciences of the Union of Soviet Socialist Republics - USSR*, 8:26–31, 1958.

[71] J Lemaitre and J L Chaboche. *Mechanics of solid materials*. Cambridge University Press, 1990.

[72] J Lemaitre and R Desmorat. *Engineering damage mechanics: ductile, creep, fatigue and brittle failures*. Springer Science & Business Media, 2005.

[73] A C F Cocks and M F Ashby. On creep fracture by void growth. *Progress in Materials Science*, 27:189–244, 1982.

[74] D J Bammann and E C Aifantis. A damage model for ductile metals. *Nuclear Engineering and Design*, 116(3):355–362, 1989.

[75] N Petrinic, C R Siviour, J L Curiel Sosa, and B C F Elliott. On competing volumetric and deviatoric damage mechanisms in simulation of ductile fracture in Ti64 alloy at high rates of strain. In *Proceedings of Euromech EMMC-10 Conference Multiphase and multi-component materials under dynamic loading, Kazimierz Dolny*, pages 467–478, 2007.

[76] G L Wulf. High strain rate compression of titanium and some titanium alloys. *International Journal of Mechanical Sciences*, 21(12):713–718, 1979.

[77] D R Chichili, K T Ramesh, and K J Hemker. The high-strain-rate response of alpha-titanium: experiments, deformation mechanisms and modeling. *Acta Materialia*, 46(3):1025–1043, 1998.

[78] W S Lee and C F Lin. Plastic deformation and fracture behaviour of Ti-6Al-4V alloy loaded with high strain rate under various temperatures. *Materials Science and Engineering: A*, 241(1):48–59, 1998.

[79] X Y Wu, K T Ramesh, and T W Wright. The dynamic growth of a single void in a viscoplastic material under transient hydrostatic loading. *Journal of the Mechanics and Physics of Solids*, 51(1):1–26, 2003.

[80] V Tvergaard. Material failure by void growth to coalescence. *Advances in applied Mechanics*, 27(1):83–151, 1990.

[81] A Molinari and T W Wright. A physical model for nucleation and early growth of voids in ductile materials under dynamic loading. *Journal of the Mechanics and Physics of Solids*, 53(7):1476–1504, 2005.

[82] V Tvergaard and J W Hutchinson. Effect of initial void shape on the occurrence of cavitation instabilities in elastic-plastic solids. *Journal of Applied Mechanics*, 60(4):807–812, 1993.

[83] V Tvergaard, Y Huang, and J W Hutchinson. Cavitation instabilities in a power hardening elastic-plastic solid. *European Journal of Mechanics, A/Solids*, 11(2):215–231, 1992.

[84] M Ortiz and A Molinari. Effect of strain hardening and rate sensitivity on the dynamic growth of a void in a plastic material. *Journal of Applied Mechanics*, 59(1):48–53, 1992.

[85] G R Johnson and W H Cook. Fracture characteristics of three metals subjec-

ted to various strains, strain rates, temperatures and pressures. *Engineering Fracture Mechanics*, 21(1):31–48, 1985.

[86] R J Clifton, J Duffy, K A Hartley, and T G Shawki. On critical conditions for shear band formation at high strain rates. *Scripta Metallurgica*, 18(5):443–448, 1984.

[87] K A Hartley, J Duffy, and R H Hawley. Measurement of the temperature profile during shear band formation in steels deforming at high strain rates. *Journal of the Mechanics and Physics of Solids*, 35(3):283–301, 1987.

[88] B Dodd and Y Bai. *Adiabatic shear localization: frontiers and advances*. Elsevier, 2012.

[89] X Liu, C Tan, J Zhang, F Wang, and H Cai. Correlation of adiabatic shearing behavior with fracture in Ti-6Al-4V alloys with different microstructures. *International Journal of Impact Engineering*, 36(9):1143–1149, 2009.

[90] H Couque, G Nicolas, and C Altmayer. Relation between shear banding and penetration characteristics of conventional tungsten alloys. *International Journal of Impact Engineering*, 34(3):412–423, 2007.

[91] Q M Li and N Jones. Shear and adiabatic shear failures in an impulsively loaded fully clamped beam. *International Journal of Impact Engineering*, 22(6):589–607, 1999.

[92] Q M Li and N Jones. Response and failure of a double-shear beam subjected to mass impact. *International Journal of Solids and Structures*, 39(7):1919–1947, 2002.

[93] T Børvik, O S Hopperstad, M Langseth, and K A Malo. Effect of target thickness in blunt projectile penetration of weldox 460E steel plates. *International Journal of Impact Engineering*, 28(4):413–464, 2003.

[94] T Børvik, M Langseth, O S Hopperstad, and K A Malo. Ballistic penetration of steel plates. *International Journal of Impact Engineering*, 22(9):855–886, 1999.

[95] T Børvik, J R Leinum, J K Solberg, O S Hopperstad, and M Langseth. Observations on shear plug formation in weldox 460 e steel plates impacted by blunt-nosed projectiles. *International Journal of Impact Engineering*, 25(6):553–572, 2001.

[96] J Rösler, H Harders, and M Bäker. *Mechanical behaviour of engineering materials: metals, ceramics, polymers, and composites*. Springer Science & Business Media, 2007.

[97] S C Liao and J Duffy. Adiabatic shear bands in a TI-6Al-4V titanium alloy. *Journal of the Mechanics and Physics of Solids*, 46(11):2201–2231, 1998.

[98] M G Da Silva and K T Ramesh. The rate-dependent deformation and localization of fully dense and porous Ti-6Al-4V. *Materials Science and Engineering: A*, 232(1):11–22, 1997.

[99] X Teng, T Wierzbicki, and H Couque. On the transition from adiabatic shear banding to fracture. *Mechanics of Materials*, 39(2):107–125, 2007.

[100] T L Anderson. *Fracture mechanics: fundamentals and applications*. CRC press, 2005.

[101] Y Bao. *Prediction of ductile track formation in uncracked bodies*. PhD thesis, Massachusetts Institute of Technology, 2003.

[102] Y Bao and T Wierzbicki. A comparative study on various ductile crack formation criteria. *Journal of Engineering Materials and Technology*, 126(3):314–324, 2004.

[103] Y Bao and T Wierzbicki. On fracture locus in the equivalent strain and stress triaxiality space. *International Journal of Mechanical Sciences*, 46(1):81–98, 2004.

[104] M Giglio, A Manes, and F Vigano. Ductile fracture locus of Ti-6Al-4V titanium alloy. *International Journal of Mechanical Sciences*, 54(1):121–135, 2012.

[105] J L Sun, P W Trimby, F K Yan, X Z Liao, N R Tao, and J T Wang. Shear banding in commercial pure titanium deformed by dynamic compression. *Acta Materialia*, 79:47–58, 2014.

[106] Q Xue, M A Meyers, and V F Nesterenko. Self-organization of shear bands in titanium and Ti-6Al-4V alloy. *Acta Materialia*, 50(3):575–596, 2002.

[107] J Peirs, P Verleysen, J Degrieck, and F Coghe. The use of hat-shaped specimens to study the high strain rate shear behaviour of Ti-6Al-4V. *International Journal of Impact Engineering*, 37(6):703–714, 2010.

[108] H Kobayashi and B Dodd. A numerical analysis for the formation of adiabatic shear bands including void nucleation and growth. *International Journal of Impact Engineering*, 8(1):1–13, 1989.

[109] J W Yoon, Y Lou, J Yoon, and M V Glazoff. Asymmetric yield function based on the stress invariants for pressure sensitive metals. *International Journal of Plasticity*, 56:184 – 202, 2014.

[110] R V Mises. Mechanik der festen körper im plastisch-deformablen zustand. *Nachrichten von der Gesellschaft der Wissenschaften zu Göttingen, Mathematisch-Physikalische Klasse*, 1913:582–592, 1913.

[111] H E Tresca. *Mémoires sur l'écoulement des corps solides*. Imprimerie impériale, 1869.

[112] A S Khan and H Liu. Strain rate and temperature dependent fracture criteria for isotropic and anisotropic metals. *International Journal of Plasticity*, 37:1–15, 2012.

[113] A S Khan, S Yu, and H Liu. Deformation induced anisotropic responses of Ti-6Al-4V alloy Part II: A strain rate and temperature dependent anisotropic yield criterion. *International Journal of Plasticity*, 38:14–26, 2012.

[114] M A W Lowden and W B Hutchinson. Texture strengthening and strength differential in Ti-6Al-4V. *Metallurgical Transactions A*, 6(3):441–448, 1975.

[115] W A Spitzig and O Richmond. The effect of pressure on the flow stress of metals. *Acta Metallurgica*, 32(3):457–463, 1984.

[116] T Neeraj, M F Savage, J Tatalovich, L Kovarik, R W Hayes, and M J Mills. Observation of tension–compression asymmetry in α and titanium alloys. *Philosophical Magazine*, 85(2-3):279–295, 2005.

[117] R Hill. Constitutive modelling of orthotropic plasticity in sheet metals. *Journal of the Mechanics and Physics of Solids*, 38(3):405–417, 1990.

[118] F Barlat, D J Lege, and J C Brem. A six-component yield function for anisotropic materials. *International Journal of Plasticity*, 7(7):693 – 712, 1991.

[119] O Cazacu and F Barlat. Generalization of Drucker's yield criterion to orthotropy. *Mathematics and Mechanics of Solids*, 6(6):613–630, 2001.

[120] A P Karafillis and M C Boyce. A general anisotropic yield criterion using bounds and a transformation weighting tensor. *Journal of the Mechanics and Physics of Solids*, 41(12):1859–1886, December 1993.

[121] M E Nixon, O Cazacu, and R A Lebensohn. Anisotropic response of high-purity α-titanium: Experimental characterization and constitutive modeling. *International Journal of Plasticity*, 26(4):516–532, 2010.

[122] A M Habraken. Modelling the plastic anisotropy of metals. *Archives of Computational Methods in Engineering*, 11(1):3–96, 2004.

[123] M S Burkins, W W Love, and J R Wood. Effect of annealing temperature on the ballistic limit velocity of Ti-6A1-4V ELI. Technical report, DTIC Document, 1997.

[124] B K Kad, S E Schoenfeld, and M S Burkins. Through thickness dynamic impact response in textured Ti-6Al-4V plates. *Materials Science and Engineering: A*, 322(1):241–251, 2002.

[125] R Hill. A user-friendly theory of orthotropic plasticity in sheet metals. *International Journal of Mechanical Sciences*, 35(1):19–25, 1993.

[126] F. Barlat and K. Lian. Plastic behavior and stretchability of sheet metals. Part I: A yield function for orthotropic sheets under plane stress conditions. *International Journal of Plasticity*, 5(1):51–66, January 1989.

[127] O G Lademo, O S Hopperstad, and M Langseth. An evaluation of yield criteria and flow rules for aluminium alloys. *International Journal of Plasticity*, 15(2):191–208, 1999.

[128] T B Stoughton and J W Yoon. Anisotropic hardening and non-associated flow in proportional loading of sheet metals. *International Journal of Plasticity*, 25(9):1777 – 1817, 2009. Exploring New Horizons of Metal Forming Research.

[129] H C Wu. Anisotropic plasticity for sheet metals using the concept of combined isotropic-kinematic hardening. *International Journal of Plasticity*, 18(12):1661–1682, 2002.

[130] T B Stoughton. A non-associated flow rule for sheet metal forming. *International Journal of Plasticity*, 18(5-6):687–714, October 2002.

[131] M Brunet, F Morestin, and S Godereaux. Nonlinear kinematic hardening identification for anisotropic sheet metals with bending-unbending tests. *Journal of Engineering Materials and Technology*, 123(4):378–383, 2001.

[132] M Wali, H Chouchene, L Ben Said, and F Dammak. One-equation integration algorithm of a generalized quadratic yield function with Chaboche non-linear isotropic/kinematic hardening. *International Journal of Mechanical Sciences*, 92:223–232, 2015.

[133] I N. Vladimirov, M P. Pietryga, and S Reese. Anisotropic finite elastoplasticity with nonlinear kinematic and isotropic hardening and application to sheet metal forming. *International Journal of Plasticity*, 26(5):659–687, May 2010.

[134] H Kuhn and D Medlin. ASM handbook. volume 8: Mechanical testing and evaluation. *ASM International, Member/Customer Service Center, Materials Park, OH 44073-0002, USA, 2000. 998*, 2000.

[135] R Gerlach, C Kettenbeil, and N Petrinic. A new split Hopkinson tensile bar design. *International Journal of Impact Engineering*, 50(0):63–67, 2012.

[136] S T Chiou, H L Tsai, and W S Lee. Effects of strain rate and temperature on the deformation and fracture behaviour of titanium alloy. *Materials Transactions*, 48(9):2525–2533, 2007.

[137] D J Parry, A G Walker, and P R Dixon. Hopkinson bar pulse smoothing. *Measurement Science and Technology*, 6(5):443, 1995.

[138] A C F Cocks and M F Ashby. *Creep fracture by void growth.* Springer, 1981.

[139] D J Bammann and M F Chiesa. Failure in ductile materials using finite element simulations. In *The 3rd International Symposium on Structural Crashworthiness and Failure*, University of Liverpool, 1993. Elsevier Applied Science.

[140] D J Bammann, M L Chiesa, M F Horstemeyer, and L I Weingarten. Failure in ductile materials using finite element methods. *Structural Crashworthiness and Failure*, pages 1–54, 1993.

[141] M F Horstemeyer, J Lathrop, A M Gokhale, and M Dighe. Modeling stress state dependent damage evolution in a cast Al-Si-Mg aluminum alloy. *Theoretical and Applied Fracture Mechanics*, 33(1):31–47, 2000.

[142] Y Hammi, M F Horstemeyer, and D J Bammann. An anisotropic damage model for ductile metals. *International Journal of Damage Mechanics*, 12(3):245–262, 2003.

[143] K Enakoutsa, Fazle R Ahad, K N Solanki, Y Tjiptowidjojo, and D J Bammann. Using damage delocalization to model localization phenomena in Bammann-Chiesa-Johnson metals. *Journal of Engineering Materials and Technology*, 134(4):041014, 2012.

[144] B D Coleman and M E Gurtin. Thermodynamics with internal state variables. *The Journal of Chemical Physics*, 47(2):597–613, 1967.

[145] Z P Bažant, M Gattu, and J Vorel. Work conjugacy error in commercial finite-element codes: its magnitude and how to compensate for it. In *Proceedings of the Royal Society of London A: Mathematical, Physical and Engineering Sciences*. The Royal Society, 2012.

[146] J L Chaboche. On some modifications of kinematic hardening to improve the description of ratchetting effects. *International Journal of Plasticity*, 7(7):661–678, 1991.

[147] B C F Elliott. *Inverse identification of constitutive parameters for simulation of impact on rate-dependent media*. PhD thesis, Uniersity of Oxford, 2006.

[148] M F Horstemeyer. *Integrated Computational Materials Engineering (ICME) for metals: using multiscale modeling to invigorate engineering design with science.* John Wiley & Sons, 2012.

[149] J R Rice and D M Tracey. On the ductile enlargement of voids in triaxial stress fields. *Journal of the Mechanics and Physics of Solids*, 17(3):201–217, 1969.

[150] H W Kuhn and A W Tucker. Nonlinear programming. In *Proceedings of the Second Berkeley Symposium on Mathematical Statistics and Probability*, pages 481–492, Berkeley, Calif., 1951. University of California Press.

[151] R D Krieg and D B Krieg. Accuracies of numerical solution methods for the elastic-perfectly plastic model. *ASME, Transactions, Series J-Journal of Pressure Vessel Technology*, 99:510–515, 1977.

[152] M F Horstemeyer, R L Carino, Y Hammi, and K N Solanki. MSU internal state variable plasticity-damage model 1.0 calibration, DMGfit production version users manual. *MSU. CAVS*, 1400:2009–R0010.

[153] F H Wu and L B Freund. Deformation trapping due to thermoplastic instability in one-dimensional wave propagation. *Journal of the Mechanics and Physics of Solids*, 32(2):119–132, 1984.

[154] Z P Bažant and T Belytschko. Wave Propagation in a Strain-Softening Bar:Exact Solution. *Journal of Engineering Mechanics*, 111(3):381–389, 1985.

[155] A Needleman. Material rate dependence and mesh sensitivity in localization problems. *Computer Methods in Applied Mechanics and Engineering*, 67(1):69–85, 1988.

[156] R De Borst, M A Crisfield, J C Remmers, and C V Verhoosel. *Nonlinear finite element analysis of solids and structures.* John Wiley & Sons, 2012.

[157] R Chait. The strength differential of steel and Ti alloys as influenced by test temperature and microstructure. *Scripta Metallurgica*, 7(4):351–354, 1973.

[158] J Casey and T D Sullivan. Pressure dependency, strength-differential effect, and plastic volume expansion in metals. *International Journal of Plasticity*, 1(1):39–61, 1985.

[159] S K Iyer and C J Lissenden. Multiaxial constitutive model accounting for the strength-differential in Inconel 718. *International Journal of Plasticity*, 19(12):2055 – 2081, 2003. Special Issue in Honour of Professor Zenon Mroz.

[160] S M Arnold, A F Saleeb, and M G Castelli. A fully associative, nonlinear kinematic, unified viscoplastic model for titanium-based matrices. *ASTM Special Technical Publication*, 1253:231–256, 1996.

[161] W P Schellart. Shear test results for cohesion and friction coefficients for different granular materials: scaling implications for their usage in analogue modelling. *Tectonophysics*, 324(1):1–16, 2000.

[162] R Hill. *The mathematical theory of plasticity*, volume 11. Oxford University Press, 1998.

[163] S Bagherzadeh, M J Mirnia, and B Mollaei Dariani. Numerical and experimental investigations of hydro-mechanical deep drawing process of laminated aluminum/steel sheets. *Journal of Manufacturing Processes*, 18:131 – 140, 2015.

[164] Ahmadi S, Eivani A R, and Akbarzadeh A. Experimental and analytical studies on the prediction of forming limit diagrams. *Computational Materials Science*, 44(4):1252 – 1257, 2009.

[165] G Charca Ramos, M Stout, R E Bolmaro, J W Signorelli, and P Turner. Study of a drawing-quality sheet steel: Stress/strain behaviors and Lankford coeffi-

cients by experiments and micromechanical simulations. *International Journal of Solids and Structures*, 47(17):2285 – 2293, 2010.

[166] E Wielewski, M R Arthington, C R Siviour, and N Petrinic. Characterising the effects of strain rate, crystallographic texture and direction of loading on the mechanical behaviour of Ti-6Al-4V. *Journal of Dynamic Behavior of Materials*, 1(4):462–471, 2015.

[167] Y Yan, H Wang, and Q Li. The inverse parameter identification of Hill 48 yield criterion and its verification in press bending and roll forming process simulations. *Journal of Manufacturing Processes*, 2015.

[168] B Raniecki and Z Mróz. Yield or martensitic phase transformation conditions and dissipation functions for isotropic, pressure-insensitive alloys exhibiting SD effect. *Acta Mechanica*, 195(1):81–102, 2008.

[169] M Arthington, C Siviour, N Petrinic, and B Elliott. Strain rate dependence of Ti64: Characterisation of mechanical properties up to failure using novel optical techniques. In *DYMAT-International Conference on the Mechanical and Physical Behaviour of Materials under Dynamic Loading*, volume 1, pages 193–199. EDP Sciences, 2009.

[170] N Petrinic. *Aspects of discrete element modelling involving facet-to-facet contact detection and interaction*. PhD thesis, University of Wales Swansea, 1996.

[171] K Murugaratnam. *A Refined Numerical Modelling Technique for Shot Peening*. PhD thesis, University of Oxford, Oxford, 2015.

[172] W W Chen and B Song. *Split Hopkinson (Kolsky) bar: design, testing and applications*. Springer Science & Business Media, 2010.